https://theses.gla.ac.uk/

Theses Digitisation:

https://www.gla.ac.uk/myglasgow/research/enlighten/theses/digitisation/

This is a digitised version of the original print thesis.

Copyright and moral rights for this work are retained by the author

A copy can be downloaded for personal non-commercial research or study, without prior permission or charge

This work cannot be reproduced or quoted extensively from without first obtaining permission in writing from the author

The content must not be changed in any way or sold commercially in any format or medium without the formal permission of the author

When referring to this work, full bibliographic details including the author, title, awarding institution and date of the thesis must be given

Enlighten: Theses
https://theses.gla.ac.uk/
research-enlighten@glasgow.ac.uk

TEM INVESTIGATION OF SILICON DEVICES

Richard Lindsay

submitted for the degree of Doctor of Philosophy at the Department of Physics and Astronomy, University of Glasgow.

September, 1998

© 1998 Richard Lindsay

ProQuest Number: 10992326

All rights reserved

INFORMATION TO ALL USERS
The quality of this reproduction is dependent upon the quality of the copy submitted.

In the unlikely event that the author did not send a complete manuscript
and there are missing pages, these will be noted. Also, if material had to be removed,
a note will indicate the deletion.

ProQuest 10992326

Published by ProQuest LLC (2018). Copyright of the Dissertation is held by the Author.

All rights reserved.
This work is protected against unauthorized copying under Title 17, United States Code
Microform Edition © ProQuest LLC.

ProQuest LLC.
789 East Eisenhower Parkway
P.O. Box 1346
Ann Arbor, MI 48106 – 1346

GLASGOW
UNIVERSITY
LIBRARY

11387 (copy 1)

SUMMARY

As the layers of materials in a silicon device decrease in thickness in order to improve the performance of the device, analytical techniques with nanometre resolution are required to characterise the materials. The aim of this project was to evaluate and demonstrate the TEM for use in materials characterisation in device technology. In doing so, new TEM techniques have been devised and existing techniques have been developed to describe the fine structure of a material and what happens at the interfaces between different materials.

To understand the areas of device technology which require materials characterisation the relevant principles behind the operation of a device have been explained. The performance of existing analytical techniques which are used in the industry have been described for future comparison to the TEM techniques used in this work. The theory behind these TEM techniques was then explained and the properties of the electron beam were investigated both theoretically and experimentally. The beam properties included the probe diameter, current and current density, as these often define the limits of useful microanalysis.

The capability of TEM imaging as a method of investigating the coarse and fine structure of device components was demonstrated. The diffraction contrast encountered in TEM imaging provides information on the atomic structure of materials. Using TEM imaging and diffraction, a new technique was devised to determine the grain size distribution of a conducting film involving the application of Voronoi statistics and other models. This technique enables the grain size distribution of a film in a fully-processed device to be determined at any level through the film thickness. A description

of the principal mechanisms for normal and abnormal grain growth was provided to explain the experimental results. A critical evaluation of the existing statistical models which mimic grain growth was given to determine their accuracy. The grain size distribution was calculated for two Al films with columnar grains and the Voronoi model was shown to be applicable to the analysis.

Two diffraction techniques were developed to enable a quantitative description of the distribution of orientations, or texture, in a film. The first uses Kikuchi diffraction patterns for the identification of individual grain orientations, and the other uses a new scanning technique to measure the level of texturing in a film. The analyses used for both diffraction techniques are original and a definition of the 'degree of texture' has been proposed. The scanning technique can be modified to evaluate the degree of texture at a particular depth through the thickness of a film thereby allowing a description of the development of the texture. The texture development was determined for a polycrystalline Si film and scanning dark field imaging was used to verify the results and provide a visual description of the grain growth in a textured film.

The limits and capabilities of TEM microanalysis have been explored using Si devices and GaAs samples. The techniques involved were EDX and PEELS. EDX was investigated for its spatial resolution and its sensitivity to traces of dopants both theoretically and experimentally. In its various forms, EDX was then was used to identify a source of unknown material which appeared to be a result of a flaw in the fabrication of the device. Compositional profiles of Al, Si and Ti across a Ti/TiN diffusion barrier were used to determine the effectiveness of the barrier in separating the Al and Si to either side of it. The possible roles of PEELS in device technology were also discussed. It was then used to determine the N composition through the same Ti/TiN barrier to complement the earlier EDX results . The results from both PEELS and EDX analysis demonstrated the high level of quantitative information available in identifying the composition of a material on a nanometre scale.

DECLARATION

This thesis is a record of work carried out by me in the Department of Physics and Astronomy at the University of Glasgow. The work described herein is my own apart from the preparation of the silicon devices. These devices were provided by Motorola Ltd, UK. Some of the work contained in this thesis has been published in the following papers:

R. Lindsay, J. N. Chapman, A. J. Craven, D. McBain, *'Polycrystalline grain structure in VLSI devices'*, IOP conference series in Microscopy of Semiconducting Materials, p423, (1997).

A. J. Craven, W. A. P. Nicholson, R. Lindsay, *'A method of studying texture development in thin films'*, Electron Microscopy and Analysis, IOP Conf. Ser. 153, p327, (1997).

R. Lindsay, J. N. Chapman, A. J. Craven, D. McBain, I. Molchanov, *'Grain size distribution and degree of texture in films used in ICs'*, in press in MRS proceedings, (1998)

R. Lindsay, J. N. Chapman, A. J. Craven, D. McBain, *'The Development of the Degree of Texture in films used in ICs'*, submitted to Ultramicroscopy

This thesis has not been previously submitted for a higher degree.

ACKNOWLEDGEMENTS

My sincere gratitude goes to my supervisors, Profs. John N Chapman and Alan J Craven, without whom much of this thesis would be full of my wrong opinions. They provided much of the inspiration for the ideas in this thesis and kept me on the right tracks. Thanks also to my industrial supervisors Donna McBain and Grant MacNeil from Motorola in East Kilbride for supplying the samples and letting me loose in the failure analysis lab at Motorola.

Although they got more out of me than I of them, the students and postdocs in SSP supplied me with invaluable advice throughout my PhD sentence. PEELS and EDX wouldn't have been possible without Dr Maureen MacKenzie who I'm sure is still hoarding one of my specimens. Thanks to Peter Aitchison for introducing me to the CM20, and for the numerous discussions on how to get rich quick. Cheers Andy for the help with the C-programming in Unix, the user friendly system. My thanks extend to the rest of the group for all the laughs we had.

Jonathan Barnard at Bristol University showed me the ropes (literally) regarding specimen preparation of which I am grateful. Thanks to Pat Nicholson, Alan Howie, Steven Connor, Donald MacDonald, Sam McFadzean, Colin How, and Billy 'Beckham' Smith for all their technical support. They were certainly kept busy.

As for funding, my greatest thanks to EPSRC and Motorola, East Kilbride, for my grants. Thanks also go to the committee of lecturers who saw fit to award me £575 for my second year report. Every penny was spent wisely.

My family have always been there to encourage and look after me so thanks Meemsk, Deesk, Del and Boab. Another special thanks to my close friends and 'the burd' who all helped me take my mind off work at nights. Thanks also to Brunswick Cellars for £1 a pint on a Thursday so that I could still afford the bus into Uni.

CONTENTS

Summary I
Declaration III
Acknowledgements IV

CHAPTER 1: ***Materials Characterisation in Silicon Devices***

1.1 Introduction 1
1.2 Silicon Device Technology 2
1.2.1 Current Device Performance 2
1.2.2 Device Fabrication 2
1.3 Device Analytical Techniques 8
1.3.1 Introduction 8
1.3.2 Secondary-Ion Mass Spectrometry (SIMS) 9
1.3.3 Auger Electron Spectroscopy (AES) 10
1.3.4 Rutherford Back Scattering (RBS) 12
1.3.5 Comparison of depth profiling techniques 13
1.3.6 X-ray Topography 14
1.3.7 X-ray Diffractometer 15
1.3.8 Scanning Electron Microscopy (SEM) 15
1.3.9 Summary of Techniques 17
1.4 Transmission Electron Microscopy (TEM) 17

CHAPTER 2: ***Instrumentation and Evaluation of Basic Techniques***

2.1 Introduction 21
2.2 TEM Configuration 21
2.3 Imaging 23
2.4 Theoretical Probe Size Considerations 26
2.5 Experimental Probe Characteristics 29
2.5.1 Introduction 29
2.5.2 Probe Diameter 29
2.5.3 Probe Current 40
2.5.4 Summary 46
2.6 Diffraction 47
2.6.1 Theory 47
2.6.2 Diffraction Techniques 49
2.7 EDX 51
2.7.1 Theory 51
2.7.2 The EDX Detector 53
2.7.3 Analysis of Data 53
2.8 EELS 54
2.8.1 Theory 54
2.8.2 The EELS Spectrometer 57
2.8.3 Analysis of Data 58

CHAPTER 3: *Specimen Preparation and Imaging of Device Structures*

3.1 Introduction **61**
3.2 Focused Ion Beam (FIB) Specimen Preparation **62**
3.3 Tripod Polishing **63**
3.3.1 Introduction 63
3.3.2 Polishing First Side 64
3.3.3 Polishing Second Side 67
3.3.4 Mounting on Copper Washer 68
3.3.5 Quality of Specimen 70
3.3.6 Tripod Polishing vs. FIB 72
3.4 Structural Information Available from Imaging **73**
3.4.1 Introduction 73
3.4.2 Thickness uniformity of Films 74
3.4.3 Structural Defects 79
3.4.4 Dopant, vacancy and Impurity Profiles 82
3.4.5 Grain Structure 83
3.4.6 Drawback of using TEM analysis 85

CHAPTER 4: *Grain Size Distribution of Conducting Films*

4.1 Introduction **88**
4.2 Grain Size Influence on Electrical Properties **88**
4.3 Grain Growth Mechanisms in Silicon Devices **90**
4.4 Existing Techniques for the Measurement of Grain Sizes **92**
4.5 A New Technique for Measuring Grain Sizes **93**
4.5.1 Introduction 93
4.5.2 Technique 94
4.6 Voronoi Statistics **98**
4.6.1 Introduction 98
4.6.2 Equiaxed Columnar, or Quasi-2D, Growth 99
4.6.3 Non-columnar, or 3D, Growth 105
4.6.4 Summary of Voronoi Statistics 107
4.7 Results **108**
4.8 Discussion **112**

CHAPTER 5: *Determining the Grain Orientation Distribution*

5.1 Introduction **117**
5.2 Effect of POs on Film Properties **117**
5.3 Growth Mechanisms for POs **118**
5.4 Identification of POs using Kikuchi Patterns **120**
5.4.1 Introduction 120
5.4.2 Technique 121
5.4.3 Calculation of the Orientation from the Kikuchi Pattern 123
5.4.4 Representation of the Orientation Distribution 129
5.4.5 Results 133
5.4.6 Summary and Discussion 135
5.5 Identification of POs using a Scanning Technique **136**
5.5.1 Introduction 136

5.5.2 Technique 137
5.5.3 Results 139
5.5.4 Discussion and Comparison 143

CHAPTER 6: *Development of the Degree of Texture through a Film*

6.1 Introduction 148
6.2 Definition of the Degree of Texture 148
6.3 Existing Texture Investigating Techniques 150
6.3.1 Overview 150
6.3.2 Electron Diffraction Techniques 153
6.3.3 Summary of Texture Techniques 154
6.4 Scanning Diffraction Texture Analysis 154
6.4.1 Experiment 154
6.4.2 Information Available from the Diffraction Pattern 157
6.4.3 Diffraction Theory for Textured Films 160
6.4.4 Determination of the Electron Intensity Around a Ring 165
6.4.5 Calculation of the Degree of Texture 170
6.4.6 Determination of the Azimuthal Distribution 173
6.4.7 Sub-texturing 175
6.5 Discussion 175
6.6 Summary 180
6.7 Dark Field Texture Analysis 181
6.7.1 Introduction 181
6.7.2 Experiment 181
6.7.3 Discussion 187
6.8 Conclusions 190

CHAPTER 7: *Compositional Analysis of Materials used in ICs*

7.1 Introduction 193
7.2 Spatial Resolution of EDX 194
7.2.1 Introduction 194
7.2.2 EDX on the VG HB5 STEM 195
7.2.3 Specimen Alignment for EDX 196
7.2.4 Experiment 199
7.2.5 EDX Analysis 200
7.2.6 Results 202
7.2.7 Conclusion 208
7.3 Sensitivity of EDX 208
7.3.1 Introduction 208
7.3.2 Experiment 209
7.3.3 Analysis and Results 211
7.3.4 Conclusions 214
7.4 EDX Analysis of a Diffusion Barrier 214
7.4.1 Introduction 214
7.4.2 Background 215
7.4.3 Experiment 217
7.4.4 Results 220
7.4.5 Conclusions 223
7.5 Investigation of Unidentified Material using various approaches in EDX
7.5.1 Introduction 224

7.5.2 Experimental Procedure 225
7.5.3 Conclusion 231
7.6 Compositional Analysis Using PEELS 231
7.6.1 Introduction 231
7.6.2 Effect of Chemical Environment on Peak Shape 232
7.6.3 Nitrogen Profile Through the Ti/ TiN Diffusion Barrier 235
7.6.4 Conclusion 240
7.7 Conclusions 241

CHAPTER 8: *Conclusions & Further Work*

8.1 Overall Aim 244
8.2 Characterising the Fine Structure of Conducting Films 244
8.2.1 Introduction 244
8.2.2 Determination of Grain Sizes 245
8.2.3 Quantifying the Texture in a Film 246
8.2.4 Discussion 248
8.3 Compositional Analysis of Device Materials 249
8.3.1 Introduction 249
8.3.2 Sensitivity and Spatial Resolution 249
8.3.3 Experiments 251
8.3.4 Discussion 251
8.4 Further Work 252

Appendices

A: Spreadsheet used in Kikuchi Analysis 254
B: Program for Calculating Intensity around the {111} Ring 255
C: Program for Mapping Intensity Distribution of Diffraction Pattern 256

CHAPTER ONE

Materials Characterisation in Silicon Devices

1.1 Introduction

Integrated circuits (ICs) occupy a key role in electronics and are to be found in almost every conceivable product of consumer, industrial and military electronics. In such a competitive industry, companies strive to continually improve the performance of each device. It is widely accepted that the performance of a device improves as the size of each component in it reduces. To maintain optimum functionality in scaling down the dimensions of the components in plane, the thickness of the materials which the device is composed has to be reduced accordingly. This process is known as miniaturisation. As the thickness of these layers of materials approach tens of nanometres or less, structural and compositional analysis of the devices require techniques having nanometre spatial resolution and, in some cases, high energy resolution as explained in chapter 7.

In this chapter, various methods of product analysis of ICs are reviewed, leading to the value and position of the transmission electron microscope (TEM) in the electronics industry. Before this, it is helpful to outline the fabrication processes which are integral to practically all ICs.

1.2 Silicon Device Technology

1.2.1 Current Device Performance

The building block of the IC is the transistor. Commercial ICs may contain over 1 million transistors[1]. Depending on their arrangement, the transistors can be used as logic devices like decoders, or memory devices like RAM chips or other electronic microcomponents. To a much lesser extent, ICs may use capacitors and resistors but, arranged correctly, these roles can be performed using transistors.

One of the most important uses for ICs is as computer memory chips or processors. Figure 1.1 shows a modern electrically erasable, programmable read-only memory (EEPROM) device. With the channel length of a transistor (i.e. the area between the source and drain) on today's ICs down to 0.18μm[2], memory chips can hold 512 Mbytes of information and processors can execute over 400 million instructions per second (MIPS). The channel length of the transistor continues to decrease at a remarkably constant 13% every year causing the function density of the chip to increase by 4 every 3 years. The graph in figure 1.2 shows the trend in RAM performance and channel length over the last 20 years. Fundamental properties of the design and the materials used in ICs will enforce limits to the scaling down of component sizes[3]. It is predicted that under current technology impenetrable barriers to further miniaturisation will occur in the decade 2010-2020; here only radical design changes or new materials will allow further miniaturisation[4], [5].

The next section will outline present day fabrication techniques to provide a basis for understanding the performance required of analytical techniques and to relate cross-sectional images seen later to the operation of the component.

1.2.2 Device Fabrication

Silicon is the second most abundant material found on Earth. It forms a very stable

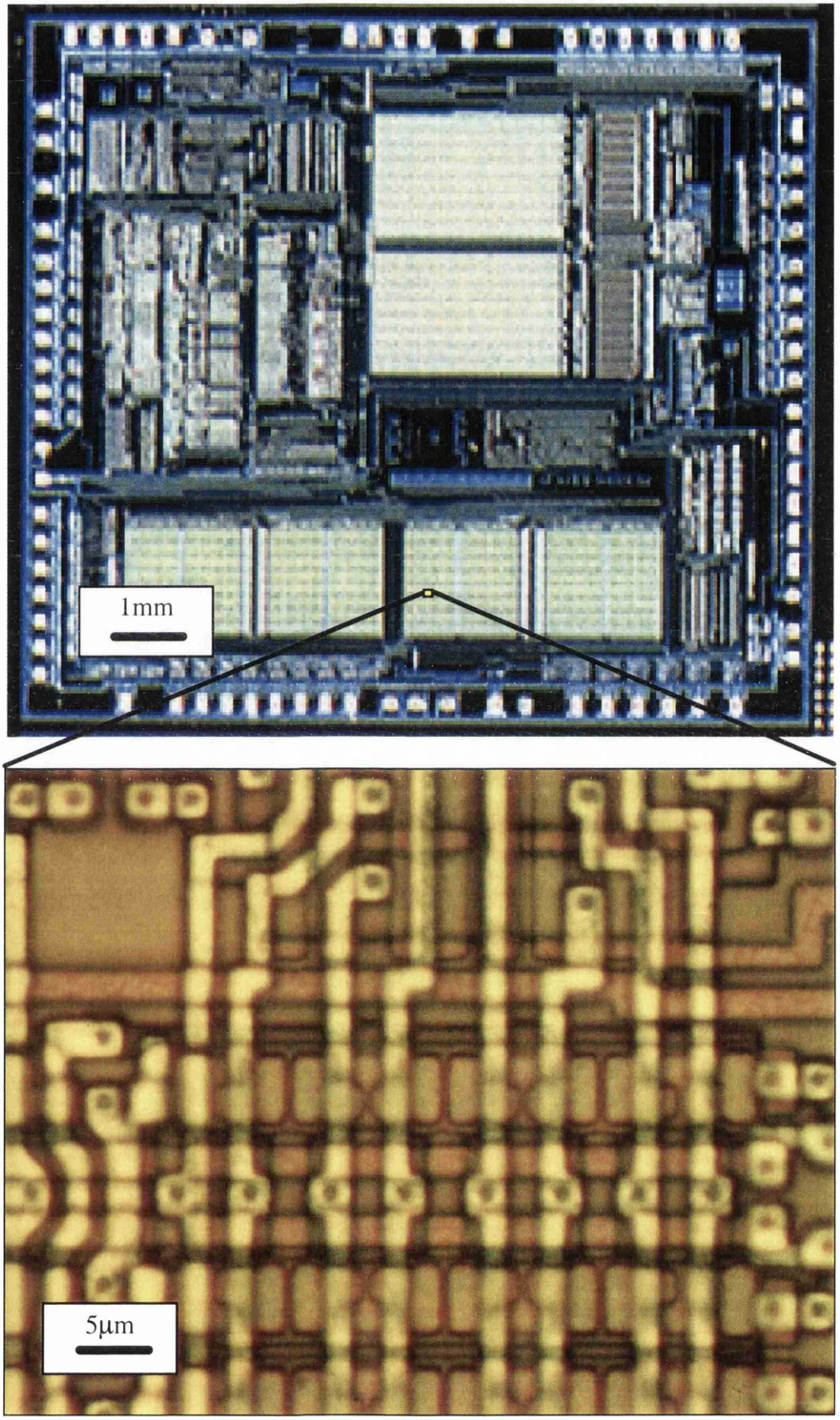

Figure 1.1: *A typical EEPROM device and a high magnification optical image of the memory array on it.*

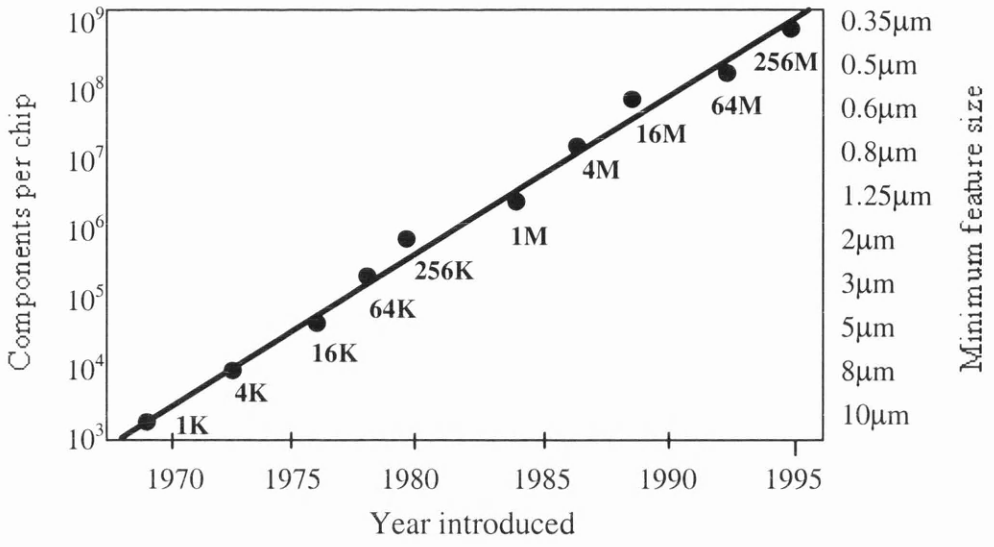

Figure 1.2: *Progress of memory devices over the last 30 years*

insulator in an atmosphere of oxygen and it has favourable electronic semiconducting properties making it the most appropriate choice for use in today's ICs. Some ICs are fabricated using gallium arsenide since this semiconductor has a higher electron mobility than silicon but this advantage is far outweighed by its other properties. These include low thermal stability during device fabrication, a poor thermal oxide for electrical insulation, high defect densities and, above all, higher fabrication costs. These confine its use as a material for ICs to very specific, high speed, applications.

Fabrication of a silicon chip begins with the production of a circular doped silicon wafer. The components on a chip are produced by the deposition and doping of various materials onto this silicon substrate with each layer patterned to give a distinct function and relationship with the surrounding area and subsequent layers.

A family of devices known as nMOS (n-channel metal-oxide-semiconductor) ICs provide building blocks in the fabrication of most of today's ICs[6]. Figure 1.3 shows a top-down view of the layout of an inverter containing 2 transistors - an nMOS and pMOS (p-channel MOS). When used together the device is known as CMOS (complementary MOS). This circuit simply changes the input from 0 to 1 or 1 to 0. Figure 1.4 shows a cross-section of one of these transistors and figure 1.5 shows the

stages involved in its fabrication. Currently, the thickness of the films involved is typically ≤1μm, sometimes as thin as ≈5nm, for oxide dielectric layers. Most ICs use aluminium as long-distance conductors, called interconnects, and doped silicon as local conductors and gates. It seems imminent, however, that copper will succeed aluminium in the near future due to its favourable conducting properties.

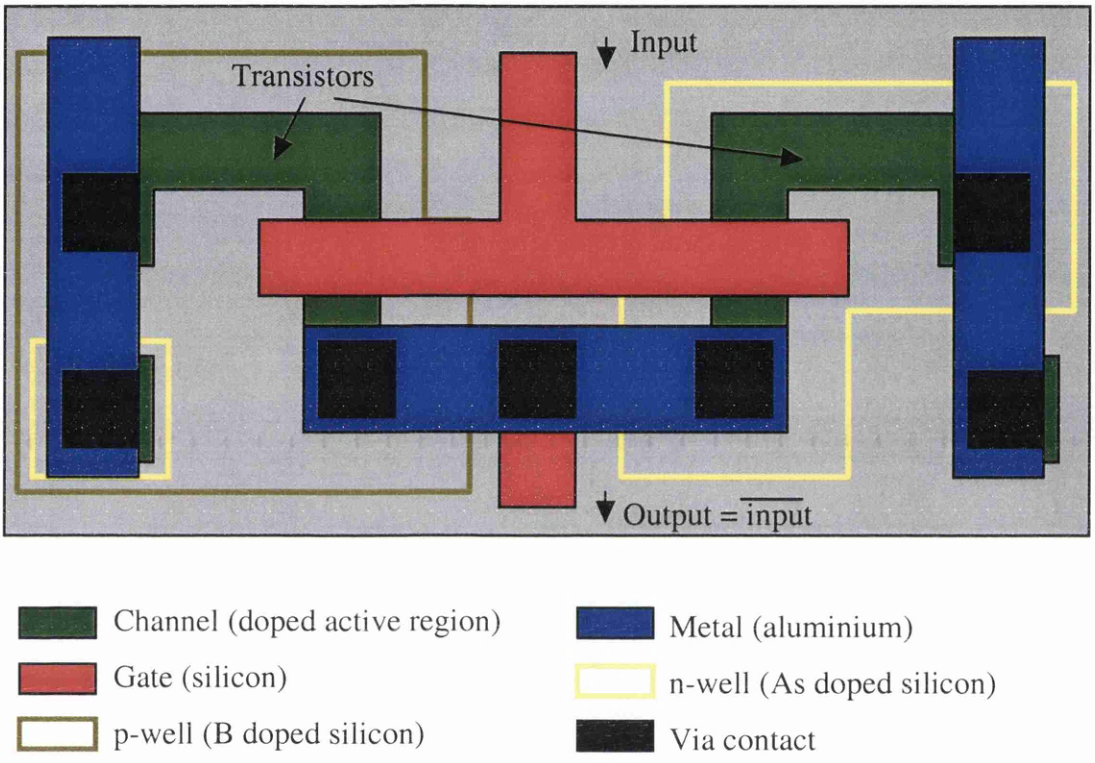

Figure 1.3: *Layout of various metals films forming a CMOS logic inverter from two transistors*

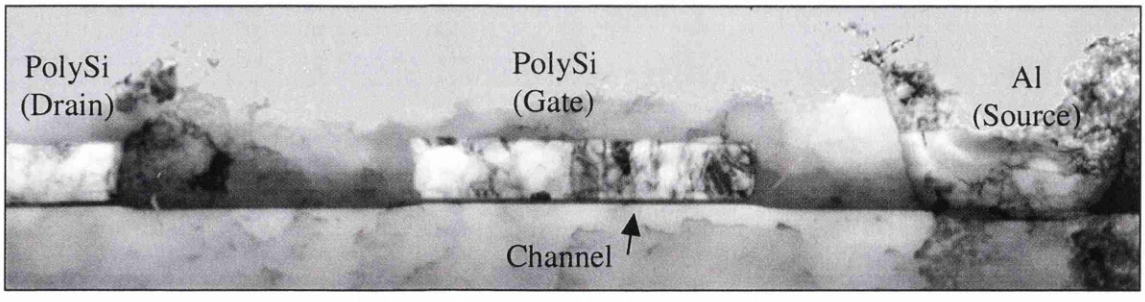

Figure 1.4: *A cross-section through an actual transistor. There are over 1 million of these in modern devices*

1. p-type Boron impurities are introduced as the crystal is grown. Impurity concentrations of 10^{15} - 10^{16} /cm^3 give a resistivity ≈25-2 ohm cm.

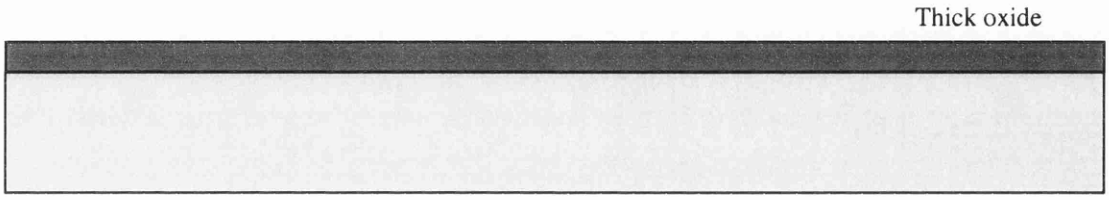

2. A layer of SiO_2, typically 0.1μm thick, is grown all over the surface of the wafer to protect the wafer and act as a barrier to dopants.

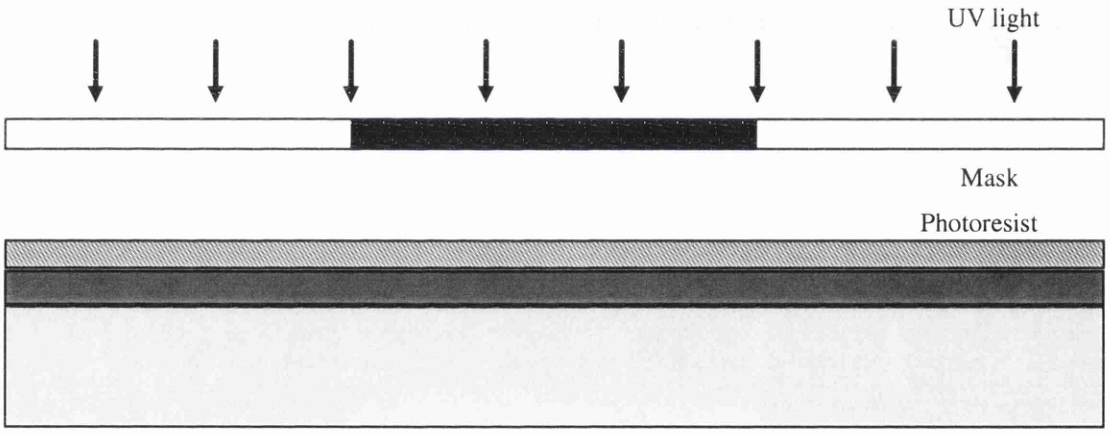

3. A photoresist is spun onto the surface and exposed to UV light through a mask to define those regions into which diffusion is to take place together with transistor channels.

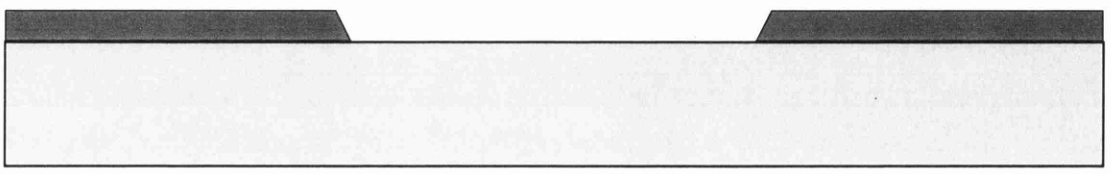

4. These areas are subsequently readily etched away, along with the underlying SiO_2.

***Figure 1.4** cont/*

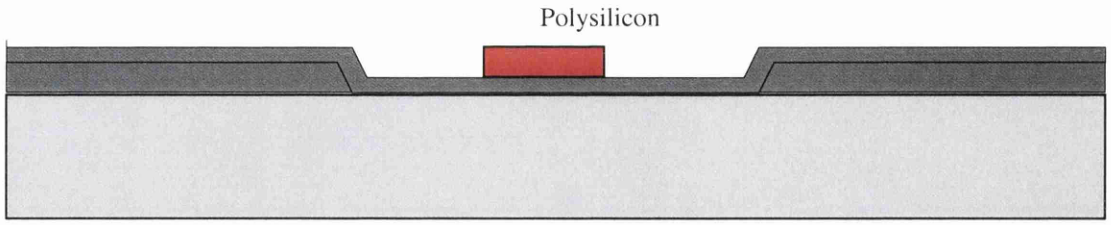

5. A thin layer (typically 0.1μm) of SiO_2 is grown over the entire chip and then polysilicon is deposited to form the gate structure. The polysilicon is heavily doped and deposited by chemical vapour deposition (CVD). Further photoresist coating and masking allows the polysilicon to be patterned.

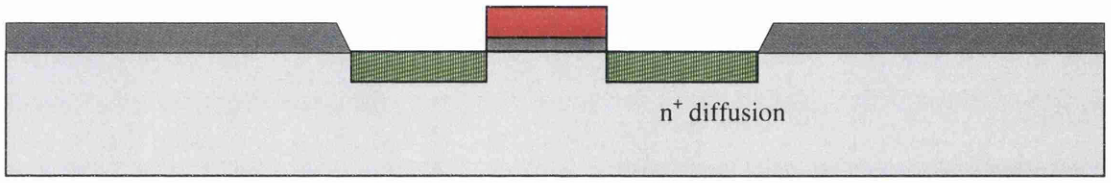

6. The thin oxide is removed to expose areas into which n-type impurities (for an n-channel device) are to be diffused to form the source and drain.

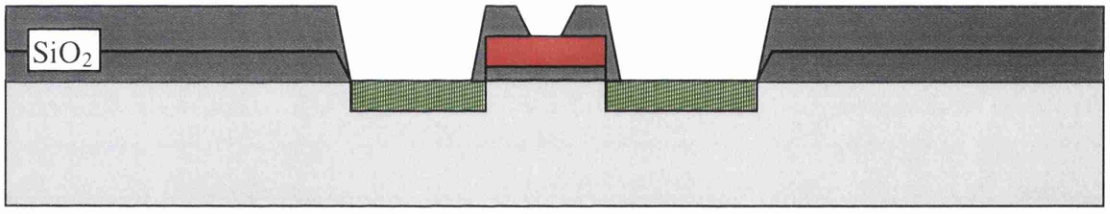

7. Thick oxide is grown all over and selected areas etched where the contacts are to be made.

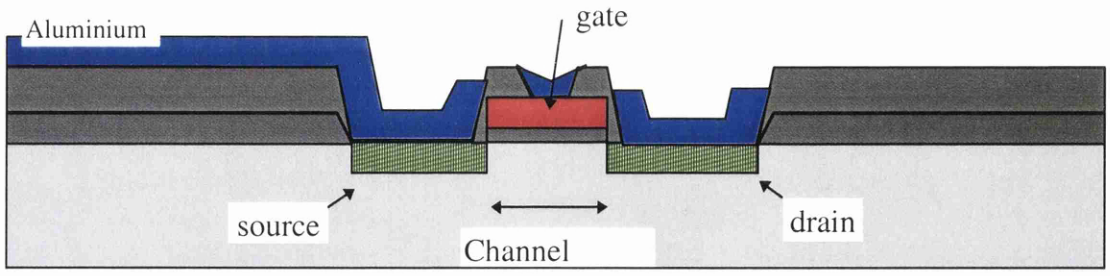

8. Metal (typically aluminium) is deposited and patterned to form the required interconnects.

Figure 1.5: *The main fabrication steps integral to almost all silicon devices*

1.3 Device Analytical Techniques

1.3.1 Introduction

It is apparent from figure 1.5 that, with such thin layers of materials, the performance and reliability of a device depends much on the internal structure of the conductive (e.g. Al, Si) films and how materials interact at the interface with subsequent layers. More specifically, properties of the materials which require monitoring are:

- defect and impurity density
- dopant concentration and distribution
- adhesion and diffusion at interfaces
- grain size and orientation distribution in films
- stress in films
- surface roughness in films
- physical structure abnormalities
- magnetic properties (for future applications, e.g. magnetic RAMs)

The current analytical techniques commonly used to investigate these properties of materials in modern devices are outlined in the next section and are summarised in 1.3.8. This list of techniques only accounts for a fraction of the work carried out in a typical failure analysis (FA) lab in industry. Other techniques may analyse the electrical performance and chemical properties of the device or highlight large defects on the chip. However, the work described in this thesis concerns the application of the TEM as a tool to characterise the fine structure and composition of device materials, so only the techniques which perform similar functions are described for comparison.

1.3.2 Secondary-Ion Mass Spectrometry (SIMS)

SIMS is routinely used as a tool to identify and quantify the concentration of dopants or impurities, although it can be used simply for major or minor compositional determinations[7]. The principle of SIMS analysis is to use an ion beam to sputter the sample surface and to use mass spectrometry techniques to identify the mass-to-charge ratios of the ionic species in the sputtered material.

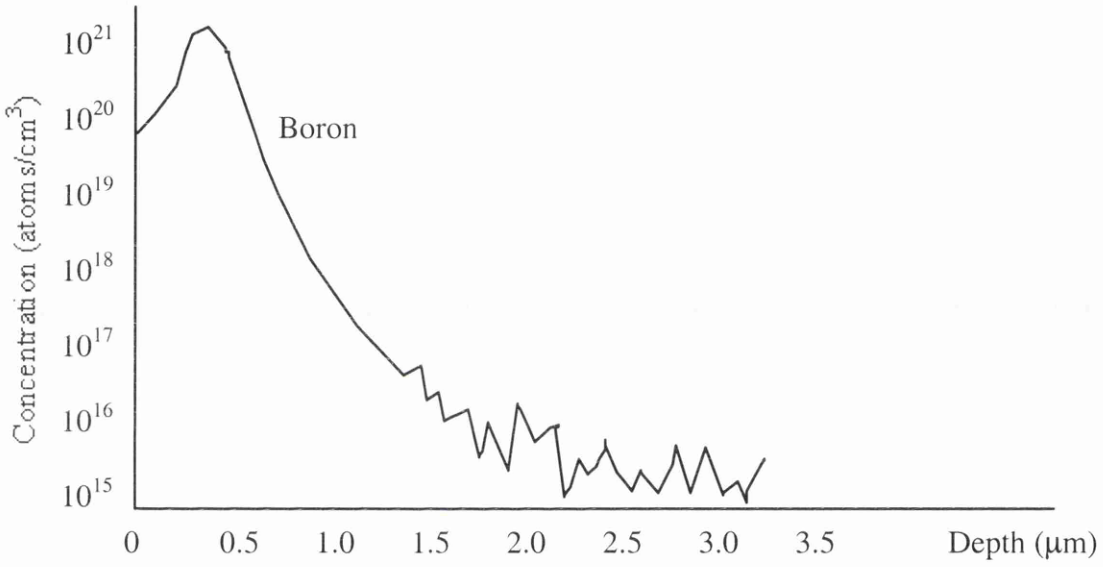

Figure 1.6: *A schematic SIMS profile of the Boron content in an implanted wafer, showing the very high sensitivity of the technique*

The fraction of the sputtered material that is ionised is <0.1% but the total volume sputtered is very large indeed, allowing the technique to be very sensitive to minute concentrations of a dopant. In fact, its detection limits can extend to 1×10^{14} atoms/cm^3, i.e. 0.002ppm, often below the dopant and contamination concentrations usually found in silicon devices. Since the SIMS technique simultaneously sputters the surface, the time scale is directly convertible to a depth scale, producing a very accurate depth-concentration resolution. In fact, depth resolutions better than 40Å are commonplace. An example of a SIMS profile is shown schematically in figure 1.6. Secondary-ion

yields vary by as much as five orders of magnitude across the periodic table. The method is only quantitative if standards for every material and matrix of interest are used. SIMS can be operated to perform elemental mapping with a scanning beam as well as depth profiling. Another important feature of SIMS is its ability to determine how dopants were processed, i.e. whether they were implanted or diffused[8]. This is useful for reverse engineering of other manufacturer's devices.

As with many analytical techniques, SIMS is a destructive technique. Analysing data can also be very complicated as the secondary ion yields depend very strongly on the chemical environment of the atoms investigated. Normally SIMS has been ineffective on insulating materials because of the implantation of charge from the primary beam. However, the recent advent of high-current focused electron neutralising beams has permitted the examination of such technologically important materials as BPSG (the boron-phosphor silicate glass used for electrical insulation and isolation in devices).

Chapter 7 includes an experiment on the detection of As dopants in Si, illustrating the sensitivity of energy dispersive X-rays (EDX) in the TEM to traces of atoms.

1.3.3 Auger Electron Spectroscopy (AES)

AES is normally used to identify elements very near the surface of a material[7]. The principle of AES analysis is to excite atoms on the surface of a sample with a modest energy (≈5keV) electron beam. Electrons in the inner shells of the surface atoms are ejected by collisions with the energetic electrons, leading to the decay of electrons from the higher shells in the same surface atom to fill the vacant states. The energy released in this second process ejects an Auger electron from another higher shell, and these electrons will have an energy characteristic of the separations between the three participating electron levels and so of the atom in which all these processes occur. *X-ray Photoelectron Spectroscopy (XPS)* is very closely related to AES only X-rays are used instead to excite the sample.

An Auger spectrum can be used to identify the elements present in the sample surface since it contains peaks at characteristic energies. However, quantitative analysis is difficult without a wide range of standards. The shape and position of some Auger peaks can also contain information on the chemical state of the atom, e.g. the Si peaks for SiO_2 and crystalline Si are at different energies. Figure 1.7 shows a schematic example where Auger spectroscopy can be used to examine surface compositions. Chapter 8 highlights how electron energy loss spectroscopy (EELS) with a higher energy resolution than AES can be used to derive the chemical state of a substance.

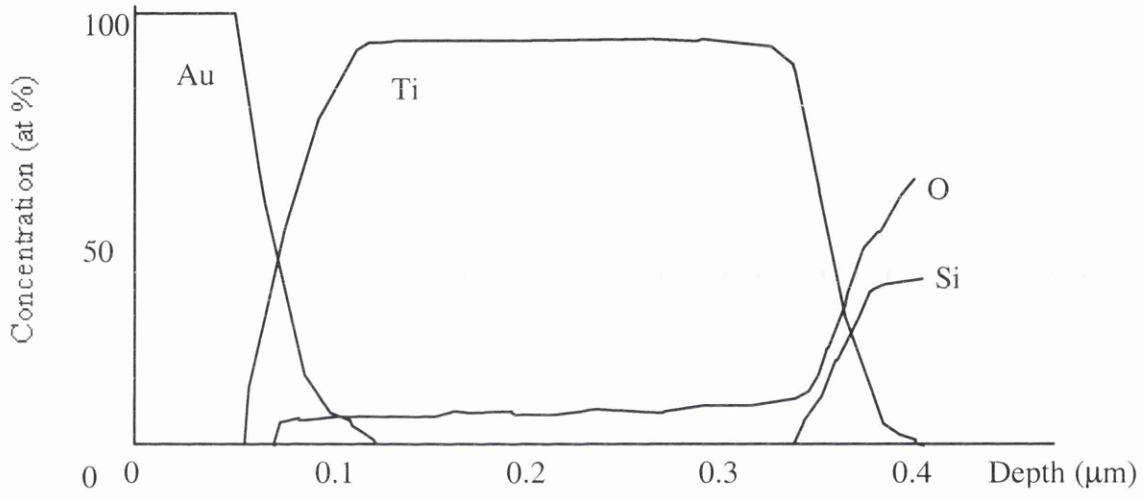

Figure 1.7: *A sputter-etched schematic Auger profile through a Au/Ti/SiO_2 sample.*

The escape depth of Auger electrons ranges from 0.5-2nm, so AES is sensitive only to atoms near the surface. A 2-dimensional profile of the distribution of chosen elements can be obtained by scanning the beam. This technique is known as scanning Auger microscopy (SAM).

AES is useful for studying surface reactions, contamination-related corrosion and surface electromigration phenomena (explained in chapter 4). It is sensitive to almost all the light elements except hydrogen. If a chemical depth profile is required, then a controlled sputtering process can be used to abrade away the sample, indeed the

technique can be used to assess the quality of the sputtering. Modern Auger instrumentation permits the incident focused probe to be ≈50nm in diameter

1.3.4 Rutherford Back Scattering (RBS)

RBS is used to obtain surface elemental information relatively quickly and easily[8]. In RBS, a high energy beam of light atoms, usually H^+ or He^+ ions with energies of 1 to 4MeV, is directed at the sample and penetrates deeply below the surface. The low mass and high energy of the ions ensures very little sputtering occurs and there is almost no lattice damage below the surface. A small fraction of the incident ions are backscattered by direct nuclear collisions and it is their energies which is measured in an RBS experiment.

In a head-on elastic collision between two particles, an incident ion of mass m and energy E_0 and a stationary atom with a mass M on the sample surface, the incident atom will be backscattered with an energy E given by equation 1.1.

$$E = \left(\frac{M-m}{M+m}\right)^2 E_0 \qquad [1.1]$$

Therefore the backscattered ions have energies characteristic of the mass of the surface atoms of the sample. As the ion penetrates into the target, it will gradually lose energy in a series of atomic collisions so the energy of an ion backscattered by an atom at a depth, D is modified as shown in equation 1.2.

$$E = \left(\frac{M-m}{M+m}\right)^2 E_0 - 2D\frac{dE}{dz} \qquad [1.2]$$

Figure 1.8 shows a schematic of an RBS spectrum showing interdiffusion between Ta and Si on a Si substrate[8]. EDX analysis performed over a Si /TiN/ Al interface shown in chapter 8, and illustrates the extent of interdiffusion between the materials. The mass

resolution is good for light elements but rapidly degrades as the atoms become heavier. For this reason it is difficult to distinguish Gallium and Arsenic signals. The non-destructive nature of RBS analysis, and the relatively rapid data collection time, make it particularly suitable for the study of thin film reactions. A major limitation is that the incident beam is usually ≥1mm in width, so electronic devices can rarely be investigated. This leads to problems if the reaction investigated is inhomogeneous over a large area.

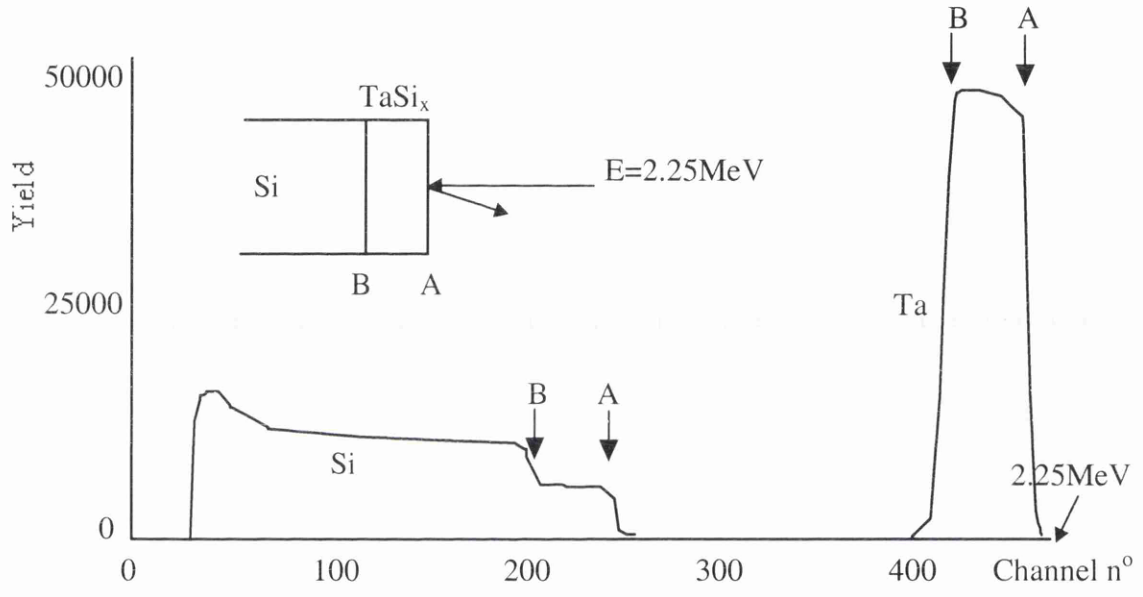

Figure 1.8: *A schematic RBS spectrum taken from a TaSi layer sputter-deposited onto a silicon substrate. Each channel is 4.3keV wide and the vertical scale is the number of $^4He^+$ ions at that energy*

1.3.5 Comparison of Depth Profiling Techniques

SIMS, AES and RBS are primarily depth profiling techniques. The important aspects of their performance are summarised in table 1.1, and are compared later to TEM compositional techniques in chapter 7.

Table 1.1: *Comparison of the performance of commonly used depth profiling techniques*[7]

	SIMS	***AES***	***RBS***
Elements detected	All	>Li	>Li
Chemical specificity	Excellent	Good	Similar mass difficult to distinguish
Detection limits	$>10^{14}$ atoms/cm^3	0.1 at %	0.1 at %
Spatial resolution	50nm-1μm	≈1μm	Poor, ≈1mm beam
Depth resolution	>25nm	25nm	25nm
Ease of obtaining quantitative results	Quantification very difficult	Approx. compos. with standards	Approx. compos. easily obtained

1.3.6 X-ray Topography

Lang transmission topography[7] is a popular method for studying defects in semiconductor crystals, e.g. the substrate. Here, the incident x-rays are diffracted by the lattice planes in the crystal , which is usually oriented so that Bragg diffraction is possible from only one set of lattice planes. A narrow slit is positioned to let this reflection through to the recording film and a complete X-ray topograph of the sample is built up by moving the crystal and the film together past the slit. In a simple experiment of this kind, extended lattice defects can easily be seen in the topograph and lattice strains as small as 10^{-3} are visible around precipitated and compositional inhomogeneities. Figure 1.9 shows the experimental procedure for X-ray topography. Chapter 3 shows lattice defects found in the device materials imaged in the TEM.

A second way of obtaining useful information on crystallographic perfection is to record the form of the rocking curve at the Bragg diffraction peak. The angular width of the peak will depend on the indices of the diffracting planes, the lattice strain and the defect density in the crystal. Using double-crystal-rocking curve analysis, detection of very small lattice strains of 10^{-5}, or less, are possible.

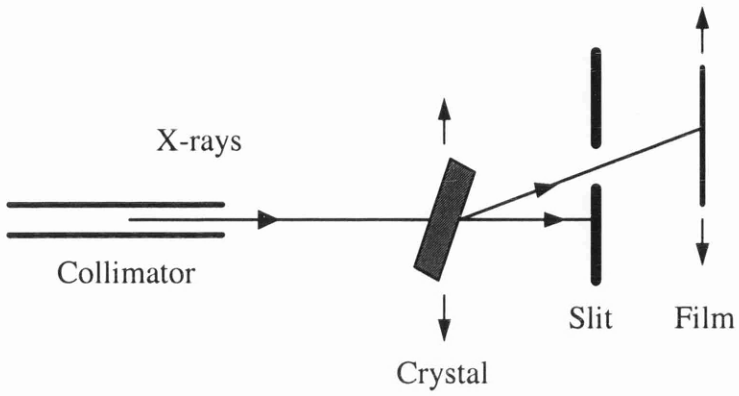

Figure 1.9: *Schematic illustration of Lang transmission topography.*

1.3.7 X-ray Diffractometer

The X-ray diffractometer[9] is not an instrument normally found in a FA lab, but more often used to study texture in films before device fabrication. It is widely accepted that the distribution of grain orientations in a conductive film significantly affects its electrical and mechanical properties. If all the grains have a common orientation with respect to the growth direction the film is said to be textured. Properties of the film normally improve with the degree of texture. The X-ray diffractometer is used to identify texture in a material, but due to the low spatial resolution (>10μm) it is often impossible to perform the analysis on fully-processed devices. Chapters 6 and 7 show how texture can be investigated for fully processed devices using the TEM.

The diffractometer measures the intensity of a reflection from a particular set of planes as the sample is rotated in three directions. The intensity is usually presented on a pole figure which is a projection of the 3D orientations onto a 2D disc[10]. Examples of this method are given in chapter 7.

1.3.8 Scanning Electron Microscopy (SEM)

The SEM has several major advantages over the optical microscope for the study of microelectronic devices: a high spatial resolution (≈1-2nm in modern machines but

depending on the signal used), a very large depth of field, and the ability to obtain excellent topographic contrast. So, in its simplest form, the SEM is a tool which allows direct observation of anomalies in the layout of components on a device. It is often used to find structural defects incurred during device fabrication. However, selective etching of fully-processed devices is often required to reach the buried defect.

Many commercial SEMs are fitted with detectors for *X-ray microanalysis*, e.g. EDX. This has proved particularly useful in the characterisation of the elements present in contamination stains.

Voltage Contrast Microscopy (VCM) is a common mode of operation in an SEM in FA labs[7]. Here, the SEM is operated to detect variations in the local potential on the sample surface. It is easy to form electrical connections to a chip so that, if the electron detector is positively biased, current carrying conductors will appear brighter when they are held at a negative bias. This technique can be especially valuable in tracing faulty connections and defects which create open circuits on a chip surface.

Electron Beam Induced Current (EBIC) is another SEM technique commonly found in FA labs[7]. Electrons of energy 10-30keV, incident on a p-n junction, generate between 10^3 and 10^4 electron-hole pairs distributed in a roughly pear-shaped excitation volume. There are two ways in which the presence of these excess carriers can be detected: by separating them across the built-in field at a p-n junction or Schottky barrier, or observing the light emitted as a result of radiative recombination. The former method is by far the most commonly used in performing charge collection microscopy on semiconductor samples. Primarily, EBIC is used to measure minority carrier currents and diffusion lengths. It can also be used to study the morphology of buried p-n junctions and defects in semiconductor crystals using EBIC imaging.

Orientation Image Mapping (OIM) is a recent technique[11] whereby the surface of a film is scanned in the SEM and the backscattered diffraction pattern is analysed to determine the orientation of each grain. The technique is very time consuming, but

since it is fully-automatic, it can be left to run overnight. The texture of a film is normally investigated, but analysis is more complicated if there exists more than one grain through the thickness of the film. The results in chapter 6 show how texture can be investigated in a film when more than one grain exists through its thickness.

1.3.9 Summary of Techniques

Table 1.2 summarises all the popular analytical techniques found in silicon device product and failure analysis labs, including some lesser techniques not described in this section[8].

1.4 Transmission Electron Microscopy

As the thickness of materials in silicon devices decreases, it is clear that most of the existing analytical techniques mentioned in section 1.3 will become inadequate for obtaining vital information. The need for techniques having nanometre resolution is amplified by the fact that electrical and mechanical properties depend increasingly on the fine structure of the materials as the thickness of each layer decreases[12].

To a certain degree, every property of the structure of a material listed in section 1.3.1 can be investigated using TEM. Specimens can be planar or in cross-section allowing every possible location on the device or angle through it to be examined. Electrons having an energy of 100-500keV, depending on the microscope, illuminate an area on the electron transparent specimen. Post specimen lenses then produce a magnified image of the specimen or its diffraction pattern onto a viewing screen or detector. The details of the modes of operation are dealt with in chapter 2. In its various modes of operation, including those involving peripheral detection systems, TEM can be used for many failure and product analysis investigations. Table 1.3 lists most of these uses for characterising the structure of the materials and components in the devices.

Table 1.2: *Analytical techniques used in modern device technology*

Primary beam	***Technique***	***Energy range (keV)***	***Secondary signal***	***Acro-nym***	***Application***
Electron	Low energy diffraction	0.02-0.2	Electron	LEED	Surface structure
	Scanning electron microscopy	0.3-50	Electron	SEM	Surface morphology
	Electron microprobe	1-30	X-ray	EMP	Surface region composition
	Auger spectroscopy	0.5-10	Electron	AES	Surface layer composition
	Transmission electron microscopy	100-1000	Electron	TEM	High resolution structure
	Scanning TEM	100-1000	Electron	STEM	Imaging, X-ray analysis
	Electron energy loss spectroscopy	100-1000	Electron	EELS	Local small area composition
Ion	Ion scattering spectrometry	0.5-2.0	Ion	ISS	Surface composition
	Secondary ion mass spectrometry.	1-15	Ion	SIMS	Trace composition versus depth
	Secondary neutral mass spectrometry	1-15	Atoms	SNMS	Trace composition versus depth
	Particle induced X-ray emission	>1	X-ray	PIXE	Trace composition
	Scanning ion microscope	5-20	Electron	SIM	Surface characterisation
	Rutherford back-scattering	>1000	Ion	RBS	Composition versus depth
Photon	X-ray fluorescence	>1	X-ray	XRF	Composition (1μm depth)
	X-ray diffraction	>1	X-ray	XRD	Crystal structure
	X-ray photoelectron spectroscopy	>1	Electron	ESCA, XPS	Surface composition
	Laser Microprobe	Laser	Ions	----	Composition of irradiated area
	Laser emission microprobe	Laser	Light	LEM	Trace elements (semiquantitative)
Neutron	Neutron activation analysis	Reactor	Gamma	NAA	Bulk (trace) composition

It is well-known in device technology that electrical and mechanical properties of a thin film are highly dependent on the distribution of grain sizes and grain orientations[12], [13]. Complete, quantitative analysis can be performed on a film to investigate these properties in the TEM. It also becomes more important how materials interface with each other when the thickness of the layers shrink. Here lies another area where TEM can be implemented to perform compositional profiles across the interface. Much of this thesis is dedicated to demonstrating the worth of the TEM in performing these analyses.

Table 1.3: *The type of information available from the common modes of operation in the TEM*

Technique	***Phenomenon***	***Information available***
Bright /dark field imaging	Observation of the unscattered or scattered electrons from a sample	Crystalline structure (e.g. grain sizes), defects, interface depths, layer uniformity and structural information
Diffraction	Pattern formed by specimen on back focal plane	Identification of the material composition, its structure, grain orientations, thickness and stress
EDX	X-rays emitted from de-excitation of electrons in the atomic core	Quantitative elemental identification for atomic $n^o > 7$
PEELS	Detection of the energy loss of electrons transmitted through specimen	Elemental identification and information on the atomic environment with an energy resolution of 1eV.

Despite its obvious virtues, the reason that TEMs are not so commonplace in product and failure analysis labs is primarily because of the cost in purchasing and maintaining the microscope. Skilled operators have to be employed to use it owing to its complexity. Indeed, the specimen preparation itself is not only costly but is a skilled job and requires a significant training time. TEM analysis is also destructive by nature and there is always a significant chance that the specific area of interest can be missed.

Fully-automised and inexpensive specimen preparation techniques need to be implemented to make the TEM an integral part of a failure analysis lab. The modes of operation should be more user friendly and automated to reduce the cost of training and increase the number of people able to use it. If both these criteria are met, more TEMs will be sold thus reducing the cost. So it is very reasonable to expect that, with devices shrinking, the TEM will become one of the most useful analytical tools in an FA lab.

References for Chapter 1

[1] L. J. Herbst, *Integrated Circuit Engineering,* Oxford University Press (1996) 4

[2] S. A. Campbell, *The Science and Engineering of Microelectronic Fabrication,* New York, Oxford Univ. Press (1996) 412.

[3] S. J. Wind, D. J. Frank, H.-S. Wong, Microelectronic Engineering, **32**, (1996) 271

[4] Y. Nishi, in *Silicon Faces the Future*, Physics World, November, (1995)

[5] S. Coffa, M. Meyyappan, H. Nishi, Mat. Sci. in Semiconductor Processing, **1**, 1-4 (1998) 1

[6] D. A. Pucknell, K. Eshraghian, *Basic VLSI design*, Prentice Hall, Australia, (1994)

[7] C. R. M. Grovenor, *Microelectronic Materials,* IOP Publishing Ltd, (1989), 239

[8] S. M. Sze, *VLSI Technology,* McGraw-Hill, (1988)

[9] H. J. Bunge, Int. Mats. Revs., **32,** 6, (1987) 265

[10] H. J. Bunge, Steel Research, **62,** 12, (1991) 530

[11] R. A. Schwarzer, Ultramicroscopy, **67,** (1997) 19

[12] S. Vaidya, A. K. Sinha, Thin Solid Films **75**, 3, (1981) 253

[13] D. B. Knorr, D. P. Tracy, K. P. Rodbell, Appl. Phys. Lett. **59,** 25, (1991) 3241

CHAPTER TWO

TEM Instrumentation and Evaluation of Basic Techniques

2.1 Introduction

Understanding the fundamental capabilities of the transmission electron microscope (TEM) in its various modes of operation is vital when considering the development of new techniques or the improvement of existing ones. In this chapter the electron-optics and instrumentation of the TEM are described. The characteristics of the electron beam are then investigated to realise the limits of analytical techniques, both theoretically and experimentally. The basic theory and instrumentation is then discussed for energy dispersive X-ray (EDX) analysis and electron energy loss spectroscopy (EELS) which are used for compositional analysis as described in chapter 7.

2.2 TEM configuration

For the vast majority of experiments described in this thesis a Philips CM20 scanning TEM (STEM) was used. For some X-ray analysis a VG HB5 dedicated STEM was used and is described in chapter 7. A schematic diagram of the Philips CM20 STEM is shown in figure 2.1. Situated at the top of the microscope is a thermally assisted field emission electron gun (FEG). Here electrons are drawn from a sharp tip by an anode having a potential difference ≈4kV. Eight accelerator rings raise the electron voltage to

200kV. The tip is heated to ≈1800°C to aid the extraction efficiency but this reduces the electron energy resolution.

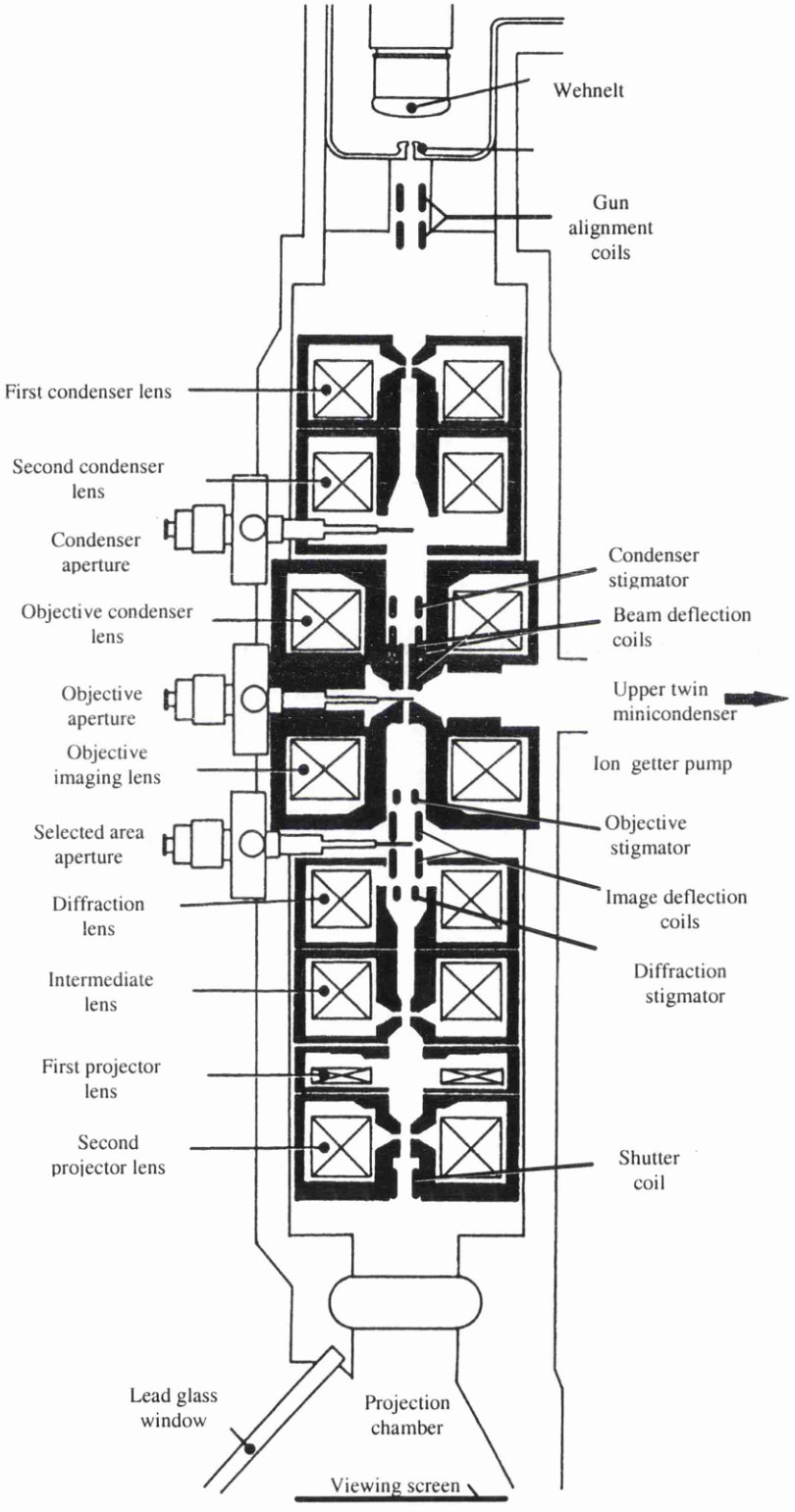

Figure 2.1: *Diagram of the electron optics in the Philips CM20 STEM*

The lenses in the microscopes are all electromagnetic (except the gun lens in FEG instruments). The TEM usually contains two condenser lenses; the first determines the demagnification of the size of the electron source and the second determines how strongly the beam is focused onto the specimen, i.e. the area illuminated. The objective lens, in which the specimen is immersed, performs two functions. The pre-specimen field works with the condenser system to focus the beam onto the specimen, whereas the post-specimen field forms the diffraction pattern on the back focal plane, normally the plane containing the objective aperture. The magnification system of the microscope consists of five lenses which lie between the specimen and the viewing screen and allows magnifications from 22× to 290k× in conventional TEM (CTEM) and from 200× to 3300k× in scanning. Throughout the microscope, the electron beam is directed by a number of deflection coils each giving the operator control of the position of the beam. As with most microscopes, the Philips CM20 has three sets of stigmators: condenser, objective, and diffraction. Each consists of an octopole and are used to correct for any astigmatism in the corresponding lenses.

Circular apertures are located at certain positions along the column and perform various functions. The condenser apertures define the beam convergence for a focused probe and help modulate the intensity of the beam. Smaller apertures here produce a smaller convergence angle which affects the spot diameter. This allows for optimal spatial resolution in scanning, microanalysis, etc, often at the expense of current in the beam. After the specimen, the objective aperture obstructs diffracted beams from contributing to the image. This has the effect of increasing the contrast of the image at the expense of image resolution. Conversely, the selected area aperture selects the circular area of an image of the specimen which contributes to the diffraction pattern.

2.3 Imaging

As mentioned earlier, images of a sample can be magnified ≤270k× in CTEM and ≤3.3M× in scanning. Examples of TEM images of silicon device structures are shown in

chapter 3. The electron optic configuration for bright field (BF) imaging is shown in figure 2.2 for both CTEM 'nanoprobe' and STEM. 'Nanoprobe' is a mode which produces a smaller probe than high resolution mode (HREM), but with a smaller area of illumination. This is due to the upper twin condenser lens (as shown in figure 2.1) being nullified. In scanning, the focused beam is scanned in a raster using scan coils with its shape and scan time defined by the operator. Normally, the diffraction pattern from the area probed is aligned to remain stationary on the viewing screen during the scan. The detector then displays the brightness of the beam on a CRT screen as it scans in synchronisation. BF imaging is the process of examining the electron beam which has not been scattered by the specimen whereas dark field (DF) imaging is observing the (usually elastically) scattered beam. To obtain a DF image the objective aperture is positioned to let through only scattered electrons. In this way, contrast in images of polycrystalline samples can be improved. Before the quality of a TEM image is assessed, it is important to understand how contrast in an image can arise.

Firstly, to obtain any significant image contrast (i.e. a change in intensity between neighbouring points on the image) the specimen has to be between ≈5nm and ≈150nm thick, the limits depending on the density of the material imaged. Contrast arises from changes in density and thickness of the material. Crystalline materials exhibit diffraction effects which greatly affect the contrast depending on the orientation, thickness and bending in the crystal. Sometimes these effects are used to investigate the structure or thickness of a material (of which many examples are illustrated in chapter 3), but often they reduce the clarity of an image. However, it is very difficult, if not impossible, to prevent these diffraction effects from contributing to the image contrast. The insertion of an objective aperture confines the electrons which contribute to the image to only those which are not scattered by the specimen. This aperture prevents the scattered electrons from contributing the final image and thus the contrast is enhanced, as the scattering point on the image appears darker than with no aperture.

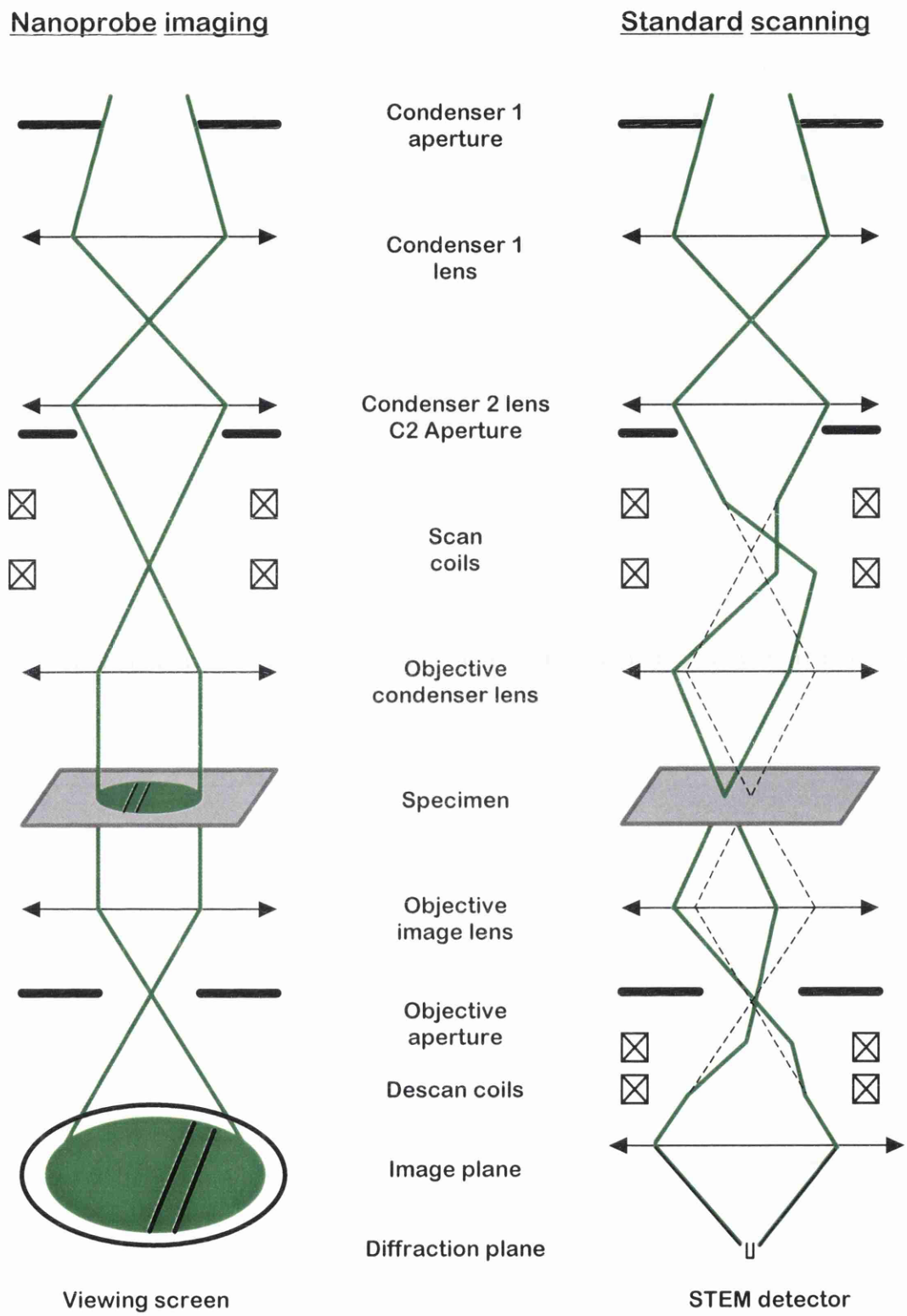

Figure 2.2: *Ray diagrams showing a schematic path of the electrons for CTEM nanoprobe and standard scanning modes*

For STEM, the image brightness has to be high enough for the detection system but not too high to reduce contrast. The brightness mainly depends on the specimen thickness, crystal orientation and beam current. Typically, the current in a STEM probe is ≈0.1nA but is highly dependent on the extraction voltage, condenser lens configuration and the condenser and objective aperture setting. The beam currents are measured for the Philips CM20 in section 2.5.

The resolution of an image depends greatly on the imperfections of the imaging lenses. For scanning, the aberrations in the upper objective lens adversely affects the resolution whereas the aberrations from both objective lenses affect the resolution in CTEM imaging. For the Philips CM20, the maximum spatial resolution is ≈0.3-0.5nm in CTEM and is quite low due to presence of the large 20mm-gap objective lens designed to enable field-free experimentation for magnetic samples (see later). The lens strength could be increased to reduce the focal length, thereby reducing the aberrations, but conventional soft magnetic materials restrict the maximum field to ≈2.5T[1]. At this field strength however severe saturation effects in the lens are likely. Superconducting materials may reach 20T, but there are problems of miniaturisation.

For STEM, diffraction effects from the probe combine with the effect of the lens aberrations to reduce the image resolution. Diffraction effects resulting from the angle of convergence of the beam in CTEM are normally much less severe, resulting in a higher resolution. Most of the experiments performed in this work are either in STEM or using focused probes, so the following sections analyse the theoretical and experimental considerations in obtaining optimal point resolution.

2.4 Theoretical probe size considerations

In scanning mode, the resolution of an image on the CRT screen is frequently determined by the radius, r, of the focused probe and is calculated using equation 2.1[2].

$$r^2 = \left(0.61\frac{\lambda}{\alpha}\right)^2 + \left(\frac{1}{4}C_S\alpha^3\right)^2 + \left(C_C\alpha\frac{\Delta V}{V}\right)^2 + \left(Mr_0\right)^2 \qquad [2.1]$$

In equation 2.1, λ is the electron wavelength (=2.51×10^{-12}m at 200keV), C_S and C_C are respectively spherical and chromatic aberration coefficients of the probe-forming lens, α is the semi-angle of beam convergence, V is the voltage through which the electrons are accelerated, M is the magnification of the source by the upper column lenses (typically ≥0.05 for FEGs), and r_0 is the radius of the source. It is not strictly accurate to add these terms in quadrature unless the beam is Gaussian. The lens aberrations prevent the beam from ever being Gaussian but, in practice, the relationship is shown to accurately describe the resultant radius of the beam. With magnetic lenses and a FEG, the effect on the resolution from the chromatic aberration is usually small (<20%)[1]. Figure 2.3

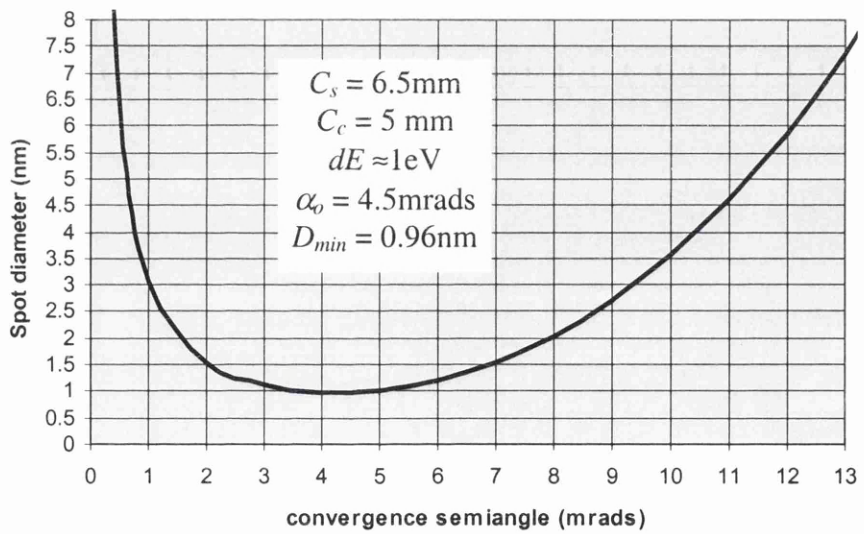

Figure 2.3: *Minimum probe diameter as a function of convergence angle for the parameters shown for the CM20*

shows how the theoretical spot diameter is affected by the convergence angle as described by equation 2.1, neglecting the source contribution. It can be shown[2],[3] that by differentiating equation 2.1, the optimum convergence angle, α_0, which produces the smallest spot diameter, D_{min}, is given by equations 2.2 and 2.3. Here the source contribution and chromatic aberrations are neglected.

$$\alpha_o = \left(\frac{1.4\lambda}{C_S}\right)^{1/4} \qquad [2.2]$$

$$D_{\min} = 2r_{\min} = 1.3\lambda^{3/4} C_S{}^{1/4} \qquad [2.3]$$

Since it is not known exactly how the various parameters add in the expression for the resolution, various constants have been quoted to replace the 1.4 and 1.3 in equations 2.2 and 2.3[1],[4]. These are shown to affect both α_0 and D_{min} by as much as 30%.

For the Philips CM20 at Glasgow University the smallest probe diameter theoretically possible is 0.73nm, where C_S=6.5mm for the 20mm-gap objective lens. This assumes an α_0 of 4.8mrads. If the probe is assumed to be of Gaussian shape, points half the diameter of the probe apart can be resolved. Thus the maximum resolution theoretically possible in scanned images is ≈0.4nm.

It is important to note that the beam spreads in the specimen. Figure 2.4 shows the enlargement of the beam diameter according to the thickness of various materials. The equation describing the graph is shown in equation 2.4[5]. For 50nm thick Si the beam will spread by ≈1.5nm.

$$b = 6.25 \times 10^5 \frac{Z}{E_0}\left[\frac{\rho}{A}\right]^{\frac{1}{2}} t^{3/2} \qquad [2.4]$$

Here b is the beam broadening in cm, Z is the atomic number, E_0 is electron energy in eV, ρ is density in gcm^{-3}, A is atomic weight in gm, and t is specimen thickness in cm. This equation tends to overestimate the beam spread by a factor of ≈1.5 due to the large limits taken on the distribution of the beam spread. For 50nm thick Si the beam will spread by ≈1.5nm.

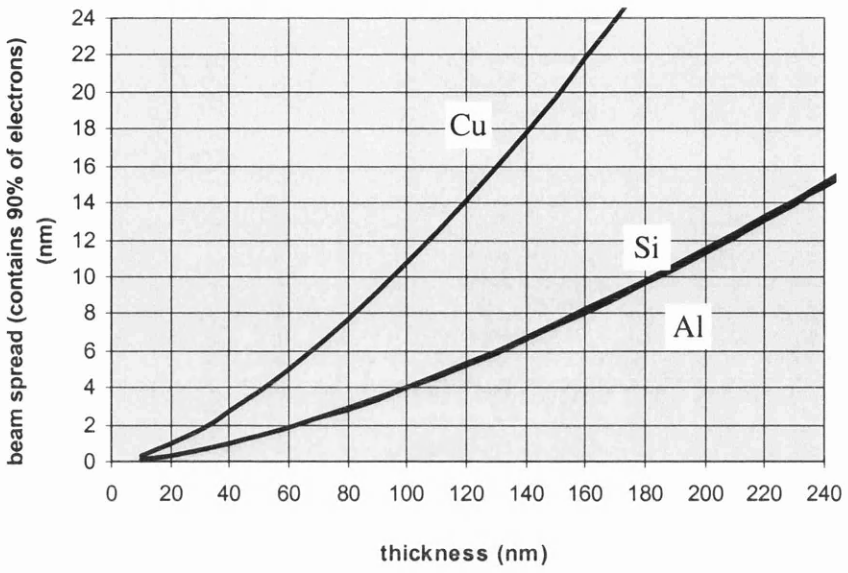

Figure 2.4: *Beam spreading as a function of specimen thickness for Si, Al and Cu*

2.5 Experimental Probe Characteristics

2.5.1 Introduction

From section 2.3 theoretical probe sizes were calculated for the Philips CM20 TEM at Glasgow University. In this section, experimental measurements of important parameters of the beam are taken. These include probe size, current and current density under various lens and aperture configurations. This information is essential when forecasting whether microanalysis will be worthwhile and more so in accurately analysing results.

2.5.2 Probe Diameter

Figure 2.5 shows how the probe diameter is affected by the first condenser, C1, lens configuration as well as the second condenser, C2, aperture setting. In this experiment, the microscope is aligned in nanoprobe mode as described earlier. The beam is focused onto the specimen which is at the eucentric height (i.e. on the tilt axis of the specimen

holder). The specimen is moved so that the beam passes through a hole to avoid beam spreading by the specimen. A spot a few millimetres wide is observed on the viewing screen. For each C2 aperture setting the condenser lens settings are changed using the 'spot size' control. The probe is then corrected for astigmatism at each 'spot size' and the spots are photographed using the plates immediately underneath the viewing screen.

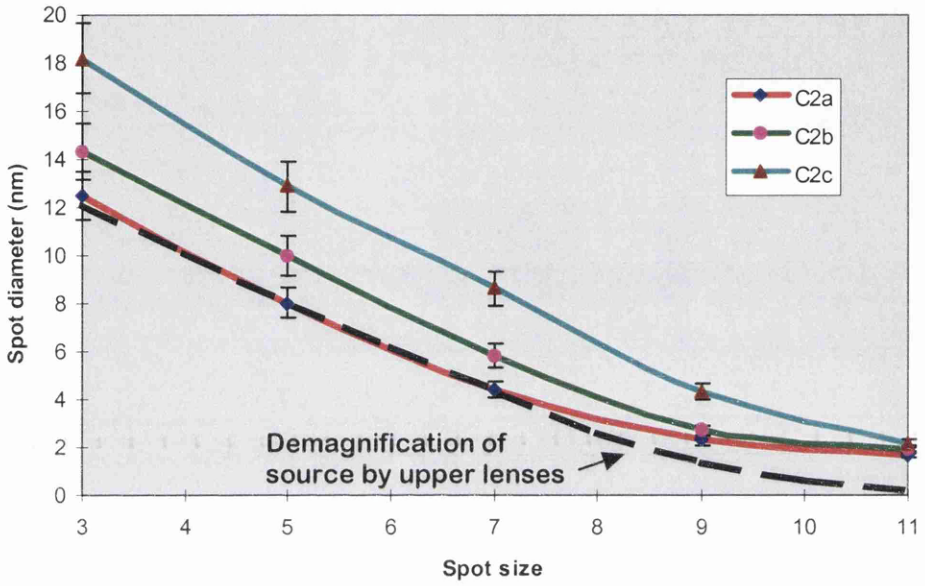

Figure 2.5: *Experimental probe diameter as a function of condenser lens settings and condenser aperture. The dashed line is the probe size contribution due to the demagnification of the electron source. The lines are guides to the eye.*

Each spot is photographed twice. This enables a more accurate calculation of the actual spot size by compensating for the spot spreading in the negative with exposure time. The spreading of the spot in the negative is illustrated graphically in figure 2.6. Here four exposure times are used and the spot diameter on the negative is measured each time. Only two are permitted in the probe size experiment as all the results have to be taken at the same time under the same microscope conditions and only 54 negatives can be used at one time. Changing the cartridge could interfere with the carefully controlled beam conditions. The actual spot size is taken as the extrapolation of the measured spot sizes back to zero time. The error in using two exposure times to infer the diameter at

zero time is ≈10% as shown in figure 2.6. The shape of this curve may change slightly according to the incident beam intensity, but it is unlikely to change the error significantly. Whatever the actual curve representing the dependence of the diameter on the exposure time, the error will always be in the same direction, e.g. the diameter may always be overestimated. So using two exposure times does not reduce the accuracy of the relative values significantly. Knowing the magnification (≈300k) at the negative, the spot diameters are calculated for each spot size and aperture setting.

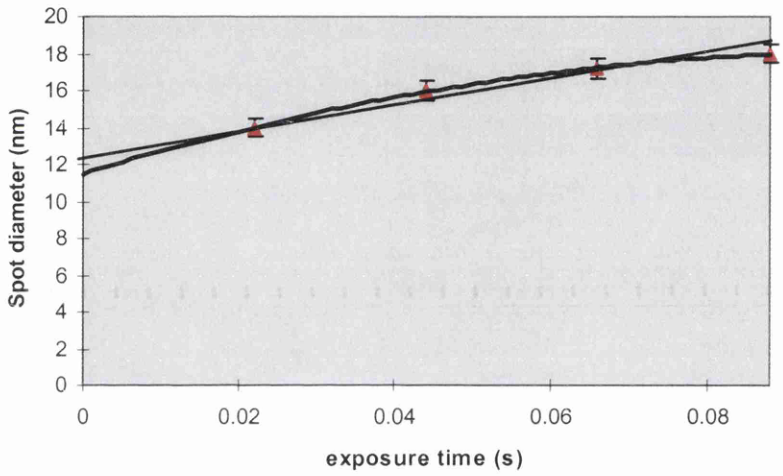

Figure 2.6: *The spot diameter as a function of exposure time. The dark curve is a polynomial fit to the data points. The line is used to show the discrepancy in using a linear fit from two data points (at 0.022s and 0.066s) to find the spot size at zero time*

To understand the relationship between spot diameter and upper column configuration the convergence semi-angle of the beam is required for each aperture. The three smallest C2 apertures, denoted C2a, C2b and C2c, have diameters 30, 50 and 100μm respectively and define the probe angle no matter the C1 and C2 lens strengths. In diffraction mode, the diffraction focus is adjusted to make the viewing screen conjugate to the objective aperture. Calibrating the camera length, C, using a Au-Pd polycrystalline sample, the radius, r, of the diffraction disc is measured to obtain the convergence semi-angle, α, ($=r/C$). The results are shown in table 2.1.

***Table 2.1**: Convergence angles for HREM and nanoprobe modes*

	Aperture diameter		
	30μm	50μm	100μm
Nanoprobe	1.4mrads	2.3mrads	4.7mrads
HREM	1.5mrads	2.6mrads	5.2mrads

Probe angles for both modes are very similar but are significantly affected by the height of the specimen or the strength of the objective lens. The observational error in the determination of the eucentric height corresponds to an error of ≈10% in α. The nanoprobe mode was originally designed to give a larger convergence angle of a focused probe. However the introduction of a 20mm-gap objective lens reduced the focused probe angles to values similar to the standard HREM mode.

From figure 2.5 and equation 2.1 it is evident that the reason for the probe diameter changing with the condenser lens settings for a given C2 aperture, i.e. a fixed α, can only be a result of the contribution of the effective source size, i.e. the 'Mr_0' term. To test this, the relative demagnification of the upper column lenses is calculated using equation 2.5[6] and 2.6. For this approach, the physical data on the position and strength of the lenses for the various 'spot size' settings is required.

$$f = \frac{25V_r(S+D)}{(NI)^2} \qquad [2.5]$$

$$\frac{1}{f} = \frac{1}{d_i} + \frac{1}{d_0} \qquad M = \frac{d_i}{d_o} \qquad [2.6a,b]$$

Here, f is the focal length, V_r is the relativistic voltage through which the electrons are accelerated, S and D are the pole spacing and the bore diameter of the lens respectively, and N is the number of coils in the windings carrying a current, I. Equation 2.5 is known to determine f approximately, with the error becoming more severe as f

decreases. The exact relation between f and the lens parameters is shown[6] to be accurate to <10% down to $V_r/(NI)^2 \approx 0.01$, i.e. $I \approx 2.7$A for N=1792 turns, as is the case here. Only at spot size 11, where I=3.0A, is the lens approximation inaccurate. The exact relationship also depends on other lens parameters. These include, the length of the field, the extent to which it is symmetrical, and the value of the maximum field[7]. Since only the relative magnification of the condenser lenses is required, the error arising from these parameters is insignificant.

The first step in calculating the magnification of the source by the upper lens system is to use equations 2.5 and 2.6 for the C1, and C2 lenses. The object distance, d_0, for C1 is determined by the position of the beam cross-over and is estimated from the physical layout of the column and from the manufacturers information. The position of the beam cross-over depends on the gun lens setting and is just above the C1 aperture for low gun lens settings and is further away for higher settings. The gun lens setting used here was 'gun lens 5' and $d_0 \approx 0.10 \pm 0.02$m. The image distances for one lens is used to calculate the object distance for the subsequent lens using data on the separation of the lenses. A schematic diagram of the CM20 describing this approach is given in figure 2.7. Now the magnification of the condenser lenses can be calculated along with the final image distance of the C2 lens. The position and the convergence angle of the probe, as focused by the objective lens, is always the same for a C2 given aperture no matter the 'spot size'. The magnification of the objective lens can be calculated simply by knowing the C2 image distance, the diameter of the C2 aperture (which is in the centre of the lens), and the angle of convergence for that aperture. The magnification of the objective lens is always the same throughout the whole experiment and is given by $M_{OBJ}=\alpha_o/\alpha_i$ as shown in figure 2.7. Dividing the source size by the magnification of the upper lenses should give the resultant spot diameter for each lens setting. Since the magnifications are only relative (as the exact position of the beam cross-over is not known), the source size is effectively scaled to fit the experimental probe diameter at 'spot size 3' for the C2a aperture as shown in figure 2.5. The dashed line in figure 2.5 is the theoretical spot diameter of the source as a function of 'spot size'.

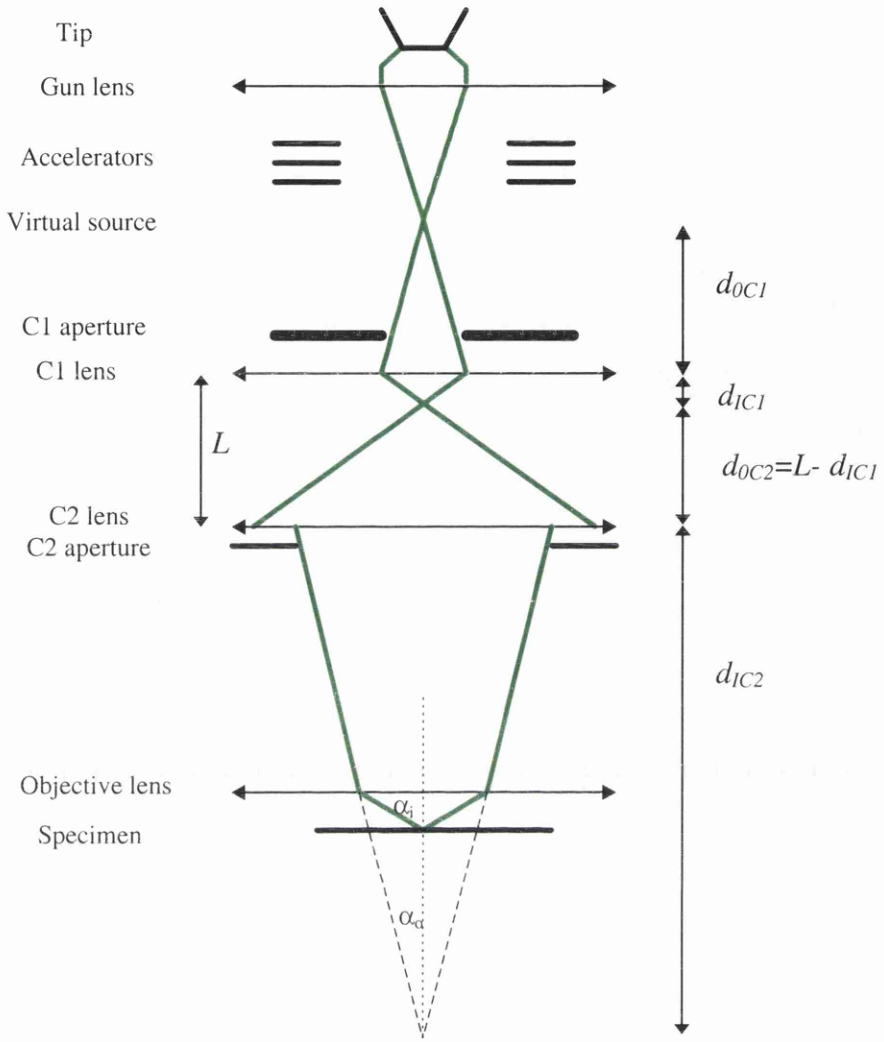

Figure 2.7: *Schematic diagram of the lens configuration in the upper column for the CM20 FEG at 4.2kV extraction voltage showing the parameters used to calculate the magnification of the source by the lenses*

It is clear from figure 2.5 that the curve representing the variation of probe diameter with lens setting for C2a closely mimics the theoretical curve until 'spot size 9' where diffraction effects begin to contribute significantly. Since it is only the relative magnification of the upper lenses which are calculated for each 'spot size' it is not possible to calculate the diameter of the source. To do this, the electron optics at the gun lens and the anode would have to be incorporated into the calculation.

By applying equation 2.1 for each of the convergence angles defined by the C2 apertures given in table 1, it is predicted that the larger apertures should give a smaller probe diameter. However, looking at figure 2.5, the probe diameters clearly increase with C2 aperture size. This would suggest that other lens aberrations are involved in increasing the spot diameters.

This first step in explaining this anomaly is to consider the spherical coefficients of the other upper column lenses. The relationship between the spot diameter and the convergence angle depicted by figure 2.3 only considered the spherical aberration arising from the upper objective lens. This lens was originally though to be the most influential in terms of the total coefficient of spherical aberration as the effect of the aberrations from the condenser lenses were thought to be demagnified. To determine the spherical aberration coefficient from the condenser lenses as a function of their strengths, equation 2.7[6] is used.

$$c_{\infty} = \frac{5f^3}{(S+D)^2} \qquad [2.7]$$

The focal length, f, of each lens is known from equation 2.5, and hence the spherical aberration coefficient at infinity, c_{∞}, can be found. The value of c_s depends on the magnification of the lens and is given by equation 2.8[7]. Since there is a succession of lenses, the effect of these coefficients on the total coefficient is given by equation 2.9[2].

$$c_s(M) = c_{\infty}(1+M)^4 \qquad [2.8]$$

$$c_{total}^2 = c_{OBJ}^2 + M_{OBJ}^8 (c_{C2}^2 + M_{C2}^8 c_{C1}^2) \qquad [2.9]$$

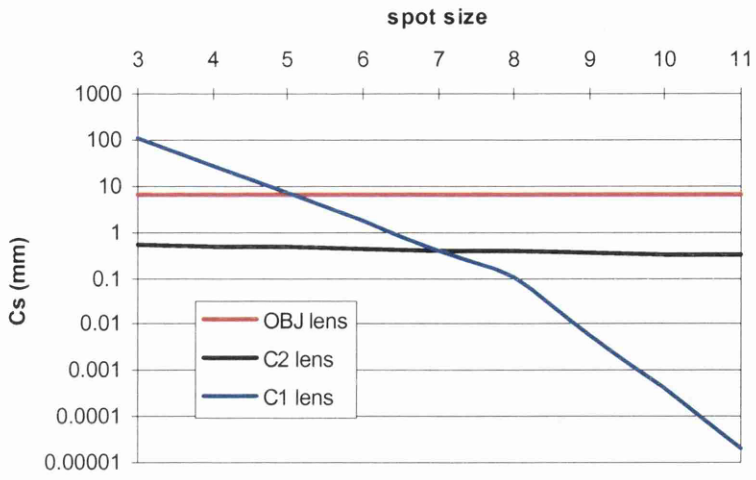

Figure 2.8: *The spherical aberration coefficients for the upper column lenses showing their contributions for each 'spot size'*

As the values of M depend on the position of the beam cross-over after the gun lens so does the value of c_{total}. The separate values of c_s are shown in figure 2.8 highlighting the predominant source of spherical aberration for each 'spot size'. Taking the position of the cross-over as before, the theoretical spot diameter is calculated using equation 2.1 with $c_s = c_{total}$, as a function of 'spot size' and aperture diameter. The results are shown in figure 2.9. The effect of the uncertainty in the cross-over position on the probe size

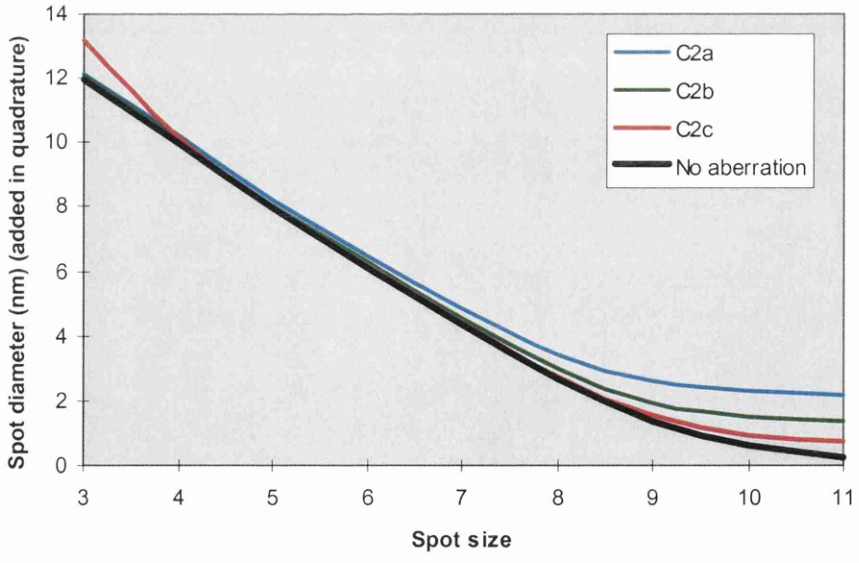

Figure 2.9: The predicted spot diameters calculated using source demagnification, diffraction and spherical aberrations

results can be seen in figures 2.10a and 2.10b where the results are shown for the extreme values (i.e. 0.12m and 0.08m). This shows how the spherical aberration can be dramatically increased for 'spot size 3' when using a lower gun lens setting. Despite these results showing that larger spot diameters are possible with the C2c aperture, they still do not agree well the experimental results for all 'spot sizes' and the C2b aperture. Another explanation is required to describe the dependence of the spot diameter on the convergence angle.

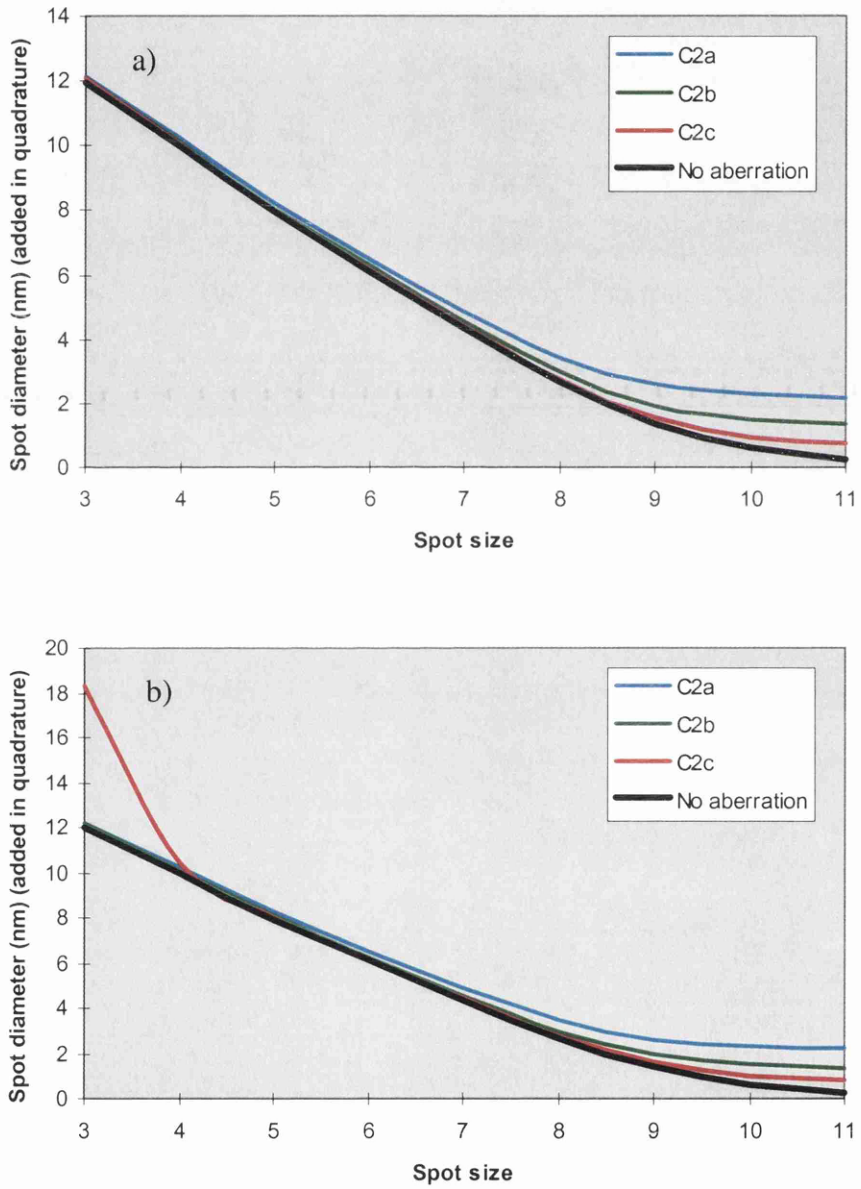

Figure 2.10: *The effect on the total spherical aberration by choosing a high (a) and low (b) gun lens setting. A low gun lens setting enlarges the spot in spot size 3 and 4, but reduces it slightly in spot size 11*

Figure 2.11 shows that the spot diameter for the three apertures at each 'spot size' may vary as α if the terms in equation 2.1 were added linearly. This could imply that the source of the aberrations is either astigmatism or chromatic aberrations as they both have components which vary linear as α[7]. The astigmatism of both the condenser and objective lenses are continually corrected at every 'spot size' using the respective stigmators, so this is unlikely to be the cause of the aberrations. It is noted however that

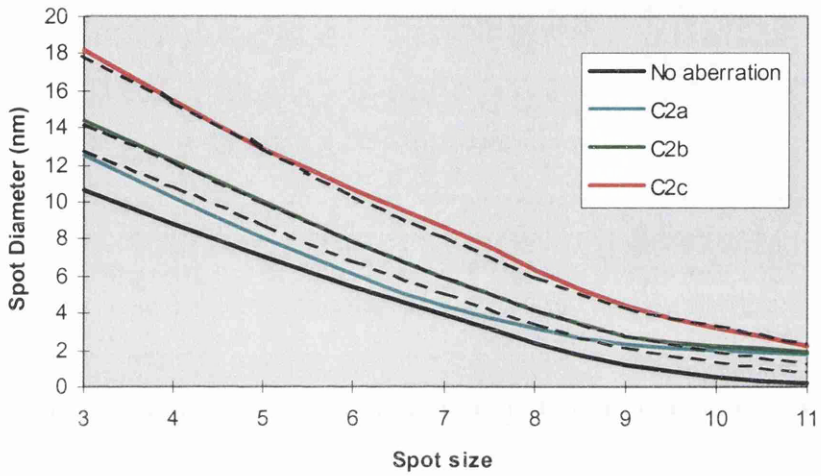

Figure 2.11: *Dashed lines assume aberrations are linearly dependent on α for comparison to the experimental data. Here only the source demagnification and aberrations are considered and are added linearly to calculate the spot diameter*

the stigmators only correct for second order astigmatism[8], which, despite being the predominant component of aberration, is not the only component. It is thus feasible that a first order (in α) component could still be present. Calculations performed on the energy spread of the electrons show that the chromatic aberrations are insignificant for the condenser and objective lenses. The energy spread of the CM20 FEG is quoted[9] as $\approx$1eV for a 40μA emission current and rises to $\approx$1.15eV at $\approx$100μA, i.e. an extraction voltage of 4.4kV. This spread is also influenced by the gun lens setting where the stronger the lens the higher the energy spread due to the Boersch[10] effect. A 1eV energy spread corresponds to a maximum beam enlargement of 0.2nm in diameter, so its effect is insignificant in the condenser and objective lenses. However, at the gun lens the energy of the electrons is $\approx$4keV so even a small chromatic aberration

coefficient in the gun lens would have a much larger effect on the spot diameter. There is also the possibility of the source size being dependent on α, as the source extends over a flat region on the tip. One would imagine that this effect could be negated by adjusting the focus of the beam, but the nature of the angular spread of the electrons emerging from the gun is not known exactly. Another reason for the angular dependence could be coma. It is known, however, that coma is normally swamped by spherical aberration in magnetic lenses[7] and has a α^2 dependence which does not agree well with the observations. Other possible explanations include electronic interference and inaccurate beam focusing, but the first would not be proportional to α and the other is user-dependent but is unlikely to have affected the probe diameters so consistently as shown in figure 2.5.

Several explanations of the enlargement of the beam with convergence angle have been put forward. The most probable reason is chromatic aberration in the gun lens, although a combination of several factors is equally possible. The accuracy in the measurements of the spot diameters is $\approx$10% for the lower (<9) 'spot sizes'. So this excludes the explanation of spherical aberration in the upper column lenses. The aim of these experiments here is to determine the probe diameters in practice. The experiment has been repeated twice as a consequence of the difficulty in explaining the results, but similar results (<20% error on average) were found on each occasion demonstrating their accuracy and reproducibility.

The experiment calculating the spot diameter as a function of lens settings is repeated for low magnification mode with the objective lens off. This mode is typically used for imaging magnetic samples in a field free environment and could be necessary for imaging silicon devices which have magnetic structures (e.g. magnetic RAMs) on them. Figure 2.12 shows the relationship between the probe diameter and condenser configuration with the objective off. Here the 'spot sizes' range from 7 to 10 and the C2a (30μm) aperture is used, since these correspond to the most commonly used settings for this mode.

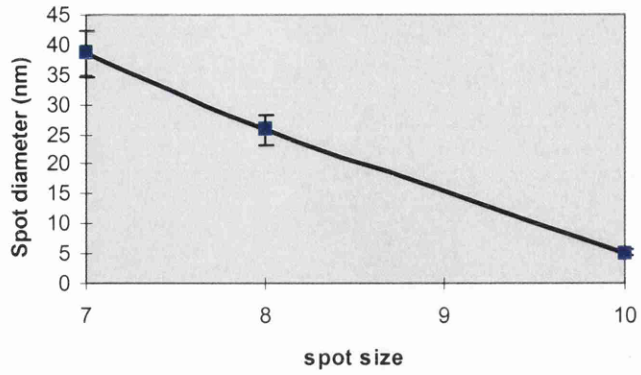

Figure 2.12: *Experimental probe diameter as a function of condenser lens strengths with the objective and upper twin off*

2.5.3 Probe current

Measurement of the probe current is performed by applying an equation which can be used to convert the automatic exposure time calculated by the microscope software to the beam current. The relationship, which is quoted by the manufacturers, is shown in equation 2.7.

$$I = 1.875 \times 10^{-9} \times 1.3 \times \frac{e}{t} \qquad [2.10]$$

In equation 2.7, I is the probe current in amps, e is the film emulsion setting (typically=2) which is used by the microscope to calculate the optimum exposure time, t in seconds. The factor 1.3 compensates for back scattered electrons at the photographic plate. Currents are calculated at each of these upper column settings for the nanoprobe mode and are shown in figure 2.13. It should be noted at this point that the absolute (but not relative) values of the current are thought to be incorrect as explained later.

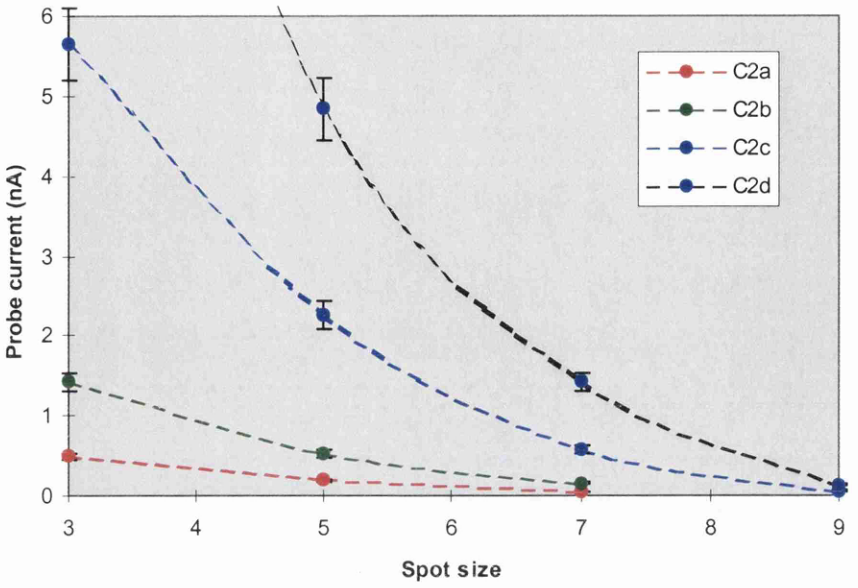

Figure 2.13: *Probe currents calculated from the automatic exposure time on the microscope for varying spot sizes and aperture sizes. The lines are a guide to the eye*

Theoretically, the current in the probe should depend on the fraction of the C2 aperture area to the whole area illuminated by C1 lens onto the plane containing the C2 aperture. This assumes that the whole area of the aperture is uniformly illuminated, which is true while the C2 aperture defines the probe angle. This is the case for the three smallest C2 apertures, namely C2a, b, and c, but not for C2d (100μm) as seen later. Referring to figure 2.7, the probe current through the C2 aperture depends on the C1 image distance, d_{IC1}, according to equation 2.11.

$$I = K\frac{{d_{IC1}}^2}{(L - d_{IC1})^2} \qquad [2.11]$$

For a given aperture size, the relative probe current is calculated using equation 2.11 as a function of 'spot size'. The results are then scaled by adjusting K to fit the results for the C2a aperture from figure 2.13. K here is 105. As the current should vary as the area of the apertures, the geometrical results for C2a are multiplied by the relative increase in areas to give the corresponding geometrical results for the C2b and C2c apertures.

Since the C2d aperture does no longer define the beam convergence, equation 2.8 is fitted to the experimental results independently from the rest, i.e. varying K to fit the results. The geometrical results are shown alongside the experimental data in figure 2.14. Both results agree to within ≈5% on average. The fact that the probe currents for C2a,b and c are proportional to the aperture area shows that the beam illumination is uniform across the C2 aperture plane. It should be noted that the probe current is too small to be detected with the automatic exposure time function on the TEM for spot sizes >7-9 depending on the aperture size.

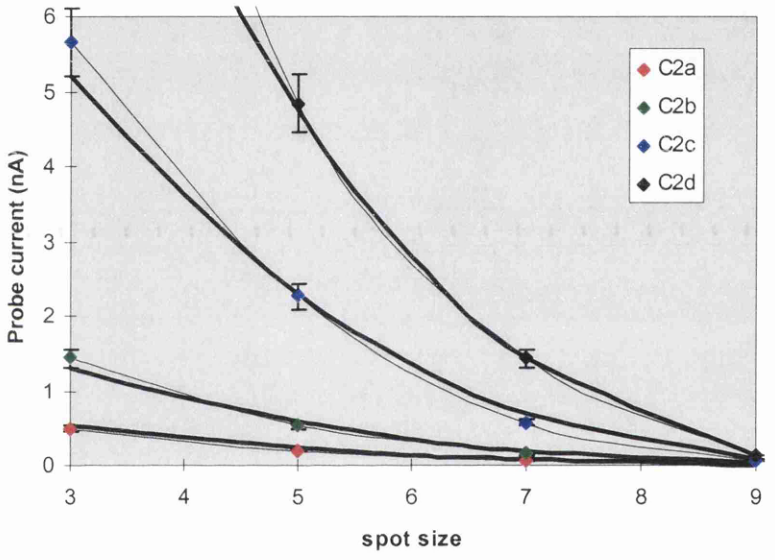

Figure 2.14: *The curves are theoretical probe currents dictated by the geometry of the beam in the condenser system. The experimental results are plotted alongside for comparison*

A focused probe can encourage contamination or damage to the material being examined so the probe current density of the beam should be calculated. Using the data on the spot diameters, D, and probe current, I, taken on the same day, it is possible to calculate the current density, $J=I/\pi(D/2)^2$, of the probe. The results of this calculation are shown on figure 2.15.

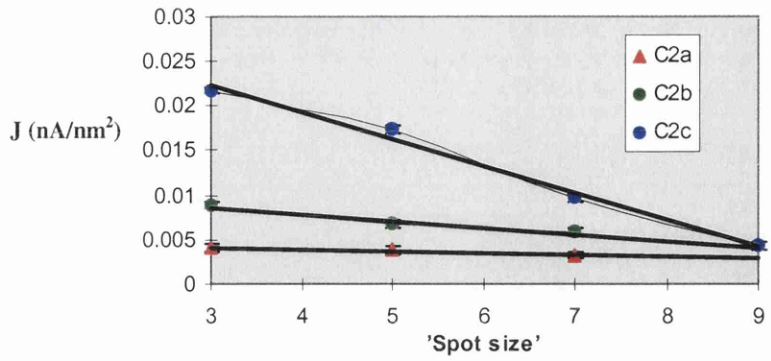

Figure 2.15: *Probe current densities as a function of C2 aperture and 'spot size'. Little faith is put on the constant used in equation 2.10 to determine the absolute current densities but the values should be correct relative to each other*

The values of J shown on figure 2.15 are noted to be much smaller than expected. For high resolution microanalysis the probe current is as little as[11] $\approx 0.1 nA/nm^2$ whereas the average value is a factor of 10 less at $\approx 0.01 nA/nm^2$. The most probable reason for this discrepancy is that the manufacturers equation is either incorrect or the emulsion setting used in the equation is misquoted by the microscope. An emulsion setting of 0.25 was used in the calculation for RX film, but perhaps this value should be closer to 25. This error results in the loss of absolute current and current density measurements but the relative values for both should remain correct.

It is possible to calculate the approximate probe current from the charge on the PEELS spectrometer aperture. For this experiment the shield current reading is nullified when the viewing screen is down. Lifting the screen, the zero loss peak is obtained and focused at an energy dispersion of 0.05eV. The beam attenuator is switched on and the energy dispersion is set to 0.0eV once the acquisition is stopped. The shield current displays the beam current and to test that the beam is not hitting the beam trap aperture, the energy offset is adjusted by ≈200eV and no marked change is observed on the shield current. Although the FEG tip had been changed between this current experiment and the earlier one described above, the emission current is approximately the same. Only a rough estimate of the probe current is required however. The shield current is

determined for the C2a aperture at 'spot size 3' to be (0.5±0.2)nA. The limits encompass the range of possible currents for the microscope configuration used before the tip was changed. This result agrees very well with the earlier result of 0.5nA. However, the calibration on this current reading has never been performed so the level of confidence in the result is low. If this result were correct it could suggest that the spot diameters are overestimated, but to get a 0.5nA probe in $1nm^2$ the spot sizes would have to be overestimated by a factor of ≈5. It is possible that the spot diameter on the negative could be overestimated by as much as ≈20% since the lowest exposure time was 0.022s and the initial beam spreading in the negative is not known. The probe diameter measured for 'spot size 9' and C2a was ≈2nm. For this convergence angle the diffraction limit is ≈2nm therefore the probe could not have been smaller than measured. At this setting, the probe current density is $\approx 0.005 nA/nm^2$, so it is likely that either the probe current is much lower than expected or the current measured by both the PEELS system and the automatic exposure timer is out by a factor of ≈10.

Using the geometrical expressions for the probe size and current in equations 2.5, 2.6 and 2.8, the theoretical current density of the probe can be calculated as a function of aperture size and 'spot size'. Equation 2.12 shows the calculation of the current density from the upper column geometry. It should be noted that the strength of the objective lens is constant throughout the measurements.

$$J = \frac{I_{probe}}{A_{probe}} = \frac{K_1 (d_{IC1} / (L - d_{IC1}))^2}{\pi (D_0 M_{C1} M_{C2} M_{OBJ} / 2)^2} = \frac{K_1 K_2 (M_{C1} M_{C2})^2}{K_3 (M_{C1} M_{C2})^2} = K_4 \qquad [2.12]$$

In dividing the probe current by the probe area, the current density is assumed be exactly constant for a particular aperture regardless of the 'spot size'. Since the current scales with C2 aperture area, the current density should also scale in the same way. Thus the current density should be constant for a given aperture size when only the demagnification of the source is considered as contributing to the spot diameter. The current density should also vary directly as the area of the C2 aperture used if it defines

the beam. The relationships between the probe current density and lens/aperture configuration is reinforced by the fact that the brightness, B is a conserved quantity in the upper column, i.e. it is constant, in both a thermionic and FEG microscope[3]. From equation 2.9 it is clear that the current density, J, is constant for a given aperture (i.e. a given α) and should scale according to the area of the aperture.

$$B = \frac{I}{(\pi r^2)(\pi\alpha^2)V} \Rightarrow J \propto B(\pi\alpha^2)V \qquad [2.13]$$

Here, V is the electron voltage and r is the radius of the beam at the gun cross-over level. Experimentally, J is approximately constant as a function of spot size for the smallest C2 aperture. The error in J is determined from the errors in I (5%), and D (10%), added in quadrature, and is 15%. The values of J for C2a are constant within

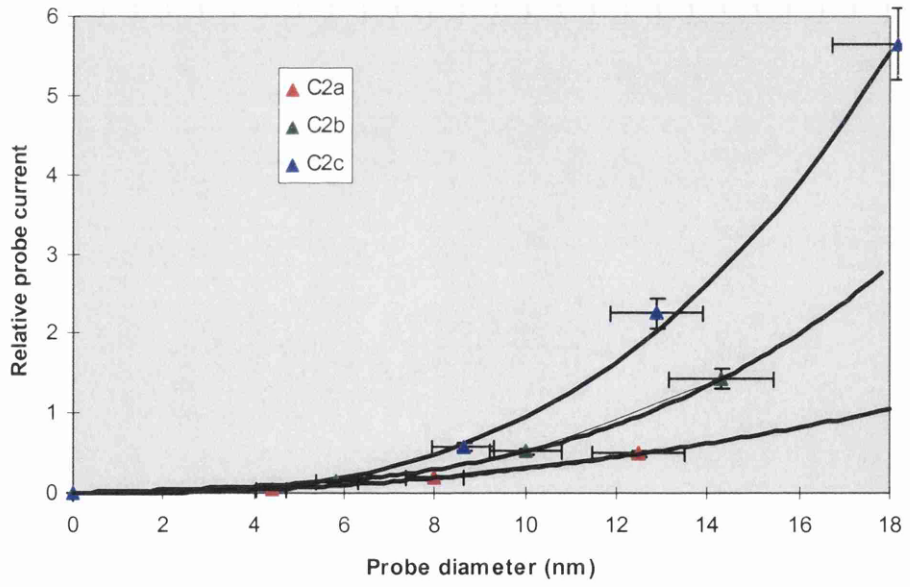

Figure 2.16: *Useful representation of the relationship between the probe current and diameter for the three smallest C2 apertures*

experimental error. However, the spot areas are enlarged due to aberrations which increase with aperture size as described earlier. Therefore the current density does not scale up according to the aperture size. Also, the relative magnitude of the aberrations

increase with 'spot size', so the probe current density decreases accordingly. Since the spot sizes involved in current measurements range from 3 to 9 only, diffraction effects are not significant in affecting the probe diameter and current density. Finally, figure 2.16 shows a useful representation of how the probe diameters and currents relate to each other for the three smallest C2 apertures.

2.5.4 Summary

Four important properties of a focused probe for the Philips CM20 in nanoprobe mode: its convergence angle, diameter, current and current density. These affect the spatial (or angular) resolution in STEM and CTEM imaging, diffraction, and any microanalysis techniques like EDX or PEELS.

The convergence angles defined by the C1 apertures are shown in table 2.1 and are lower than expected in a TEM due to the larger gap in the objective lens which was designed for magnetic specimens. This implies that diffraction effects should limit the minimum probe diameter available. However it is clear from the probe diameters in figure 2.5, that the magnification of the electron source by the upper column lens limits the probe diameter for most of the 'spot sizes'. It appears that there is no other reason for the diameters increasing with aperture size than the presence of surplus aberrations in the upper lenses or gun. The evidence suggests that the main source of aberrations is in the gun lens where chromatic aberrations present before the accelerators could produce the results observed.

Relative probe currents are calculated as shown in figure 2.13 and agree very well with calculations made from the geometry of the electron optics. The current varies as the area of the C2 aperture apart from the largest C2 aperture where it is no longer beam defining. Using both the relative probe diameters and probe currents calculated from the geometry of the microscope, it can be shown that the current density should be constant for a given aperture, and should vary as the area of the aperture used. The probe current density is calculated from the experimental results and compared to those

predicted by the geometry. Owing to the aberrations present, which increase in magnitude with convergence angle, the probe current densities are reduced significantly below those predicted.

2.6 Diffraction

2.6.1 Theory

Discovered in 1927, electron diffraction is the phenomenon of the scattering of electrons as they pass through a material. Scattering can occur elastically where the electrons change direction while losing almost no energy to the atoms of the material, or inelastically, where the change in direction is accompanied by a significant loss in energy. For an electron transparent amorphous material, having little or no regular atomic structure, the electrons are scattered by the sample in a distribution approaching that of scattering by a single atom. In a crystalline sample, the atomic arrangement in the material is such that at given scattering angles the scattered waves are in phase causing their amplitudes to add. Outwith these directions the intensity rapidly decays to zero. This results in a number of strongly diffracted beams with the scattering angles dependent on the structure of the material. These angles are known as Bragg angles, 2θ, and are defined by equation 2.14.

$$2d\sin\theta = \lambda \qquad [2.14]$$

Here, d is the spacing between the parallel planes responsible for the diffracted beam. For a crystalline material, where the atoms are arranged in an array of repeating unit cells, the intensity of these spots are dependent on the atomic structure factor and the position of the atoms in the unit cell. The complex wave representing the electron beam scattered from a unit cell is given by equation 2.15[12].

$$A_{cell} = \frac{e^{2\pi i\mathbf{k}\bullet r}}{r}\sum_i f_i(\theta)e^{2\pi i\mathbf{K}\bullet\mathbf{r}_i} \qquad [2.15]$$

Here $\boldsymbol{k}$ is the electron wave vector in the specimen, $\boldsymbol{K} = \boldsymbol{k}_{diff} - \boldsymbol{k}_{init}$, θ is half the scattering angle, $\boldsymbol{r}_i$ is the location of each atom in the unit cell, f_i is the atomic scattering amplitude for the ith atom, and r is the radius of the sphere describing the electron wavefront. The summation on the right hand side is also known as the structure factor of the crystal. Defining $\boldsymbol{r}=x_i\boldsymbol{a}+y_i\boldsymbol{b}+z_i\boldsymbol{c}$ and considering $\boldsymbol{K}=\boldsymbol{g}=h\boldsymbol{a}^*+k\boldsymbol{b}^*+l\boldsymbol{c}^*$ (where $\boldsymbol{a}^*$,$\boldsymbol{b}^*$, and $\boldsymbol{c}^*$ are the respective reciprocal lattice vectors) for an infinite, perfect crystal with the location of the atoms in the basis given by x_i, y_i, and z_i, one can arrive at equation 2.16[12] which determines the structure factor, F_{hkl}.

$$F_{hkl} = \sum_i f_i e^{2\pi i(hx_i+ky_i+lz_i)} \qquad [2.16]$$

This completely general equation is integral in recognising and analysing diffraction patterns. It tells us, for crystalline silicon, with its diamond-like structure, that reflections from the {hkl} planes are only possible if *hkl* are all odd, or all even *but* divisible by four. For example {200} reflections will not be present.

Summing over all unit cells in a specimen of thickness, t, the expression for the intensity of a diffracted beam, $|\phi|^2$ as given in equation 2.17a.

$$|\phi_g|^2 = \left(\frac{\pi t}{\xi_g}\right)^2 \frac{\sin^2(\pi\, t s_{eff})}{(\pi\, t s_{eff})^2} \qquad [2.17a]$$

where

$$\xi_g = \frac{\pi V_C \cos\theta_B}{\lambda F_g} \quad \text{and} \quad s_{eff} = \frac{\sqrt{w^2+1}}{\xi_g} \qquad [2.17b,c]$$

In equation 2.17a, ξ_g is the extinction distance for the diffracted beam, F_g is the structure factor for the unit cell, V_c is the volume of the unit cell and w is the deviation from the diffraction vector in **k**-space and is dimensionless. This equation is important

when considering diffraction intensities in the analysis in chapter 7 when quantifying texture. A graphical representation of this equation is shown in figure 2.17[13].

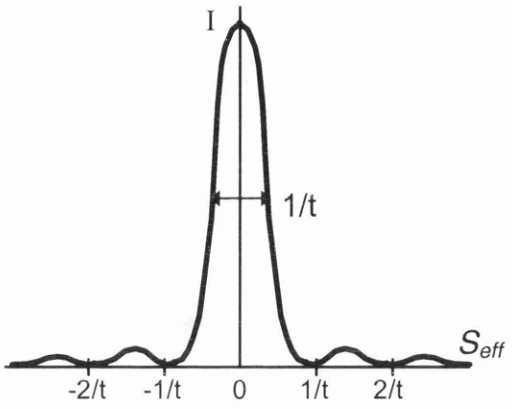

Figure 2.17: *Intensity of a diffraction spot as a function of deviation from the Bragg condition in reciprocal space*

2.6.2 Diffraction Techniques

A diffraction pattern is formed when the scattered and unscattered beams are focused onto the back focal plane of the objective lens. Figure 2.18 shows diffraction patterns from amorphous, single crystal and polycrystalline samples. There are several types of diffraction pattern for a crystalline material depending on the nature of the incident

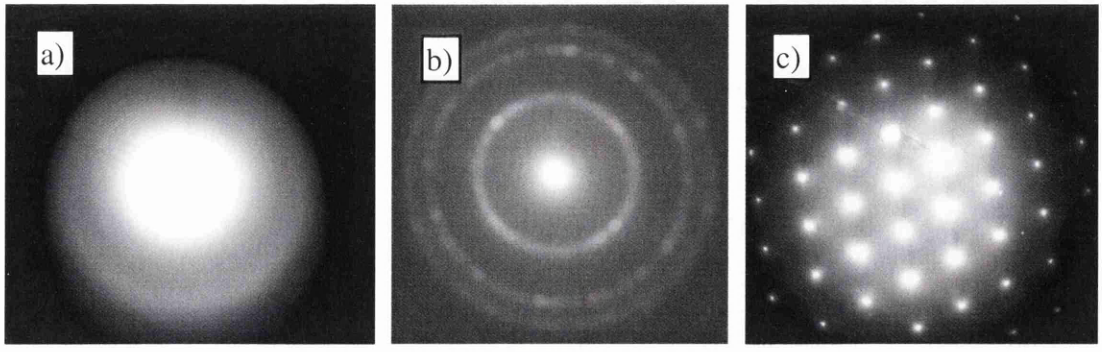

Figure 2.18: *Examples of electron diffraction patterns for a) amorphous, b) polycrystalline, and c) single crystal specimens*

beam and the thickness of the specimen. The spot pattern in figure 2.18c arises when near-parallel electrons pass through a thin specimen and the objective lens focuses parallel electrons to the same spot. Convergent beam electron diffraction (CBED) arises when the beam forms a cone as it focuses on the specimen. The diffraction spots are then spread out into discs having a diameter proportional to the angle of convergence. Under certain conditions, detailed information can be ascertained from the internal patterning of the CBED discs[14], e.g. orientation, lattice parameter, strain, etc.

If the specimen is thick enough (>50nm) and has a low defect density, Kikuchi patterns will appear with CBED. These arise from a combination of inelastic then elastic scattering, producing dark and bright lines as well as diffraction spots. Crystal imperfections cause the Kikuchi lines to become diffuse with parallel illumination, as here there is a larger volume of specimen illuminated than with CBED[15]. The Kikuchi patterns can be seen as a direct projection of crystal planes onto the diffraction plane and in this way are ideal for identifying crystal orientations. Chapter 5 uses these patterns to identify preferred orientations in polycrystalline silicon (polysilicon, or polySi) films. Normal selected area diffraction (SAD) simply uses an aperture in the column to select an area on the specimen which will contribute to the diffraction pattern. It avoids having to tailor the angle of convergence to fit the size of the area directly, e.g. one can illuminate a small area with parallel illumination.

Backscattered diffraction patterns are often used to investigate texture[16] and are a result of scattering by a beam of electrons incident at an angle of ≈30°, although normal incidence can also be used. The spatial resolution and intensity of these patterns are poorer than transmitted patterns but allow diffraction analysis on bulk samples. A comparison of the electron diffraction methods, including backscattered diffraction patterns, for local texture measurement is given in table 2.2.

Table 2.2: *Comparison of electron diffraction methods for local texture analysis and related measurements.*

Type of pattern	*Equip-ment*	*Resolution*		*Main Applications*
		Spatial	*Angular*	
Spot	TEM (SAD)	>0.2μm	0.1°	Estimate of orientation, phase, DF imaging. Dislocations, Burger vector analysis
Transmission Kikuchi	TEM (SAD)	>0.2μm	0.1°	Coarse crystal orientations, orientation difference, dislocation density
	TEM (probe)	≈10nm	0.2°	Fine grain orientation, deformed materials, grain growth
Backscattered Kikuchi	SEM	0.2-2μm	1-2°	Bulk sample crystal orientation, fracture processes, dynamic studies (on hot stage)
Channelling	SEM	10μm	½°	Bulk sample crystal orientations, orientation difference, stress
Micro Kossel	SEM	2μm	0.4°	Lattice parameters, stress, phase, orientation difference

2.7 EDX

2.7.1 Theory

EDX analysis is used in the TEM, primarily, to identify the composition of a material. When incident electrons of 200keV are incident on a thin specimen, X-rays are produced by two different mechanisms resulting in bremsstrahlung and characteristic X-rays. Bremsstrahlung X-rays are produced when electrons are accelerated in the electric field of the atomic nuclei and can have an energy anywhere between zero and 200keV. Their energy distribution is approximately the same for any material so the bremsstrahlung X-rays do not give any chemical information, but can be used to give an estimate of the mass-thickness of the specimen.

Incident electrons may remove an electron from an inner shell of an atom if they have sufficient energy to overcome its binding energy. The subsequent de-excitation of the

atom may result in the production of an X-ray and has an energy characteristic of the atom involved. A typical EDX spectrum is shown in figure 2.19.

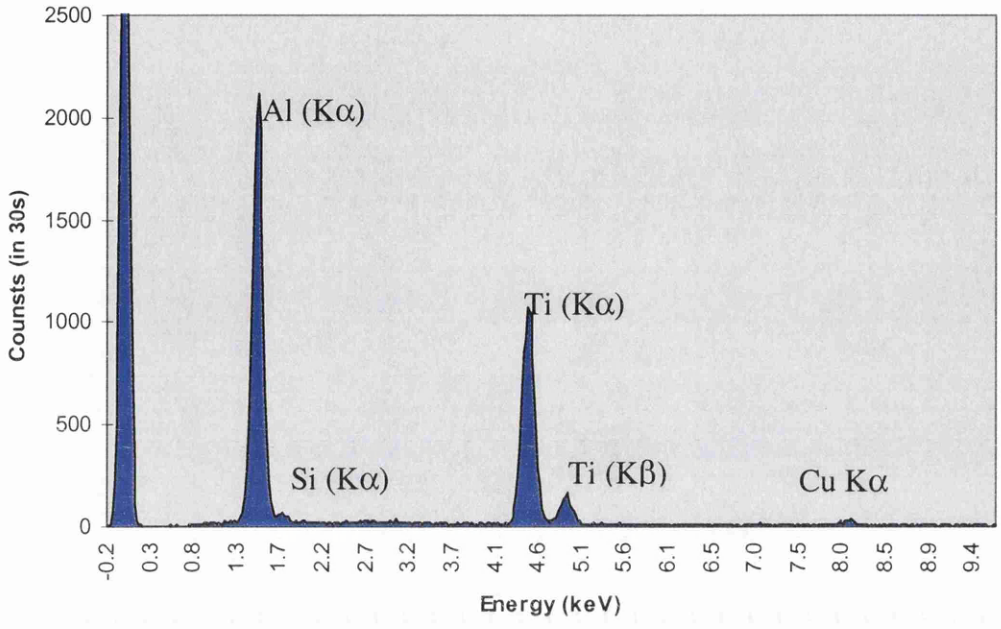

Figure 2.19: *A typical EDX spectrum showing Al (Kα), Si (Kα), Ti (Kα, Kβ) and Cu (Kα) peaks*

Characteristic radiation is emitted isotropically while Bremsstrahlung intensity falls off markedly with increasing angle to the incident beam direction. Thus, with the detector normally positioned between 90° and 160° to the emergent beam, the peak to background ratio is very high. The cross-section for the production of a Kα X-ray, i.e. from the de-excitation from the L to the K energy band, is defined in equation 2.18[17].

$$\sigma_c = s\omega\sigma_{ik} \qquad [2.18]$$

Here, σ_{ik} is the total cross-section for the K shell, ω is the fluorescence yield and s is the partition function or branching ratio i.e. the ratio of the Kα X-rays to the total number of X-rays from the K shell.

For most of the EDX analysis performed on silicon devices in chapter 7 there is no need to determine absolute values of atomic concentrations; only relative values. It can be shown[18] that the atomic ratio, C_A/C_B of two elements present in the specimen is directly proportional to the intensity ratio, I_A/I_B of two characteristic X-ray lines as in equation 2.19.

$$\frac{I_A}{I_B} = \frac{k_A \varepsilon_A}{k_B \varepsilon_B} \frac{C_A}{C_B} \qquad [2.19a]$$

where

$$k = \sigma_{ik} \omega s \qquad [2.19b]$$

Here, ε is the detector efficiency. The situation is more complicated in the case of the L shell in that the fluorescence yields for the L shells are not so accurately known and radiationless transitions may occur between shells. However, all the quantitative analysis performed in this work involved K X-rays.

2.7.2 EDX Detector Performance

The X-ray detector on the Philips CM20 is a Si(Li) atmospheric thin window detector and is attached level with the specimen. As the beryllium window is very thin it allows detection of elements having an atomic number of 6 and above. The energy resolution of the detector is nominally 136eV and the collimator lies at an angle of 100.5° to the emergent beam. Both the experimental detection limit and the spatial resolution of the system are investigated in chapter 7.

2.7.3 Analysis of Data

In order to analyse data quantitatively the background must be stripped from the peaks of interest. If the peak to background ratio is sufficiently high then the background can

be removed using a linear fit and this is found to be the case for all work performed on silicon devices in chapter 7.

If the specimen is thick then corrections have to be made for fluorescence and absorption effects. For our analyses, the areas of interest on the specimens were found to be thin enough that absorption be ignored. Although, specimens up to 300nm thick can be investigated using EDX, but fluorescence would have to be considered for accurate analysis.

Detailed EDX analysis is described in chapter 7 for various situations including the determination of the spatial resolution available with EDX and the elemental profiles across a TiN diffusion barrier.

2.8 EELS

2.8.1 Theory

In EELS, the energy lost by inelastically scattered electrons is measured and used to provide information on the chemical composition of the specimen which is irradiated. If an incident electron ejects an electron from an inner shell to the continuum, this will produce an ionisation edge in the energy loss spectrum. The edge onset is at the binding energy for that shell, thus the edges are characteristic of the material being irradiated and can be used to determine the chemical composition. Excitation of electrons to empty valence states rather than to the continuum, results in peaks superimposed on the edge which provides information on the atomic environment of the element [19].

A typical energy loss spectrum is shown in figure 2.20[20]. The energy loss spectrum contains a large zero loss peak resulting from electrons which have lost less energy than the resolution of the system. The next most intense feature is the first plasmon peak where electrons have lost energy to the valence or conduction electrons, a process

known as a plasmon excitation. The region containing the zero loss and the valence excitations is called the low-loss region. Characteristic edges are superimposed on the background, i.e. the tail of the low-loss peaks and these ionisation edges contain fine structure which can be split into two regions. Near edge fine structure (ELNES) is within 50eV of the edge threshold and extended edge fine structure (EXELFS) can extend for several hundreds of eV beyond the edge. Multiple scattering can also occur, leading to a redistribution of the energy spectrum. The probability of an electron experiencing two plasmon or two core excitations is low. However, the probability of a core and a plasmon excitation occurring increases as the thickness of the specimen increases.

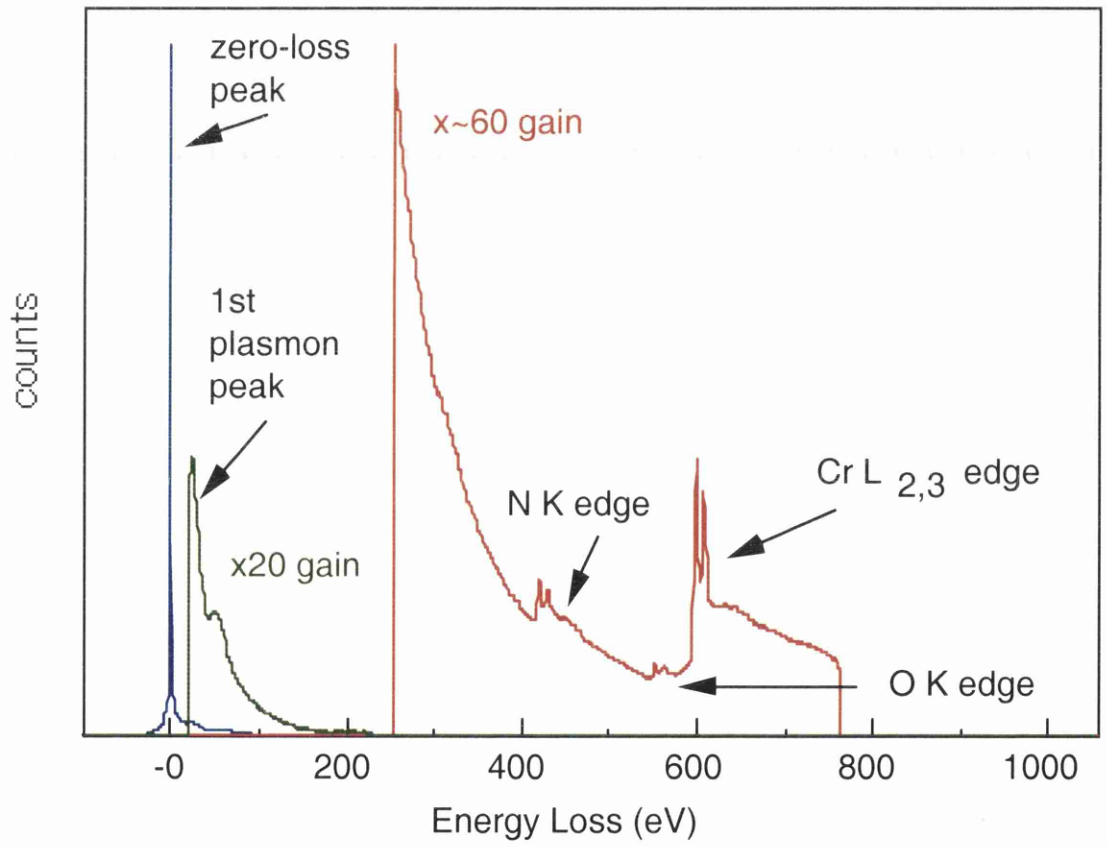

Figure 2.20: *A typical PEELS spectrum of a CrN layer showing the characteristic peaks*

It is possible to obtain quantitative information from the ionisation peak intensities. Equation 2.20 can be used to find the number of atoms, N of an element present in the irradiated specimen[19].

$$I_k(\Delta,\alpha,\beta) = N\sigma_k(\Delta,\alpha,\beta)I_o \qquad [2.20]$$

Here, $I_k(\Delta,\alpha,\beta)$ is the background-subtracted intensity in a window of energy width Δ, I_o is the intensity in the zero loss peak and $\sigma_k(\Delta,\alpha,\beta)$ is the partial cross-section for the window Δ. The intensity in the window and the partial cross-section are functions of the convergence and collection semi-angles, α and β as the collector aperture only allows electrons into the spectrometer which have been scattered through an angle less than β.

However, for the analysis in chapter 7, it is the atomic ratios that are of interest rather than the absolute number of atoms in the sample. Using equation 2.20, the atomic ratio of two elements, a and b may be calculated using equation 2.21.

$$\frac{N_a}{N_b} = \frac{I_{ka}(\Delta_a,\alpha,\beta)\sigma_{ka}(\Delta_a,\alpha,\beta)}{I_{kb}(\Delta_b,\alpha,\beta)\sigma_{kb}(\Delta_b,\alpha,\beta)} \qquad [2.21]$$

Specimen thickness can also be determined from the energy loss spectrum. For independent scattering events within a foil, the probability of several successive collisions of an electron occurring is given by a Poisson distribution. Thus, the intensity in the zero loss peak, I_o is given by equation 2.22.

$$I_0 = I_t \exp\left(-\frac{t}{\lambda_T}\right) \qquad [2.22]$$

Here I_t is the total intensity reaching the spectrometer, so if λ_T is known for the specimen, then the thickness can be calculated.

Specimen thickness is limited to ≈100nm for useful EELS data as the peak to background ratio falls rapidly with thickness, making it difficult to distinguish edges. If the specimen is too thin, however, then there is very little scattering and the signal to noise ratio is low. At 200keV the optimum thickness is ≈40nm.

2.8.2 The EELS spectrometer

A GATAN model 666 parallel-detection electron energy loss spectrometer was used to collect the spectra on the Philips CM20. A schematic diagram of the detector is shown in figure 2.21. Once through the entrance aperture the electrons are focused with two quadrupole and two sextupole lenses. A magnetic sector disperses the electrons into an energy spectrum and this dispersion in then increased by four quadrupole lenses and

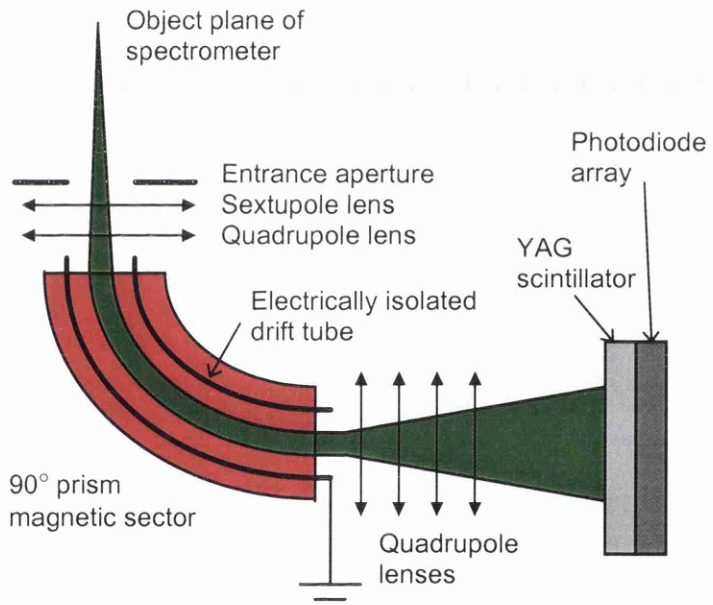

Figure 2.21: *A schematic diagram of the Gatan 666 PEELS detector*

projected onto a single crystal yttrium aluminium garnet (YAG) scintillator. The scintillator is coupled to a linear photodiode array consisting of 1024 channels and enables simultaneous collection of electrons which have lost different amounts of energy. The electrically isolated drift tube allows the energy offset of the spectrum to be

varied by applying a voltage to it. The final energy dispersion of the spectrum is determined by the four quadrupole lenses which can be varied from 0.05 to 2.0eV per channel.

2.7.3 Analysis of data

Analysis of the EELS data is performed using the EL/P versions 2.1 and 3.0 software provided by Gatan. This software performed various operations on the spectra to aid quantitative analysis. The program provides mathematical tools and routines which allow the extraction of meaningful data from the EELS spectra including relative specimen thickness and the relative concentrations of the elements present. All of the spectra are analysed in a similar way to allow comparisons to be made between different data sets.

An outline of the processes performed to extract quantifiable information from the raw data is as follows. The dark currents are removed from the spectra and the energy scales are calibrated by setting the channel in the low-loss spectrum with the maximum number of counts equal to 0eV. The same channel in the corresponding edge spectrum is set to the value of the energy offset applied by the voltage scan module (VSM) during acquisition, e.g. 99eV for Si $L_{2,3}$ edge. The EL/P routine to compute the sample thickness is applied to the low-loss spectrum to calculate the t/λ value. The background before the first edge of interest in the edge spectrum is stripped off using the background fit provided by EL/P. The plural scattering is then removed from the edge spectrum using the Fourier-Ratio routine. This routine required the input of the background-subtracted edge spectrum and the corresponding low-loss spectrum whereby the low-loss spectrum is deconvoluted from the edge spectrum. Smearing effects introduced by the detection system are reduced using a sharpening process which used the zero-loss peak collected through a hole in the specimen.

Quantification of the new spectra is performed by integrating the counts in each edge over a window of width Δ. Different values of Δ could be used for different edges as

plural scattering was removed. Equation 2.20 is used to calculate the atomic ratios but it requires that the partial cross-sections for each element are known.

A more detailed account of these, and further, processing steps are described in chapter 7 in the quantification of the Ti to N atomic ratios across a TiN diffusion barrier.

References to Chapter 2

[1] A. V. Crewe, Journal of Microscopy, **178**, 2, (1995) 93

[2] C. Colliex and C. Mory, in *Quantitative Electron Microscopy,* Proceedings of the 25th Scottish Universities' Summer School, eds. J. N. Chapman and A. J. Craven, SSUSSP Publications, Edinburgh, (1983)

[3] A. V. Crewe, Ultramicroscopy, **23** (1987) 159

[4] G. Black and E. H. Linfoot, Proc. Roy. Soc (London) A239 (1957) 522

[5] G. W. Lorimer, in *Quantitative Electron Microscopy,* Proceedings of the 25th Scottish Universities' Summer School, eds. J. N. Chapman and A. J. Craven, SSUSSP Publications, Edinburgh (1983)

[6] M. E. Haine, in *The Electron Microscope: The Present State of the Art*, Spon , (1961), 8

[7] P. Grivet, in *Electron Optics: Part: Optics*, Pergamon Press, Oxford, (1972) 155

[8] Philips Electron Optics, 'Alignment of the TEM' CM20 Manual

[9] Philips Operating Instructions 'CM20/STEM Electron Microscope' Customer Support Manual

[10] J.J. Hren, J. I. Goldstein, D. C. Joy, *Introduction to Analytical Electron Microscopy*, Plenum Press (1979)

[11] Private communication, A. J. Craven, and J. N. Chapman, University of Glasgow, UK

[12] D. B. Williams and C. B. Carter, in *Transmission Electron Microscopy: Diffraction II,* Plenum, New York (1996) 204

[13] G. Thomas, and M. J. Goringe, in *Transmission Electron Microscopy of Materials*, John Wiley & Sons, New York, (1979) 94

[14] J. C. H. Spence and J. M. Zuo, in *Electron Microdiffraction*, Plenum, New York, (1992) 85

[15] R. A. Schwarzer, Textures & Microstructures, **20,** (1993) 7

[16] R. A. Schwarzer, Micron, **28**, 3, (1997) 249

[17] J. N. Chapman, W. A. P. Nicholson, and P. A. Crozier, Journal of Microscopy, **136**, 2 (1984) 179

[18] G. Cliff and G. W. Lorimer, Journal of Microscopy, **103** (1975) 203

[19] R. F. Egerton, in *Electron Energy Loss Spectroscopy in the Electron Microscope,* Plenum New York (1985)

[20] M. MacKenzie, PhD Thesis, University of Glasgow, (1997)

CHAPTER THREE

Specimen Preparation and Imaging of Device Structures

3.1 Introduction

For any TEM analysis of a sample, the area of interest must normally be <250nm thick to get useful information. Conventional specimen preparation techniques involved grinding and dimpling the area on the sample to a thickness of ≈30μm then ion milling down to electron transparency[1], [2]. However, the accuracy in preparing a particular electron transparent site is ≈0.2mm. To perform any useful TEM analysis on a silicon device, a site-specific accuracy of ≈1μm is required. So, as soon as the TEM began to appear in device product analysis labs around two decades ago, preparation techniques were developed for site-specific TEM analysis[3].

Fundamentally, there are two specimen preparation techniques available today for the TEM, each having their own variations. The Focused Ion Beam (FIB)[4] machine is the predominant technique and is found mainly in failure analysis labs due to the nature of the specimens produced by the technique. The other is the Tripod Polisher (TP)[5], along with its similar counterparts, which is found more in long-term research institutes and, to a lesser extent than the FIB, in failure analysis labs. Each produce site-specific TEM samples but with significantly different properties. The TP technique is used for the samples described in this thesis as it has the required properties for longer term research. It is important to understand and compare both techniques, so operation of the

FIB machine is explained before moving on to the TP. Attention is then directed to the information obtainable from TEM imaging of TP specimens, information that would not be so evident using FIB techniques.

3.2 Focused Ion Beam (FIB) specimen preparation

Before using this technique, a thin strip (≈50μm) of a device is prepared which contains the site of interest in the middle of one face as shown in figure 3.1. The specimen is then mounted on a washer and inserted into the FIB for cross-sectioning. The principle behind the technique is to use an ion beam (normally Ga^+) to gradually etch away

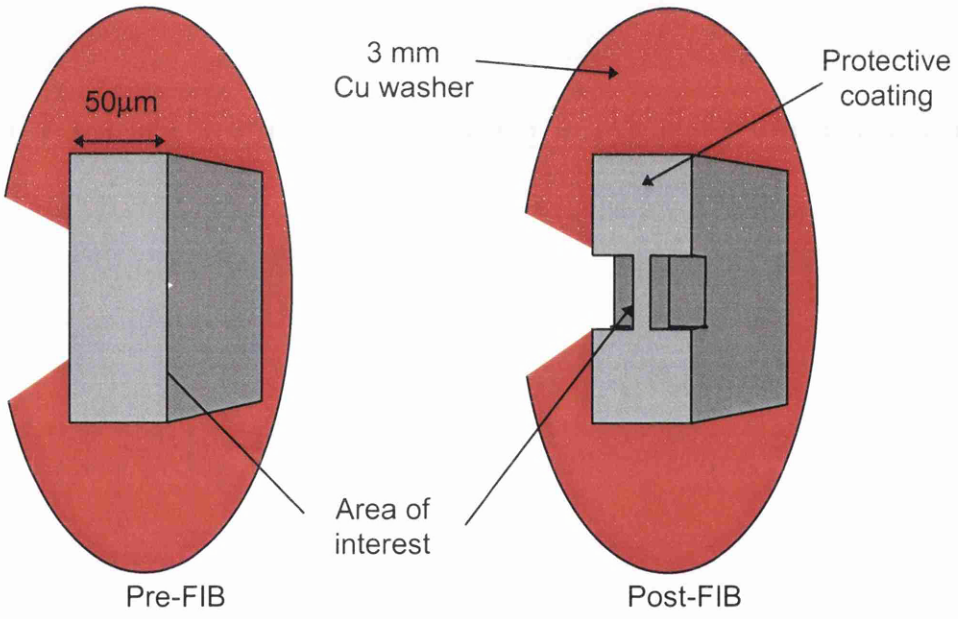

Figure 3.1: *FIB specimen preparation. The electron transparent area of interest is approached from either side by ion milling at progressively lower beam energies*

towards the region of interest from both sides, leaving only the specific area electron transparent. The FIB is equipped with an ion or electron detector, depending on the model, which allows simultaneous imaging of the specimen while thinning. Before the FIB thinning a protective metal layer (usually Pt) is deposited to protect the surface of

the area of interest from the damaging ion beam. Typical thinned areas are 15-20μm wide and 5-10μm deep.

Due to the imaging capability of the FIB, the technique is very useful for failure analysis, since a particular structure can be etched away slice by slice to reveal the buried point defect. Combined with the point resolution offered by the ion beam of ≈5nm[6], the FIB is the predominant tool for TEM specimen preparation in failure analysis labs.

The disadvantages of the technique lie in the cost of the machine and the small electron transparent area of the specimen. The nature of the FIB trenches in the specimen prevent TEM analysis where significant specimen tilt is necessary, e.g. in some texture analysis. Users also find there is often significant lattice damage present due to the bombardment of the ions on the specimen. The depth of damage is normally ≈20nm on each side wall, even the application of the protective coating can damage the top surface over a distance as much as 40nm[7]. For the purposes of the work in this thesis, it is necessary to have many repeating structures for accurate materials characterisation, so FIB prepared samples are not suitable in this case.

3.3 Tripod Polishing

3.3.1 Introduction

For all the devices examined in this thesis, the tripod polisher (TP) is used to prepare them for TEM, although a dimpling technique[1] is used to prepare the GaAs sample described in chapter 7. A photograph of the TP is shown in figure 3.2. For the TEM, the specimen has to be prepared which is <3mm diameter and having the area of interest electron transparent. The idea behind this technique is to grind away the material from both sides of the line of interest at a small angle. This way, the line of interest becomes the electron transparent apex of a wedge. Besides the TP, this technique requires two

optical microscopes of ≈60× and ≈400×, a revolving wheel mechanical polisher, and cleaning agents, glues. Both an ion milling machine and an SEM are optional.

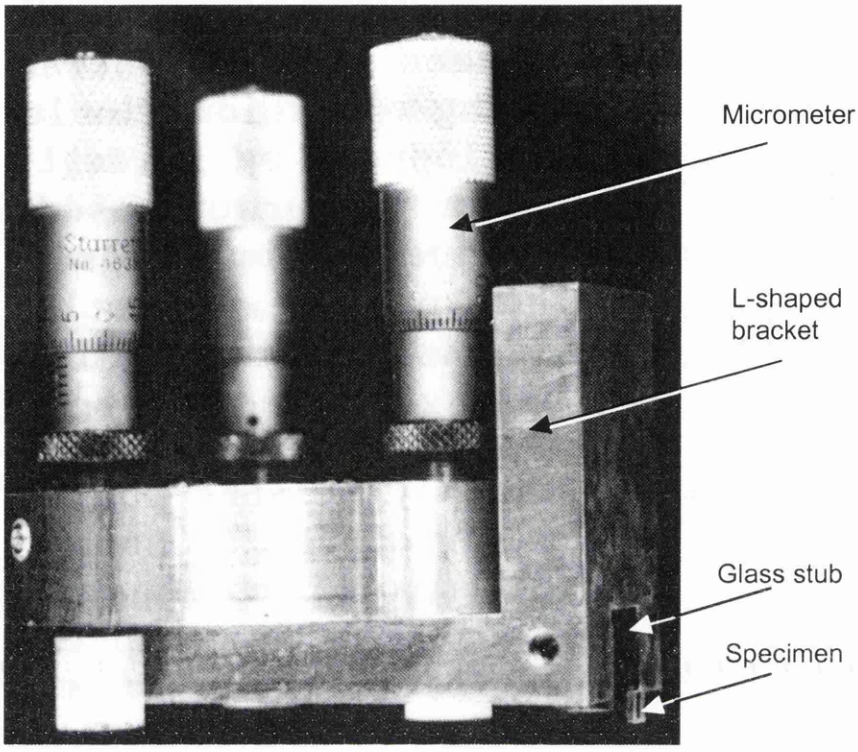

Figure 3.2: *Image of the tripod polisher developed by IBM (Ron Anderson et al)*

3.3.2 Polishing First Side

Before the specimen is attached to the TP, a ≈3×3mm^2 square containing the region of interest is cut out of the device. Quick Stick 135 mounting wax is then used to glue the specimen onto the glass stub of the polisher as shown in figure 3.3a. The line of interest should be approximately parallel to the base of the glass stub. The height of the micrometers are adjusted to be level with the line of interest using a large glass slide with the specimen overhanging, and the micrometers are locked at this position. A lapping film containing fine particles of diamond is attached to a wheel using water surface tension. Here the water is 'squeegeed' out providing excellent adhesion of the film to the wheel. The TP is held gently on top of the revolving wheel in the direction shown in figure 3.3b. Running water reduces damage to the specimen when grinding.

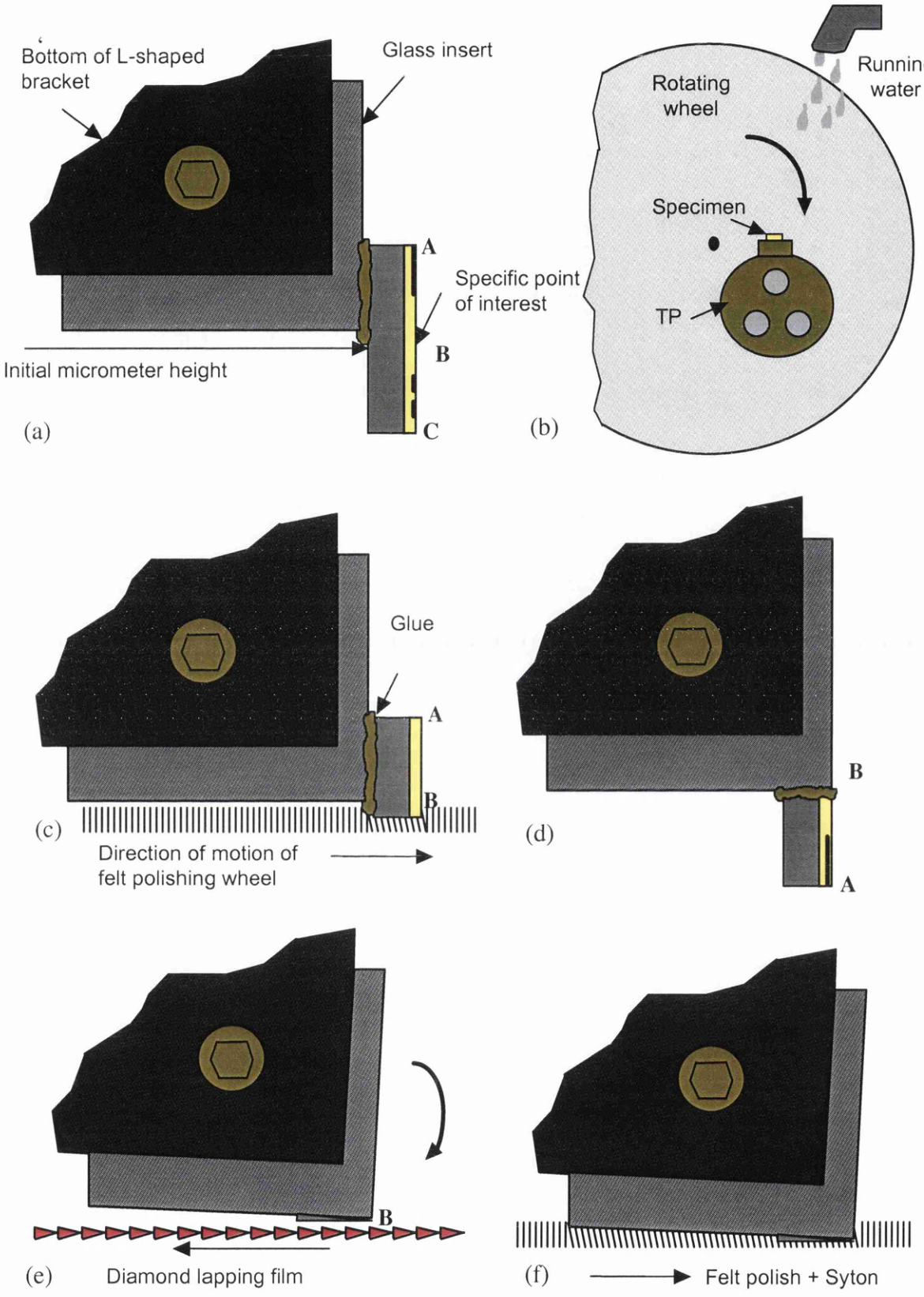

Figure 3.3: *The stages of tripod polishing for cross-sectional specimens*

Diamond lapping film with particle sizes of 30μm is used initially for course grinding. As the line of interest is approached, films having successively smaller particle sizes are used to remove the scratches from the previous film and reduce the rate of removal of material. Table 3.1 states the grade of film used for the approximate distance to the line of interest. It is important that, particularly with the lapping films having lower particle sizes, the trail of removed material should not return to the specimen. It is advisable to start each abrasion from the centre of the wheel, slowly moving out to the ends. Large stresses on the specimen can arise if it is brought onto the outside of the wheel first.

Table 3.1: *Grade of film used for specimen thickness*

Distance to line of interest	>200μm	>60μm	>30μm	>15μm	>7μm	>2μm
Grade of film (diamond size)	30μm	15μm	6μm	3μm	1μm	0.5μm

These are typical values but can be adjusted according to the level of experience of the processer. A method of determining the distance of the polished surface to the line of interest under the 60× microscope is to compare the device with a piece of paper which is normally ≈100μm thick. Close to the line of interest, the 400× optical microscope is used to observe the distance to the line on the device in plane.

The back two micrometers can be adjusted to align the lateral grinding angle to that of the line of interest. When the surface of the abraded specimen is <2μm from the line of interest, a fine, felt polish is used. For this, it is important to change the direction of the TP on the wheel. Syton HT 50 colloidal suspension is used during the final polish to remove all scratches. The optical microscope is now used to view the specimen in cross-section as this provides greater accuracy in determining the line of interest. An SEM can be used to improve the accuracy in determining the exact line of interest, such a practice will become increasingly necessary as device sizes shrink. The 400× optical microscope was sufficient for the specimens studied here.

Once the line of interest has been reached, the glass stub holding the specimen is unscrewed and placed specimen-down on filter paper in a petri-dish containing acetone. The acetone dissolves the wax and, after 20-30mins, the glass stub is lifted off the specimen. The acetone is pipetted out and replaced by alcohol for 5mins to further clean the specimen.

3.3.3 Polishing Second Side

Before the specimen is mounted onto the bottom of the stub, the TP is 'planarised'. This means that the three micrometers are levelled with the glass stub. This is most easily accomplished by observing the stub from the back for unevenness. The 30μm diamond lapping film is used to both level the TP and produce a slightly rough surface for the wax to adhere to. The glass stub is removed and the specimen mounted on its bottom side with the device side of the chip facing forward, parallel to the front of the glass stub (figure 3.3d). The specimen should be moved around gently with toothpicks to remove air bubbles underneath it. After 5mins, when the wax has set, the stub is attached to the TP. The back two micrometers are lengthened by 0.5mm (one turn) to produce a wedge angle of ≈ ¾° as shown in figure 3.3e. The smaller this angle, the more uniform the thickness of the final electron transparent cross-section. A deeper electron transparent region is also obtained. However the specimen shall require more care in the final polishing stages; moving onto the fine polishing at an earlier time. It is often difficult to place the specimen onto the stub lying entirely flat so angles below ½° are not advisable.

The grinding process is repeated, going through the various grades of diamond lapping film and felt polishing as before. However some difficulties in determining the distance from the line of interest arise. Once <100μm away form the line of interest, the wax usually obscures the device so it is advisable to gently cut off a small portion of the hardened wax with a razor blade from one end of the sample. By knowing the distance between regularly spaced rows of structures in an array (from high magnification optical images) it is possible to count the number of rows from the line of interest under the 60×

microscope. As the thickness reduces to <20μm, the 400× optical microscope should be used in the same way. Below 10μm, silicon transmits light. For white light, the transmitted colour is dependent on the thickness of the sample according to table 3.2.

Table 3.2: Colour of transmitted white light through thin silicon

Thickness (μm)	10-8	7-5	4-3	2-½	<½
Colour	Dark red	Bright red	Orange	Yellow	White

As the grinding surface approaches the line of interest, adjustments can be made on the heights of the back two micrometers to control the lateral angle of the grinding surface. It is wise to enter the very final stages of polishing having a small lateral angle on the specimen. This causes one end of the specimen to erode away first and the point of erosion on the wedge apex gradually moves inward. Another advantage of cross-sectioning at a slight angle through the device structures when polishing from the first side, is that it is possible to obtain 3D information of identical structures in the sample.

During the felt polishing, the specimen should be observed in cross-section under both the transmitted light and 400× microscopes. If required, the specimen can be viewed in an SEM to observe its thickness and angle. The thinning should be planned to reduce the amount of felt polishing as much as possible. Ideally, felt polishing should only be used to remove any scratches from the grinding and could be used only for specimens <1μm thick. This polishing process is much more apt to preferentially thin the materials which make up the components and, if prolonged, usually results in the erosion of the top surface materials like high metal levels.

3.3.4 Mounting on Copper Washer

At this point various people apply different techniques to mount the specimen onto a supporting grid, or washer, for use in the TEM. Some choose to let the specimen fall off the stub (as performed after polishing the 1st side) then placing the grid, which is loosely glued to a glass slide, onto the specimen. However, this involves working with a very

thin and fragile specimen. The method used here is to directly place a Cu washer onto the specimen while it remains on the stub. Five-minute epoxy resin is applied to the specimen using a sharpened cocktail stick, with care taken to avoid covering the region of interest. The Cu washer is then placed down gently onto the epoxy using tweezers with the hole over the region of interest. After one hour of allowing the epoxy to set, the stub is placed on filter paper in a petri-dish of acetone with the washer face-down. The stub is left for ≈30mins to allow the wax to dissolve completely. Care should be taken not to leave the stub in too long in case the epoxy dissolves. The stub is lifted off the specimen, and the petri-dish is filled with fresh acetone for ≈5mins then the specimen is soaked in two alcohol baths of ≈5mins each. Spots of Silver Dag are placed on either side of the specimen to obtain electrical contact to the Cu washer as shown on figure 3.4. This prevents charging in the specimen with the electron beam in the TEM. Figure 3.5 shows a very low magnification TEM image of the whole length of the electron transparent apex of a specimen.

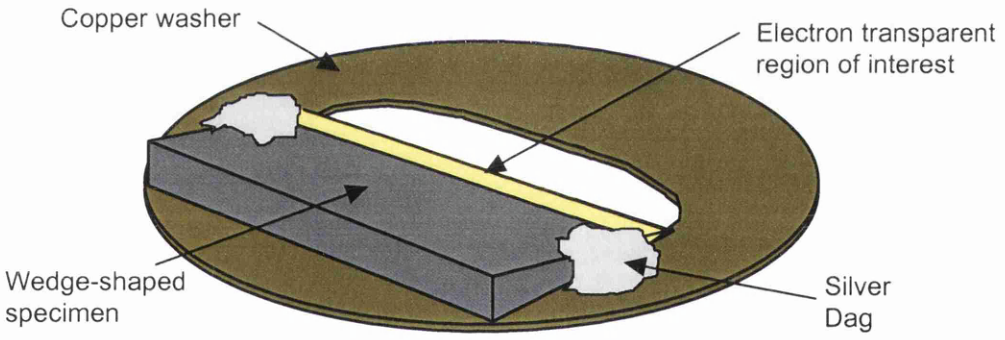

Figure 3.4: *The resulting specimen glued onto a Cu washer*

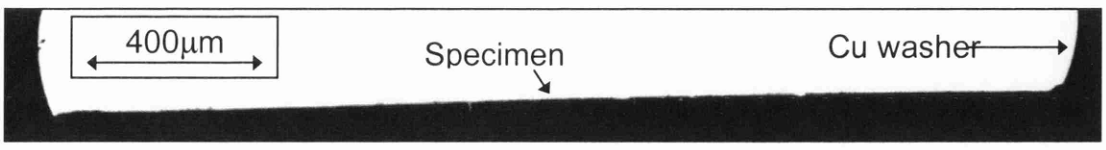

Figure 3.5: *Low-mag TEM image of whole e-t region of specimen on the Cu washer*

Normally the specimen should be ready for TEM analysis, however, if the region is not thin enough or requires cleaning, it may be ion milled. To clean a typical sample, ion milling should take ≈10mins. Most samples cross-sectioned in this work were not ion milled. Ion milling invokes significant preferential etching (as shown in figure 3.6), more so than the felt polishing, and thus should be avoided wherever necessary.

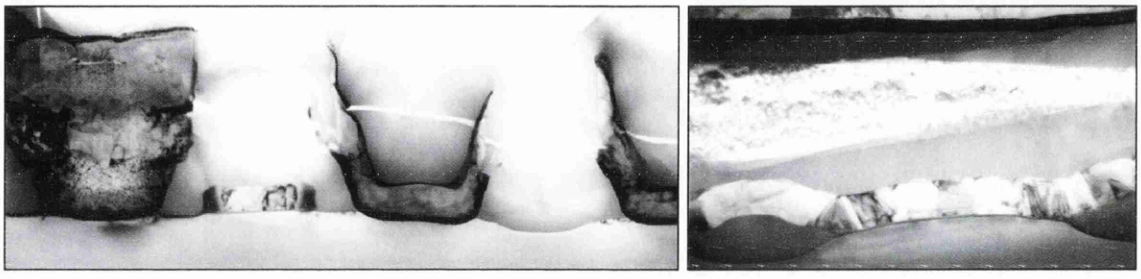

Figure 3.6: *Images showing the extent of preferential thinning as a result of 15mins ion milling. The SiO_2 (both) thins very quickly whereas the Ti barriers (left) thin very slowly*

3.3.5 Quality of specimen

Tripod polished specimens can be up to 2mm in length (limited by the washer) with an electron transparent region up to ≈20μm deep. Normally, the length of the samples prepared here are ≈1mm in length and an electron transparent region <15μm deep. The cross-section in figure 3.7, illustrates the length of the specimen possible using the TP. The accuracy in cross-sectioning the desired structure is very high; the resolution is ≈1μm or higher with an optical microscope >400× or an SEM. Every TEM specimen made using the TP has contained the desired structure. Here, the success rate for a TEM specimen from a silicon chip is approximately three in four. This success rate could be improved if the surface of the wheel under the lapping film was smoother and the lapping films changed more often. The training period to achieve such a level of success is ≈1-2 months constant experimentation.

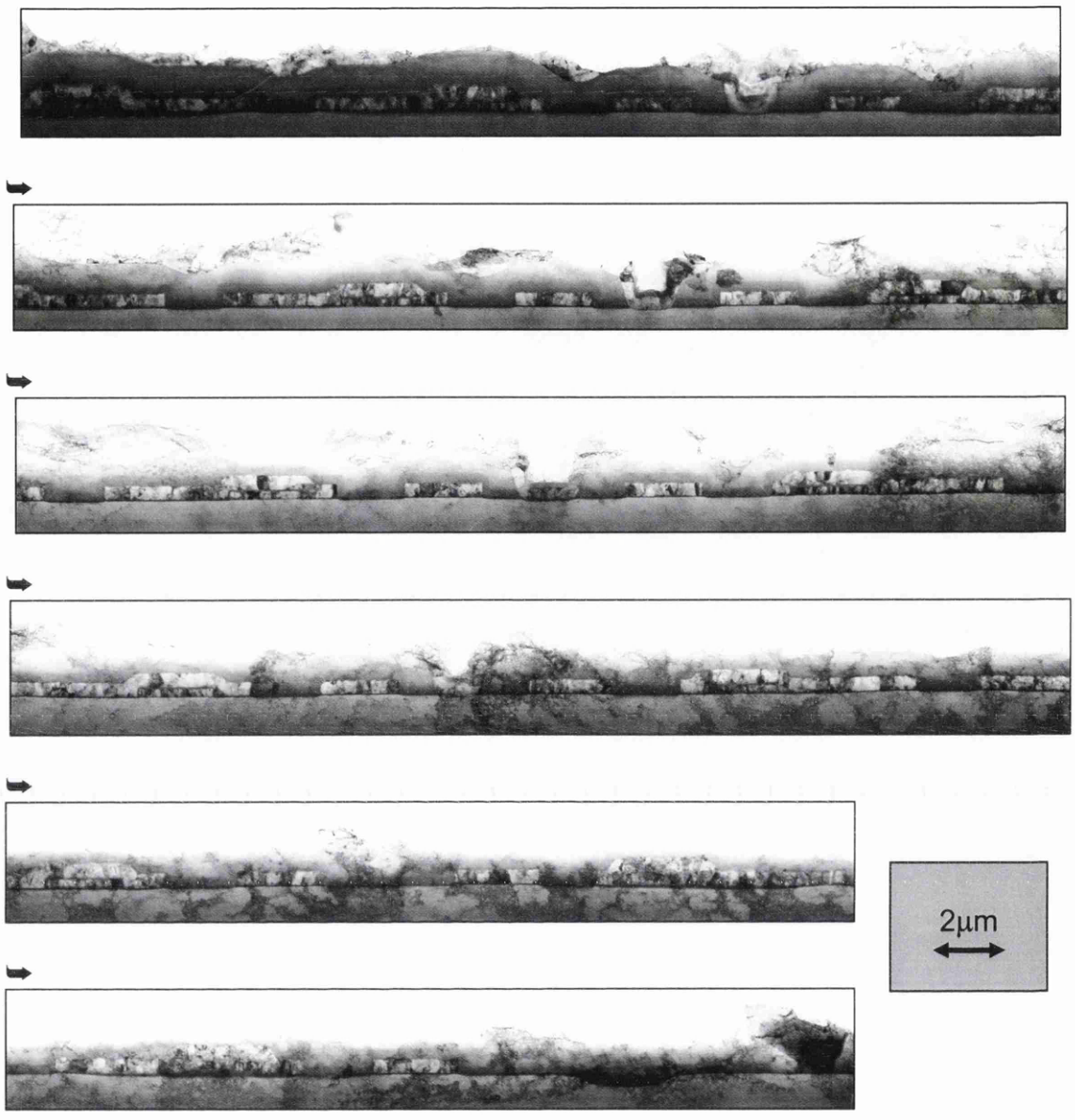

Figure 3.7: *A montage of TEM images illustrating the length of the e-t region available using the tripod polisher. The whole image is ≈100μm in length and accounts for ≈¼ of the useful e-t region on this specimen*

Syton often deposits onto the specimen during polishing and is not normally completely removed with the acetone-ethanol baths. Only if the syton particles obscure particular structures of interest is it desirable to ion mill the specimen. Cracks (shown in figure 3.8) and dislocations are only found in a few particularly thin parts of the electron transparent region if the specimen has been prepared well. For most of a well-prepared specimen, almost no significant lattice damage is evident. Diffraction patterns of very

thin regions of the Si substrate show that there is little or no surface amorphisation. Figure 3.9 shows the quality of the finish of a specimen without the use of ion milling.

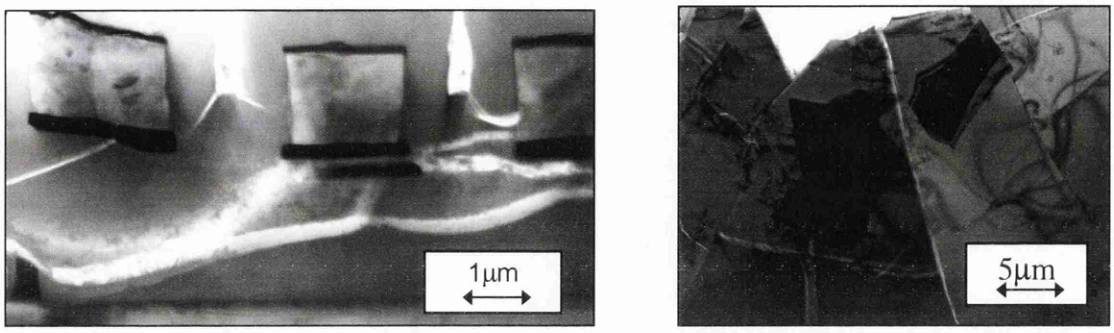

Figure 3.8: *Cracks characteristic of tripod polishing. Normally, these only appear on very thin regions*

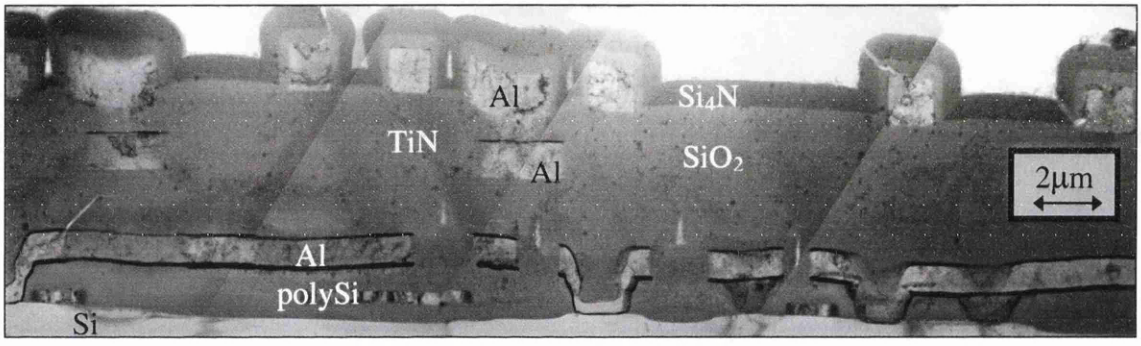

Figure 3.9: *A montage of TEM images showing the high quality of finish by the tripod polisher, without ion milling*

3.3.6 Tripod Polishing vs. FIB

Table 3.3 compares the performance of tripod polishing and the FIB, as techniques for TEM sample preparation. Considering the specimen length as shown in table 3.3, it is clear that the TP is the technique of choice for materials research, whereas the FIB is preferable for failure analysis. The initial price of the FIB is much higher than the TP however, if one is to be used in an industrial failure analysis lab, the cost of diamond lapping film, etc., can be as much as £50,000 per year for one tripod polisher[8].

Table 3.3: *Comparison between the FIB and Tripod polisher*

Property	*FIB*	*TripodPolisher*
Accuracy in obtaining region of interest	≥7nm	routinely <1μm, <100nm with SEM
Length of electron transparent region	≈15μm	≈1-2mm
Time taken	2hrs (pre-FIB) +2hrs (FIB)	≈4-10hrs (depending on skill level)
Quality of specimen	Very good, a little surface damage caused by ion beam	Very good, cracks sometimes present, any 'dirt' paricles removed by ion milling
Cost of tool	>£100,000 + operating costs	≈£1000 initial +£500-£50,000 / year
Success rate	>90-100%	>80-100% (skilled)

3.4 Structural Information Available from Imaging

3.4.1 Introduction

With many materials and structures present in a cross-section prepared by tripod polishing, various analytical techniques can be explored and developed. In the remainder of this chapter, imaging is used to observe both the consistency of the device structures and the fine structure of the materials. TEM imaging can identify the possible areas where the device could fail at present, or upon further miniaturisation in the future.

The following list shows the areas where imaging can be used to investigate properties of the materials in modern devices.

- Thickness uniformity of films of materials and surface roughness
- Defects, voids, and implantation damage
- Dopant penetration depths
- Grain structure
- Abnormalities in fabrication

The reason much of this information can be determined using the TEM is due to the diffraction contrast inherent to TEM imaging. It should be noted that much of this information could not have been obtained as accurately with FIB prepared specimens. Furthermore, all of this structural information could not be derived from any other analytical technique at this resolution.

3.4.2 Thickness Uniformity of Films

Through miniaturisation, layer thicknesses of materials in the devices are shrinking by ≈13% every year. It becomes increasingly important to deposit, or grow, films having a uniform thickness. Virtually all films used in modern ICs are <1μm thick, so analysis of their surface roughness and thickness uniformity has to be performed on a nanometre scale. TEM imaging can provide this vital information accurately when the sample contains a significant amount of the material of interest.

Concerning thickness uniformity, interest lies mainly with conductive films and diffusion barrier layers. If the thickness of a conductive film varies, the electrical resistance varies along the film, or 'wire'. Other electronic properties like electromigration, where voids are created through transport of the material due to the changing flux of electrons, are likely to be adversely affected. A rough surface creates points of high electric fields in certain device structures, e.g. capacitors and gates, providing regions of low breakdown barriers. Any thickness non-uniformity upon deposition of metals becomes much more severe if depositing on a near-vertical wall like a contact via. Here, the resistance can increase dramatically and can even cause a short circuit.

In figure 3.10, an image of a 3-level metallisation device is shown where the thickness of the Al in metal 2 changes by a factor of ≈50% within a short distance as indicated by the letter **A**. It may be necessary to increase the distance between metal 2 and 3 at the Al contact for fabrication reasons; however it would be more likely that the flux of incident Al atoms at **A** was unusually low during the fabrication of the film. The height

of metal 3 immediately above the contact in figure 3.10 is below that of the rest of metal 3, implying that the thickness variation was unintentional. It would also seem a difficult processing step during fabrication for the thickness of the metal 2 film to be varied as such, intentionally. In this case, it seems an anomaly in the device fabrication has occurred.

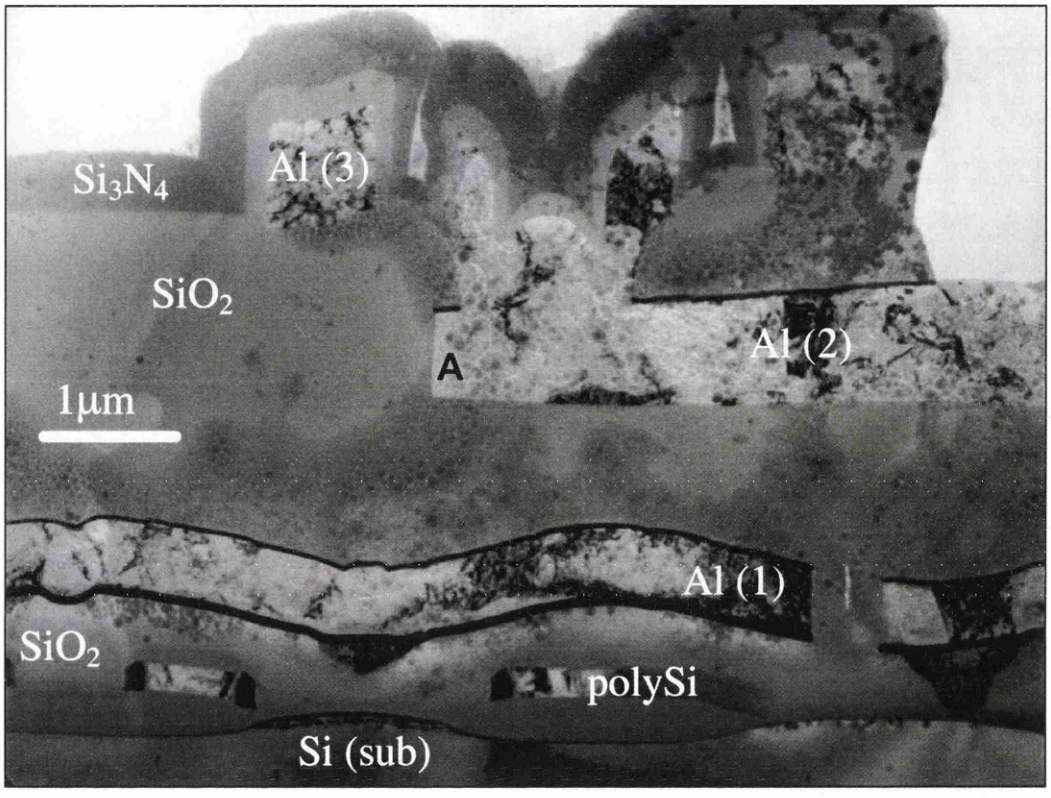

Figure 3.10: *Image showing the significant change in thickness of the Al (2) layer at the contact*

The same metal 2 is used to make contacts with metal 1 at a via (a hole in the SiO_2). Figure 3.11 shows how thickness variations in this layer, and in metal 1, can lead to sizeable variations in the contact wall thickness. As mentioned earlier, 3D information of identical structures situated along the TEM specimen can be obtained if prepared using the TP. So here it is also possible to examine the contact wall thickness right round the via hole if desired. It is found that this level of thickness non-uniformity exists through the contact. The change in resistance at these contacts will be very

significant and if the width of the contacts were to shrink, without reducing the distance between subsequent metal films, short circuits are likely to form.

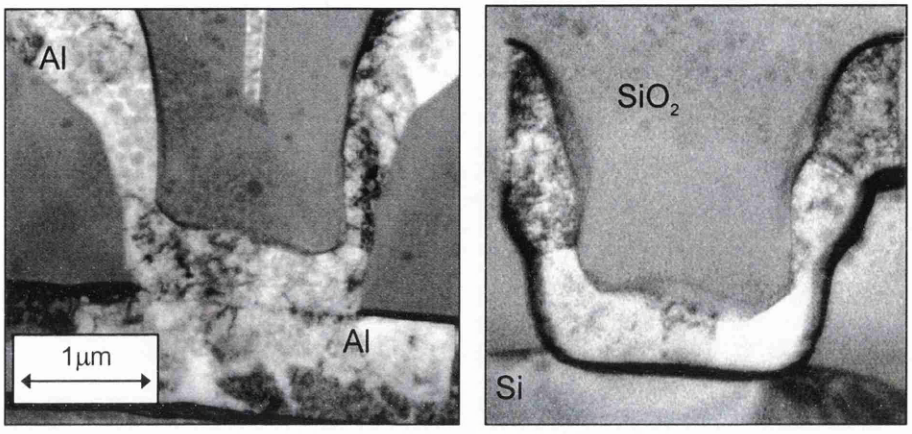

Figure 3.11: *Two images of Al contacts showing the large thickness variation of the Al on the sidewalls*

A diffusion barrier is a thin layer of material which prevents interdiffusion between two materials[9]. It must be thick enough to adhere to both films and keep them apart, but still be as thin as possible to avoid interfering with the electrical properties of either

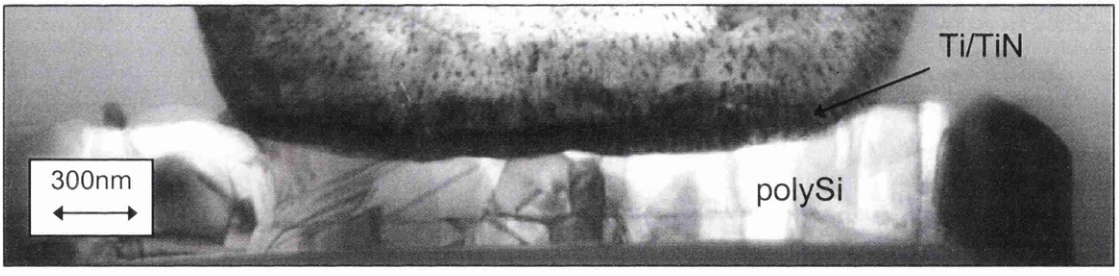

Figure 3.12: *Image showing the thickness variation of the Ti/ TiN diffusion barrier*

film. Thus, its thickness must be very uniform. Figure 3.12 shows the thickness variation of a Ti / TiN diffusion barrier, used to separate Al and Si. The thickness of the Ti / TiN film is significantly non-uniform, but in chapter 7 it is shown that it succeeds in separating both the Si and Al. The EDX analysis in chapter 7 also shows that the thickness of the Ti / TiN could be thinner and still act as a diffusion barrier. However, it is likely that the control over its thickness during fabrication is not ideal, as shown in figure 3.12.

When a polycrystalline material is deposited, the thickness at each point will depend on the growth rate of that grain dominant at that point. The growth rate is a function of the grain orientation. The surface roughness depends on the deposition conditions as this controls the orientations of the grains. If a thin isolating layer of material is deposited between two conducting polycrystalline films with significant surface roughness, regions of high electric field can be established, as well as shorter distances, between the

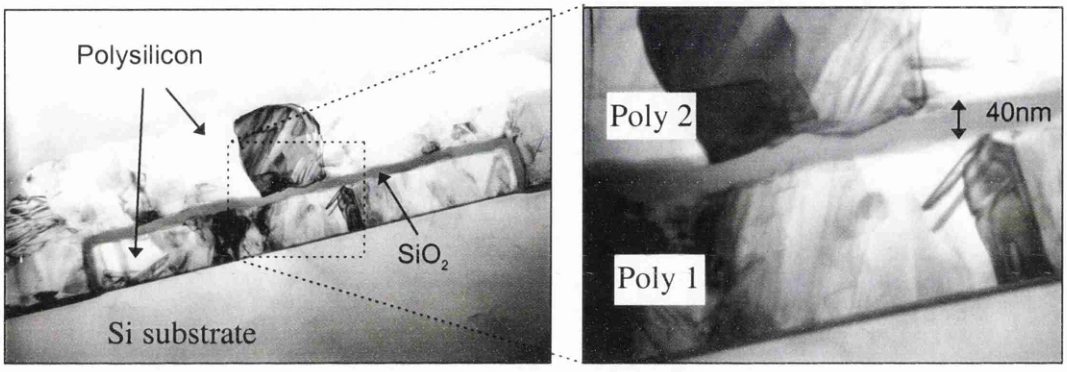

Figure 3.13: *Images illustrating how surface roughness could cause electrical breakdown of a capacitor*

films. This can result in premature electrical breakdown across the insulator. Figure 3.13 shows an example where surface roughness can cause a capacitor to break down. This effect will worsen with device miniaturisation. With the ample amount of material obtainable using the TP, accurate surface roughness measurements can be made with

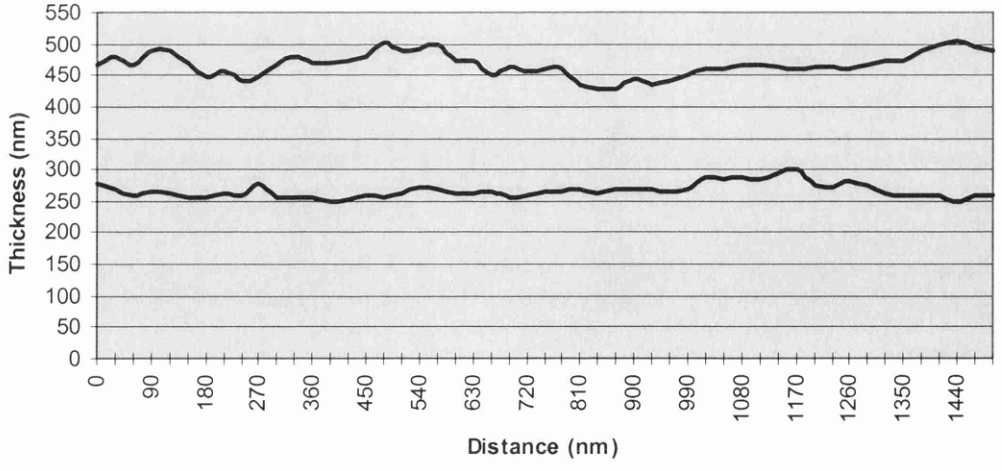

Figure 3.14: *Profiles of the thickness variation of both polySi films in a storage capacitor*

nanometre resolution. Figure 3.14 shows a typical surface roughness profile for the poly 1 and poly 2 films in a storage capacitor like the one in figure 3.13. Here the thickness is measured at 40nm steps. Repeating this analysis on five capacitors, a histogram showing the thickness variation of each film is given in figure 3.15.

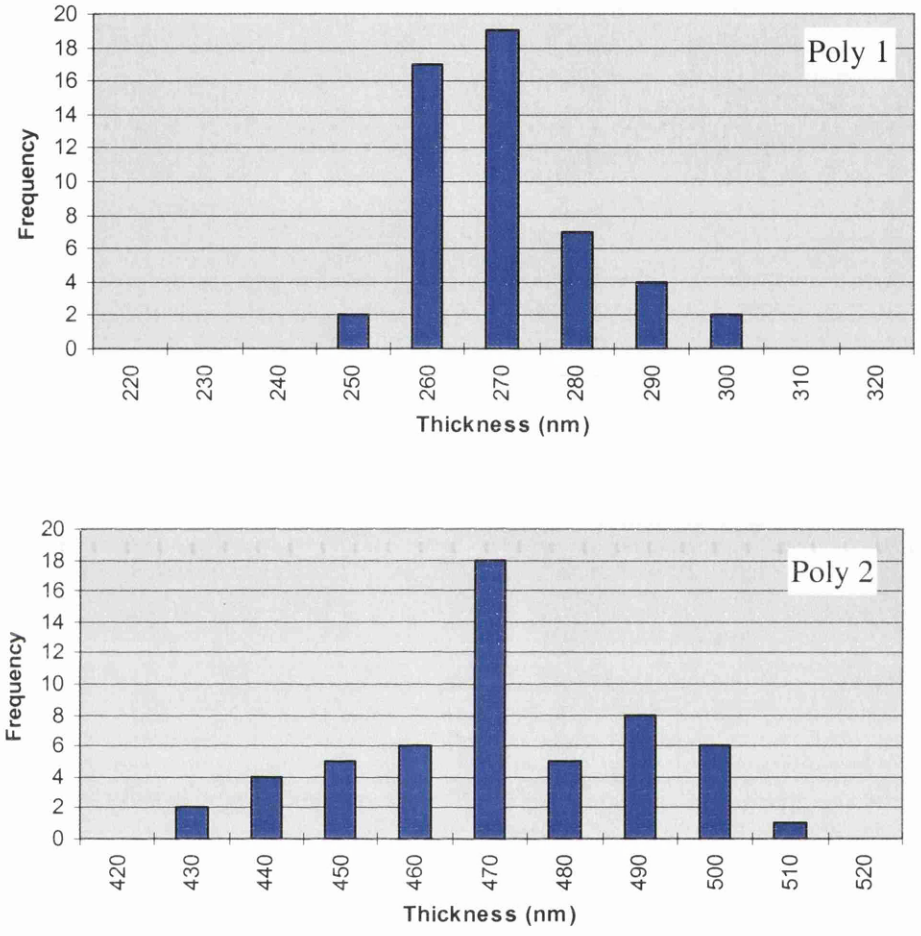

Figure 3.15: *A histogram showing the thickness distribution for poly 1 and poly 2*

The results are as follows. For poly 1, the average thickness is 266±2nm with a standard deviation of 11nm. The range in film thickness is 50nm. For poly 2, the average thickness is 467±3nm with a standard deviation of 19nm. Here the thickness varies by 76nm. There is a 5% error in the magnification calibration on the images. This would affect the average values accordingly but have little affect on the thickness distributions.

The surface roughness of poly 1 is of the order of the thickness of the inter-poly oxide which is 40nm. This is an alarming result in terms of the high possibility of electrical breakdown of the capacitor and is a consideration for future devices. Chapter 5 shows that these films are randomly oriented and that their surface roughness could be improved if the grains were deposited having a preferred orientation (PO).

Figure 3.16: *Image showing the thickness uniformity of a 15nm layer of SiO_2, 'tunnel oxide'*

On the other hand, current fabrication processes can control the surface roughness of some materials down to <1nm. Figure 3.16 illustrates how uniform the thickness of a 15nm thick SiO_2 film can be controlled. It is predicted that these 'oxide' layers can be shrunk to <1nm and maintain a uniform thickness in future devices[10].

3.4.3 Structural Defects

Imaging a long cross-section of a device is ideal for detecting structural defects. These defects include lattice defects, voids, and ion implantation damage and can arise as a result of faults during fabrication or after a time in use. The defects which occur through specimen preparation obscure any defects which occur during device fabrication. However, with a large specimen area, the source of the defects are normally manifest.

Dislocations and twinning can be imaged readily in the TEM, primarily due to the diffraction effects providing contrast to the image. Often these dislocations can be observed more clearly using dark field imaging, as described in section 2.3. Figure 3.17 shows an image of dislocations present in the Si substrate. These almost certainly arise

during specimen preparation. Common dislocations in the substrate are (311) type extended defects due to stress from thermal SiO_2 growing laterally under Si_3N_4 films. No such films were present in any samples here.

Figure 3.17: *Lattice defects on the substrate immediately below the device structures, most likely due to specimen preparation*

Twinning and stacking faults are phenomena commonly observed as a result of plastic deformation and recrystallisation[11] and so are of considerable importance in controlling the mechanical properties of a film. Figure 3.18 demonstrates the contrast produced by such lattice phenomena in a polySi film by the TEM. Indeed, the same contrast can arise from grain boundaries at an angle to the plane of the sample. Further diffraction analysis will identify the cause of the diffraction contrast. Although twins and stacking faults are less severe than grain boundaries in terms of lattice disorder, they can reduce the mechanical strength of a film and should be monitored.

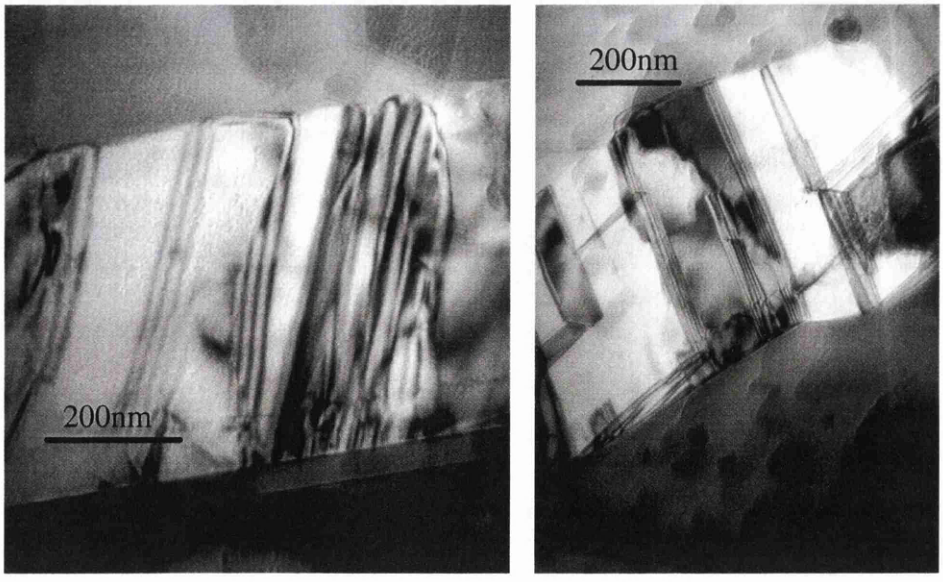

Figure 3.18: *Lattice irregularities like twins or stacking faults can be readily observed and identified from further diffraction analysis*

Voids in a conducting material can cause short circuits and their size usually increases through use (e.g. as a result of electromigration[12]). With the thickness of conducting films between 0.1-1μm, voids are difficult to observe without the nanometre resolution characteristic of the TEM. Figure 3.19 shows an image where several voids are created through the fabrication process. Being in the insulating SiO_2, these voids are probably harmless to the operation of the device. However, they are ideal places for traces of undesirable materials to be deposited during fabrication, and perhaps cause problems during the life of the device.

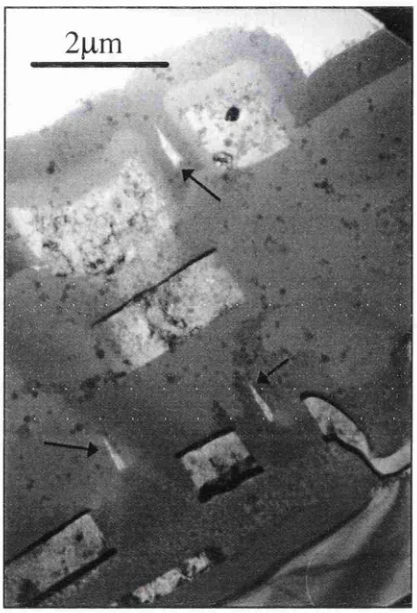

Figure 3.19: *Voids in the SiO_2 (marked with arrows) created during fabrication are probably harmless, but could provide sites for unwanted impurities*

At some point during the fabrication of most devices, dopants are implanted into the active regions at the source and drain of the transistors. In such a critical area, it is of considerable importance to determine the lattice damage done to the substrate by the ion beam. Figure 3.20 demonstrates how the TEM can be used to give an indication of the extent of this lattice damage. Normally, annealing occurs after ion implantation to heal the disruption of the silicon lattice[13] but, from figure 3.20a, there seems to be some degree of lattice damage remaining.

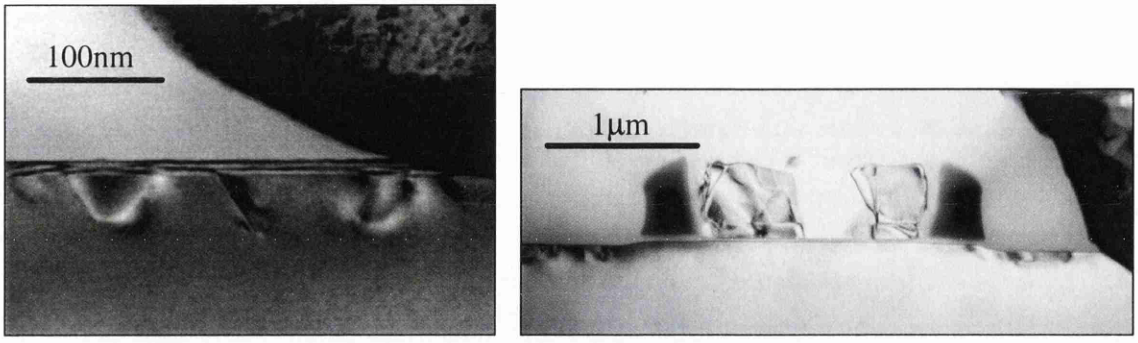

Figure 3.20: *TEM images showing the lattice damage caused by ion implantation in the active regions of the device*

3.4.4 Dopant, Vacancy and Impurity Profiles

As mentioned earlier, diffraction contrast is prevalent in TEM imaging. This means that any disruption of the regular lattice in a crystal produces contrast in an image. Impurities, vacancies and dopants all affect the regular arrangement of atoms in a crystal

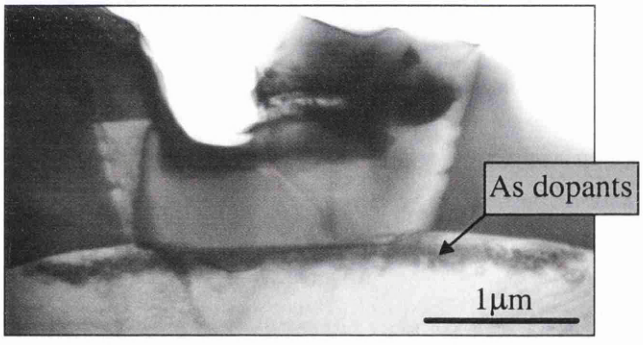

Figure 3.21: *Diffraction contrast allows indirect imaging of minute traces of dopants*

and therefore can be visible in TEM images. This can clearly be useful to trace the depth profile of ion implanted or diffused dopants into the substrate. SIMS, mentioned in section 1.3.2, can perform this analysis with greater resolution of dopant concentration, but it is inferior to the TEM regarding spatial resolution. The concentration resolution possible using EDX on the TEM is determined in chapter 7. Figure 3.21 shows the penetration depth of ion implanted boron into the substrate. The distribution of implanted ions into the substrate is such that most lie at a distance from the surface

defined by the ion energies, i.e. very few remain close to the surface. This relationship is approximately linear[13], and for 100keV ions, the penetration depth is ≈400nm.

3.4.5 Grain Structure

The grain structure of a conducting film is becoming increasingly influential on the electrical and mechanical properties of the film. It is very difficult to observe the outline of grains in any analytical technique apart from imaging in the TEM. The reason for this is that the orientation of the atomic lattice in a material does not affect how the material looks. However, if diffraction effects are involved in the imaging of the material, as in the TEM, different grain orientations have different intensities.. Figure 3.22 shows the level of grain contrast possible in imaging. This is, however, not always the case as is demonstrated in the grain size analysis in chapter 4. Grain contrast is usually increased in dark field imaging where only the electrons scattered by the specimen are imaged. An example is shown in figure 3.23.

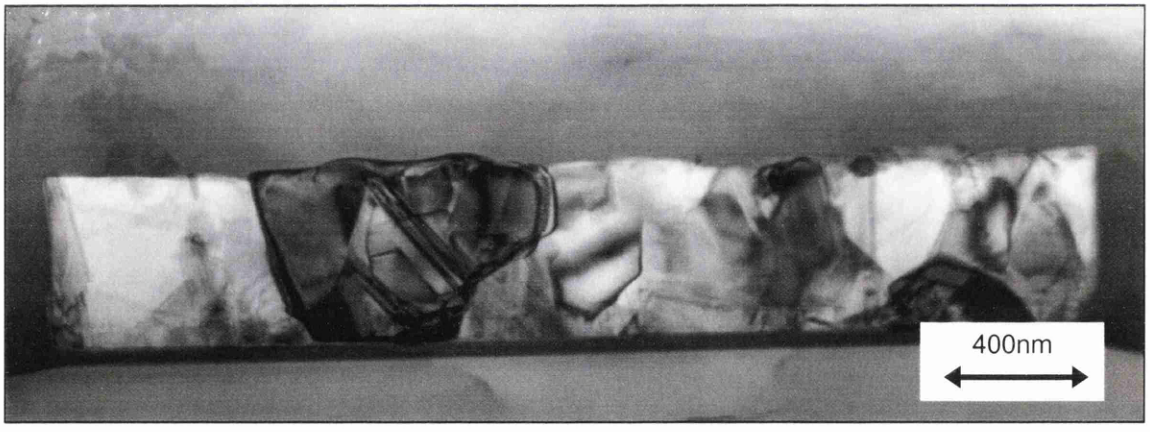

Figure 3.22: *Bright field image of a polySi film showing the quality of the grain contrast available from the TEM*

Buried contacts are structures where the polySi contacts the Si substrate at an active region, reaching ≈50nm deep into the substrate. In a recent incident problems in a line of devices were attributed to an unusually high resistance at the buried contacts and it was suspected from SEM images that there was possibly material accidentally deposited along the bottom surface of the contact. The device was cross-sectioned and the buried

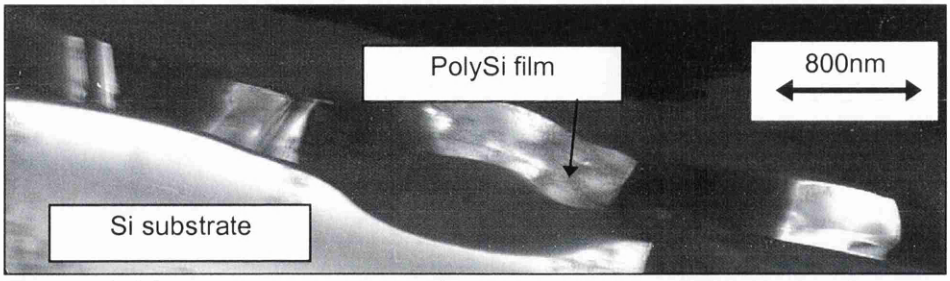

Figure 3.23: *Grain contrast is often improved by imaging the electrons scattered by the specimen, i.e. dark field imaging*

contacts were imaged on the TEM. Figure 3.24 shows two images of the buried contacts with figure 3.24a only exhibiting a high resistance. The interface between the polySi and substrate is shown by the arrow in both figures and it is clear that the crystal orientation of the substrate continues through much of the polySi at the contact. This indicates that no other significant material is likely to be present at the interface. Further EDX and diffraction analysis confirms this. The high resistance of the contact could be attributed to the diffused dopants migrating to the interface (visible in figure 3.22a) as opposed to being evenly distributed through the polySi film as intended. This would cause the undoped regions to have a higher resistance.

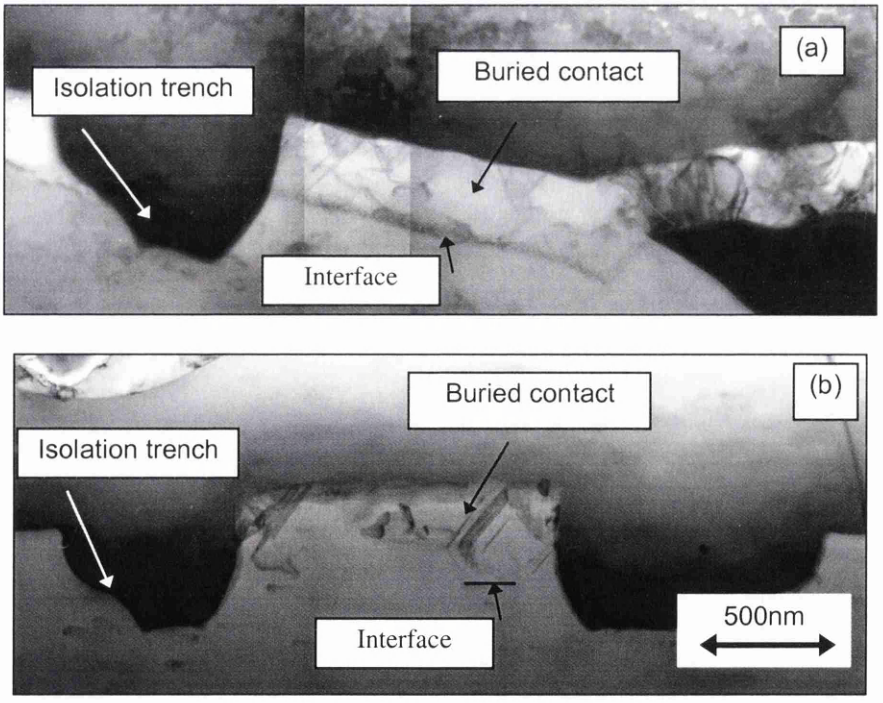

Figure 3.24: *The upper buried contact in (a) was found to have an unusually high resistance so imaging and EDX was used to investigate the problem*

Impurities present during the deposition of a material can cause the grain structure of the film to change significantly. The grain structure in the polySi film shown at **A** in figure 3.25 changed during deposition, possibly as a result of oxygen being introduced at some stage. Further elemental analysis eliminates the possibility of any impurities along this line, and the anomaly is attributed to a change in polySi deposition conditions. The lower polySi film is deposited as a processing step to aid the production of buried contacts and protect regions of SiO_2. By comparing figures 3.25 and 3.22, it is also apparent that both films were subject to different deposition or doping conditions.

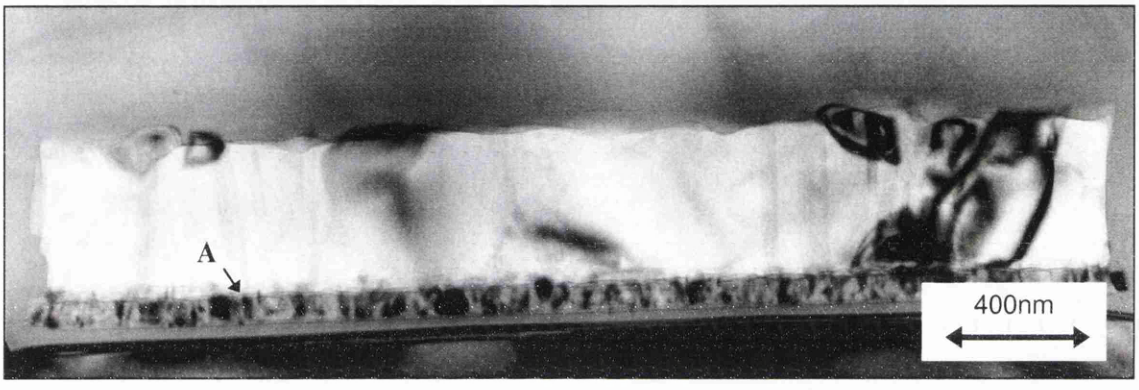

Figure 3.25: *Image showing the change in grain structure of two subsequent polySi films. This was probably due to the higher doping level of the lower film*

3.4.6 Drawback of using TEM analysis

With a large electron transparent area in the cross-section, there is a reasonable chance of detecting anomalies or faults in the fabrication of the device. However, the specimen preparation itself can be shown to confuse the TEM analysis. As an example, on a new 3-level metallisation device an unidentified layer of material was observed in imaging in the TEM. This layer is immediately under metal 2 shown in figure 3.26. At first the layer was though to be Al which had penetrated through the Ti/ TiN diffusion barrier so various analytical techniques were applied on the TEM as described in chapter 7. The layer was found to be a build up of Si which had brushed up against the thicker Ti/TiN 'wall' on the specimen during the final polishing stage of specimen preparation. This shows that the TEM analysis can introduce new defects into the specimen which could

be misleading. However, despite there being no fabrication problem, the TEM demonstrated its potential in analysing and identifying irregularities in devices.

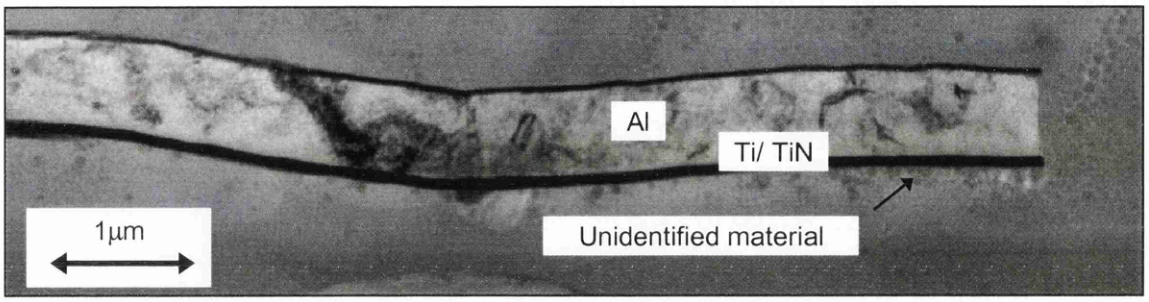

Figure 3.26: *Image showing the presence of an inidentified layer of material under the Ti / TiN diffusion barrier. Various TEM techniques were used to identify its nature*

References for Chapter 3

[1] C. P. Scott, A. J. Craven, P. Hatto and C. Davies, Journal of Microscopy, **182,** 3, (1996) 186

[2] J. C. Bravman, and R. Sinclair, Journal Of Electron Microscopy Technique, **1**, 1, (1984) 53

[3] R. Anderson, S. Klepeis, J. Benedict, W. G. Vandygrift and M. Orndorff, *Inst. Phys. Conf. Ser. No 100: Section 7* (1989) 491

[4] F. A. Stevie, T. C. Shane, P. M. Kahora, R. Hull, D. Bahnck, V. C. Kannan, and E. David, Surface and Interface Analysis, **23,** 2, (1995) 61

[5] R. Anderson, *Specimen Preparation for Transmission Electron Microscopy of Materials-III*, ed. Anderson, et al., Mater. Res. Soc. Proc. 254, Pittsburgh, PA USA, (1992) 141

[6] H. Bender, P. Roussel, Inst. Phys. Conf. Ser. 157, (1997) 465

[7] N. I. Kato, and N. Miura, in print in *Mater. Res. Soc. Proc.* (1998)

[8] P. Flaitz, IBM Analytical Services, NY, *private communication*

[9] C. R. M. Grovenor, *Microelectronic Materials,* IOP Publishing Ltd, (1989), pp239-243

[10] S. Coffa, M. Meyyappan, H. Nishi, Mat. Sci. in Semiconductor Processing, 1, 1-4 (1998) 1

[11] G. Thomas, and M. J. Goringe, in *Transmission Electron Microscopy of Materials*, John Wiley & Sons, New York, (1979) 94

[12] D. B. Knorr, D. P. Tracy, K. P. Rodbell, Appl. Phys. Lett. **59**, 25, (1991) 3241

[13] S. M. Sze, VLSI Technology, McGraw-Hill, (1988)

CHAPTER FOUR

Grain Size Distribution of Conducting Films

4.1 Introduction

In modern devices, the thickness of conducting films is <1μm and will reduce to <100nm in the near future. At this thickness, the electrical and mechanical properties of the films are greatly influenced by the distribution of both the grain sizes and their orientations. Analytical techniques are required on a nanometre scale to characterise a thin film according to these parameters. Chapters 5 and 6 describe techniques to determine the distribution of the grain orientations in a film. In this chapter, a new TEM technique is described, along with the complementary statistical analysis, which determines the grain size distribution in a conducting film. Before this, the role of the grain size distribution on the electrical properties is described, along with the mechanisms for grain growth for the films studied here.

4.2 Grain Size Influence on Electrical Properties

Various electrical and physical properties of a film depend on the distribution of grain sizes. These properties include resistivity[1], electromigration[2],[3], surface roughness[4], and interdiffusion[5].

The ability of grain boundaries to scatter electrons and disrupt the electron wave through the material causes an increase in resistivity. Clearly, the larger the grains the smaller the density of grain boundaries. Consequently the resistivity decreases for larger grain sizes. Electromigration is the accumulation of material along the direction of the flow of electrons in a film. It arises from the change in flux[6] of electrons at grain boundaries and thus worsens with smaller grain sizes. Equation 4.1, describes the mean time to failure (MTF) of a device according to the grain size distribution and distribution of grain orientations in an interconnecting material[2].

$$MTF \propto \frac{D}{\sigma^2} \log\left(\frac{I_{111}}{I_{200}}\right)^3 \qquad [4.1]$$

Equation 4.1 is an empirical relationship where D is the average grain size and σ is the standard deviation of the distribution. The factor I_{111}/I_{200} describes the ratio of X-ray peak intensities for the given reflections and reflects on how textured the film is in the [111] direction. The equation is intended only for fcc materials. However every interconnect metal used in modern and, most likely, future devices has an fcc structure.

Large grains which survive through the thickness of the film, however, can produce a large surface roughness. This is attributed to the variation of growth rates depending on the orientation of the grains. A small-grained randomly-oriented sample will generally have a rough surface but the thickness variation will be very small. Indeed, if the grains have similar orientations in the growth direction, i.e. the film is textured, the surface should be smoother. Surface roughness plays a role in determining how thin the dielectric can be between conducting materials (see chapter 3). The diffusion of other materials into the film is enhanced at the grain boundaries due to the atomic disorder there. Smaller grains have a larger density of grain boundaries and are thus more susceptible to interdiffusion. Junction spiking[5], where metal protrudes through a diffusion barrier into the polySi is just one of the unfavourable results of high diffusivity of a film.

It is apparent that all the undesirable properties of a film can be reduced if the film is grown as a single crystal, i.e. epitaxial growth. Here, no grain boundaries exist as well as no surface roughness. Growing a single crystal on an amorphous material, as commonly found in devices, is virtually impossible given operable deposition conditions. The closest to this situation is when the grains are large and all oriented in a common direction, i.e. textured. Here the surface roughness is small and the adverse effects of the grain boundaries are minimised due to the low-angle interconnection of lattice planes at the boundary.

4.3 Grain Growth Mechanisms in Silicon Devices

Before the determination of the grain size distribution of a thin film of polycrystalline material is discussed, it is necessary to outline the mechanisms of grain growth to appreciate fully the results of the analysis used here. The way in which the deposition conditions affect the grain size is also discussed to demonstrate the control that the engineer has in affecting the size distribution.

Grain structure characteristics are often defined by grain growth occurring during film formation and during post-formation processing. There are basically two types of grain structures in thin polycrystalline films depending on whether the majority of grains survive all the way through the thickness of the film. In most physical vapour deposition processes the spacing of the nucleating atoms will be small[7]. If the grain boundaries are immobile, the initial grain size at the base of the film is $\leq$10nm. As the film increases in thickness, the average in-plane grain size may increase due to growth competition at the surface arising from surface energy differences or growth-velocity anisotropies. This results in grains which are smaller than the thickness of the film with in-plane sizes increasing through the film. Such structures develop in materials with low grain boundary mobility and pure silicon films have such near-columnar structures even when deposited as high as $0.85\times T_m$ (melting temperature). This is the case for the film studied in chapter 6.

By contrast, fcc materials, like Al studied here, do not produce this structure, even at temperatures as low as $0.2\times T_m$. Instead, these films have an in-plane grain size which is uniform throughout the thickness of the film, and remains comparable to the film thickness. Here, bulk grain boundary motion occurs during film growth and the structure is said to be equiaxed columnar. The growth process can be considered to take on a quasi-2D character. Normal grain growth is characterised by equation 4.2 where $\overline{D}_0$ is the initial average grain size, and t is time. However it rarely occurs in polycrystalline films[7].

$$\overline{D} - \overline{D}_0 \propto \sqrt{t} \qquad [4.2]$$

The development of grooves where grain boundaries intersect surfaces can lead to grain growth stagnation, resulting in films with log-normally distributed grain sizes (see later). Abnormal grain growth, as it is known, can lead to grain sizes which are substantially larger than the film thickness, and the grain sizes are described by equation 4.3[8].

$$\frac{dr_s}{dt} = M\left[\frac{2(\gamma_s^* - \gamma_s)}{h} + \overline{\gamma}_{gb}\left(\frac{1}{\overline{r}} - \frac{1}{r}\right)\right] \qquad [4.3]$$

Here, r_s is the radius of the secondary grain, $\overline{r}$ is the average grain radius when normal grain growth occurs, M is the average grain boundary mobility, h is the thickness of the whole film, $\overline{\gamma}_{gb}$ is the average grain boundary energy, γ_s is the surface free energy of the considered grain, and γ_s^* is the average surface energy. From this equation, the rate of grain growth not only depends on its size but its surface energy, or orientation. This is the case for the evolution of texture in films like the one used in chapter 6. Equation 4.3 also shows that the importance of the surface energy decreases with increasing thickness.

Grain growth can be controlled by various means during, and after, deposition. The following table summarises the effect of the most influential processing conditions, showing the extent to which process engineers can control the grain structure.

Table 4.1: *Control of grain growth in thin films*[8].

Condition	***Effect on Grain Structure***
Temperature	In metallic films, grain growth occurs at $T \geq 0.2T_m$. This rises to $T \geq 0.75T_m$ for semiconductor films. High T results in large D since the grain boundary mobility is high. Rate of grain growth also scales with T.
Substrate topography	The periodicity and symmetry of the substrate surface provides interface energy anisotropy for in-plane rotation of grains. Influences the orientation of films.
Precipitates	These exert a drag force on grain boundaries suppressing normal grain growth. Can lead to secondary grain growth dramatically increasing the average grain size.
Impurities	Also exert a drag force on boundaries but this time are shown to restrict the grain size in films deposited at low rates.
Ion bombard-ment	Grain growth initiates at significantly lower temperature. Rate of grain growth enhanced due to the beam-generated defects on grain boundary mobilities. However, it can also be used to amorphise materials

4.4 Existing Techniques for the Measurement of Grain Sizes

As mentioned earlier the electric, magnetic and mechanic properties of a thin film are strongly influenced by the grain size distribution. There exist several techniques which determine the grain sizes either directly or indirectly.

Indirect measurements of the grain size distribution include examining the magnetic[9], electronic or ultrasonic[10] response from a thin film of material. For example a magnetic technique involves measuring the room temperature curve of the magnetisation against the applied field and fitting the curve to a superposition of Langevin[9] functions, each one corresponding to a particle size value. All these indirect techniques use standards for comparisons but normally produce results with an accuracy $\geq 1\mu m$.

Direct techniques image the grain structure, almost always in-plane, and use some sort of image analysis algorithm to increase the grain boundary contrast, or predict where the grain boundaries are[11]. Similar techniques use Fourier transform analysis to obtain a grain size distribution[12]. The direct techniques have one common problem, how to determine the positions of the grain boundaries having no contrast. Some techniques compare simulated grain size distributions to the in-plane image of the actual film to judge the most probable grain sizes. X-ray diffractometry[13] can be used to map the positions where the diffraction pattern changes at the boundaries but has a spatial resolution of ≈1μm, inadequate for modern processed devices. Orientation imaging (OIM)[14], mentioned in chapter 1, can be implemented in the SEM to map the grain boundaries as well as the grain orientations. This process has a resolution of ≥10nm but is very costly and, although fully-automated, run-times can exceed 24hrs.

4.5 A New Technique for Measuring Grain Size Distributions

4.5.1 Introduction

As mentioned in section 3.4.5, the orientation of the atomic lattice in a material does not normally affect how the material 'looks'. This implies that the determination of grain sizes will be impossible from imaging if the grain boundaries are not visible. The diffraction contrast prevalent in TEM imaging provides grain contrast, particularly in dark field imaging. However, these grain boundaries often have little or no contrast, creating difficulties in determining the grain sizes. The only physical difference between each neighbouring grain is its orientation and hence the diffraction pattern will be different for each grain. The principle of this new technique is to map where the diffraction pattern changes along a cross-section of a film thereby defining the positions of the grain boundaries. The distances between the grain boundaries are known as intercepts through the grains and do not describe the grain sizes. Voronoi statistics[15] are used to convert the intercept data to the distribution of grain sizes.

4.5.2 Technique

The accuracy of any statistical distribution is dependent mainly on the number of individual measurements taken. The same applies here when measuring the distribution of grain sizes, so ideally, the tripod polisher should be used for sample preparation as it produces a large electron transparent region. Only if the grains are very small, <100nm, can accurate statistical analysis be performed on FIB prepared samples.

Aluminium films in a 3 level metallisation silicon device are used to demonstrate this technique and are cross-sectioned for the TEM using the tripod polisher as described in chapter 3. The grains in the films are equiaxed columnar, i.e. have the same width through the thickness of the film. The grains are ≈1μm in width and the thickness of the films are 0.75μm and 1.0μm for metal 1 and metal 2 respectively. This experiment does not require the grains to be columnar but, if they are not, the 3-dimensional statistical model, as shown later, has to be employed to calculate the grain size distribution.

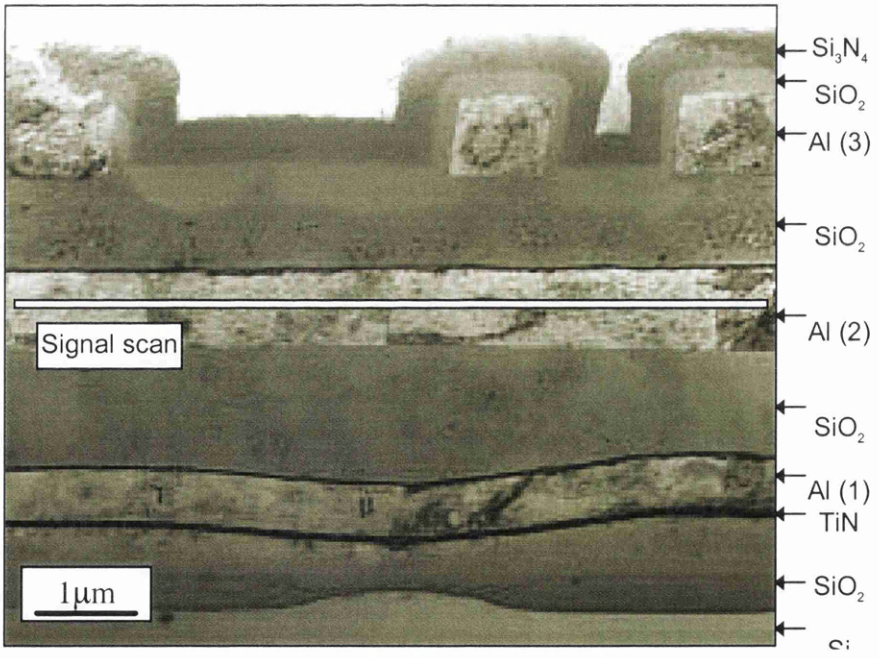

Figure 4.1: *A BF image showing the position of the proposed slow signal scan*

The microscope is aligned in STEM imaging mode whereby the convergent beam

diffraction pattern is observed on the viewing screen. The camera length in the microscope is set low enough to observe a Kikuchi pattern for ease in recognising the changing pattern and identifying bending in the specimen. A bright field (BF) and dark field (DF) image of the sample containing the film of interest is acquired and displayed on the CRT screens. The BF image is saved to a 512×512 pixel image file using a PC connected to the STEM unit and figure 4.1 shows an example of such an image. The PC is connected to the STEM unit via a Video Signal Mixing Unit (VSMU) which is set to select either the BF or DF signal during a scan. An image processing program 'Digital Micrograph' is used to control the shape of the scan and acquire the signal from the STEM detector.

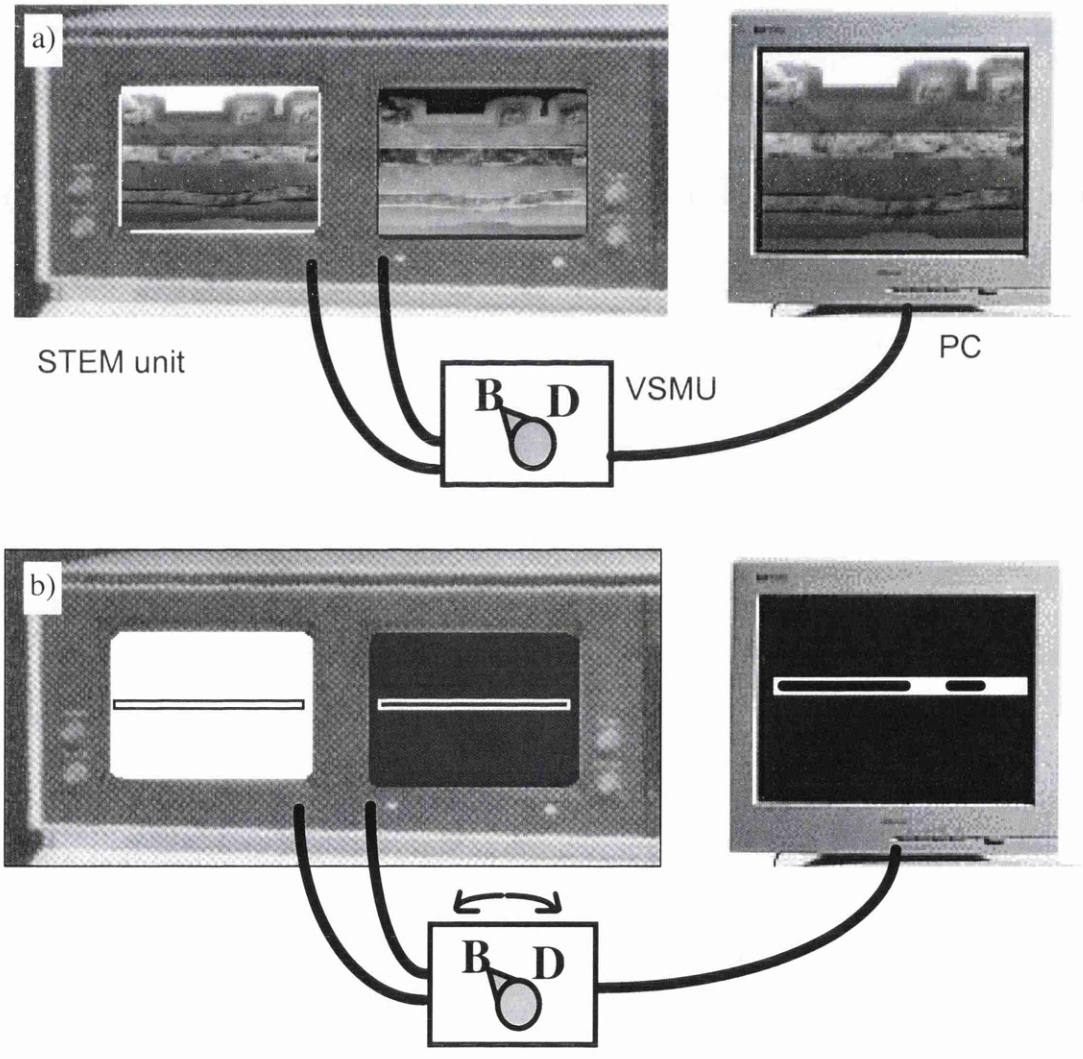

Figure 4.2: *The microscope and scan set-up for acquisition of the signal scan*

Once the scanned image is saved, the height of the scan is reduced to ≈3-5 pixels high and aligned along a desired line (normally the centre) on the film as shown in figure 4.2b. Care must be taken to avoid unnecessary time delays during the following process steps as the specimen may drift meantime. The scan time is increased to allow >1s for the probe to cross each grain. The Philips CM20 STEM does not allow the scan times to be set so high, so the PC is used to define the large scan time. The brightness, or gain, of the BF signal is increased to produce a white screen during the BF image acquisition. Conversely, the DF signal is reduced to produce a black screen where the DF image was. Thus one CRT screen is white and the other black, and the signal relayed to the PC during scanning is either white or black depending on the setting on the VMSU, which is controlled by the operator.

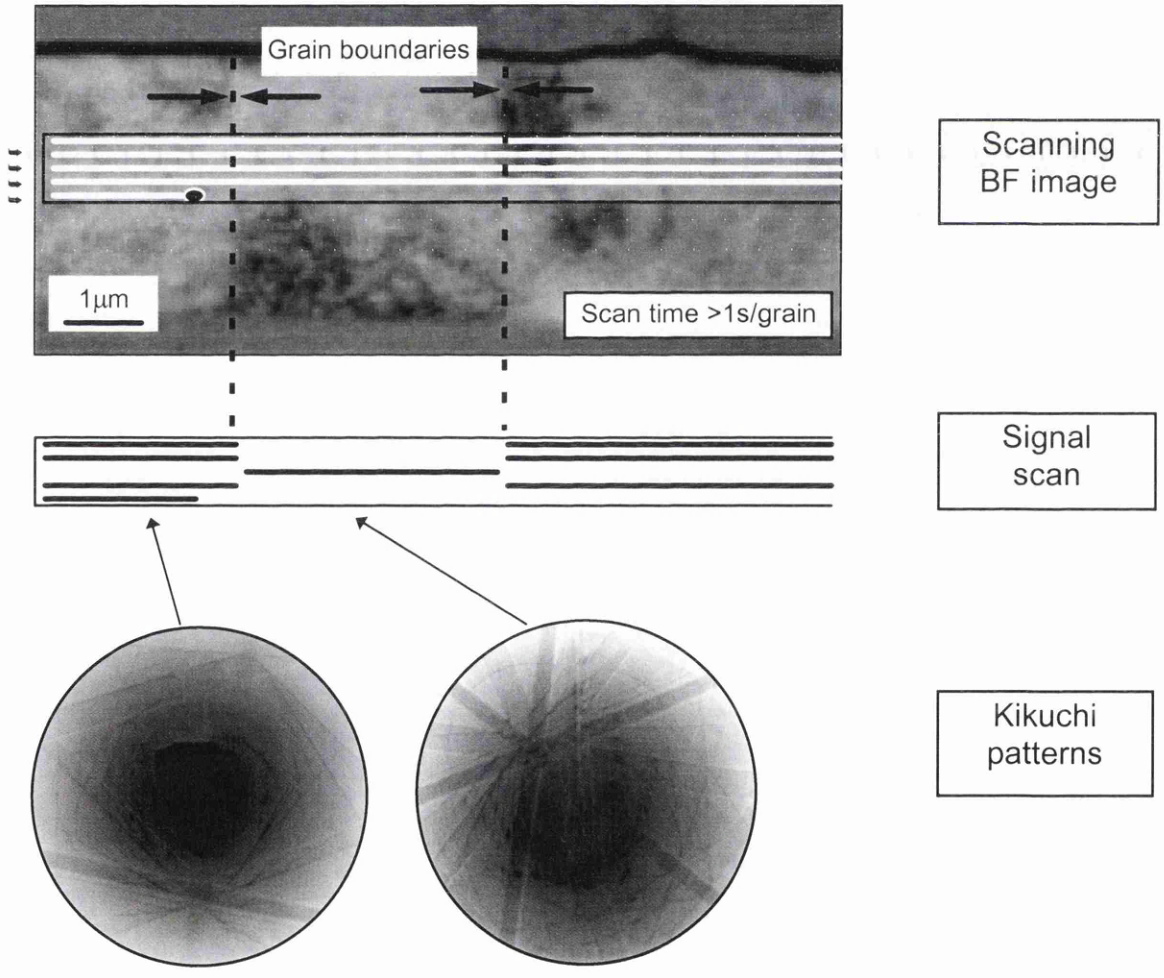

Figure 4.3: *The details of the acquisition of the signal scan. The signal is changed when the observed Kikuchi pattern changes*

The viewing screen is then lowered to view the Kikuchi diffraction pattern from the first grain in the proposed scan. While observing the diffraction pattern, the scan is started and the black or white signal is scanned into an image on the PC which will be 512×5 pixels wide. On crossing a grain boundary the diffraction pattern changes and this is registered by the operator by changing the output signal to the PC from black to white and vice versa on crossing the next grain boundary during the scan. The scan configuration is described in figure 4.3. Thus the boundaries are identified by the positions of the signal transitions. The signal level is only changed when the existing diffraction pattern disappears, as this prevents underestimation of the grain boundary separation when the film is more than one grain thick. The signal scan need only be one pixel deep, but to improve the accuracy of the measurements and reduce the number of operator errors, multiple scans which effectively retrace the same linescan should be used. This results in a scan like the one shown in figure 4.4 when stretched vertically for clarity. The signal scan is compared to the corresponding BF image of the film as shown, demonstrating the agreement with the visible grain boundaries and revealing those with no contrast.

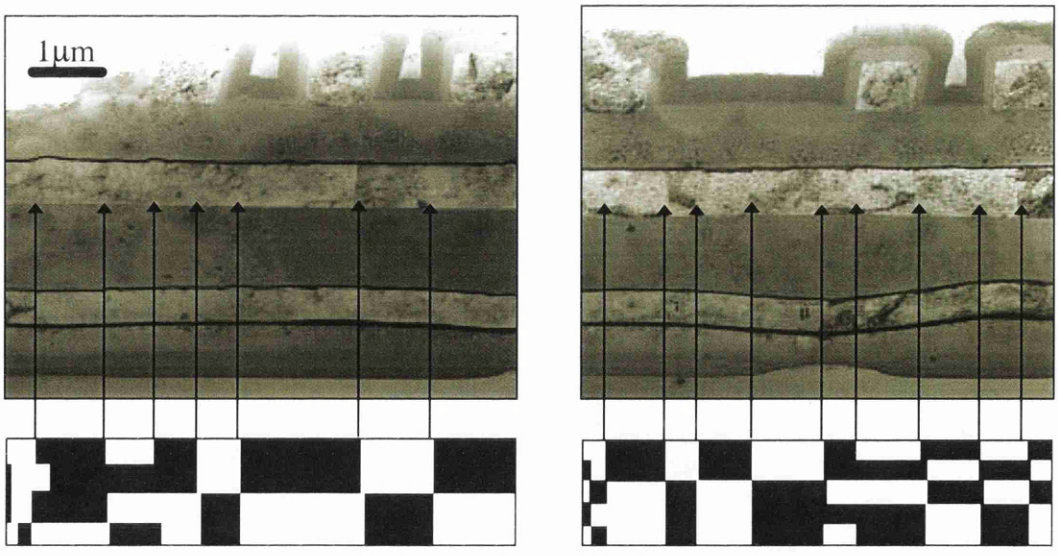

Figure 4.4: *Comparison of signal scans to BF images of same horizontal scale. The signal scans are stretched vertically for clarity*

Ideally, this experiment could be performed once along a long section of the Al film. However, the device used, only had isolated strips of Al so multiple experiments were

performed covering as much of the specimen as possible. Knowing the scale of each signal scan, data on the grain boundary separations, or intercepts, is acquired. Poisson Voronoi statistics are used to convert these data to the grain size distribution, although it is by no means the only model which is used to simulate grain growth[16].

4.6 Voronoi Statistics

4.6.1 Introduction

Voronoi diagrams describe the shape of an arrangement of cells which arise from the following processes.

- A random distribution of nucleation sites
- Each site grows instantaneously, isotropically, and at the same speed
- They grow until the boundaries of neighbouring cells meet
- Each boundary bisects the two closest nuclei

These processes closely mimic grain growth and can be used to describe both equiaxed columnar (grains having the same in-plane size throughout the film), and near-, or non-columnar 3D growth. For the 2D model, the grain size does not take into account the dimension in the growth direction, i.e. thickness. This third dimension, here, is not of interest as it is only the planar grain sizes which affect the electrical properties for a given film thickness.

The theory does have subtle differences with reality[17] insofar as it does not take into account any physical processes which determine the structure of the grain, any non-equilibrium behaviour, and that the cell walls are not curved like real grain boundaries. However, experimental grain size distributions show the theory to be very accurate[18].

4.6.2 Equiaxed Columnar, or Quasi-2D, Growth

Figure 4.5a shows a 2D Poisson Voronoi diagram which mimics equiaxed columnar growth shown in figure 4.5b. On it, the terms used to describe the cell parameters are shown. Central to this model, from which all parameters can be calculated, is the intensity, λ, (or 2D density) of the cell nuclei. The expected values of these parameters are all calculated from equation 4.4[15].

$$E_m V_s = \frac{2^{(m-s+1)}\pi^{[(m-s)/2]}\Gamma[(m^2 - sm + s + 1)/2]\Gamma(m/2+1)^{(m-s+s/m)}\Gamma(m - s + s/m)}{(m-s)!\Gamma[(m^2 - sm + s)/2]\Gamma[(m+1)/2]^{(m-s)}\Gamma[(s+1)/2]m\lambda^{s/m}} \quad [4.4]$$

Here, $E_m V_s$ is the expected value of a parameter described by m, the number of dimensions in the approach, (i.e. m=1 for properties on a line, m=2 for planar properties, and m=3 for volume properties) and s, the dimension of the measured quantity, e.g. for area, s=2, for perimeter, s=1, etc. Note that s must be $\leq m$. Γ is the gamma function and is given by $\Gamma(\alpha) = \int_0^\infty x^{\alpha-1}e^{-x}dx$.

Table 4.2: *Expected values of cell parameters in 2D*

Characteristic	***Symbol***	***Numerical value***
Intensity of cell centroids	λ_2	λ
Number of edges	E(N)	6
	$E(N^2)$	37.781
E_2V_2 Area	E(A)	λ^{-1}
	$E(A^2)$	$1.280\lambda^{-1}$
E_2V_1 Perimeter	E(P)	$4\lambda^{-1/2}$
	$E(P^2)$	$16.945\lambda^{-1}$
E_1V_1 Length of cell edge	E(L)	$0.67\lambda^{-1/2}$
	$E(L^2)$	$0.63\lambda^{-1}$
E_1V_1 Intercept length	E(I)	$0.785\lambda^{-1/2}$
	$E(I^2)$	$0.804\lambda^{-1}$

*From a modified version of equation 4.4.

Table 4.2 shows the expected values of various characteristics of a typical Poisson Voronoi cell in 2D calculated from equation 4.4.

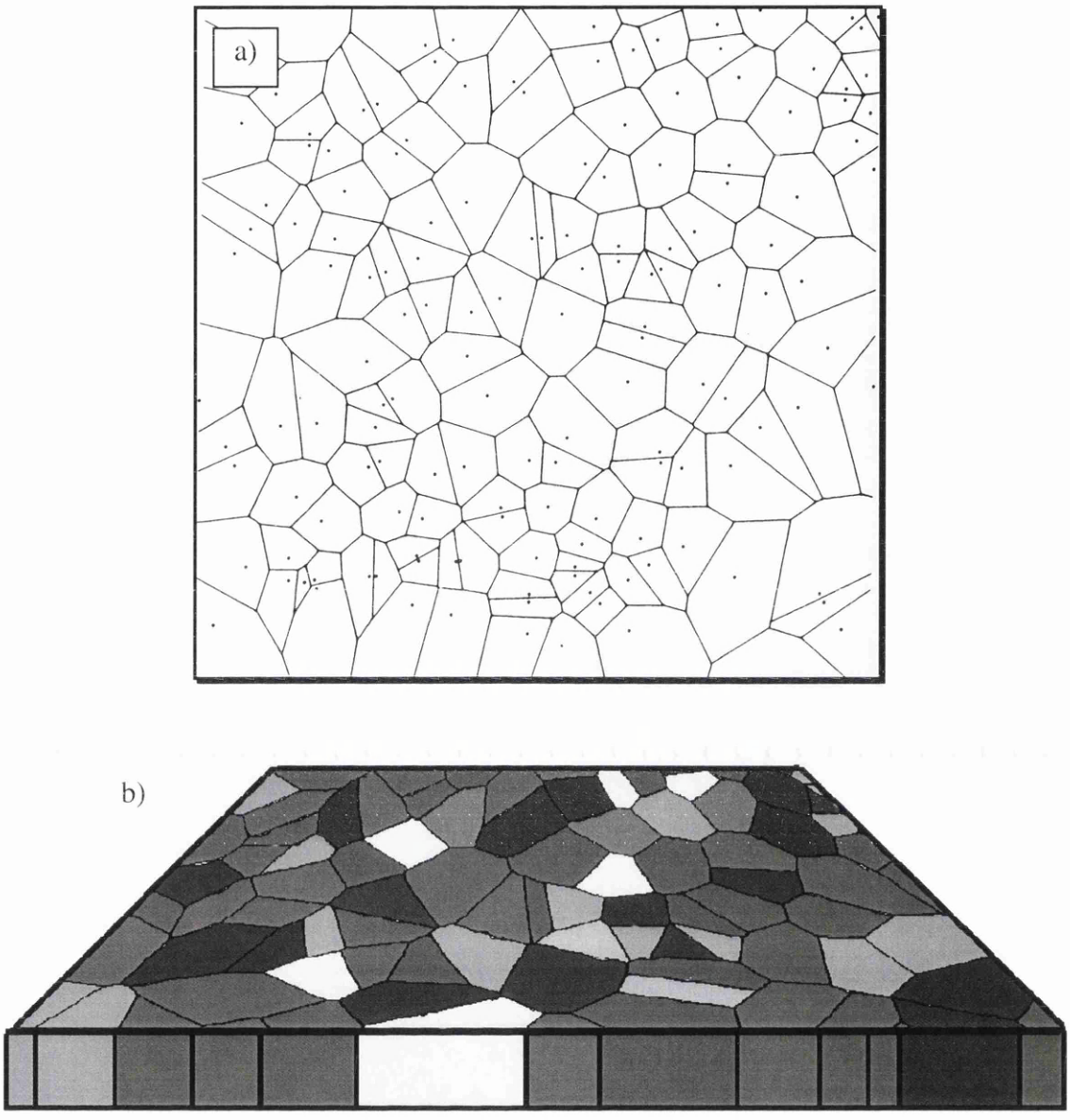

Figure 4.5: *a) a section of a 2D Poisson Voronoi Diagram which is describes columnar grain growth as in b)*

The average cell or grain size, D, is defined as the *median* diameter of a set of grains in plane. The median has the desirable property that the probability is ½ that a sample value will exceed the population median regardless of the nature of the distribution. It is useful here as the average of one distribution, e.g. diameter, does not necessarily correspond to the average of a distribution, e.g. area, when a non-linear function relates them. However, the median of both distributions do correspond.

The intercept measurements both underestimate the average grain size and give a different grain size distribution curve. Voronoi statistics only provide the grain area and perimeter distributions for the model, so the grain size has to be inferred from one of these. The grain size itself is defined as the average diameter through a grain and can be calculated using either equation 4.5 or 4.6. The relation between the grain size and the area in equation 4.6 is more accurate. Equation 4.5 actually gives the mean 'caliper width' of a grain and the values obtained from both equations are very similar for non-elongated grains.

$$D = \frac{P}{\pi} \qquad [4.5] \qquad\qquad D = \sqrt{\frac{4A}{\pi}} \qquad [4.6]$$

Although equation 4.6 is normally used[19], different authors use slightly different expressions[20],[21]. Calculations performed in this work, however, show that these equations are a good approximation but not exact. To obtain an exact expression, the variance in the radius of the grain must be taken into account. Equation 4.7 shows how the average radius is calculated from the radius around the grain.

$$A = \frac{1}{2\pi}\frac{1}{2}\int_0^{2\pi} r^2 d\vartheta = \frac{< r^2 >}{\pi} \qquad [4.7]$$

But $<r^2>-<r>^2 \geq 0$, (only equal when grains are circular) so equation 4.6 should be modified to equation 4.8.

$$D \leq \sqrt{\frac{4A}{\pi}} \qquad [4.8]$$

Thus, the more irregular the grain shape is for a given area, the smaller the average diameter. Equation 4.8 is quite meaningless unless it is known by how much the variance in r reduces the diameter. A calculation is performed on a square shaped grain of unit inner radius as shown in equation 4.9.

$$r = \frac{6}{\pi}\int_0^{\pi/6} \frac{1}{\cos\vartheta} d\vartheta = \frac{6}{\pi}\frac{1}{2}\ln\left|\frac{1+\sin\vartheta}{1-\sin\vartheta}\right|_0^{\pi/6} = 1.04 \qquad [4.9]$$

For a circle with the same area as this square, equation 4.6 and $D=2r$, gives $r=1.05$, a difference of 1%. More generally, the ratio, R_D, of the average diameter of an n-sided polygon to the diameter calculated from its area using equation 4.6 is given by equation 4.10.

$$R_D = \frac{2\sqrt{\frac{\pi}{n}\tan\left(\frac{\pi}{n}\right)}}{\ln\left|\frac{1+\sin(\pi/n)}{1-\sin(\pi/n}\right|} \qquad [4.10]$$

This equation implies that the smaller the number of sides the grain has, the larger the ratio, R_D, is, i.e. the larger the error in using equation 4.6 to calculate the grain size. In the worst case, a triangular set of grains would create a 2.0% error. Even this error is insignificant in the calculations involved in determining the grain size distribution. However, this only accounts for regular shapes and the deviation from equation 4.6 increases as the grains become elongated. The random distribution of grain shapes creates difficulties in providing an exact relation of the grain area to its grain diameter, hence the reason it is quoted differently by various authors.

Using equation 4.6 to relate the area to the diameter of each grain, it remains to relate the intercept values to the distribution of grain areas. The model predicts a certain distribution of grain areas, with the average area calculated from the average intercept length. Equation 4.11 can be derived from the expected values for A and I in table 4.2 and using equation 4.6.

$$\overline{D} = \left(\frac{4}{\pi}\right)^{\frac{3}{2}} \overline{I} \approx 1.44\overline{I} \qquad [4.11]$$

The expected distribution of grain sizes is determined from the distribution of grain areas predicted by the model. The distribution of grain areas is a three-parameter generalised gamma function as given in equation 4.12[15].

$$f(A) = b^q A^{q-1} \frac{\exp(-bA)}{\Gamma(q)} \qquad [4.12]$$

Here, b=3.0 and q=3.3 being empirical values. Using equation 4.12 and differentiating the probability function[22], the grain size distribution is shown in equation 4.13.

$$f(D) = b^q \left(\frac{\pi D^2}{4} \right)^{q-1} \frac{\exp(-b\pi D^2 / 4)}{\Gamma(q)} \frac{\pi D}{2} \qquad [4.13]$$

The grain size distribution is shown in figure 4.6. It should be noted that the average grain size is 1.04×the peak value, and can be used to fit the curve to the results. From this curve, the standard deviation is given by equation 4.14.

$$\sigma_D = 0.27\overline{D} \qquad [4.14]$$

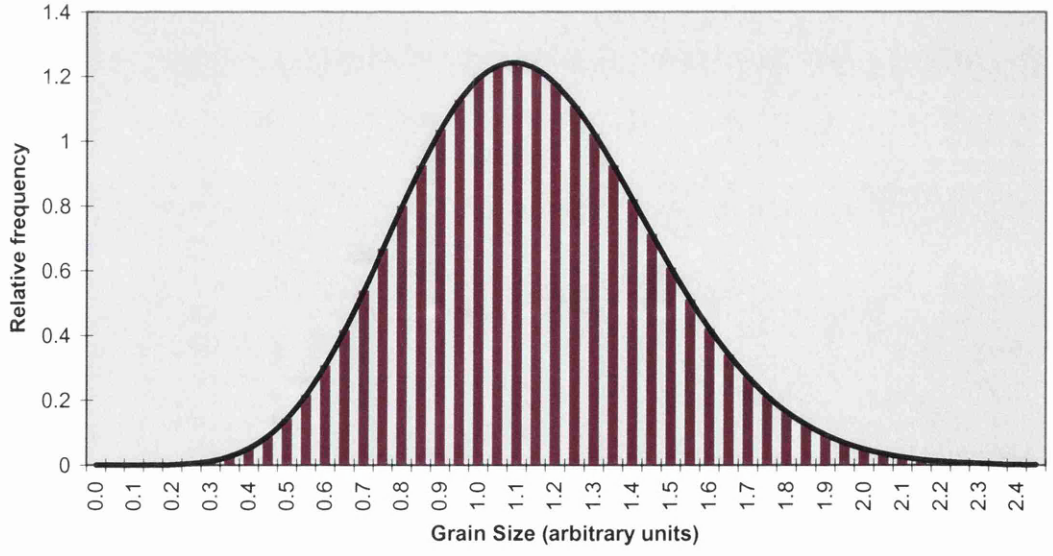

Figure 4.6: *The expected grain size distribution for columnar grains as predicted by Voronoi statistics*

If the expected values for the perimeter from table 4.2 and equation 4.5 are used it can be shown that the standard deviation of the grain caliper size distribution is $0.24\overline{D}$. However, equation 4.14 more accurately describes the standard deviation of the grain size distribution.

In most texts, the grain size distribution is approximated to a log-normal distribution[8],[19] of the form shown in equation 4.15.

$$f(D) = \frac{1}{D\sigma_l\sqrt{2\pi}}\exp\left[-\left(\frac{1}{\sqrt{2}\sigma_l}\ln\frac{D}{D_{50}}\right)^2\right] \qquad [4.15]$$

Where D_{50} is the median grain size, or diameter, and σ_l is the standard deviation of the plot of ln$D$ values. The graph has a peak at D=D_{50} and is a Gaussian in a linear graph. If the complete grain size distribution is calculated directly it is possible to determine σ_l. Very complicated calculations are involved in relating the normal standard deviation, σ_D, to σ_l; however, σ_D is only used for graphical representation and has little physical meaning.

Now that $\overline{D}$ and σ_D can be calculated (as well as the shape of the distribution), all that remains is the determination of the errors in each of these values. Using the expected intercept values in table 4.2, the error in determining the mean grain size, $\Delta\overline{D}$, is given by equation 4.16.

$$\Delta\overline{D} = \left(\frac{4}{\pi}\right)^{\frac{3}{2}} 1.96\frac{\sigma_l}{\sqrt{n_l}} \qquad [4.16]$$

This can be written as equation 4.17, assuming the standard deviation of the intercept distribution is as predicted by theory. This gives an indication of the number of measurements required for a given level of accuracy.

$$\frac{\Delta\overline{D}}{\overline{D}} = \frac{\Delta\overline{I}}{\overline{I}} = \frac{1.96\sigma_I n^{-1/2}}{1.83\sigma_I} \approx \frac{1}{\sqrt{n_I}} \qquad [4.17]$$

The error is quoted for 95% confidence and implies that for a 10% error in the average grain size, the number of measurements needed is at least 115. This number reduces to 29 measurements for 20% error, and so forth.

4.6.3 Non-Columnar, or 3D, Growth

Statistical distributions also exist for non-columnar grain growth where the grains are considered 3-dimensional. The calculations leading to the grain size distribution are similar to those mentioned in the previous section but the parameters are slightly different. Table 4.3 lists these parameters predicted by equation 4.4.

Table 4.3: *Expected values of relevant cell parameters in 3D*

Characteristic	*Symbol*	*Numerical value*
Intensity of cell centroids	λ_2	λ
Number of faces/cell	E(F)	15.5
	$E(F^2)$	252.4
E_3V_3 Volume	E(V)	λ^{-1}
	$E(V^2)$	$1.18\lambda^{-2}$
E_3V_2 Surface area	E(S)	$5.82\lambda^{-2/3}$
	$E(S^2)$	$36.1\lambda^{-4/3}$
Average caliper width	E(b)	$1.46\lambda^{-1/3}$
	$E(b^2)$	$2.16\lambda^{-1/3}$
E_1V_1* Intercept length	E(I)	$0.687\lambda^{-1/2}$
	$E(I^2)$	$0.632\lambda^{-1}$

*From a modified version of equation 4.4.

The theoretical value of the mean caliper width of the 3D grains is already predicted by the model and taken as a good approximation of the average grain size of the distribution. Here the distribution of grain widths is Gaussian with $\overline{D} = 2.12\overline{I}$, and a standard deviation of $0.12\overline{D}$.

For a more accurate interpretation of the grain size distribution, the volume distribution of a set of grains is used as shown in equation 4.18[23].

$$f(V) = \frac{\alpha}{\Gamma(\alpha)}(\alpha V)^{\alpha-1}\exp(-\alpha V) \qquad [4.18]$$

Equation 4.18 is similar to equation 4.12 with α=6.18 for the volume distribution. Using equation 4.18 and 4.19 it can be shown that equation 4.20 describes the grain size distribution more accurately.

$$V = \frac{4}{3}\pi\left(\frac{D}{2}\right)^2 \qquad [4.19]$$

$$f(D) = \frac{\alpha}{\Gamma(\alpha)}(\alpha\frac{\pi D^3}{6})^{\alpha-1}\exp(-\alpha\frac{\pi D^3}{6})\frac{\pi D^2}{2} \qquad [4.20]$$

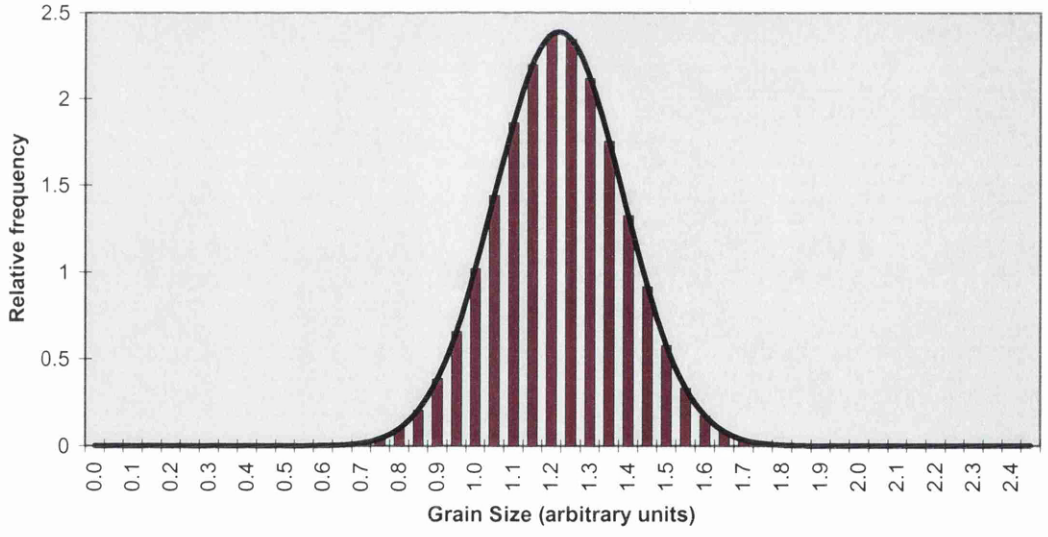

Figure 4.7: *The expected grain size distribution for non-columnar grains as predicted by Voronoi statistics*

The grain size distribution described by equation 4.20 is approximately a Gaussian distribution as shown in figure 4.7. It is of similar shape to the distribution of grain caliper widths as mentioned earlier, but, with a smaller average. Here, $\overline{D}$ is given by

equation 4.21 using table 4.3, and the standard deviation is shown in equation 4.22 as calculated from the data.

$$\overline{D} = 1.80\bar{I} \qquad [4.21]$$

$$\sigma_D = 1.30\overline{D} \qquad [4.22]$$

The error in the average grain size, $\Delta\overline{D}$, is slightly different than the 2D case and is given by equation 4.23 using values from table 4.3.

$$\frac{\Delta\overline{D}}{\overline{D}} = \frac{\Delta\bar{I}}{\bar{I}} = \frac{1.96\sigma_I n^{-1/2}}{1.71\sigma_I} = \frac{1.15}{\sqrt{n_I}} \qquad [4.23]$$

Thus, for columnar growth, the number of measurements required for an accuracy of 10% is 132.

4.6.4 Summary of Voronoi Statistics

Voronoi statistics are used to convert the intercept values obtained from the grain size technique, to a complete description of the distribution of grain sizes. The model describes the distribution of grain areas for normal grain growth. The grain size distribution can be inferred from this by using equations 4.6 and 4.13, or 4.19 and 4.20, depending on whether the grains are columnar or not. The average values for the grain size distribution, in each case, are proportional to the average intercept lengths and calculated using equations 4.11 and 4.21. The error in the average grain size is proportional to the error in the mean intercept length and is affected by both the number of measurements taken and the standard deviation of the intercept values.

The grain size distribution is shown in figures 4.6 and 4.7 for columnar and non-columnar grains respectively. These distributions are significantly different with the spread in grain sizes less for non-columnar grains[8]. As a test, the experimental

distributions of intercepts can be compared to the distribution predicted by tables in the model as shown in figure 4.8 for both types of grain. If the data agrees with neither distribution then the model will not be valid for the analysis. Otherwise the model is assured to produce accurate and reliable results if enough measurements are taken.

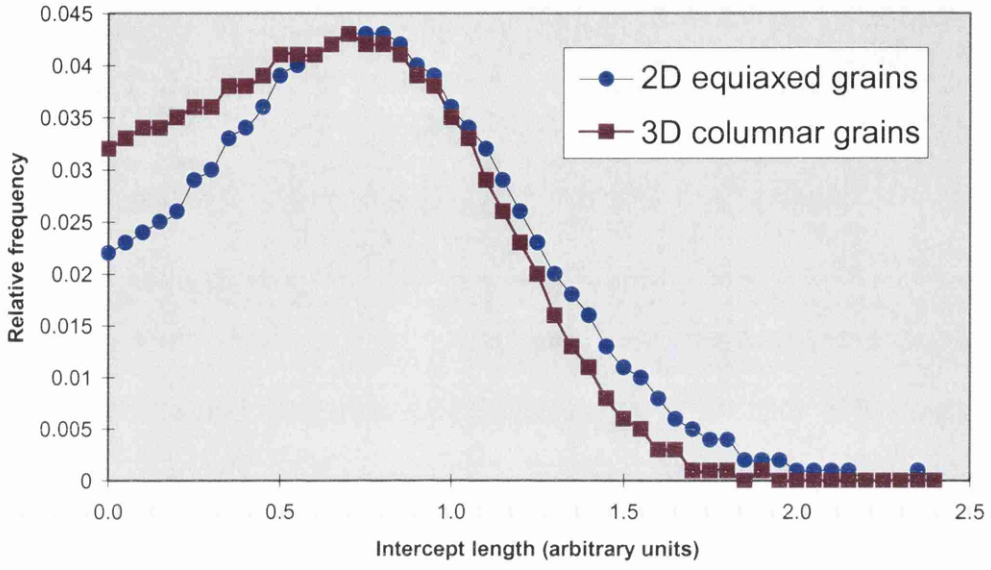

Figure 4.8: *The expected intercept distribution for columnar and non-columnar grains*

4.7 Results

The previous section explored and developed statistical models for use in determining the grain size distribution of a film whose intercept lengths are known. Using the grain size technique, as described earlier, intercept lengths are measured for two Al films and their distributions for each film shown in figures 4.9 and 4.10 respectively. The number of intercept measurements taken for metal 1 is 40, and 81 for metal 2.

The first step in determining the grain size distribution is to compare the intercept distribution to the relevant model for the type of grain. The grains in the film are known to be columnar from imaging so the 2D Voronoi model is used. The theoretical

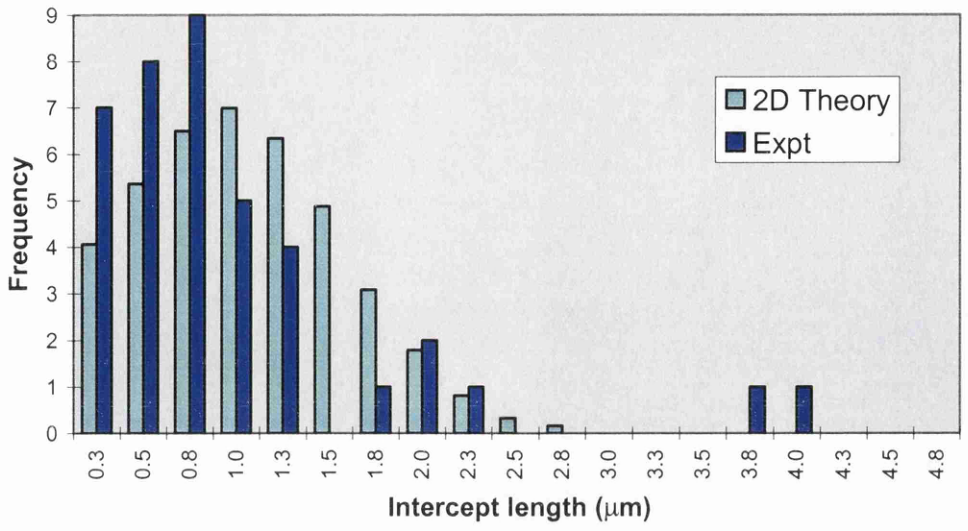

Figure 4.9: *Comparison between the experimental and theoretical intercept lengths for metal 1, where 40 measurements were made*

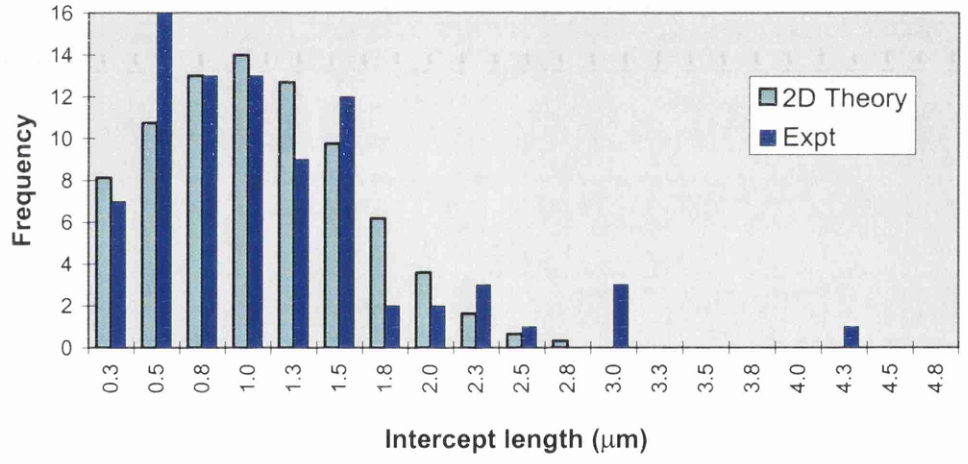

Figure 4.10: *Comparison between the experimental and theoretical intercept lengths for metal 2, where 81 measurements were made*

intercept distribution is shown against the data in figures 4.8 and 4.9 where the theoretical distribution is scaled horizontally according to the average intercept length measured. It is clear that the theory agrees more with the data for metal 2, and this is likely to be a result of the two-fold increase in measurements taken in this case. The lesser agreement of metal 1 to the model could, however, suggest that the grain growth is abnormal. Normal grain growth is characterised by the presence of grains which have

sizes $<5\overline{D}$, whereas in abnormal grain growth particularly large grains $\approx 100\overline{D}$ [24] can be present. Several large grains having $I \approx 4\bar{I}$ are observed in the intercept distribution for metal 1. This is not an indication of abnormal grain growth (<5) but the results are not conclusive. Further experimentation on a different specimen would be required to reach a more conclusive result.

Considering the growth conditions for both Al films were identical, besides the duration of deposition, the fact that the model agrees with metal 2, implies that the reason for the lesser agreement for metal 1 is a consequence of the smaller number of intercept measurements taken there. The number of measurements were limited by the area available on the TEM specimen.

The average intercept length is found to be 0.99±0.32 μm for metal 1 and 1.01±0.16 μm for metal 2. Using equations 4.11 and 4.16, the average grain size, $\overline{D}$, is (1.43±0.47)μm and (1.45±0.23)μm, a relative error of 33% and 16%. The standard deviation of the distribution is calculated using equation 4.14 and is 0.38μm and 0.39μm for metals 1 and 2 respectively. The theoretical grain size distribution described by equation 4.13 is scaled so that the peak is at $\overline{D}/1.04$, as mentioned earlier. In this case, the x-values are multiplied by $\overline{D}/(1.04\times1.15)$, in effect, condensing the x-axis. The predicted grain size distribution for both films are shown in figure 4.11. Table 4.4 summarises the results from the analysis.

Table 4.4: *Summary of Results*

Aluminium Film	***Metal 1 (t=0.75μm)***	***Metal 2 (t=1.0μm)***
n	40	81
L	0.99	1.01
ΔL	0.32	0.16
σ_L	1.06	0.73
$\overline{D}$	1.43	1.45
$\Delta\overline{D}$	0.47	0.23
σ_D	0.38	0.39

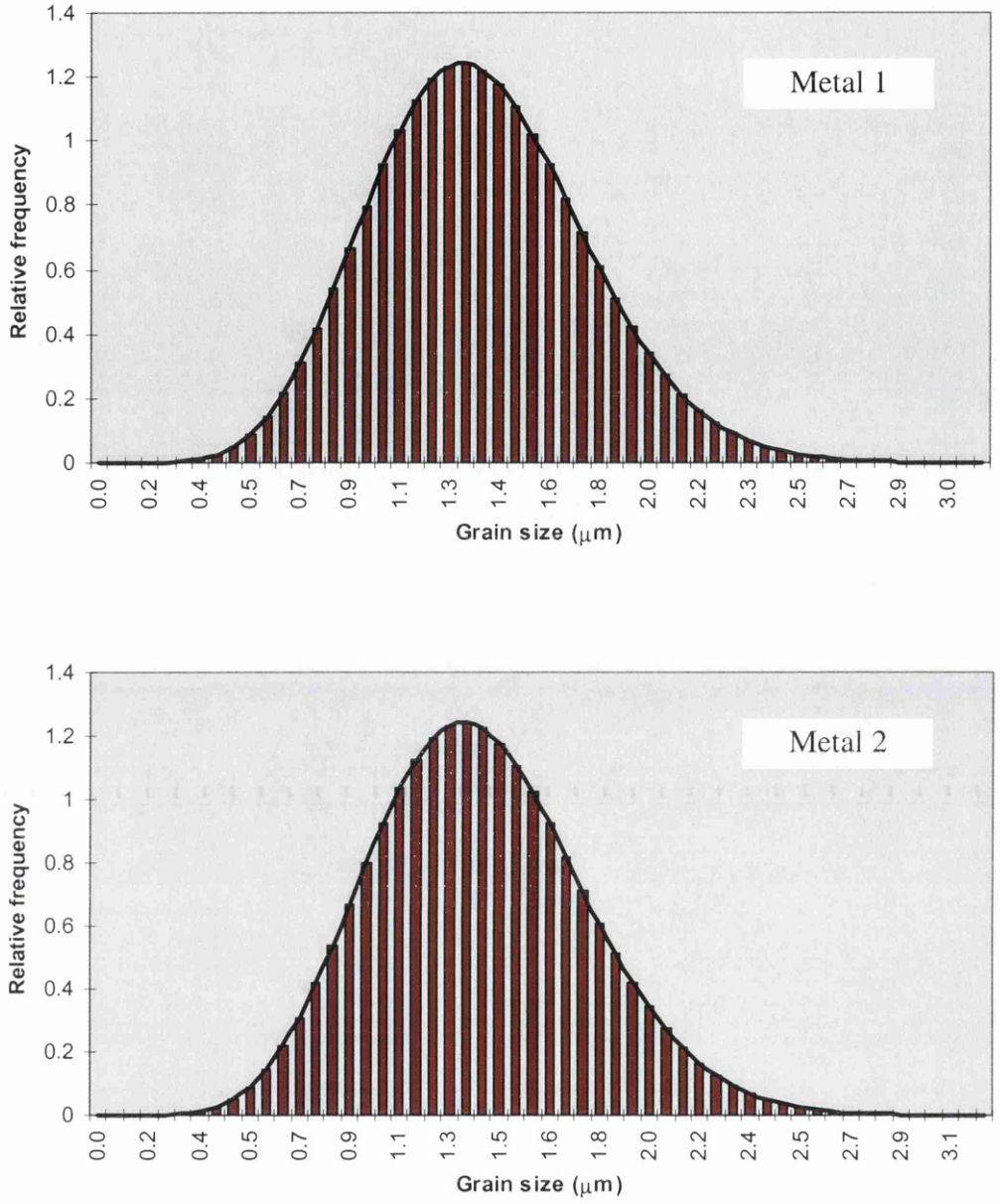

Figure 4.11: *The predicted grain size distribution for metal 1 and metal 2. The error in* $\overline{D}$ *is greater for metal 1 mainly due to the smaller number of intercept measurements, however, the shape of the curve should be correct*

Having similar $\overline{D}$ *s,* the data on both films could perhaps be superimposed. The intercept data from both distributions are combined and the resultant distribution is in no closer agreement with the theoretical curve, as shown in figure 4.12. This implies that the two distributions are not identical, as the effective increase in number does not improve the agreement of the distribution. On closer inspection, it is quite likely that

the unusually large grain sizes are exaggerating the average intercept length for metal 1. This is a perhaps an indication of some bimodal (having two peaks) grain growth in metal 1[25], as abnormal grain growth was not completely excluded. More sample area would be required to investigate this further, or, better still, plan view imaging of metal 1 would show any indication of bimodal grain growth.

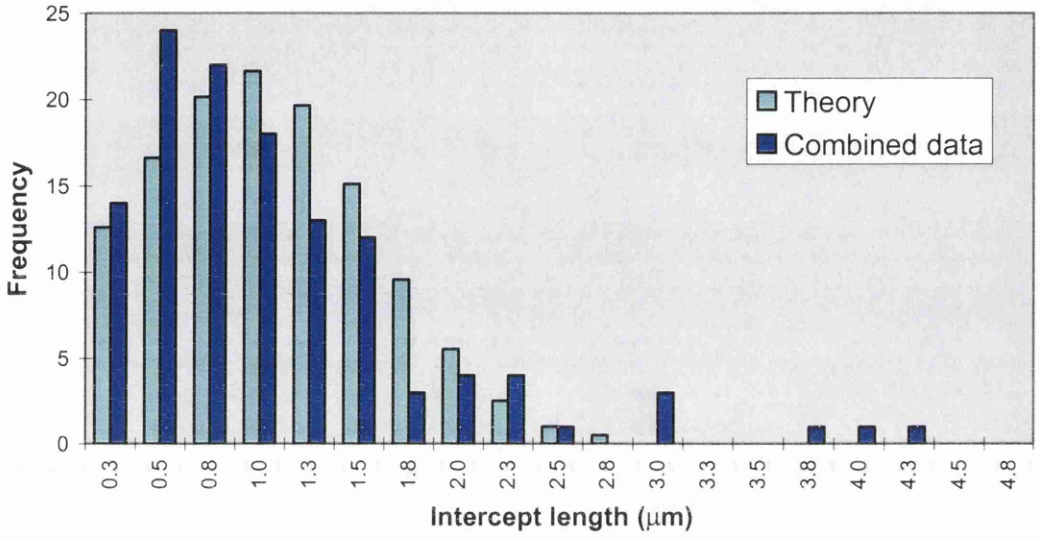

Figure 4.12: *Intercept data from both Al films combined and compared to theory. No significant improvement in the agreement is found*

4.8 Discussion

In the previous section, grain size distributions are calculated for two Al films using a diffraction technique to determine the position of every grain boundary. Now that the technique and analysis has been covered, this section discusses two things: the merits and disadvantages of the technique and the validity and applicability of the analysis.

The main advantage of this technique is its ability to identify every grain boundary in a cross-section of the film. Only diffraction techniques with nanometre spatial resolution, are able to locate a grain boundary on a nanometre scale. Performing the technique on a cross-sectional specimen allows observation of the nature of the film growth. Different

statistical models are used for different types of grain structure and existing grain size techniques cannot directly observe the structure of the film in the growth direction. Another major advantage of cross-sectional analysis is the ability to monitor the grain size distribution as a function of film thickness. This could be valuable in confirming theoretical grain growth models. More practically, the grain size of a doped film often changes according to the level of damage at the top surface. So, measurement of the change in the grain size distribution through the film would be beneficial[26]. The thickness of the electron transparent specimen is so small that the thickness of the transect, containing the intercepts, is very thin, enabling very accurate grain size analysis. Using the tripod polisher as a specimen preparation technique produces a large usable electron transparent area maximising the statistical accuracy.

The technique requires no dedicated equipment for the experimentation. If a PC is not available to acquire the image and signal scan at the same scale there are alternative ways to acquire the intercept data. A simple computer program could be written which registers a grain boundary every time the space bar is hit. Inputting the scan time to the program, it could perform all the statistical analysis immediately. The only requirement for the microscope is the ability to scan along a film giving >1s per grain. This was not immediately available on the Philips CM20, but could be programmed by an engineer if required. Once aligned, the technique itself takes several minutes, depending on the scan length. The results can be compared to cross-sectional images to verify the validity and mark obvious mistakes (although none were identified in the experimentation here).

There are no significant disadvantages in this technique which would not be applicable to all the other comparable techniques. It is sometimes difficult to observe the diffraction pattern changing, or mistaking specimen bending for a grain boundary, but retracing effectively the same line during the scan ≤5 times, reduces the observational error almost completely. Specimen preparation clearly presents more difficulties and time consumption than, for example, OIM, where the films can be examined in bulk. However, material will inevitably have to be removed from processed devices to reach down to the film of interest, and these could alter the grain size distribution.

There exist several analytical models which characterise various parameters of grain structure but most agree very well with each other and with experimental results. If the model agrees with the experimental data wherever possible, i.e. intercept lengths, and the mechanics of the model agree with the actual grain growth mechanisms, then the results which the model predicts should be accurate. Experiment has shown that the average grain size of equiaxed grains, as considered here, should be between 2-4×h, the film thickness[18]. For the films studied here, the average grain sizes were 1.9h and 1.5h for metal 1 and 2 respectively. Many different processing conditions govern the size of the grains, including upper and lower surface roughness, anneal time and subsequent processing conditions and these could cause this inconsistency with the prediction. It is not surprising that metal 1 has a higher $\overline{D}/h$ ratio than metal 2, as this film was subject to more post-deposition heat cycles which cause the grain sizes to increase. The accuracy in $\overline{D}$ for metal 2, on which 81 intercept measurements were made, was determined to be 16% for a 95% confidence level. The log-normal shape of the distribution is fairly well established as correct and agrees with the model used in this analysis.

The fact that the actual grain sizes were not measured, but inferred, creates a few difficulties in calculating statistical distributions other than those previously calculated in the texts. The analysis involved in determining grain size distributions is not a straightforward one, hence the diversity of approaches and assumptions by various authors. There will always be some level of modelling required to predict grain size distributions as it is a 3-dimensional property which can only ever be viewed in 2-dimensions. New theories have been produced since the middle of this century and are progressively becoming more refined. However, the uncertain nature of grain growth will place a fundamental limit on the level of accuracy obtainable by a model which is used to predict the grain size distribution.

References for Chapter 4

[1] C. R. M. Grovenor, in *Microelectronic Materials,* IOP Publishing Ltd, (1989) 199

[2] S. Vaidya, A. K. Sinha, Thin Solid Films **75**, 3, (1981) 253

[3] D. B. Knorr, D. P. Tracy, K. P. Rodbell, Appl. Phys. Lett. **59,** 25, (1991) 3241

[4] S. Hasegawa, S. Yamamoto, and Y. Kurata, J. Electrochemical Soc., **137**, 11 (1990) 3666

[5] C. R. M. Grovenor, in *Microelectronic Materials,* IOP Publishing Ltd, (1989) 239

[6] S. A. Campbell, in *The Science and Engineering of Microelectronic Fabrication,* New York, Oxford Univ. Press (1996) 412

[7] C. V. Thompson, Interface science, **6**, (1998) 85

[8] C. V. Thompson, Annu. Rev. Mater. Sci. **20** (1990) 68

[9] A. Maraner, F.Toninato, S. Vitale, and P.Tiberto, J. Appl. Phys., **81 (8)**, 2 (1997) 3975

[10] D. Nicoletti, and A. Anderson, J. Acoustical Soc. Of Amer., **101**, 2 (1997) 686

[11] D. T. Carpenter, J.M. Rickman, and K. Barmak, in press in MRS conference proc. (1998)

[12] E. R. Generazio, Mater. Eval. **46**, 4, (1988) 528

[13] L. H. Zhao, T. M. Lu, and M. G. Lagally, Acta Crystal. Sect A-Found. Of Crys., **38**, Nov, (1982) 800

[14] R. A. Schwarzer, Ultramicroscopy, **67,** (1997) 19

[15] A. Okabe, B. Boots, K. Sugihara, in *Spatial Tessellations,* Wiley, (1992) 273

[16] D. Harker, and E. Parker, Trans. Am. Soc. Met., **34**, (1945) 156

[17] V. Novikov, in *Grain Growth and Control of Microstructure in Polycrystalline Materials*, CRC Press, New York (1997) 47

[18] K. Barmak, J.M. Rickman, and C. Michaelsen, J. Electronic Mats. **26**, 11 (1997) 1370

[19] Y. C. Joo, and C. V. Thompson, J. Appl. Phys., **76 (11),** (1994) 7339

[20] R. L. Fullman, Trans AIME, **197**, (1953) 447

[21] V. Novikov, in *Grain Growth and Control of Microstructure in Polycrystalline Materials*, CRC Press, New York (1997) 8

[22] I. Molchanov, Dept of Statistics, Univ. Glasgow, UK, *private communication*

[23] T. Kiang, Z. Astrophys, **64**, (1966) 433

[24] V. Novikov, in *Grain Growth and Control of Microstructure in Polycrystalline Materials*, CRC Press, New York (1997) 116

[25] E. Dahlem-Klein, H. Weiland, A. Fiszer, H. J. Bunge, Scripta Metallurgica, **22**, (1988) 317

[26] C. Marsh, Oxford Univ, UK, *private communication*

CHAPTER FIVE

Determining the Grain Orientation Distribution

5.1 Introduction

As mentioned in chapter 4, many electrical and physical properties of a thin film are influenced by the grain sizes and orientations. It is widely accepted that the TEM is the technique of choice when characterising the grain structure of a film, both because of its nanometre resolution and the diffraction contrast present in imaging. Already the strength of the TEM has been demonstrated in chapter 4, where the grain size distribution of a film was determined. This chapter moves on to describe how the TEM can be used to characterise the orientations of the grains of a film in a device.

Two diffraction techniques are developed which investigate the grain orientations. One technique analyses the Kikuchi patterns from individual grains and the other examines a single diffraction pattern from an area scanned across a film of material. Before this, an overview is given of how grains having preferred orientations (POs) affect the properties of a film and how the deposition conditions affect the grain orientations.

5.2 Effect of POs on Film Properties

Among the physical and electrical properties of a film that are affected by POs, conductivity[1], electromigration[2], surface roughness[3] and interdiffusion[4] are the most

important. In general, the presence of a PO improves all of these properties, but the extent of the improvement also depends on the PO itself[5].

In a film with a PO, the atomic planes in neighbouring grains meet at a low angle at the grain boundary, reducing the energy band misfit. This results in a lower boundary resistance than between randomly oriented grains, thereby increasing the conductivity of the film. As described in chapter 4, electromigration worsens if the grains do not extend through the film thickness and are randomly oriented[6]. The existence of POs results in more grains surviving though the film and having similar orientations, causing the resistance to electromigration to improve.

Grains having the same orientation in the growth direction will grow at the same rate if the angle of incidence is the same[7]. Therefore, POs in a film normally result in a much smoother film surface. Investigation of the surface roughness of a polysilicon film is described later in this chapter. One of the main mechanisms for atoms from different materials to diffuse into each other is along the grain boundaries. This is always an undesirable effect. Grain boundary diffusion is reduced if the grains have the same orientation.

5.3 Growth Mechanisms for POs

As with many physical systems, atoms, which are incident on a substrate during deposition, will settle in a position which minimises the potential, or more strictly the free, energy of the system. In other words, as the film grows, the grains which have the highest surface energy will grow at a faster rate as the incident atoms will deposit on their surface[5]. This does not necessarily mean that the POs have the highest surface energy. Firstly, if the growth is 3D, (which is the case for polySi on SiO_2), the atoms grow from the sides of a pyramid which have the highest surface energy. Thus, the resulting grain has an orientation whose top surface does not have the highest surface energy. Secondly, other growth kinetics have to be considered. These include atomic

mobility, gas pressure, hydrogen content in the dangling bonds, and chemical reactions. The mobility is a function of deposition and substrate temperature, and depends on the element itself. At high temperatures the influence of the surface energy on the PO is at its greatest, as the atoms have more energy to rearrange into the favoured positions. As the temperature reduces, the growth mechanisms change, resulting in a different, or no, PO.

The electrical properties mentioned above are affected by the PO, so it is very useful to know how the various deposition conditions can determine it. Normally, polySi is deposited by chemical vapour deposition (CVD) where silane is pyrolized at ≈600°C[8], i.e. $SiH_4 \rightarrow Si + 2H_2$. A high hydrogen pressure in the deposition chamber promotes a <110> PO as it increases the mean free path of the incoming Si atoms on the wafer surface. (A <110> orientation means that the <110> direction is parallel to the substrate surface normal.) If, however, the pressure is very high the flux of atoms reduce the rearranging time, decreasing the extent of any PO[5]. A high T also reduces the number of H atoms on the surface. Table 5.1 shows the effect of deposition temperature and pressure, p_r, and film thickness, d, on the PO for different deposition techniques.

Table 5.1: *The effect of various processing conditions on the PO of polySi*[5]

Method	***Feed Gases***	***Substrate temperature (°C)***	***Characterising parameters***	***Orientation***
Molecular beam	----	400-700	d<1μm	<110>
		400-700	d>1μm	<100>
Evaporation	----	≤350		<111>
		400 -700		<110>
PECVD (rf)	$SiH_4 + H_2$	100	p_r=0.4 Torr	<111>
		300		<110>
	$SiH_4 + SiF_2 + H_2$	300	p_r=2.3 Torr	<110>
		300	p_r=1.1 Torr	<100>
Photo CVD	$Si_3H_8 + H_2$	615	p_r=2.0 Torr	<110>
Catalytic CVD	$SiH_4 + H_2$	400	p_r=6.0 Torr	<100>
LPCVD	SiH_4	600-650		<110>
		650-700		<100>
(P-doped)	$SiH_4 + PH_3 + N_2$	≥600	[P/Si]=8×10^{-4}	<311>
APCVD	$SiH_4 + H_2$	850-1050	d=0.6μm	<111>

In table 5.1, PECVD is plasma enhanced chemical vapour deposition, LP- is low pressure, and AP- is atmospheric pressure. It is clear that the preferred orientations for polySi are <100>, <110>, <111> and <311>, depending on the deposition technique. It is also known that the best film characteristics are observed using PECVD and the worst using LPCVD[3]. For the two polySi films used to demonstrate the orientational analysis described later, the poly 1 is 270nm thick, and poly 2 is 470nm thick, both being deposited by LPCVD at 625°C. There is little benefit in predicting the POs of these films from table 1 as both films are subject to many post-deposition heat processes and are doped to a certain thickness from the surface of the film. The fact that the POs cannot be predicted from results on simple films, emphasises the need for cross-sectional orientational analysis on fully-processed devices.

To summarise, the following factors which affect the grain orientations are:

- gas and substrate temperature
- film thickness
- deposition method and direction
- gas pressure
- dopant type & concentration
- post-deposition heat cycles

5.4 Identification of POs using Kikuchi Patterns

5.4.1 Introduction

One way of determining the distribution of orientations in a film in cross-section is to probe each grain and examine the Kikuchi diffraction pattern observed in the TEM. Kikuchi patterns are observed when the grains are ≥30nm thick to allow for both inelastic and elastic scattering of the same electron. This method is particularly useful for detecting variations in local texturing where the grains are small[9]. This way, grain

orientations can be determined with an angular resolution ≈¼° The time scale for such an experiment can be large if many grains are investigated, in which case the scanning diffraction technique described later in this chapter could be used. Variations on the Kikuchi method have been performed by several authors but the experimentation is normally done in plane, i.e. only the zone axis has to be determined. For example, a common technique involves using the diffraction alignment coils to shift a selected position on a Kikuchi line onto a reference mark, (e.g. a pointer)[10]. The corresponding voltage drop in the coils is registered by a computer and, knowing the orientation on the selected Kikuchi line using Kikuchi maps, the grain orientation is determined. There are various reasons for investigating the POs in cross-section, as mentioned earlier, so more complex analysis than that required for in-plane measurements has to be implemented. The crystal plane orientations are often determined in cross-section e.g. for semiconductor interfaces in HREM. However, normally[11] SAD is used and the accuracy is considerably less than using Kikuchi patterns. In this section, the grain orientations are determined individually from Kikuchi patterns using original analysis.

5.4.2 Technique

The principle behind this technique is to focus the electron beam onto a grain in the film of interest in cross-section and take, typically, three measurements from the Kikuchi pattern to identify the orientation of the grain to within 1°. A capacitor containing the two films investigated for the presence of POs is shown in cross-section in figure 5.1.

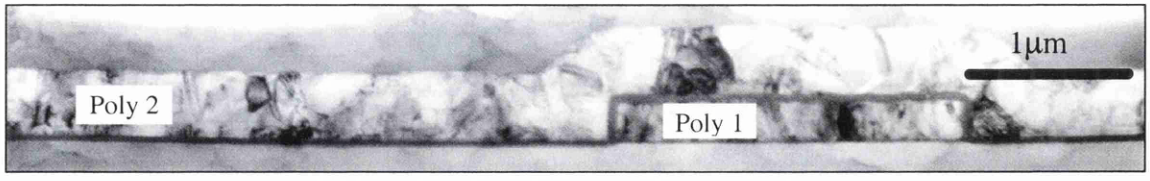

Figure 5.1: *Image of the two polySi films studied for POs using the Kikuchi method*

The polySi films are known as poly 1 and poly 2 where poly 1 is ≈270nm thick and poly 2 is ≈470nm thick. The grains in each film are normally 50-400nm across, however the

technique can probe grain sizes down to ≈5nm. At this grain size Kikuchi patterns are not formed so the determination of the grain orientation is much more difficult.

Probing the grains can be performed two ways. One approach is to focus the beam onto a grain in imaging, then switch to diffraction to observe the diffraction pattern on the viewing screen. Otherwise the microscope is set up in scanning and the beam is positioned onto a neighbouring grain while observing the diffraction pattern on the viewing screen. This way the specimen is no longer viewed but time is saved switching between imaging and diffraction. The former method is used here as only the sizeable grains are investigated for their orientation as these will provide a good indication of the presence of POs. In addition, it is possible to accidentally leave the film of interest and probe either another polySi film or the substrate if the film is not imaged regularly. Around 100 grains are probed individually for this experiment. The diffraction patterns are exposed on photographic film and an example of a Kikuchi pattern from a poly 1 grain is given in figure 5.2a.

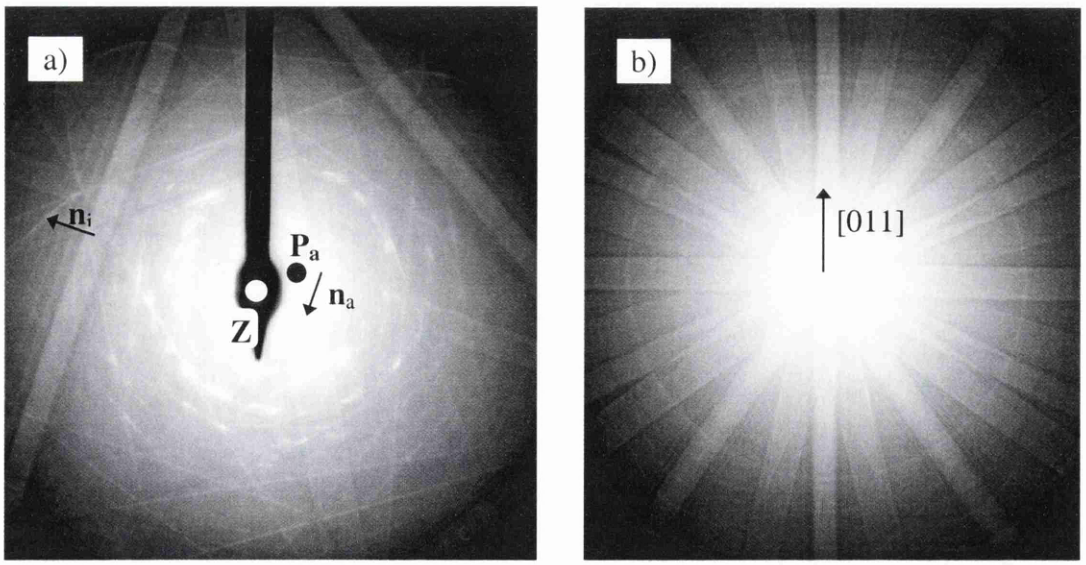

Figure 5.2: *a) An example of a Kikuchi pattern from which the grain orientation is determined, and b) shows the substrate Kikuchi pattern used to determine the substrate normal direction in the diffraction patterns*

5.4.3 Calculation of the Orientation from the Kikuchi Pattern

The orientation, **g**, of a crystal is the direction in the crystal which is perpendicular to the substrate surface. To calculate **g** from the Kikuchi pattern, the surface normal direction in the diffraction plane has to be determined. This can be achieved by either defocusing the diffraction spot until the whole specimen is seen and the growth direction is apparent, or, more accurately, by inferring the growth direction from a Kikuchi pattern of the single crystal substrate. The latter is used here and the substrate Kikuchi pattern is shown in figure 5.2b.

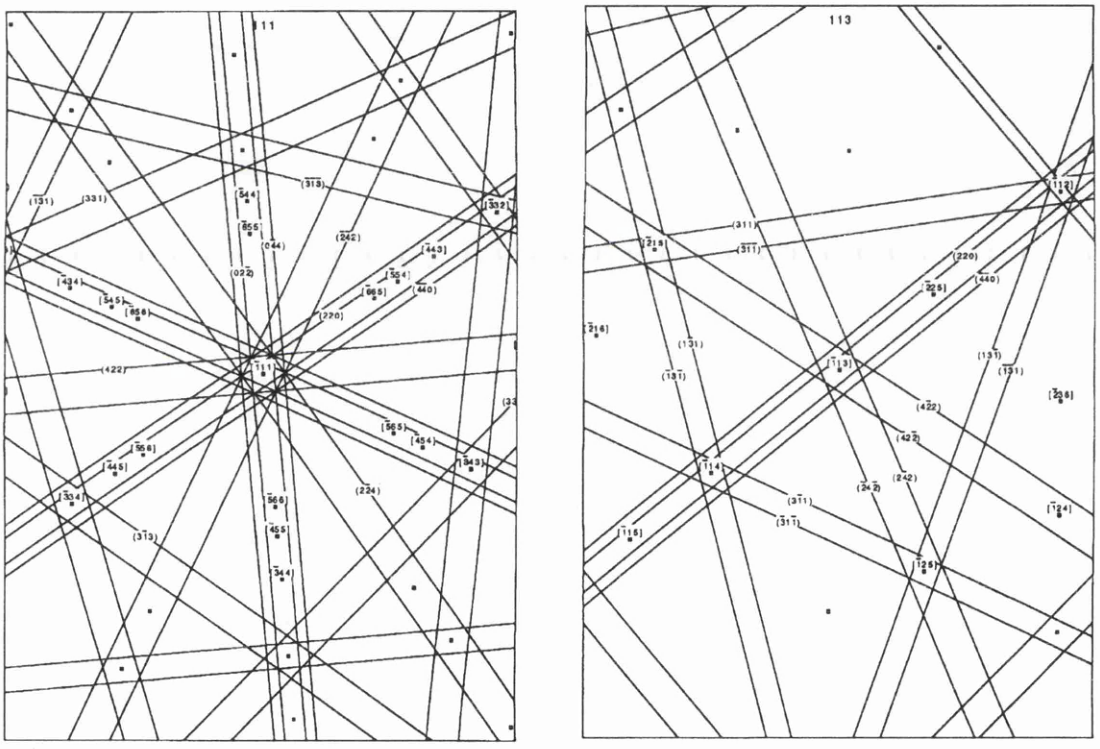

Figure 5.3: *Two sections of a Kikuchi map which are used to identify the zone axis of a Kikuchi diffraction pattern*

The first stage in determining the grain orientation is to identify the zone axis, **Z**, in the Kikuchi diffraction pattern from the grain in cross-section. This can be found by direct comparison of the pattern to a Kikuchi map for Si. Two areas of such a Kikuchi map at different zone axes are shown in figure 5.3. Often, however, the Kikuchi pattern does not have a well defined **Z** as is shown in figure 5.2a. To determine **Z**, up to two angles,

φ_1 and φ_2, along directions given by Kikuchi normals are measured from a known approximate pole, $\mathbf{P}_a$. The angular scale of the diffraction pattern can be calculated simply by using the camera length, L, (in cm) and the scale is given by $1/L$ rads/cm. Note that this calculation is only required if **Z** cannot be determined accurately by comparison to Kikuchi maps.

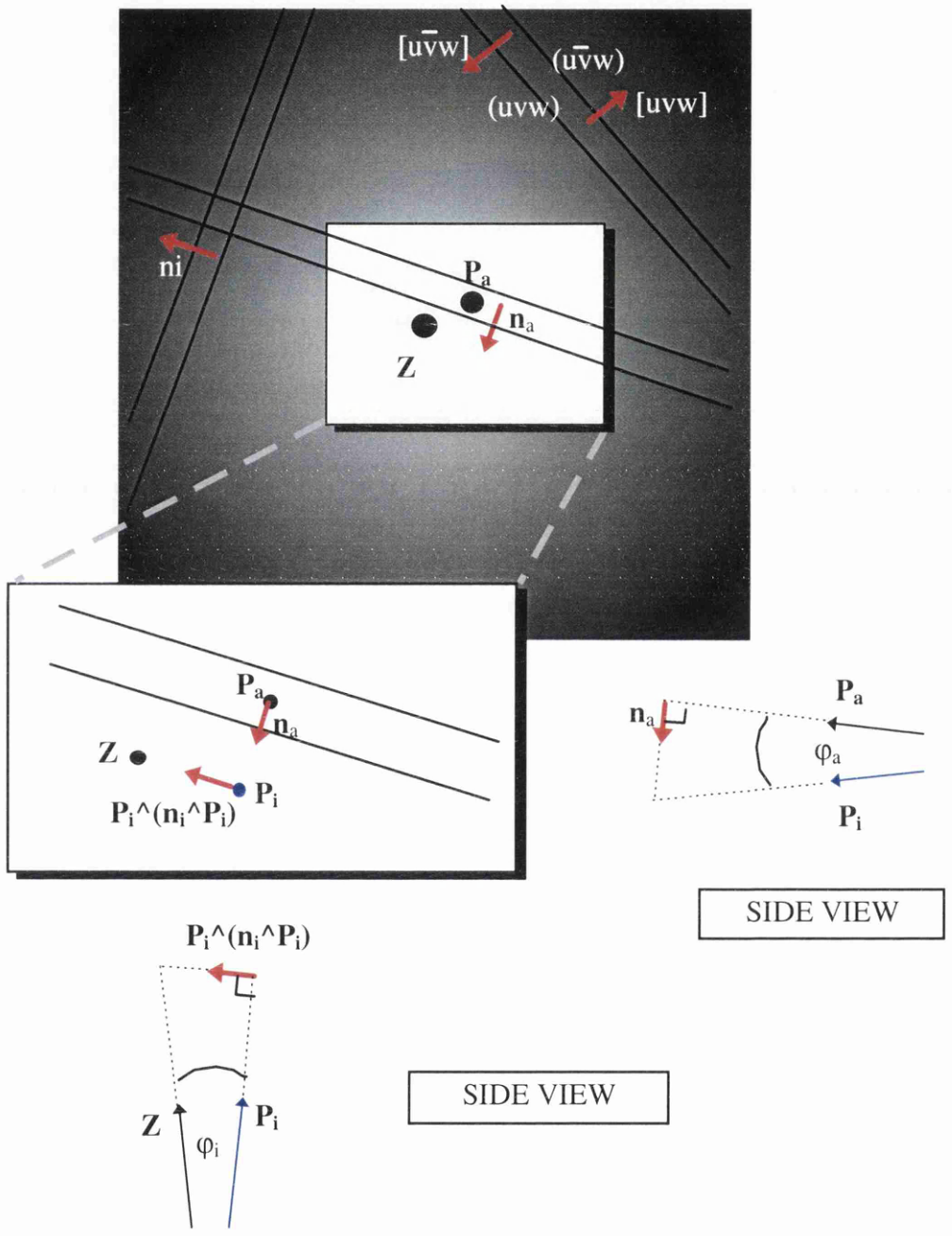

Figure 5.4: *The geometry used to determine the zone axis, **Z**, of a pattern from a known pole, $\mathbf{P}_a$. Note that all vectors are unit vectors, i.e. they describe directions only*

To describe the full calculation which may be involved in determining **Z** from $\mathbf{P_a}$, a worst-case example is given here. Figure 5.4 shows a schematic of the Kikuchi diffraction pattern shown in figure 5.2a. Vectors which are known immediately from comparison to Kikuchi maps are $\mathbf{n_a}$, $\mathbf{n_i}$ and $\mathbf{P_a}$. The first two are just normals to the lattice planes having the same indices as the Kikuchi lines. The correct direction of the normal of a Kikuchi line always points inwards, towards the other Kikuchi line, as shown in figure 5.4. Equations 5.1a and 5.1b can be used to calculate the intermediate pole, $\mathbf{P_i}$, (if two angles are required) and then **Z**.

$$\mathbf{P}_i = \mathbf{P}_a \cos\varphi_a + \mathbf{n}_a \sin\varphi_a \qquad [5.1a]$$

$$\mathbf{Z} = \mathbf{P}_i \cos\varphi_i + \mathbf{n}_i \sin\varphi_i \qquad [5.1b]$$

In these, and all subsequent equations, the vectors are unit vectors, i.e. they denote a direction only. The diffraction pattern describes a small region on the surface of a sphere in reciprocal space. Due to this curvature, a Kikuchi normal, e.g. $\mathbf{n}_i$, is not perpendicular to the approximate pole, $\mathbf{P}_i$, unless the pole is in the centre of the Kikuchi lines. This creates an error, $\delta\varphi$, in calculating **Z** using $\mathbf{n}_i$ as in equation 5.1b. This error is a function of both the angle between $\mathbf{n}_i$ and $\mathbf{P}_i$, and the angle between $\mathbf{P}_i$ and **Z**. To get a general idea of $\delta\varphi$ as a function of these angles, both are considered as having the same value, φ, i.e. $\mathbf{P}_i$ is half way between the Kikuchi line centre and **Z**. Figure 5.5 shows the geometry involved in the calculation of $\delta\varphi$ as a function of φ. The angle φ is measured as the angular distance between $\mathbf{P_i}$ and **Z**. The tangent of this angle determines the ratio of the length of $k_n.\mathbf{P}\text{^}(\mathbf{n_i}\text{^}\mathbf{P_i})$ and $k_p.\mathbf{P_i}$, as shown in the diagram. The length of $k_n.\mathbf{n_i}$ is equal to that of $k_n.\mathbf{P}\text{^}(\mathbf{n_i}\text{^}\mathbf{P_i})$ and the error in φ caused by calculating **Z** from $\mathbf{n_i}$ instead of $\mathbf{P}\text{^}(\mathbf{n_i}\text{^}\mathbf{P_i})$ can be found geometrically using cosine and sine rules. Equation 5.2 shows the relationship between $\delta\varphi$ and φ. The dependence of $\delta\varphi$ on φ is graphed in figure 5.6.

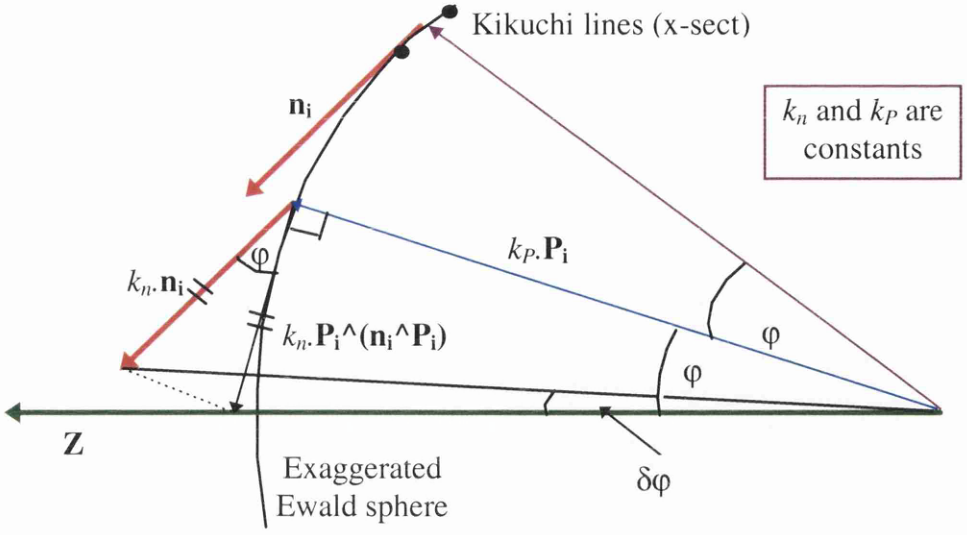

Figure 5.5: *An exaggerated diagram showing how using a Kikuchi normal, $\mathbf{n}_i$, close to $\mathbf{P}_i$ rather than the projection of $\mathbf{n}_i$ $\perp^r$ to $\mathbf{P}_i$ can create an error $\delta\varphi$ in* **Z**. *The angle φ determines the ratio of the lengths of $k_n.\mathbf{P}_i\wedge(\mathbf{n}_i\wedge\mathbf{P}_i)$ and $k_P.\mathbf{P}_i$*

$$\sin(\delta\varphi) = \frac{2\sin(\varphi/2).\sin(180-3\varphi/2)}{\sqrt{4\sin^2(\varphi/2)+1/\sin(\varphi)-4\sin(\varphi/2).\cos(180-3\varphi/2)/\sin(\varphi)}} \qquad [5.2]$$

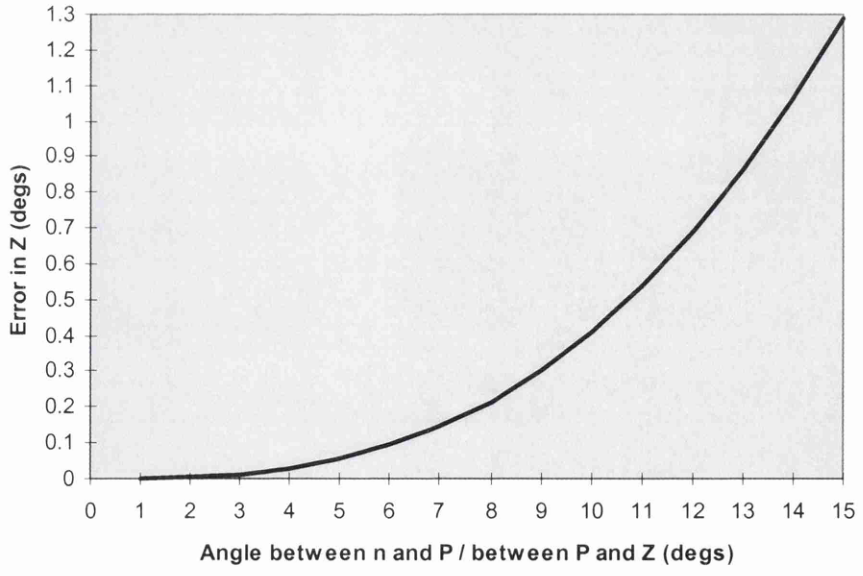

Figure 5.6: *Graph showing the expected error in* **Z**, *$\delta\varphi$, as a function of the angle between* **n** *and* **P** *(also the angle between* **P** *and* **Z**)

It is clear from figure 5.6 that only when both the angle between $\mathbf{n}_i$ and $\mathbf{P}_i$, and that between $\mathbf{P}_i$ and $\mathbf{Z}$, are >10° is the error in using $\mathbf{n}_i$ appreciable, i.e. >0.5°. If this is the case then $\mathbf{n}_i$ should be replaced with $\mathbf{P}_i\text{^}(\mathbf{n}_i\text{^}\mathbf{P}_i)$ which is the projection of $\mathbf{n}_i$ perpendicular to $\mathbf{P}$, to compensate for the curvature in the Ewald sphere. Fortunately, in all of the patterns examined here, the angular scale of the whole pattern is <10° so $\mathbf{n}_i$ can be used as in equation 5.1b. Here, however, this factor is included in the following calculations for maximum accuracy.

With the zone axis being determined directly from the Kikuchi map or by using equations 5.1a and 5.1b, all that is required to determine the grain orientation is the surface normal direction and any other known direction on the pattern. Figure 5.7 shows the geometry of the vectors concerned in determining this direction on the Kikuchi pattern of a grain.

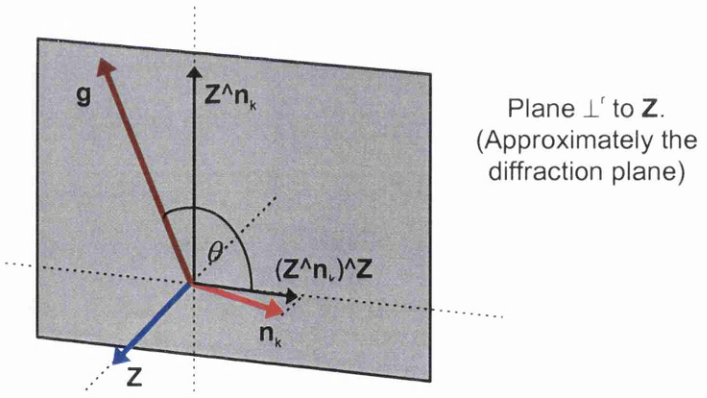

Figure 5.7: *The geometry involved in determining the orientation, **g**, from **Z** and $\boldsymbol{n}_k$ on the Kikuchi pattern. $(\mathbf{Z}\text{^}\boldsymbol{n}_k)\text{^}\mathbf{Z}$ is the projection of $\boldsymbol{n}_k$ onto the plane perpendicular to **Z***

Typically, the normal to a Kikuchi line, $\mathbf{n}_k$, (normally chosen as one of $\mathbf{n}_a$ or $\mathbf{n}_i$) is used in the calculation, however, this vector is seldom found to be exactly perpendicular to the zone axis. Again, due to the curvature of the Ewald sphere, this vector should be modified to be perpendicular to **Z**. In a similar way as in the calculation of **Z**, the projection of $\mathbf{n}_k$ onto this plane is given by $(\mathbf{Z}\text{^}\mathbf{n}_k)\text{^}\mathbf{Z}$. The surface normal direction is

known from a diffraction pattern of the substrate and the angle, θ, between it and $\mathbf{n}_k$ can be measured with a protractor. Referring to figure 5.7, the orientation, **g**, is given by equation 5.3.

$$\mathbf{g} = (\mathbf{Z}\hat{}\mathbf{n}_k)\sin\theta + \left[(\mathbf{Z}\hat{}\mathbf{n}_k)\hat{}\,\mathbf{Z}\right]\cos\theta \qquad [5.3]$$

Clearly, performing this analysis on each individual Kikuchi pattern could be very tedious and time consuming. To reduce the time of analysis, a spreadsheet is used to calculate the grain orientation from each pattern. The number of parameters recorded for each pattern ranged from 3 to 6, depending on whether the zone axis has to be calculated from an approximate pole. These are: φ_1, φ_2, $\mathbf{n}_a$, $\mathbf{n}_i$, $\mathbf{P}_a$ and θ. For an estimation of **g**, only the last three parameters are required with $\mathbf{P}_a$=**Z**. On gaining familiarity with the layout of the Kikuchi map for Si, the analysis time for each pattern reduces to ≈2-3min. The orientation, calculated by the spreadsheet using the equations above, can be quite difficult to interpret, e.g. **g**=[11.4,-0.03, 45.1]. However, the user would input one or two approximations, to this orientation and the spreadsheet is made to calculate the angle between them. For this example, **g**≈[1,0,4], giving a discrepancy of 0.4°. A error of <2° is accepted here but becomes a contribution to the final error in the orientation. The approximation to a low-index vector is only performed for clarity in the listing of orientations and could be avoided when representing the orientations on a stereographic projection (see later) if higher accuracy is required. An extract from the Excel spreadsheet is given in table 5.2. Appendix A shows the complete spreadsheet.

Table 5.2: *Excerpt from spreadsheet used to calculate the grain orientation*

Film No		***Pole,* Z**		***Kikuchi normal,* n**	***θ***	***Orientation,* g**	***Error* (°)**
72	(-1	1.6	2.4)	(-1,1,-1)	-6	(-5,4,-5)	2.0
74	(1	3	3)	(0,-4,-4)	49	(-4,-2,3)	2.4
75	(-1	1.3	1.1)	(-3,-1,-1)	-12	(-9,-5,-2)	1.0
76	(-1	6.5	16)	(-1,0,0)	-41	(-7,-6,2)	1.0
79	(-1	6	7)	(-1,0,0)	-40	(-4,-3,2)	1.7
81	(-2	3	3)	(0,-4,4)	41	(-3,-4,2)	3.0
83	(-1	2	20)	(-4,-4,0)	20	(-2,-1,0)	1.7

The spreadsheet produces an orientation and its associated error for each grain examined. The error is a combination of the error in determining **Z**, φ_1, φ_2, θ, and in approximating **g** to a lower-index vector. The error in the first four parameters can be improved using a higher camera length and there is typically an error in each of ≤1°. The resulting error in the determined orientation is ≤3°.

5.4.4 Representation of the Orientation Distribution

At this stage it is possible to list the frequency of the occurrence of each orientation, but it is much more informative to visualise how these vectors relate to each other to identify any clustering of orientations. The normal way to represent a set of vectors is to convert the 3-dimensional coordinates into 2 angular coordinates. From here, the orientations can be displayed on a 2D graph called a stereographic projection, or a Wulff net[12]. The Wulff net is shown in figure 5.8a with the coordinates, Φ and Θ shown. The angles Φ and Θ are calculated from $\mathbf{g}=(g_x, g_y, g_z)$, as given by equation 5.4.

$$\tan\Theta = \frac{\mathbf{g}_y}{\mathbf{g}_z} \quad \text{and} \quad \tan\Phi = \frac{\mathbf{g}_x}{\sqrt{\mathbf{g}_y^2 + \mathbf{g}_z^2}} \qquad [5.4]$$

The angles Φ and Θ are not the polar angles of the vector **g**. The angle Θ describes the tilt angle of the plane of the great circle whose tilt axis is the x-axis in figure 5.8a. The angle Φ describes the angle around this great circle from the y-axis. The nature of these angles are shown in figure 5.8b. There are variations on the interpretation of the angles used when representing vectors in a stereographic projection[13], but this approach is chosen for its relative simplicity. The approach normally adopted in the literature uses arc lengths along two or three great circles from known vectors (i.e. [001], [010] and [100]) to determine the position of an orientation on the projection[14].

The angles Φ and Θ are not orthogonal in the projection. Rather than manually plotting the vectors on a trace of a Wulff net according to their polar angles, it would be more

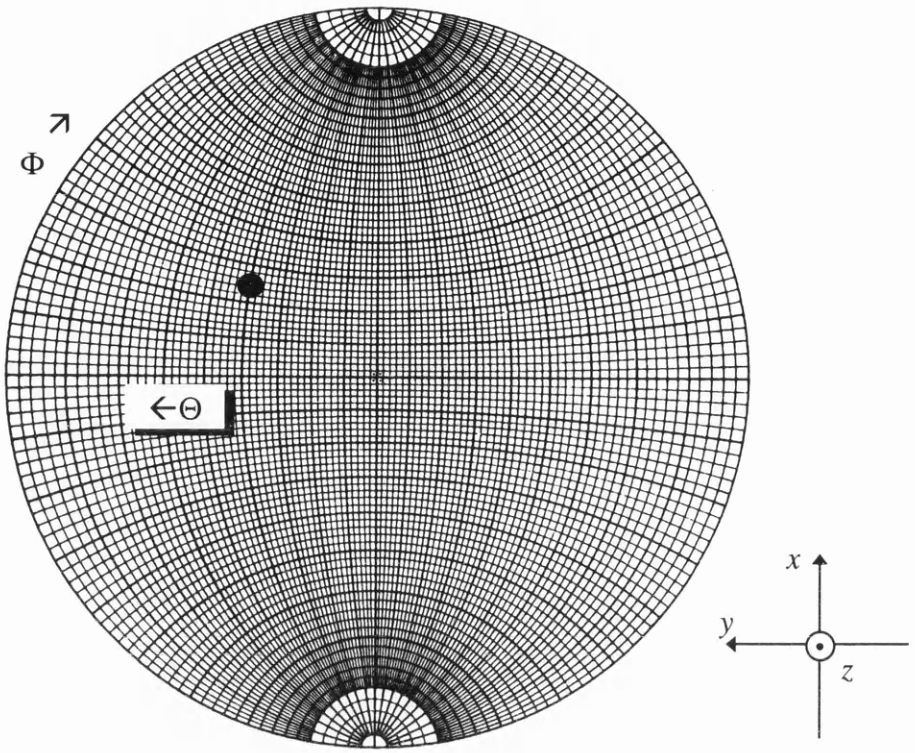

Figure 5.8a: *The Wulff net used to visualise the grain orientations in 2D. The gridlines are separated by 2° in Φ and Θ. The spot corresponds to* **g** *in figure 5.8b*

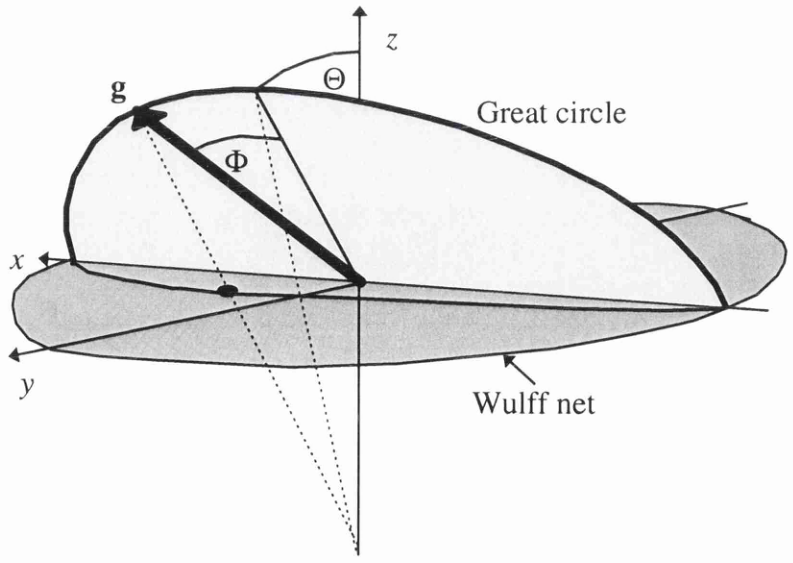

Figure 5.8b: *Diagram showing the relation between the vector angles Θ and Φ, and* **g** *for the representation of* **g** *on the Wulff net*

efficient to determine the x and y coordinates of the projection of **g** on the Wulff net. This enables a fully automatic representation of the orientation distribution. The geometry used in this type of stereographic projection is shown in figure 5.9[9],[15].

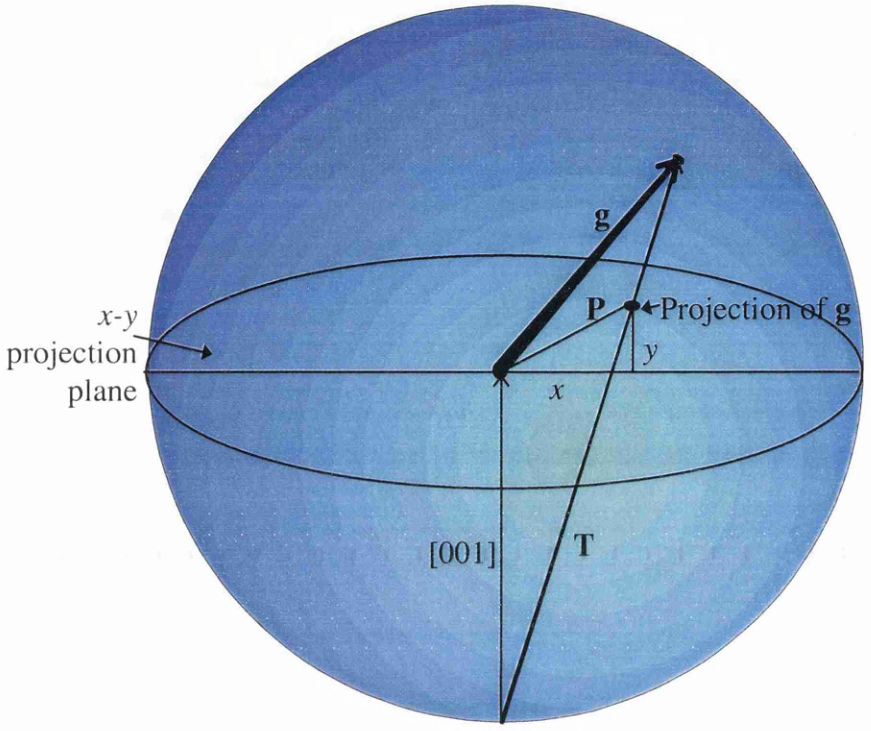

Figure 5.9: *The principle behind a common type of stereographic projection*

From figure 5.9, **T**=(g_x, g_y, g_z+1). Being perpendicular to (001), the projection vector, **P**=(x,y,0). Therefore equation 5.5 can be used to calculate x and y.

$$(0,0,1) + (x,y,0) = k.(g_x, g_y, g_z+1) \Rightarrow k = \frac{1}{g_z + 1} \qquad [5.5a]$$

$$\Rightarrow x = \frac{g_x}{g_z + 1} \quad \text{and} \quad y = \frac{g_y}{g_z + 1} \qquad [5.5b]$$

Here k is a constant and **g** is a unit vector. Normally, the symmetry of the crystal structure of a material allows the distribution of orientations to be confined to a localised section of the whole Wulff net. For the Si studied here, it can be shown that,

due to its symmetry (Si has 4 triad axes), every orientation can be represented by the sector shown in figure 5.10 where $0° \leq \Phi \leq 35.3°$ and $0° \leq \Theta \leq 45°$. This is a result of there being no physical difference between orientations having different permutations or signs of the same indices. The vectors corresponding to this sector are described by indices of non-decreasing values from left to right, e.g. [012], [234], [011], etc. To plot the

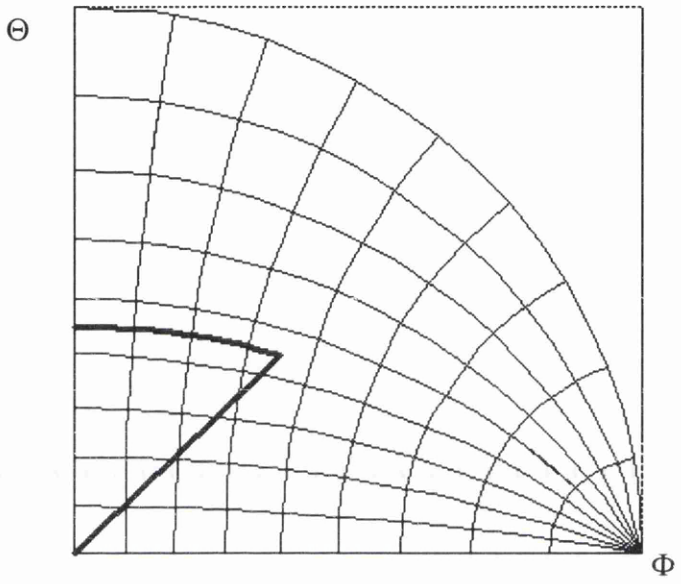

Figure 5.10: *The cubic nature of Si allows all the orientations to be confined to the sector shown within the heavy lines*

gridlines in figure 5.10 as a function of Φ, the polar coordinates for a fixed Φ and $0° \leq \Theta \leq 90°$ are converted into unit vectors and equation 5.5b is used to determine the orthogonal x and y values for these vectors. The same method is used for Θ. The outer limits of the curved triangle in figure 5.10 are given by equation 5.6, where 5.6c is calculated using equation 5.5b and noting that $g_x^2+g_y^2+g_z^2=1$ with $g_y=g_z$. So each point in figure 5.10 is plotted according to its x and y values, but the overlying grid describes its Φ and Θ components.

$$x = 0, \quad y = x, \text{ and } y = \sqrt{\frac{1-x^2}{2}} \qquad [5.6a,b,c]$$

5.4.5 Results

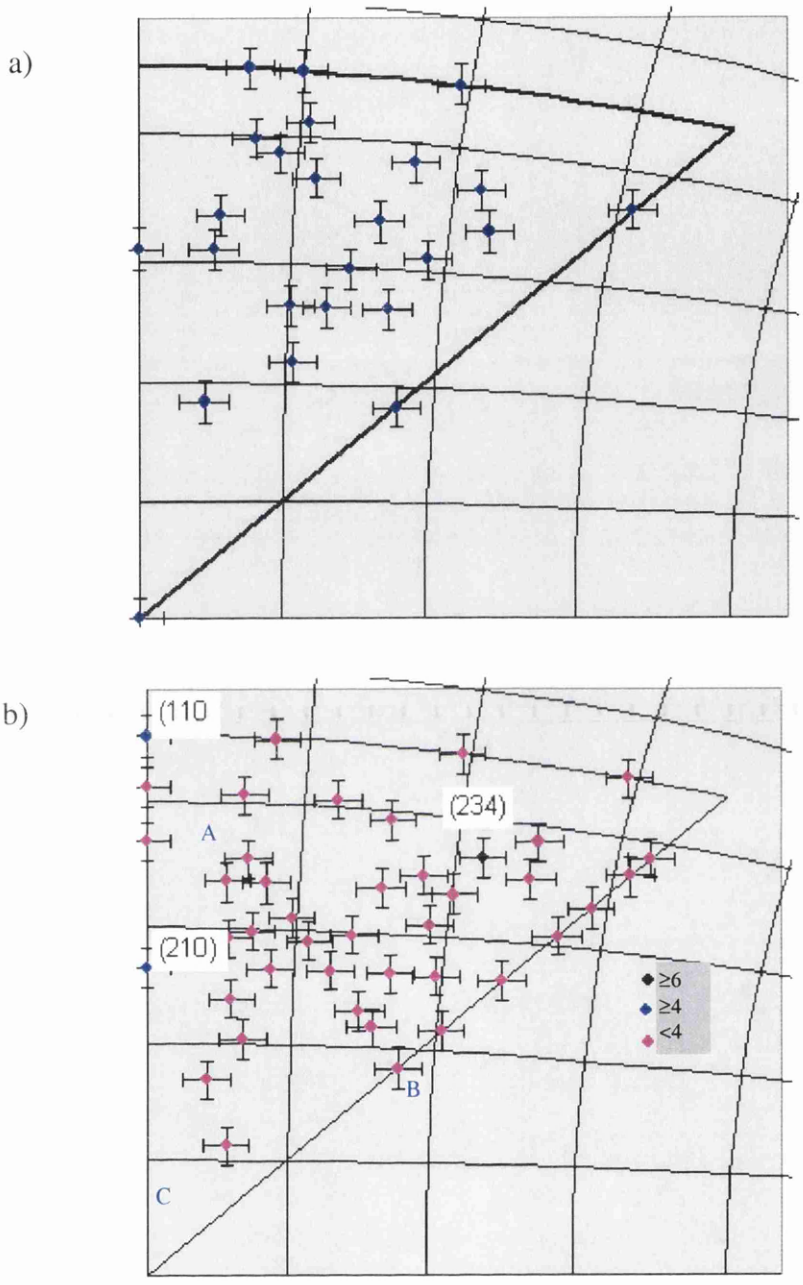

Figure 5.11: *Stereographic projection for the poly 1 (a) and poly 2 (b) grain orientations. Note the high density region from A to B, and the low density region from A to C, cf, figure 5.13*

Figures 5.11a and 5.11b show the orientation distribution for poly 1 and poly 2 respectively. For poly 1, orientations were determined for 32 grains and 60 were measured for poly 2. The error in each orientation is <3° and is mainly due to the

conversion of **g** to a low-index vector. To help identify the presence of preferred orientations, the charts in figure 5.12 highlight the most frequently occurring orientations. Figures 5.10 and 5.11 illustrate the absence of any significant POs in both films, although <234>, <011> and <012> orientations do appear slightly more often than the others in poly 2. This could be attributed to random error, but it could suggest that these orientations are slightly more abundant. Their significance is, however, not appreciable and the properties of the film will be similar to that of one which is completely randomly oriented. There is not even any clustering of orientations within the sector describing all the possible orientations. The results strongly suggest that the films are essentially randomly oriented.

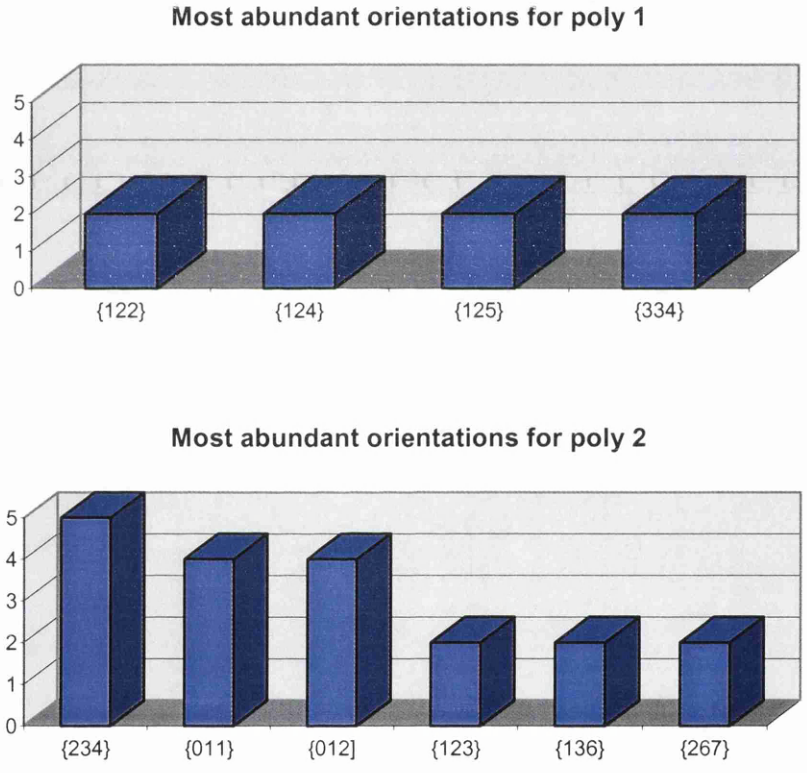

Figure 5.12: *Histogram of the most abundant orientations for both films. The graphs indicate the absence of any significant POs.*

One might be tempted to scale the frequency of the orientations shown in figure 5.12 according to their multiplicity to compensate for the orientations whose indices are less likely to appear. For example, in a completely randomly oriented sample, there will be

more <123> orientations than <100> ones. However, the fact remains, in this example, that there *are* more grains oriented in the [123] direction than in the [100] direction. Representing the orientations in low-integer indices constricts the distribution of orientations as shown in figure 5.13 for the maximum integer being 5, 10 and 15 respectively. Here, 4000 vectors having random indices up to the maximum integer are plotted. Not all the possible vectors are plotted for the maximum integer of 10 or 15, but the sparsely and intensely populated regions within the sector are clear. This has to be borne in mind when evaluating any clustering of orientations. For example, there is both the characteristic sparsely populated band up the left hand side of the sector and the highly populated band coming from A to B on figure 5.11b.

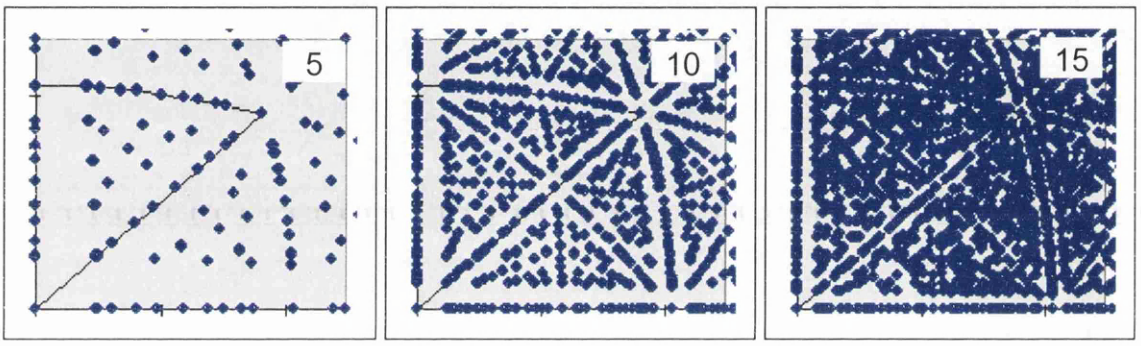

Figure 5.13: *4000 random vectors having a maximum index of 5, 10 and 15. This highlights the distribution of possible* ***g*** *vectors lying within the sector used*

5.4.6 Summary & Discussion

In this experiment, the electron beam was focused onto tens of large grains in two polySi films and the resulting Kikuchi diffraction patterns are analysed to determine the grain orientation. Both films are shown to have no significant POs and are most likely to be completely randomly oriented as no clustering was observed. The experimentation takes around one hour for 50 grains, then, once the analysis is constructed, the determination of the orientations takes ≈3-5mins in total per grain. The orientation distribution of ≈20 grains may be enough to identify whether POs exist or if the film is

randomly oriented. However >500 measurements are required to quantify the orientations accurately.

The benefits of this technique are that every PO present is clear from the stereographic projection and accurate quantitative information is possible. The error in each orientation is typically ≈2-3° but can be as small as ½° if measurements are taken very accurately and the orientations are not approximated to integer indices. There is the possibility of relating grain size with orientation, or comparing the orientations at the top and bottom of a film. The spatial resolution is much less than selected area diffraction and can reach ≈5nm.

The main drawback of this technique is the lengthy time scale required to obtain the orientation distribution, and the repetitiveness of the analysis. A good familiarity with Si Kikuchi maps is also necessary to reduce the time scale significantly. Once the method of analysis is set up, the manual Kikuchi technique can successfully identify the presence of POs in several hours.

5.5 Identification of POs using a Scanning Technique

5.5.1 Introduction

The Kikuchi method of determining POs is not time-efficient when a large number of grains are investigated. The new technique described here involves scanning a focused probe in a raster across an area on a film in cross-section. The resulting diffraction pattern is used to identify the presence of POs. Like the Kikuchi method, the accuracy of this technique depends on the number of grains included in the scan. In the texture analysis in chapter 6, the diffraction pattern is analysed more closely to enable a quantitative description of the POs present. In this section, however, the diffraction pattern is observed purely to determine whether POs exist and what is their direction.

5.5.2 Technique

For this technique, the microscope is first aligned in the standard STEM mode whereby a diffraction pattern from the area scanned is observed on the viewing screen. The beam pivot points are aligned to maintain a stationary diffraction pattern throughout the scan. During the pivot point alignment, the objective alignment coils are wobbled to vibrate the beam. The objective aperture is focused onto the diffraction plane and the pivot points are adjusted to stop the central diffraction spot vibrating. This way the pivot points are aligned to the objective aperture. A more accurate method involves observation of a scanned image of a diffraction grating while the beam is wobbled. The pivot points are adjusted to obtain an orthogonal image of the grating. The latter technique is much more difficult and, for most camera lengths, is not necessary.

In the technique, information on the POs is obtained from the diffraction pattern and its resolution depends on the convergence angle of the probe on the specimen. Under normal operation in STEM, the convergence angle is too large for accurate analysis even with the smallest C2 aperture (see table 2.1 for values). To reduce the convergence, the C2 strength is increased and the upper objective strength is decreased while maintaining a focused probe on the specimen. This set up is shown in figure 5.14. A good way to

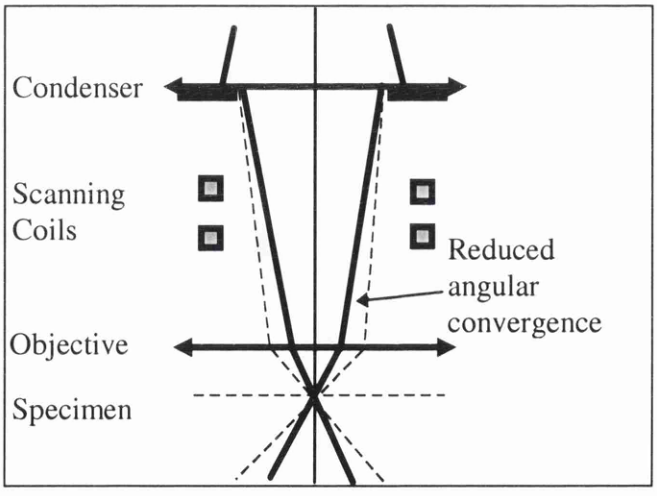

Figure 5.14: *Diagram showing the upper column configuration for reduced angular convergence*

achieve this configuration is to reduce the current (which is normally ≈4500mA) in the objective lens by ≈300-400mA. While looking at the scanning image, the C2 strength is increased until the beam is focused back on the specimen. Observing the diffraction pattern on the viewing screen shows that the diameters of the diffraction discs from a crystalline material have reduced by a factor of ≈3-4. Subsequently, the spatial resolution is sacrificed at the expense of the improved angular resolution. However, the spatial resolution is of lesser importance in this case.

For maximum accuracy in examining the diffraction pattern, in particular for the analysis shown in chapter 6, the astigmatism in the diffraction lens should be minimised. Perhaps the best way to do this is to insert an objective aperture while the beam has stopped scanning. Only the unscattered beam is visible. The beam is spread to produce parallel illumination on the specimen to obtain a fine spot on the diffraction plane. The aperture is then brought close to this spot until it is almost touching it. The diffraction focus is adjusted to under-focus the diffracted beam. Then the beam x-y shifts are used to slowly bring the beam onto the edge of the aperture. At the edge of the

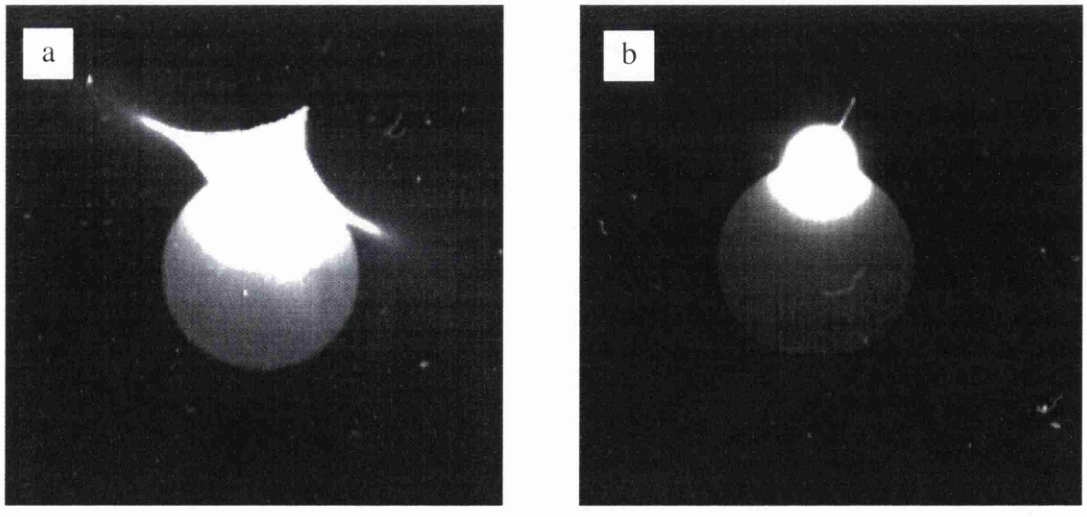

Figure 5.15: *When the objective aperture cuts the beam and the diffraction focus is defocused, any diffraction astigmatism is characterised by a caustic (a). The corrected stigmation is shown in b)*

aperture the spot has two shadows: an elliptical one arising from the beam being defocused, and a 4-pointed caustic arising from any diffraction astigmatism. An

example of this is shown in figure 5.15. The latter cannot normally be observed without defocusing. The diffraction stigmation is adjusted to remove the caustic, leaving a circular shadow (figure 5.15b) which reduces as the diffraction plane is focused again.

With the microscope aligned, the area to be scanned is defined by the operator. Normally this area should cover as much of a film as possible to increase the number of grains which contribute to the diffraction pattern. The rectangular nature of the scan is ideally suited for cross-sectional analysis on films. Indeed, with the appropriate beam blanking facility, any shape of scan can be implemented. The same films are studied as before in section 5.4, and the typical areas scanned are shown in figure 5.16.

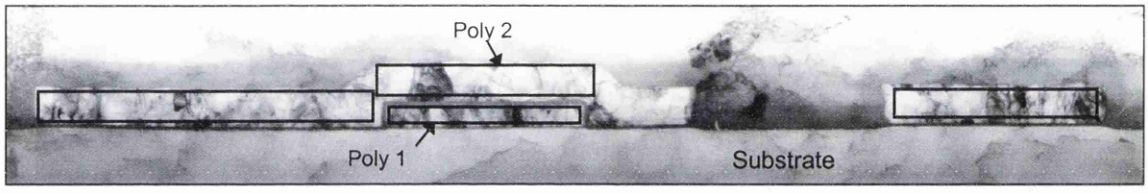

Figure 5.16: *Image showing the regions on each memory cell which are scanned to reveal the presence of POs*

As each area on the polySi is scanned, a photograph of the diffraction pattern is taken. The camera length should be adjusted to allow the first three or four order reflections to be present in the negative. In this case the camera length was 970mm on screen and 1100mm at the negative. The scan time for one complete scan is less than the exposure time to ensure all grains are included in the diffraction pattern. Typical scan times are ≈0.1s, and exposure times are ≈0.5s. An area on the substrate is scanned and the resulting diffraction pattern is used to determine the surface normal direction in the diffraction plane.

5.5.3 Results

Figures 5.17a and 5.17b show examples of diffraction patterns from regions of poly 1 and poly 2 respectively. Due to the larger grain sizes in poly 2, the scan covers a smaller number of grains reducing the amount of information available in the diffraction pattern.

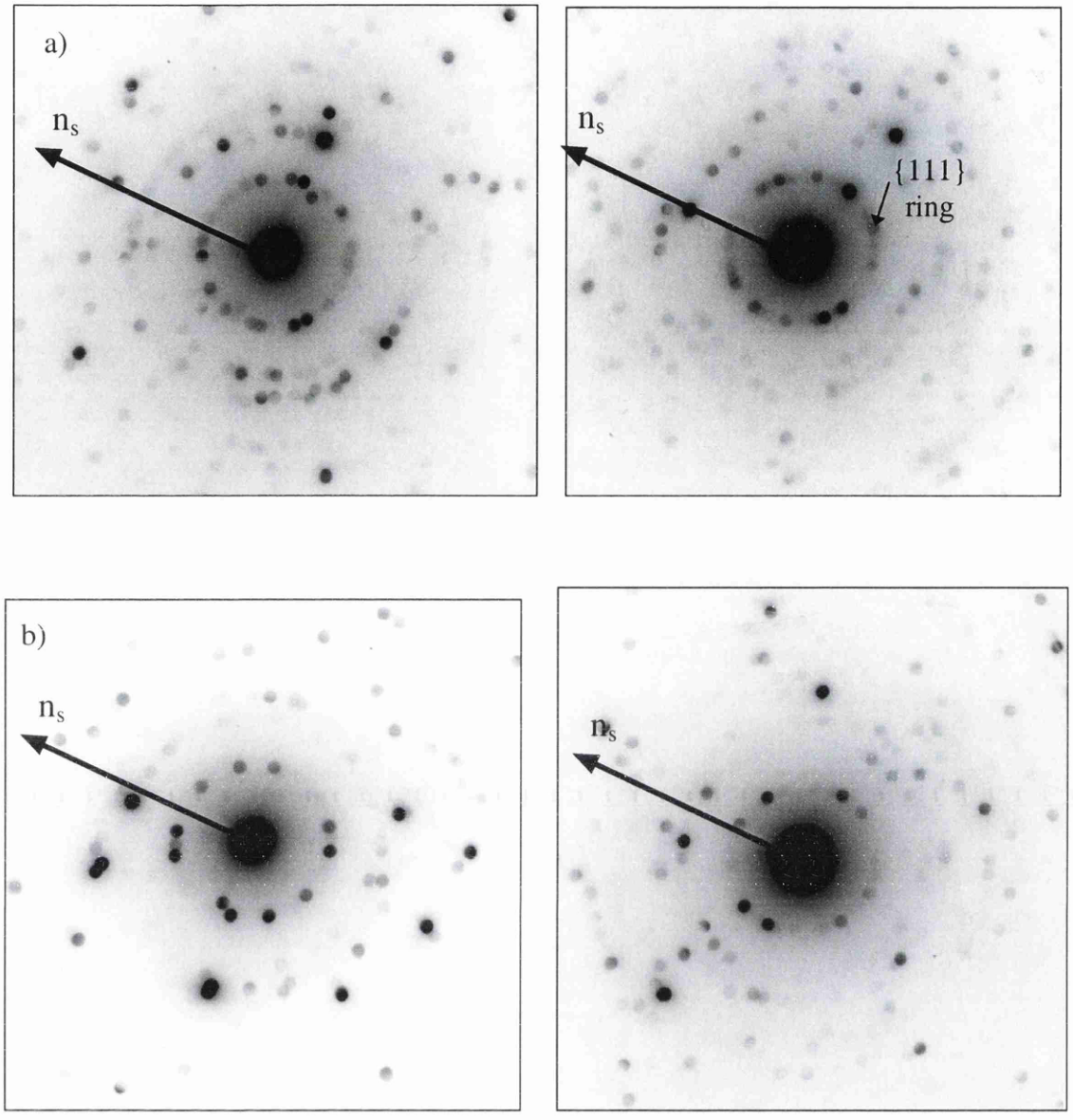

Figure 5.17: *Two examples of the diffraction patterns for a) poly 1 and b) poly 2. Superimposed is the surface normal direction ,* $\boldsymbol{n}_s$

The length of the scan is limited by the fact that the structures investigated are isolated. For isolated structures, beam blanking would allow for more grains to be included in the scan, but since this is not an option currently available, the diffraction patterns from four poly 2 regions are manually superimposed to improve the accuracy of the results. The superposition is shown in figure 5.18.

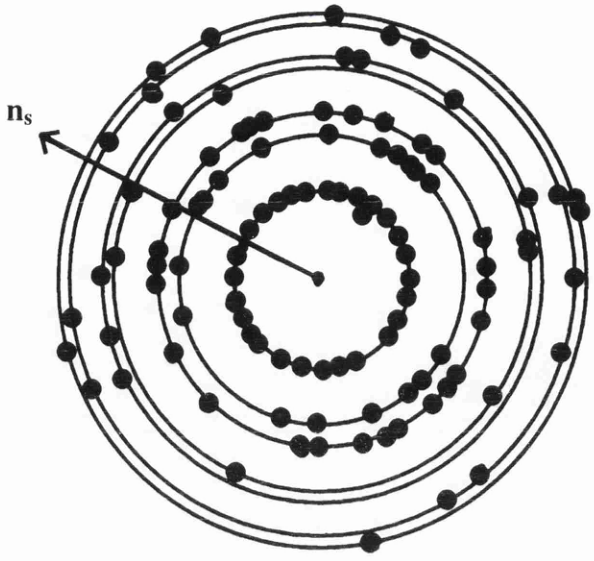

Figure 5.18: *Four diffraction patterns superimposed highlighting the random nature of the poly 2 grain orientations*

It is clear from figures 5.17a and 5.18 that the distribution of spots are approaching rings. It is likely that, given more grains in the scan, the diffraction pattern would consist of complete rings. This suggests the presence of randomly oriented grains in both poly 1 and poly 2, which is in accordance with the results from the Kikuchi pattern analysis as before. If appreciable POs existed, the distribution around the rings would be non-uniform as reflections would become localised in certain directions relative to the surface normal. It is also likely that there would be a high degree of symmetry about the surface normal direction if the POs were distributed uniformly around this direction. Figure 5.19 shows the theoretical distribution of reflections for grains having POs, **G**=[011], [001], [012] and [234], as these orientations were either marginally more abundant in poly 2 (as shown by the Kikuchi method) or are commonly observed polySi POs (shown in table 5.1). To calculate the positions of the spots, the possible reflections, **r**, (not necessarily a unit vector) are identified first, e.g. {111}, {220}, {311}, etc. Then the angle, ϑ, between each reflection is calculated using equation 5.7a. Knowing the length of the reflection ($L=\sqrt{h^2+k^2+l^2}$), its x and y co-ordinates (equation 5.7b) are plotted on the graph where **G** is the y axis.

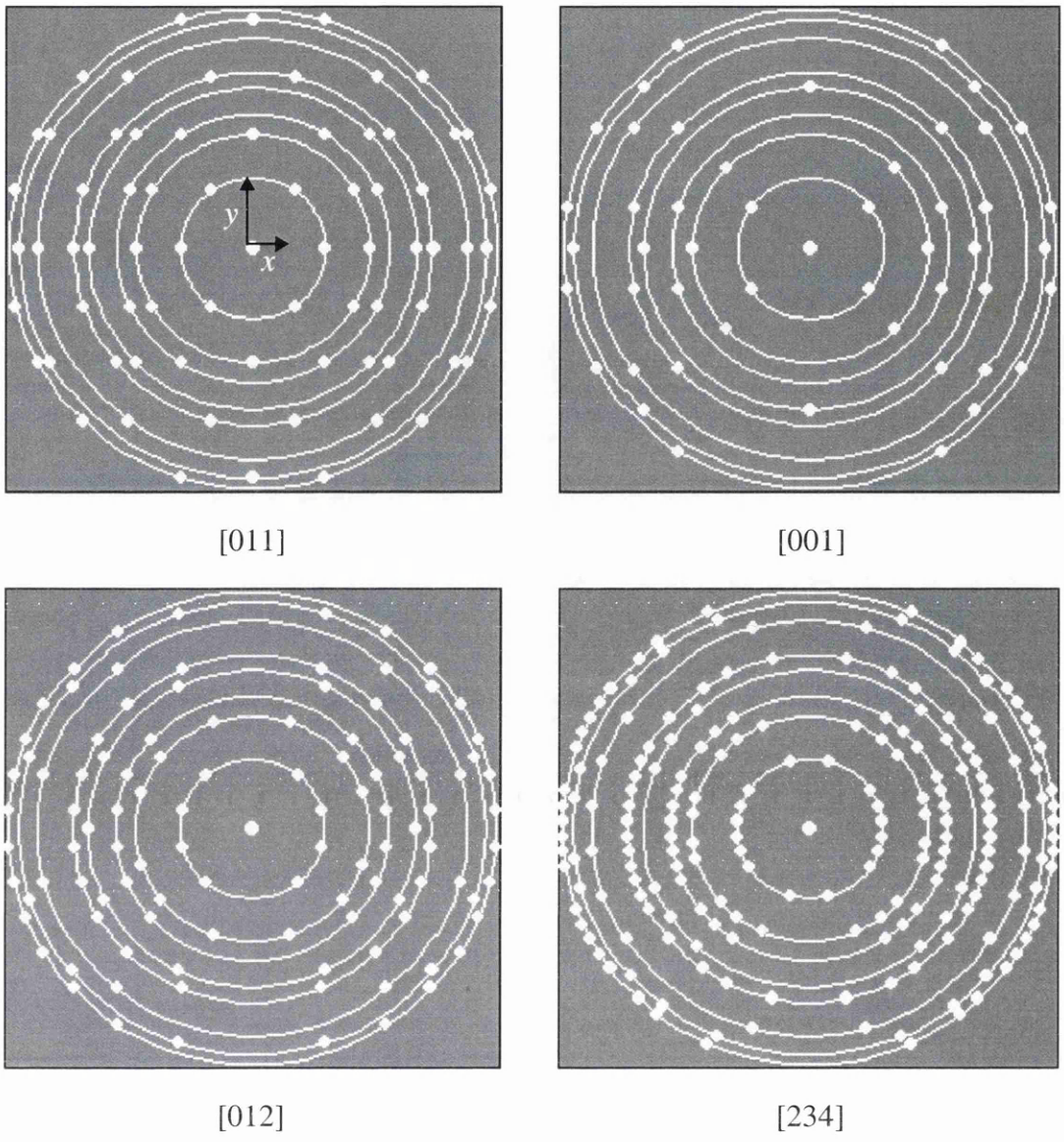

Figure 5.19: *Theoretical diffraction patterns for films having grains oriented in the PO as indicated*

$$\cos\vartheta = \frac{\mathbf{G}.\mathbf{r}}{|\mathbf{G}||\mathbf{r}|} \qquad [5.7a]$$

$$x = L_{hkl}\cos\vartheta \quad \text{and} \quad y = L_{hkl}\sin\vartheta \qquad [5.7b]$$

The (000) spot at the centre of the diffraction pattern corresponds to (x, y)=(0, 0). Comparing the diffraction patterns to those in figure 5.19, it is clear that there is no sparsely populated band along the surface normal direction or any indication of

symmetry in the patterns from both films. This reinforces the idea of the films having randomly oriented grains. Greater attention is given to the determination of the distribution of orientations from such diffraction patterns in chapter 6.

5.5.4 Discussion & Comparison

In this technique, a probe is scanned across a region on a film in cross-section and the resultant diffraction pattern is used to identify the existence of POs. The resolution in the diffraction pattern is improved to provide a more accurate description of the distribution of grain orientations. This is achieved by reducing the convergence angle of the probe using the condenser and objective lenses. The positions of the spots in the diffraction pattern are compared to those in theoretical patterns for various POs. If the positions are similar and the same symmetry exists, then POs exist and have the direction given by the theoretical pattern. If the reflections have uniform intensity around a ring or they have no symmetry about the surface normal direction, then the grains are randomly oriented and the existence of any POs is insignificant. It should be noted that a diffraction pattern may contain both rings and more intense regions which are symmetrical about the surface normal direction. In this case, only a fraction of the grains are oriented in the preferred orientation. This fraction can be determined using the analysis given in chapter 6. The time taken for the experimentation is ≈2mins per scan, after an initial ≈30min microscope set-up. This implies that, for a continuous film, the experimentation time could be as little as ≈30min. The time to examine each diffraction pattern is 2-10min depending on the complexity of the pattern. In fact, considering all the other TEM techniques mentioned in section 5.4, this can provide the quickest means of identifying the presence of POs in device thin-films.

There are distinct differences between the two diffraction techniques described in this chapter. The Kikuchi method can produce much more quantitative information on the exact distribution of grain orientations. However, the severe drawback is the large amount of experimental and analytical time required to obtain the distribution. The scanning technique offers a very quick method of identifying the presence of POs,

however the quantitative description of the distribution of grain orientations is not immediately deducible. This technique can be shown to produce very quantitative information when analysing the diffraction pattern from many grains as shown in chapter 6. The scanning technique requires more grains to be analysed than the Kikuchi method owing to the fact that not every grain contributes reflections in the inner rings in the diffraction pattern. In fact, to identify the presence of POs, it is shown in chapter 6 that as much as a thousand or more grains may be required. This is not the case for the Kikuchi technique where as little as ≈50 grains, or less, could conclusively identify POs as any clustering of orientations would be easily identified. Due to the versatility of the Kikuchi method, the orientations of selected grains can be found. These may include grains which grow or shrink laterally or grains which have a curved surface, thereby increasing the surface roughness. An example is shown in figure 5.20 where information on the grain orientation would be difficult to obtain by any planar means due to the shallow depth of the grain. It also can be used where the shape of a film, or cluster of grains, are not suitable for the rectangular nature of the scanning technique. Fortunately, the shape of films in cross-section are normally compatible with the rectangular selected area in the scanning technique. Frequently, there are regions on a device which contain the film of interest in a continuous form, as opposed to the isolated structures investigated here. In this case, there may be many grains included in the scan allowing more quantitative and conclusive results.

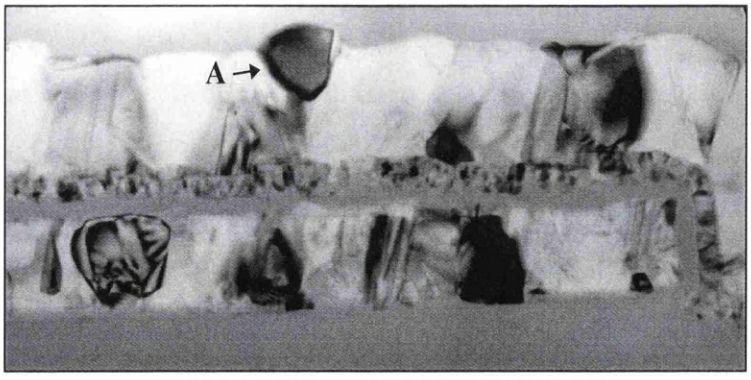

Figure 5.20: *The Kikuchi technique allows for the determination of individual orientations of grains, e.g. for those with unusually high growth rates, as at* ***A***

There is another fundamental difference between the results possible from each technique. The orientation distribution from the Kikuchi method is in terms of the number of grains, whereas, that of the scanning technique is in terms of the volume of grains. The ultimate aim of these, and similar, techniques is to predict the physical properties of a film using the description of its orientations. The question is whether the number fraction or volume fraction of grains in a PO more accurately describes the film properties. For columnar growth, as described in chapter 4, the grain sizes are not significantly affected by their orientation. Thus, with many grains investigated, both approaches will give very similar results[16]. However, in near-columnar growth, the POs grow laterally, and the other grains will shrink. Thus the number fraction of grains oriented in the PO will be less than the volume fraction of grains because the PO grains are larger. The physical properties of the film mainly depend on the density of grain boundaries so it may be more appropriate to describe the distribution of orientations according to the number fraction of grains. This way, the smaller grains have as much weight on the result as the larger grains, which is probably more appropriate in influencing the electrical properties. A simple way of visualising this is to consider two sets of two adjacent grains having the same total width as shown in figure 5.21.

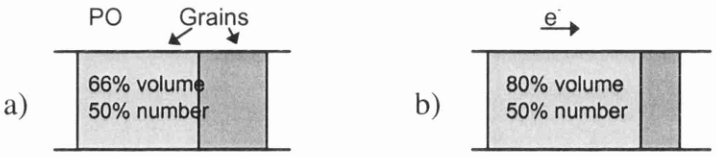

Figure 5.21: *Diagram showing that the number fraction of grains, not the volume fraction, affects the electronic properties. Both films have the same number of grain boundaries, and only the number fraction of a PO reflects this*

In the first case, the LHS grain is twice the size of the other, and, in the second case, it is four times the size of the other. In the first instance the volume fraction of the larger grain is 67% whereas it is 80% for the second case. However the number fraction for both cases is 50%. The electrical properties depend on the number of grain boundaries crossed by the electrons. Both cases have an equal number of grain boundaries so both should have the same electrical properties. Only the grain distribution described by the number fraction agrees with this test. It must be noted that this situation was the worst

case scenario. Often the smaller grains do not extend all the way through the film and the decision to take the number or volume fraction becomes unclear. This problem is not addressed in the literature, and perhaps the reason is that the solution depends on different grain structures or that, in reality, the difference between the results from both approaches is insignificant. It is likely to be a combination of the two. It is noted that for electromigration issues, using equation 4.1, which describes the mean lifetime of a metal interconnect, implies that the properties of the film depend on the volume fraction of orientations. This equation is empirical and is only an approximation, however, it may only be accurate for the normal columnar fcc grain structure.

References for Chapter 5

[1] C. R. M. Grovenor, *Microelectronic Materials,* IOP Publishing Ltd, (1989), 199

[2] S. Vaidya, A. K. Sinha, Thin Solid Films **75**, 3, (1981) 253

[3] S. Hasegawa, S. Yamamoto, and Y. Kurata, J. Electrochemical Soc., **137**, 11 (1990) 3666

[4] C. R. M. Grovenor, *Microelectronic Materials,* IOP Publishing Ltd, (1989), 239-243

[5] H. Kakinuma, J. Vac Sci Tech. A-Vac Surf. Films, **13**, 5 (1995) 2310

[6] S. A. Campbell, *The Science and Engineering of Microelectronic Fabrication,* New York, Oxford Univ. Press (1996) 412.

[7] A. van der Drift, Philips Res Repts, **22**, (1967) 267

[8] S. M. Sze, *VLSI Technology,* McGraw-Hill (1988) 233

[9] H. J. Bunge, Int. Mats. Revs., **32,** 6 (1987) 265

[10] R. A. Schwarzer, Textures & Microstructures, **20,** (1993) 7

[11] C. Vannuffel, J. Beaucour, J. P. André and J. P. Chevalier, Micro. Semi. Mater., *Inst. Phys. Conf. Ser. No 100,* (1989) 115

[12] F. C. Phillips, *An introduction to Crystallography,* Longmans, Green & Co Ltd (1963) 10

[13] J. W. Edington, *Electron Diffraction in the Electron Microscope*, MacMillan Press, (1975) 82

[14] B. D. Cullity, *Elements of X-ray Diffraction*, Addison-Wesley Pub, (1959) 60

[15] M. M. Wooflson, *An Introduction to X-ray Crystallography,* Cambridge Uni Press (1978) 5

[16] H. J. Bunge, *Experimental Techniques of Texture Analysis,* Deutsche Gesellschaft fur Metallkunde e.V, (1986), pp 1-12

CHAPTER SIX

The Development of the Degree of Texture through a Film

6.1 Introduction

Obtaining quantitative information on the texture of a conducting film is of considerable importance in silicon technology. As mentioned in chapter 5, many electrical and mechanical properties of a film are strongly influenced by the texture in the film. There are relatively few analytical techniques which can be used to investigate the texture of a film, let alone ones which can describe the texture quantitatively. In this chapter, the diffraction patterns from the scanning technique described in chapter 5 are analysed to obtain quantitative information on the texture of a polySi film. Due to the versatility of the technique, it is also possible to describe how the texture develops through the film. Scanning dark field imaging is then used to describe the mechanisms for texture development in the polySi film and to compare its quantitative results with the diffraction technique. Before this, a definition of the 'degree of texture' is given, as it is not immediately obvious and it does not seem to have been quantified so far in the literature. Existing techniques are also reviewed which determine the texture of a film, allowing comparison of the techniques described here.

6.2 Definition of the Degree of Texture

The texture of a polycrystalline, single-phase material is defined by the orientation distribution function (ODF) of the crystallites of which the material consists[1]. In

general this function is assumed to be the volume fraction of the crystallites having the orientation vector **g**,

$$\frac{dV(\mathbf{g})}{V} = f(\mathbf{g})d\mathbf{g} \qquad [6.1]$$

There are numerous ways of specifying **g**, but there are four standard approaches[2]. Firstly, **g** can be specified by the indices [*uvw*] of the crystal direction parallel to an external direction, e.g. the normal to the substrate surface. Secondly, it can be described by an orientation matrix where $\mathbf{g}=[g_{ij}]$, where $g_{ij}=\cos\langle x_i,x'_j\rangle$ and x_i is an axis of the crystal coordinate system with respect to the axis x'_j of the sample coordinate system. A third approach is to specify a rotation axis by spherical polar coordinates, Θ and Ψ, and the rotation angle, Ω, so that $\mathbf{g}=\{\Theta, \Psi, \Omega\}$. Finally, the Euler angles may be used where $\mathbf{g}=\{\varphi_1, \Phi, \varphi_2\}$. Each approach has its own advantages and disadvantages, hence all have been used in the description of textures. For pole figures, which are projections of the distribution of a particular grain orientation, Euler angles are most commonly used to describe texture and have the form of equation 6.2[2].

$$\frac{dV}{V} = f(\varphi_1,\Phi,\varphi_2)\frac{\sin\Phi}{8\pi^2}d\Phi d\varphi_1 d\varphi_2 \qquad [6.2]$$

The factor $\sin\Phi$ represents the size of the volume element in orientation space and the factor $8\pi^2$ takes care of the normalisation of the texture function for the random orientation density.

In device technology, it would be more helpful to describe the texture of a film by two or three variables rather than an ODF if there is only a little loss of information. This way, texture information could be more readily related to certain properties of a material, e.g. the conductivity may vary directly with one of these variables and inversely as another. Pole figures are not easily interpretable and their relation to the film properties is often obscure. Here, a definition of the 'degree of texture' is proposed as the fraction of a volume in a film which is oriented in the texture direction within the

a small angle known as the mosaic spread. The mosaic spread[3] of the grains is the width of the angular distribution of the orientations of a completely textured sample. It arises due to the spread in growth directions of the crystallites and is typically 3-4°. Besides the texture direction and the degree of texture, the mosaic spread must also be mentioned when describing the texture as it clearly affects the orientation distribution and is shown to affect the film properties[4]. It must be noted that, in some films, the ODF may be too complex to be characterised by three variables but this is unlikely to apply to device films such as silicon and aluminium. It is possible however to determine the degree of texture for various sub-textures, as shown later, but their relation to the properties of the film become more complex. On the other hand, it is unlikely that both the degree of texture and the mosaic spread can be described by a single variable as this will result in a significant loss of information and make the new definition difficult to interpret. In general most desirable properties of a material improve with a higher degree of texture, G, and a smaller mosaic spread, 2α, for a given texture direction[4].

6.3 Existing Techniques for Investigating Texture

6.3.1 Overview

The vast majority of techniques which investigate the texture of a material can be sub-divided into three categories depending on whether X-rays, neutrons or electrons are used. For the first two, the texture of a material is almost always described using pole figures[5], however, pole figures are used less commonly with electron techniques. X-ray pole figures are normally measured using a texture goniometer[6] such as the 'Eulerian cradle' shown schematically in figure 6.1. Here a detector is adjusted, either manually or by motor operation, to be at a Bragg angle, 2θ, with respect to the incident beam. Then the sample is rotated through at least two angles in order to make all sample directions successively parallel to the incident beam direction. The measured intensity

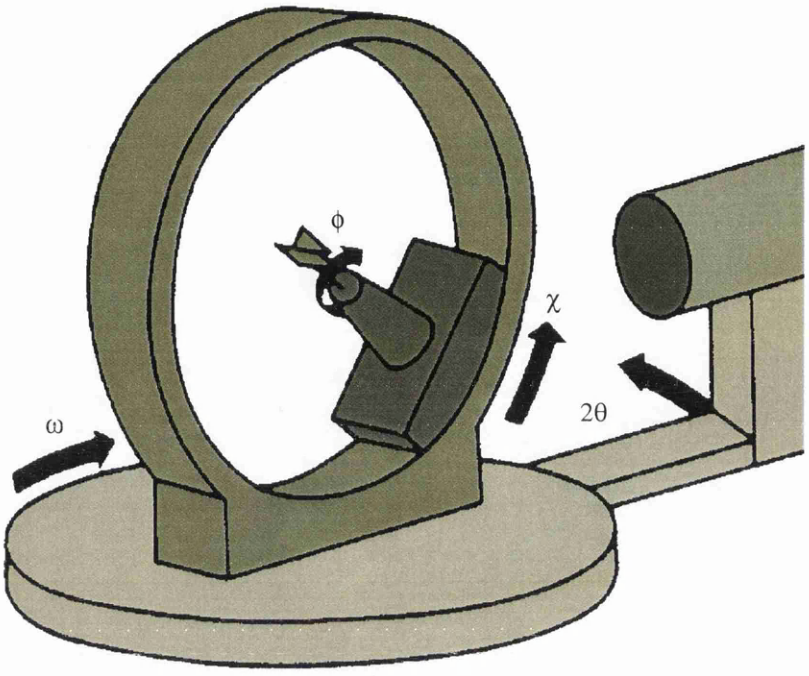

Figure 6.1: *The geometry of the Eulerian cradle as a texture goniometer*

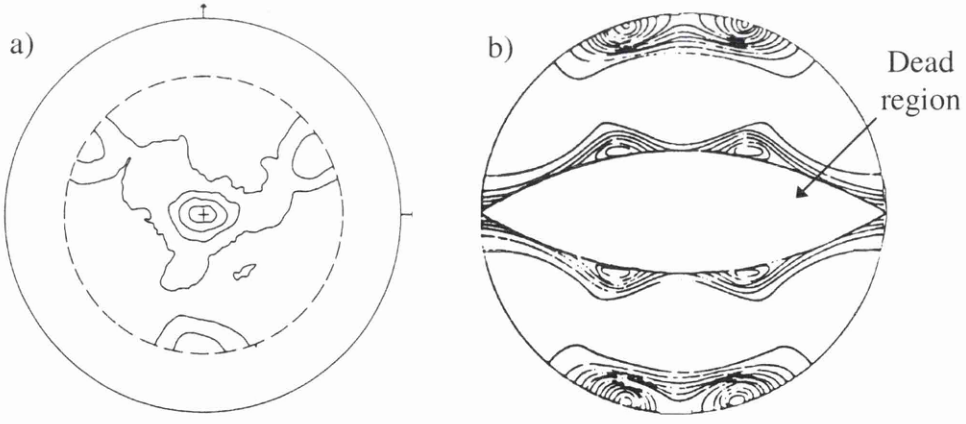

Figure 6.2: *An example of a) X-ray, and b) Electron, pole figure showing contour lines of certain reflections*

values are generally not yet pole density values. They have to be corrected for background scattering, absorption, defocalisation[2], and have to be normalised to multiples of the random distribution. A computer performs this task and the data can be plotted in the form of pole density charts in any desired projection. An example of a pole figure using x-ray or neutrons in is given in figure 6.2a[6], and the same using

electrons is given in 6.2b[2]. For the electron diffraction pole figure, the TEM is set up to measure the intensity around a diffraction ring while the specimen is tilted. This is achieved by either tilting the beam before the specimen, or deflecting the beam after the specimen, and placing a Faraday cup in the centre of the diffraction pattern. The lens-shape 'dead' regions found in the electron diffraction pole figure arise from the tilting of the specimen during the pole density measurements but can be reduced by rotating the specimen 90° and repeating. The stereographic projections, as shown in chapter 5, are effectively the inverse of the pole figure[2] in a similar way to inverse Fourier transforms.

For individual grain orientation determination, the resolution of X-ray techniques is >50μm, and is >1mm for normal pole figure determination[1]. The pole figures have an accuracy of ≈10% mainly due to the angular intensity corrections[2]. Neutrons only have a resolution of >1cm but larger samples can be used owing to the increased penetration depth. This is often preferable in practice. A higher statistical accuracy is obtained using neutrons because of the larger volume investigated and the absence of any angular-dependent scattering factor. The most serious disadvantages of neutron diffraction is its restricted availability due to its high cost and its inapplicability for use with small samples. Electron diffraction techniques have a much higher spatial resolution but dynamical scattering effects cause difficulties in correlating the measured intensity to the pole density. This problem can be solved satisfactorily by suitable calibration methods.

Clearly, the X-ray and neutron diffraction techniques are suitable only for single, continuous films covering a surface >1mm^2. This is never the case for modern devices and so only electron diffraction techniques can be useful in describing the texture of a film in a processed device. However the other techniques should not be discarded as the texture of stand-alone films can be investigated on a substrate using these techniques and the deposition conditions can be optimised before the device is processed. The main problem with this approach is that, often, the post-deposition heat cycles can alter the texture of a film during device fabrication.

6.3.2 Electron Diffraction Techniques

There are essentially four common techniques which can be used to determine texture quantitatively using electron diffraction. The first is the selected area diffraction (SAD) pole figure as described in the previous section. The second is to probe each grain individually as in chapter 5. The third is to use an adapted SEM and scan the beam slowly across the surface of the film and at each point the backscattered Kikuchi pattern is digitally acquired and processed to evaluate the crystal orientation[7],[8]. This fully-automatic technique can map the whole surface of the film according to its grain orientation and, consequently, the grain sizes. Here the beam energy and incidence angle can be adjusted to control the penetration depth of the electrons. The final method is the scanning diffraction technique described in chapter 5 and the quantitative analysis which is required to obtain quantitative information is explained in the remainder of this chapter.

Other electron microscopy techniques do exist, e.g. crystal orientation determined directly from high-resolution imaging[9], but are very seldom used since they are either difficult to perform or unsuitable for the majority of films. Table 6.1 outlines the merits and disadvantages of each type of existing electron diffraction technique.

Table 6.1: *Comparison of the three existing electron diffraction techniques*

Technique	*SAD pole figure*	*Individual grain orientation*	*SEM backscattering*
Spatial resolution	≈0.5μm	>5nm	>500nm
Angular resolution	≈0.2°	≈0.2°	1-2°
Experimental Time	≈2-5hrs	3-10hrs	≈10hrs (fully-automatic)
Comments	Produces dead regions	Time-consuming for high statistical accuracy	Unsuitable for non-columnar growth

6.3.3 Summary of Texture Techniques

Table 6.2[1] provides an overview of the existing analytical techniques which can quantify the texture of a film to some degree.

Table 6.2: *Overview of all texture techniques*[1]

	Neutrons	***X-rays***		***Electrons***	
		normal focus	micro focus	SAD	micro-diffraction
Penetration depth	≈1cm	10-100μm		≈100nm	
Lateral resolution	≈1cm	1mm	50μm	1μm	1nm
Price of equipment	high	low		medium	
Sample preparation	easy	medium		difficult	
Statistical accuracy	high (1%)	medium (10%)		medium(10%)	

6.4 Scanning Diffraction Texture Analysis

6.4.1 Experiment

In this experiment a textured polySi film is used to demonstrate how the scanning diffraction technique described in chapter 5 can be used to obtain quantitative information on the degree of texture of a film. The same microscope configuration is used to scan a region on a polySi film in cross-section. The upper column lens strengths are modified to reduce the angle of convergence of the beam as described before in figure 5.12. This improves the angular resolution in the diffraction pattern. The pivot points are aligned to the objective aperture to make the diffraction pattern stationary and the diffraction stigmation is corrected.

The polySi film used in this experiment is shown in figure 6.3. The 715nm film was deposited on a Corning (type 7059) glass substrate using plasma enhanced chemical vapour deposition (PECVD). The partial pressures for the gases were [SiF_4]=300sccm,

[SiH_4]=10sccm, and [H_2]=500sccm at 300Pa. The substrate temperature was 300°C. According to table 5.1, the polySi film should be [110] textured and this is shown later to be the case. More information on the grain structure of this type of deposition is given in ref. [10].

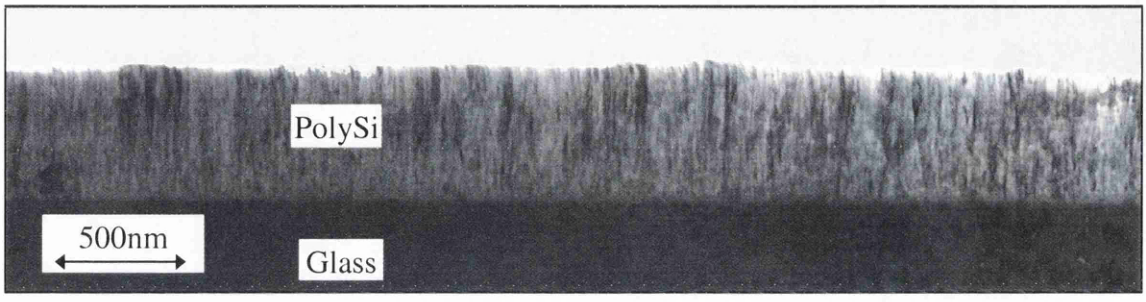

Figure 6.3: *Overview of the polySi film studied in cross-section for texture*

For this experiment the polySi film was prepared for the TEM using the tripod polishing technique as described in chapter 3. The thickness of the film varied from ≈40nm at the surface, to ≈60nm at the substrate, as determined from energy loss spectroscopy (EELS)[11]. The shape of the scan could be set up to scan across a rectangle having the same width as the film, i.e. ≈700nm. The resultant diffraction pattern could be used to find the texture of the whole film. However, if a number of linescans are performed through the film at regular intervals parallel to the substrate surface, it is possible to map how the texture develops as it grows. The latter method is performed first, and the other is done later to compare with the average results from the linescans.

Linescans of length ≈8μm parallel to the substrate surface were performed at a number of distances from the substrate. Figure 6.4 shows the experimental procedure where 12 linescans are positioned at regular distances from the substrate. The average grain width is observed at ≈10nm from imaging, and so ≈4000 grains were sampled in each linescan. The time taken for 1 complete linescan was 0.05s and the resulting diffraction pattern exposed for 0.1s onto a photographic plate, i.e. the time taken for 2 complete scans. Two such patterns are shown in figure 6.5. Each pattern is a superposition of the diffraction patterns from the individual crystallites in the area scanned. They consist of

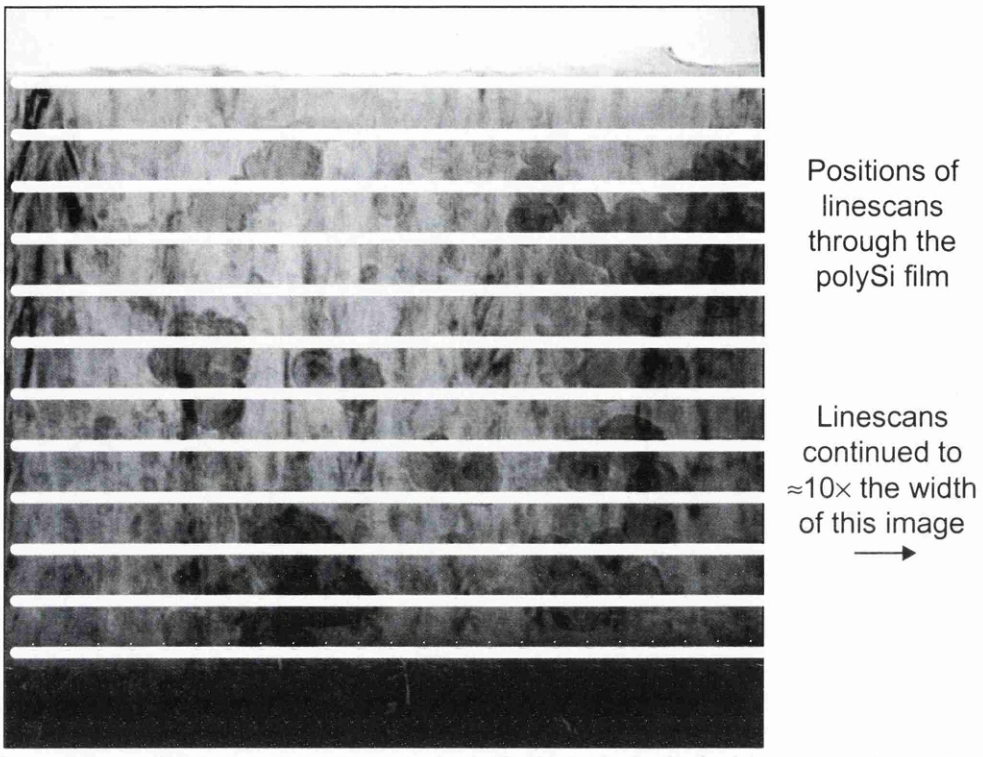

Figure 6.4: *Outline of the experiment to determine the texture development through the film using the diffraction patterns from a series of linescans. The black patches are carbon deposited to prevent charging in the TEM*

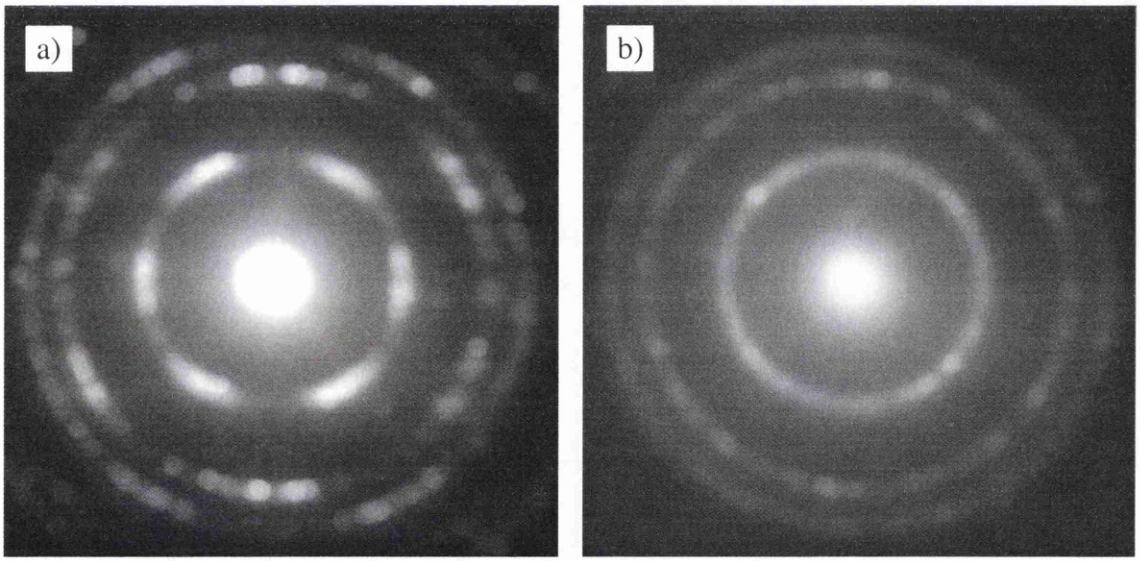

Figure 6.5: *Diffraction patterns from linescans positioned at the top surface of the film in a), and close to the substrate in b)*

spots which have a diameter corresponding to the convergence angle of the beam. These spots may group to form arcs or rings, and the reduction of the angle of convergence helps to resolve them.

6.4.2 Information Available from the Diffraction Pattern

The aim of this analysis is to determine the degree of texture and the mosaic spread from a single diffraction pattern of an area scanned on a film. It is also possible to determine other characteristics of the distribution of grain orientations from such a pattern. Table 6.3 describes all the characteristics of the orientation distribution which can be derived from a diffraction pattern as shown in figure 6.6.

Table 6.3: *Method of determining the information available from the diffraction pattern*

Characteristic	*Method of measurement*
Texture direction(s)	Comparison to theoretical diffraction patterns
Degree of Texture	Calculations on the intensity distribution around a ring
Mosaic spread	FWHM of peak in texture direction, e.g. [220] peak
Angular tilt offset	Angle between surface normal direction and first [220] peak
Effective mosaic spread	Convolution of the tilt offset and the mosaic spread, FWHM of {111} peaks
Azimuthal distribution	Intensities of opposite reflections about the texture direction

The origin of the tilt offset is not well understood. Here, in a textured sample, the grain orientations prefer to form a cone at a semi-angle, θ, to the surface normal direction. This causes the reflections in the texture direction to split by 2θ as shown by the two [220] reflections in figure 6.6. Another result is that the {111} spots do not have widths equal to the mosaic spread, 2α, but are widened by the tilt offset, θ to a FWHM of $2\alpha+2\theta$. This is labelled the effective mosaic spread, $2\alpha_e$, as it describes the resulting spread in grain orientations more accurately. It is likely that physical properties of the film depend on the effective mosaic spread rather than the mosaic spread. Clearly, in the absence of a tilt offset, both terms are equivalent. The phenomenon of the tilt offset is seen in other systems[12].

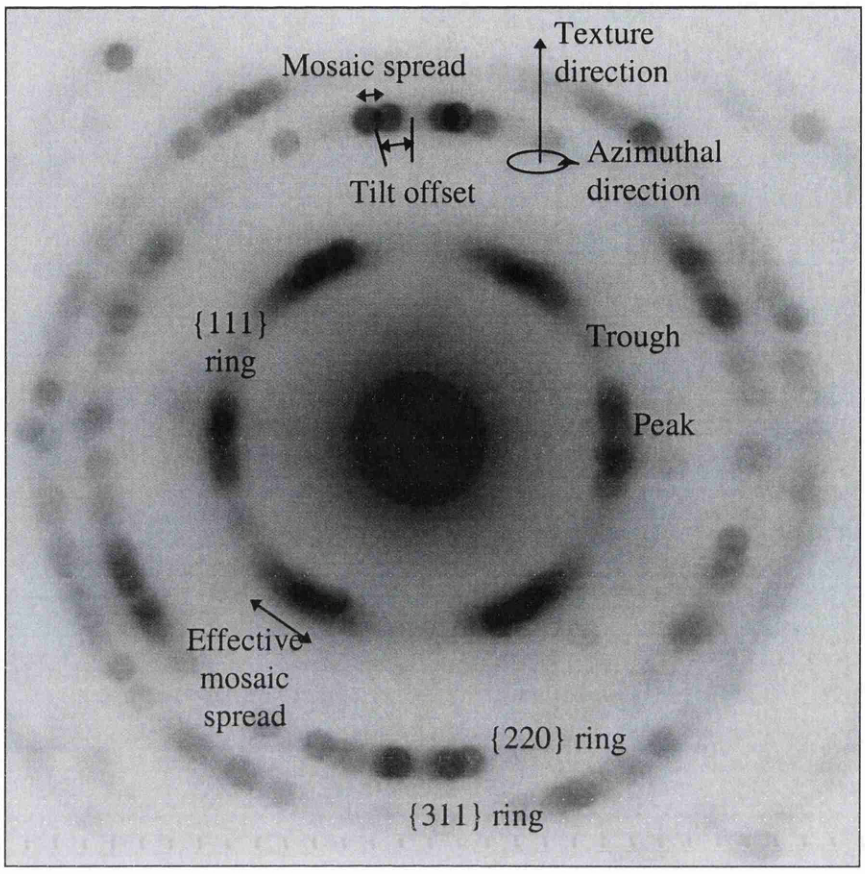

Figure 6.6: *A negative of the diffraction pattern showing the terms used to describe the texture of a film. Such a negative is used in the analysis*

Both the degree of texture and the azimuthal distribution of orientations are not immediately obvious from the patterns and, to different extents, they are the subject of the remainder of the chapter.

One possible method of determining the degree of texture is to relate it to the electron intensity distribution around a given diffraction ring. From figure 6.5 it is clear that this distribution is different for randomly oriented grains and for those oriented in the texture direction. For the randomly oriented sample, the ring intensity is effectively uniform, whereas a textured sample creates localised regions of intense 'peaks' and less intense 'troughs'. Other methods could include comparing the relative elastic electron intensities of the parts of the {111} and {220} rings which lie in the texture direction. For a randomly oriented sample, this intensity ratio is given by simple theoretical

calculations for determining ring intensities. The calculation involves the reflection multiplicities, M, structure factor, F_{hkl}, and the length of the reciprocal lattice vector, g, and is shown in equation 6.3

$$\frac{I_{111}}{I_{220}} = \frac{M_{111}\left|F_{111}\right|^2\left|g_{220}\right|^2}{M_{220}\left|F_{220}\right|^2\left|g_{111}\right|^2} = \frac{8\times(2\times10.9)\times8}{12\times(4\times3.2)\times3} = 3.0 \qquad [6.3]$$

A quick way to calculate M for a set of vectors $\{uvw\}$ is to divide 48 by two for every zero or pair, and divide by 6 if all indices are the same. For example M=48/2/2=12 for {220}. The fraction I_{111}/I_{220} is zero when all the grains are oriented in the [110] direction as there is no intensity on the {111} ring arising from elastic scattering. There are three significant drawbacks to this approach in calculating the degree of texture. Firstly, the [220] reflections in a [110] textured sample are prone to dynamical scattering effects. Secondly, the electron detection system is more likely to experience saturation effects at this reflection. Although saturation is a problem in practice it can be avoided by adjustment of the emission current and exposure time. Finally, the outer limits of the intensity ratio may be known for 0% and 100% texture, e.g. here they are 3.0 and 0, but the exact relationship between the ratio and the degree of texture is very difficult to calculate between these limits.

It is decided that the best approach to determining the degree of texture from the diffraction pattern is to examine the elastic electron intensity around the innermost ring. This ring is chosen because it has the highest signal to noise ratio, where the noise is inelastic scattering and 'fog' in the negatives. Taking the diffraction patterns from this experiment as an example, the {111} ring would be used in the analysis. It is shown later that the textured pattern signifies the presence of [110] texturing. However if this analysis were implemented on a film which was [111] textured the {220} or {200} ring (depending on structure) would be used. This is a consequence of over-exposure and dynamical scattering effects from the reflection in the texture direction, so involving it in the analysis reduces the accuracy of the results.

6.4.3 Diffraction Theory for Textured Films

In this section the influence of the orientation distribution on the intensity around a diffraction ring is discussed. Again the {111} ring is used as an example, but similar results are expected for other rings. A diffraction pattern from a crystallite can be described by the pattern made by the reciprocal lattice points which lie in a plane perpendicular to the incident beam direction. When the beam transmits through many grains, as is the case here, the diffraction pattern is the same plane through the superposition of all the individual reciprocal lattices. For a large number of randomly oriented grains, the shape of reciprocal points merge to create concentric spheres in reciprocal space which have a radius equal to $|g_{hkl}|$. Such a sphere containing all the {111} reciprocal points, or reflections, is shown in figure 6.7a. Hence, the diffraction pattern which is the plane through this sphere perpendicular to the beam direction, contains rings. For a completely textured sample, all the grains have a common

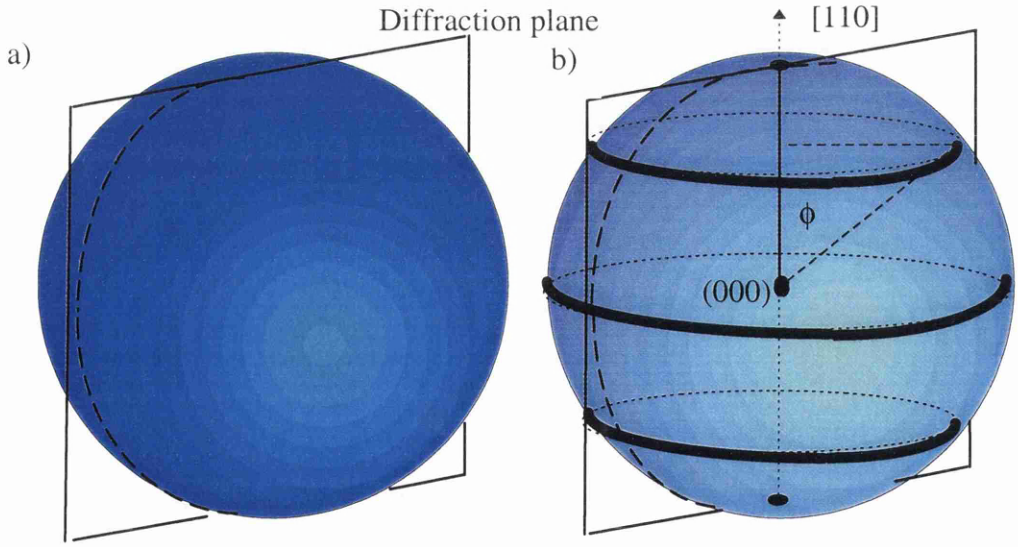

Figure 6.7: *Reciprocal spheres of {111} reflections for a randomly oriented and textured sample. The number and position of the bands depend on the texture direction*

orientation so the {111} reciprocal points can only lie at a number of well-defined angles to the texture direction (almost always the surface normal direction). This results in a higher density of reflections at these angles corresponding to a number of discrete bands around the sphere, and no intensity between the bands. This situation is described in figure 6.7b where the number and position of the bands is determined by the texture direction. An example of the diffraction pattern from a [110] textured sample is shown in figure 6.8 where six spots are observed on the {111} ring. This number of spots can be calculated theoretically. Each cubic structure has eight {111} reflections, so there is a maximum number of eight bands around the {111} sphere. However, unless the texture direction, [*uvw*], has three different non-zero indices some bands will superimpose to reduce the total number present. Using the cosine rule to calculate the angles between the texture direction and the {111} reflections, the number of individual bands can be shown to equal to the number of permutations of {u+v+w}. For example, [110] texturing gives {2},{0}, and {-2}, implying 3 bands. The number of spots around the ring is twice the number of bands, so there are 6 spots on the {111} ring for [110] texturing.

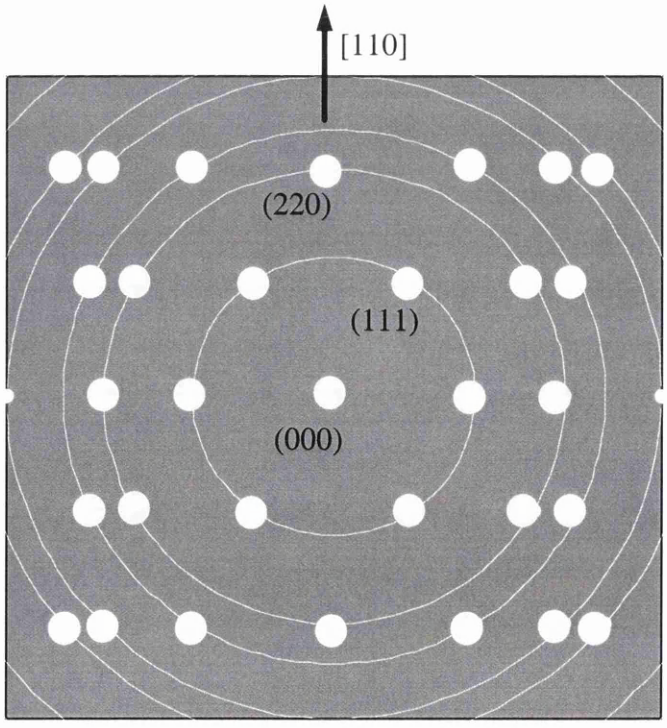

Figure 6.8: *The [110] textured diffraction pattern superimposed on the rings for clarity*

To obtain more quantitative information from the localisation of reflections into bands, diffraction theory is utilised. In the volume scanned, the reflection intensities from each grain will depend on its thickness. However, it can be shown[13],[14], that for grain sizes $\leq \xi_g/3$, where ξ_g is the extinction distance for the (*hkl*) reflection (=60.2nm for {111} reflection), the intensity of a reflection varies linearly with the volume having the reflection in that direction. This describes the conditions for kinematic scattering. For grain sizes $\geq \xi_g/3$ the model is less accurate as the integrated intensity begins to oscillate as a function of volume oriented in that direction, as shown in figure 6.9 (dynamical scattering). Here the intensity at each deviation from the Bragg angle, w, is calculated using a simplified version of equation 2.13a[15] for a certain crystal thickness. Then the values are integrated over the rocking curve in the range $-10 \leq w \leq 10$ to give the integrated intensity for a given crystal thickness, t, as calculated in equation 6.4.

$$I_t = \int_{-10}^{10} \frac{\sin^2\left(\pi\, t\sqrt{1+w^2}\,/\,\xi_g\right)}{1+w^2} dw \qquad [6.4]$$

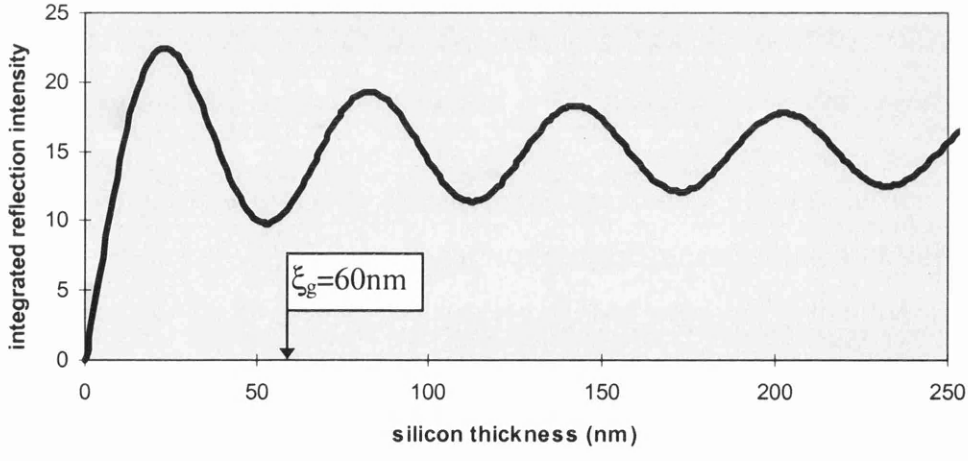

Figure 6.9: *Rocking curve measurements show that the intensity varies directly as the crystal thickness until $\xi_g/3$ where it begins to oscillate*

The limits are chosen as the diffraction intensity beyond them is negligible. It may be argued that, if the grain sizes are all larger than the specimen thickness, which is constant, the intensity of a reflection is again proportional to the volume oriented in that direction. This should hold if the specimen thickness is constant throughout, and only if there is a large number of grains present.

The theory relating the reflection intensity distribution to the orientation distribution must first be considered in 3-dimensional reciprocal space. Referring to figures 6.7a and b, and assuming kinematic scattering, the spot intensity at a given point on the sphere is proportional to the volume oriented in that direction. The total intensity on the {111} reciprocal sphere from any fixed volume of film will be the same, whether the film is textured or not. However, this does not imply that the integrated intensity around the diffraction ring will be the same for both cases. Instead, the integrated intensity depends on the distribution of reflections as a function of angle, φ, to the texture direction as shown in figure 6.7b. The reason this effect has to be taken into account is that, in the calculation of the degree of texture later, the reflection intensities around the {111} ring arising from grains which are oriented in the texture direction are compared to those from randomly oriented grains. If the reflections are confined to a band, as is the case for a textured sample, the intensity of the corresponding {111} diffraction spot depends on its angle to the texture direction. Thus the reflection intensity does not only depend on the volume oriented in that direction. This effect is not present for randomly oriented grains where a sphere of uniform intensity results. For the analysis described later, only the effect on the integrated intensity around the diffraction ring is required for a given texture direction. To calculate this, the intensity of the eight {111} reflections are calculated as a function of φ, taking into account the multiplicity of each band. The relative integrated intensity, I_T, around the {111} ring is given by equation 6.5a and the same is given for a randomly oriented sample, I_R in equation 6.5b. Here I_0 is the intensity from a single (111) reflection.

$$I_T = 2 \times \left(\sum_{i=1}^{8} \frac{I_0}{2\pi g \sin \phi_i} \right) \qquad I_R = \frac{8 I_0}{4\pi g^2} \times 2\pi g \qquad [6.5a, b]$$

Combining the two the ratio, I_T / I_R, is given by equation 6.6.

$$\frac{I_T}{I_R} = \frac{1}{4\pi} \sum_{i=1}^{8} \frac{1}{\sin \phi_i} \qquad [6.6]$$

For [100] texturing the ratio I_T/I_R is 0.78; for [110] it is 0.88; and for [210] it is 0.83. (With a [111] texture direction the {220} ring is analysed and the ratio I_T/I_R is 0.88). For texture directions with higher indices the fraction approaches 1 as the diffraction spots are spread more evenly around the ring. For [110] texturing, the I_T/I_R ratio suggests a possible error in the degree of texture, G, of ±0.12. However, in the analysis described later, because both the average intensity, a, around the ring and the difference between this average and the trough intensity, b, are affected in a similar way by this ratio, it can be shown that a maximum error in G will be ±0.05 for G=0.5. This error decreases to zero as G approaches either 0 or 1. It is therefore reasonable to approximate that the total intensity (and thus the average intensity) around the {111} ring is the same whether the area is textured or not. For greater accuracy, particularly for <100> texturing, the intensity of the peaks, excluding the contribution from random orientations, will be divided by I_T / I_R to determine the average intensity; then a and b will be calculated as normal.

There is thus a theoretical basis for quantifying the volume fraction of grains which are oriented in a certain direction from the reflection intensities around a diffraction ring. So, to a first approximation, the degree of texture will vary as the ratio of the {111} reflection intensities which belong to textured grains (at the corresponding peaks) to those arising from other grains. It must be noted that this only applies to a polycrystalline material with grain sizes $\leq \xi_g/3$, and under certain conditions where the grain sizes are larger than the specimen thickness. In both cases, there must be a large number of grains to achieve satisfactory statistical accuracy, and this can be checked by examining the reflections arising from the randomly oriented areas on a ring as

explained later. To use this approach, the electron intensity around the rings must be determined from the diffraction pattern.

6.4.4 Determination of the Electron Intensity Around a Diffraction Ring

There are several ways to calculate the electron intensity around the inner ring either directly or indirectly. Direct methods involve the use of a detector under the viewing screen in a TEM. This could be a Faraday Cup detector which measures current at a specific point or a calibrated CCD camera. For any small detector the diffraction pattern would have to be moved around using deflection coils onto the detector aperture[2]. Indirect methods involve the digitisation of the photographic negative then a conversion between the levels of grey on the image to the relative electron intensity. The latter method is performed here and is similar to the photometric method[16]. The negatives are digitised using a scanner connected to a PC. Care is taken to align each negative in the same direction when scanning. The scanner digitises the intensity of the transmitted light through the negative into a greyscale value between zero and 255 where zero signifies no transmission (negative is black) and 255 signifies full transmission (white). The nominal greyscale is related to the transmitted light intensity, J_T, and the incident intensity, J_0, as described by equation 6.7.

$$\frac{y}{255} = \frac{J_T}{J_0} \qquad [6.7]$$

This ratio depends on the number of grains, n_g, exposed on the photographic film and this is proportional to the relative number of incident electrons, n_e, and is described by equation 6.8[17] where z_0 is the thickness of the emulsion.

$$\frac{J_T}{J_0} \propto e^{-n_e z/z_0} \qquad [6.8]$$

Using equations 6.7 and 6.8, it is possible to calibrate the greyscale on the digitised image as a function of electron intensity. However, it is not known how accurate the

scanner is in obeying equation 6.7 so it is calibrated using filters of known optical density, D. The optical density is defined by equation 6.9[18] for the region outside saturation and hence n_e can be shown to be proportional to D.

$$\frac{J_T}{J_0} = 10^{-D} \Rightarrow n_e \propto D \qquad [6.9]$$

Thus the relationship between the greyscale and optical density is the equivalent relationship between the greyscale and the relative electron intensity. Figure 6.10 shows the graph of D (or n_e) against y. It is clear from figure 6.10 that either the intensity resolution of the scanner deteriorates at low y, or that equation 6.8 exhibits saturation effects at high D. Indeed, it is known that for X-ray films, D is directly proportional to the exposure (or intensity) up to D=1.0[17]. Thus, another method of relating the greyscale values to the relative electron intensity is required.

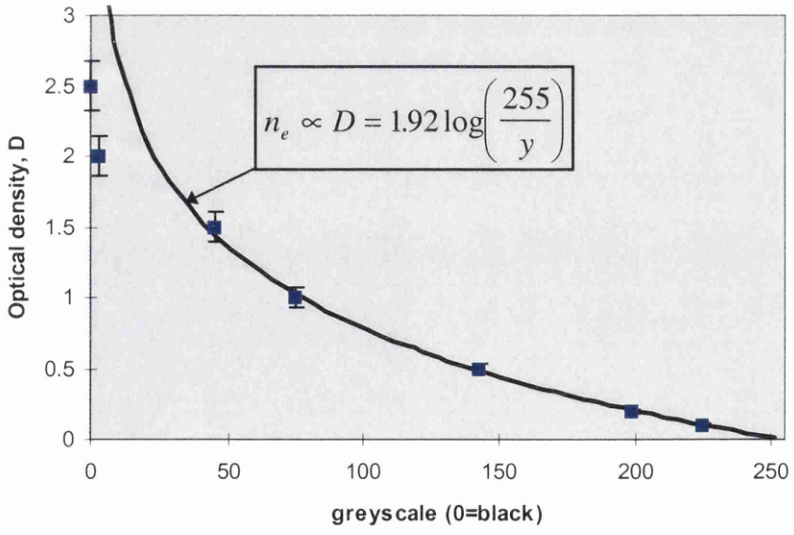

Figure 6.10: *Relationship between the optical density (proportional to n_e) and the greyscale value. This equation does not describe the saturation regions well*

A method to relate n_e and y, is to expose a TEM image (or diffraction pattern) for a number of different exposure times. The relative intensity of electrons at a point on the negative varies directly as the exposure time, so its effect on the greyscale value can be monitored. Figure 6.11 shows the results of the greyscale of a particular point on an

image as a function of exposure time. Thus the relationship relating n_e to y is given by equation 6.10.

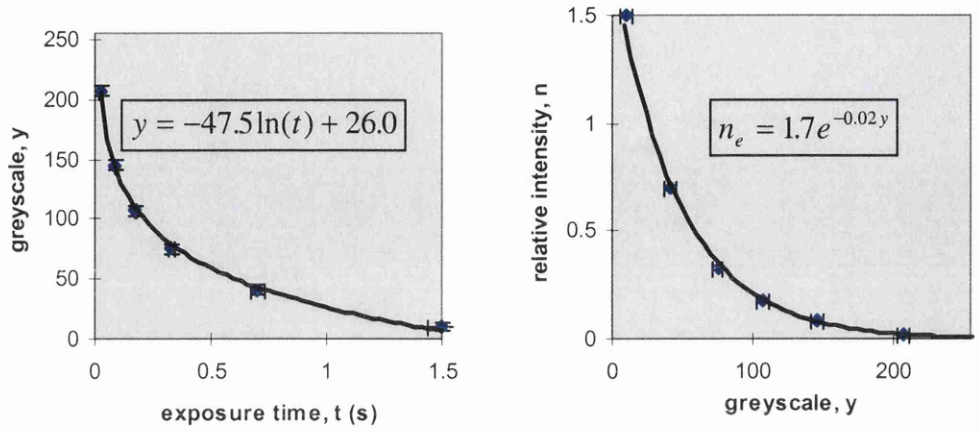

Figure 6.11: *Greyscale as a function of exposure time and, inversely, the relative intensity as a function of exposure time. This relationship is accurate for all greyscale values*

$$n_e = 1.7e^{-0.021y} \qquad [6.10]$$

For this analysis, n_e has to be measured as a function of angle around the innermost ring. This ring is, for many structures, the {111} ring and so will be referred to as such. An accurate way of obtaining n_e as a function of angle is to use a computer program which extracts the greyscale values around the {111} ring in the digitised diffraction pattern. The code for this program is shown in appendix B. Here a square of fixed dimension is fitted to superscribe the {111} ring and is cropped from the digitised image. It is then saved as a binary 'raw' file. The only information saved in such a file is the greyscale value of each consecutive pixel from the top left to bottom right of the image. Each pixel is therefore represented by one byte of information. The C-program then accepts this file and calculates the coordinates of each pixel as a function of angle around the {111} ring. At each angle, which is taken in steps of 0.1°, there is only one pixel chosen and it lies in the centre of the width of the ring. With the diffraction astigmatism corrected for, each diffraction ring should be circular. If not, the program can be written to follow the ring, but the angular scale is less accurate. At each coordinate, the

greyscale value is retrieved and the conversion to n_e can be done in the program or in a spreadsheet where the information is later graphed. Figure 6.12 shows

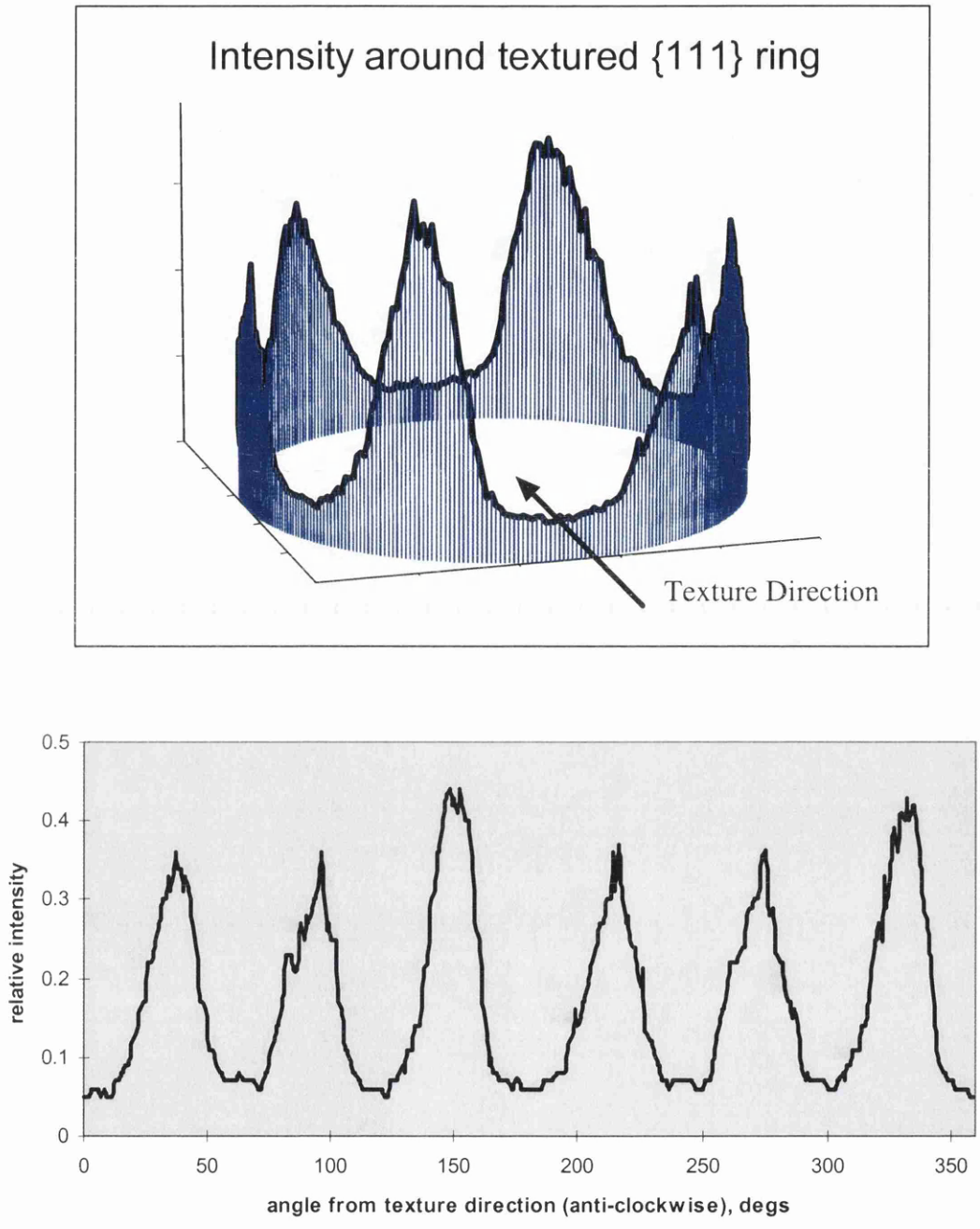

Figure 6.12: *A 3D and 2D representation of the same intensity profile around the {111} ring for the textured sample in figure 6.6. The inelastic contribution is yet to be subtracted*

an example of n_e as a function of angle around the {111} ring for a [110] textured film. With a slight modification, the program can be used to show the electron intensity over

the whole negative. Figure 6.13 shows the electron intensity distribution in the diffraction pattern for a textured sample. This image shows the 2D profile of the peaks and highlights the possible areas on the diffraction pattern where texture analysis can be applied.

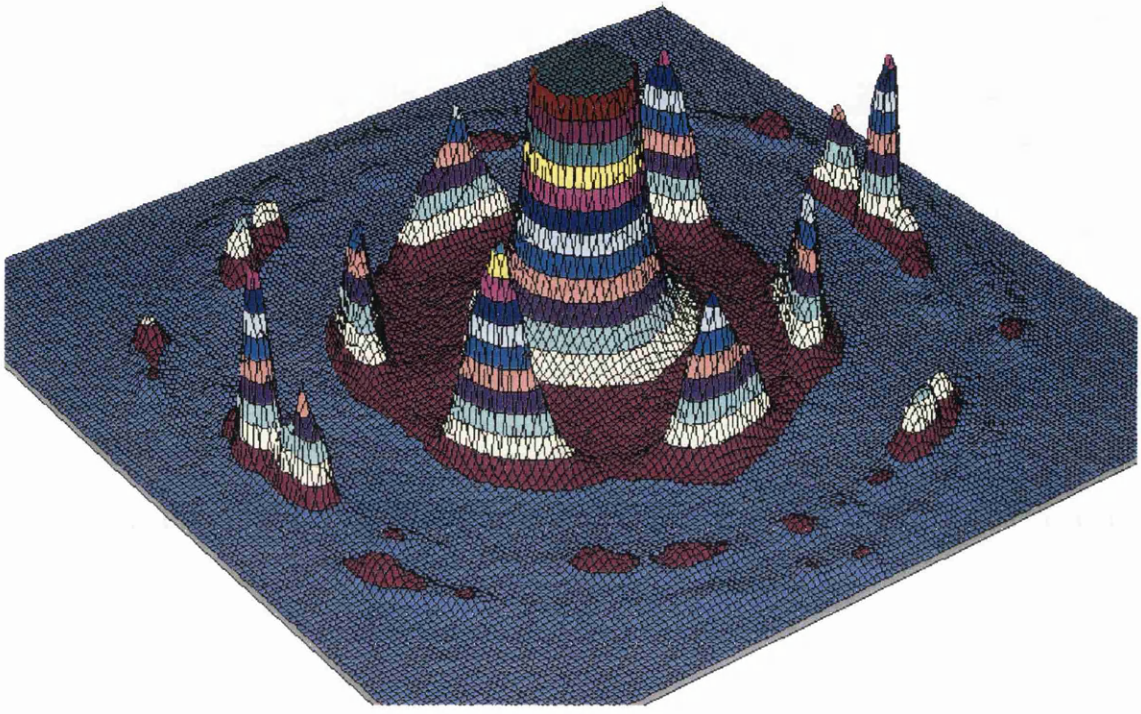

Figure 6.13: *This diffraction map gives significantly more information on the intensity distribution of the reflections than the diffraction pattern itself. The central spot is truncated for clarity*

So far, n_e around the ring still contains the contribution from the inelastically scattered electrons and, to a lesser extent, the fog in the photographic film. This intensity gives no information about the distribution of grain orientations and reduces the accuracy of the analysis. To subtract this contribution from n_e, the average of the electron intensity just outside and just inside the ring is calculated. This measurement is performed by the C-program itself and takes the average of two sets of data points.

Due to the nature of the backlit scanning when digitising, the greyscale value of a particular point can be influenced by the darkness of the surrounding area. This effect incurs a minor error in n_e but causes the centres of peaks, or arcs, in the diffraction

pattern to have a more pointed formation. The effect is practically unavoidable but only introduces a small error (≈1%) in the subsequent calculations since it only affects a small angular region of the {111} ring.

6.4.5 Calculation of the Degree of Texture

The diffraction theory mentioned earlier suggests that it is possible to obtain quantitative information from the electron intensity distribution around a diffraction ring. The graphs in the previous section show that a simple calculation can be made to accurately determine the elastic electron intensity at a given point on the ring. It now remains to relate this intensity distribution to a value of the degree of texture.

Firstly, an ideal film is considered. This film contains a large number of grains which are oriented evenly around the surface normal, or texture, direction, i.e. have a random azimuthal orientation distribution. The azimuthal plane is perpendicular to the surface normal direction. One way of producing an equation which relates the {111} ring intensity profile to the degree of texture is to consider a volume of a film containing completely randomly oriented grains and a similar volume which is partially textured, i.e. a significant fraction of the grains have a common orientation. Typical ring intensity profiles are shown in figure 6.14 for these two cases where the peaks are represented by rectangles to make subsequent calculations easier to interpret. The widths of the rectangles are equal to $2\alpha_e$ and the error in representing the peak in this way is not considered as the true shape of the peak is not known (although often approximated to a Gaussian[3]) , particularly if a tilt offset exists. As mentioned earlier, b, is defined as the average elastic electron intensity around the ring, calculated simply from the individual values of n_e around the ring after the background has been removed. The term a is defined as b minus the trough intensity. The trough intensity is effectively constant around the ring and describes the intensity arising from the randomly oriented grains. It's value is the average trough intensity calculated using user-defined windows around the ring. It is noted at this point that there exist several approaches to relate the intensity profile of figure 6.14 to the degree of texture, but the approach used here

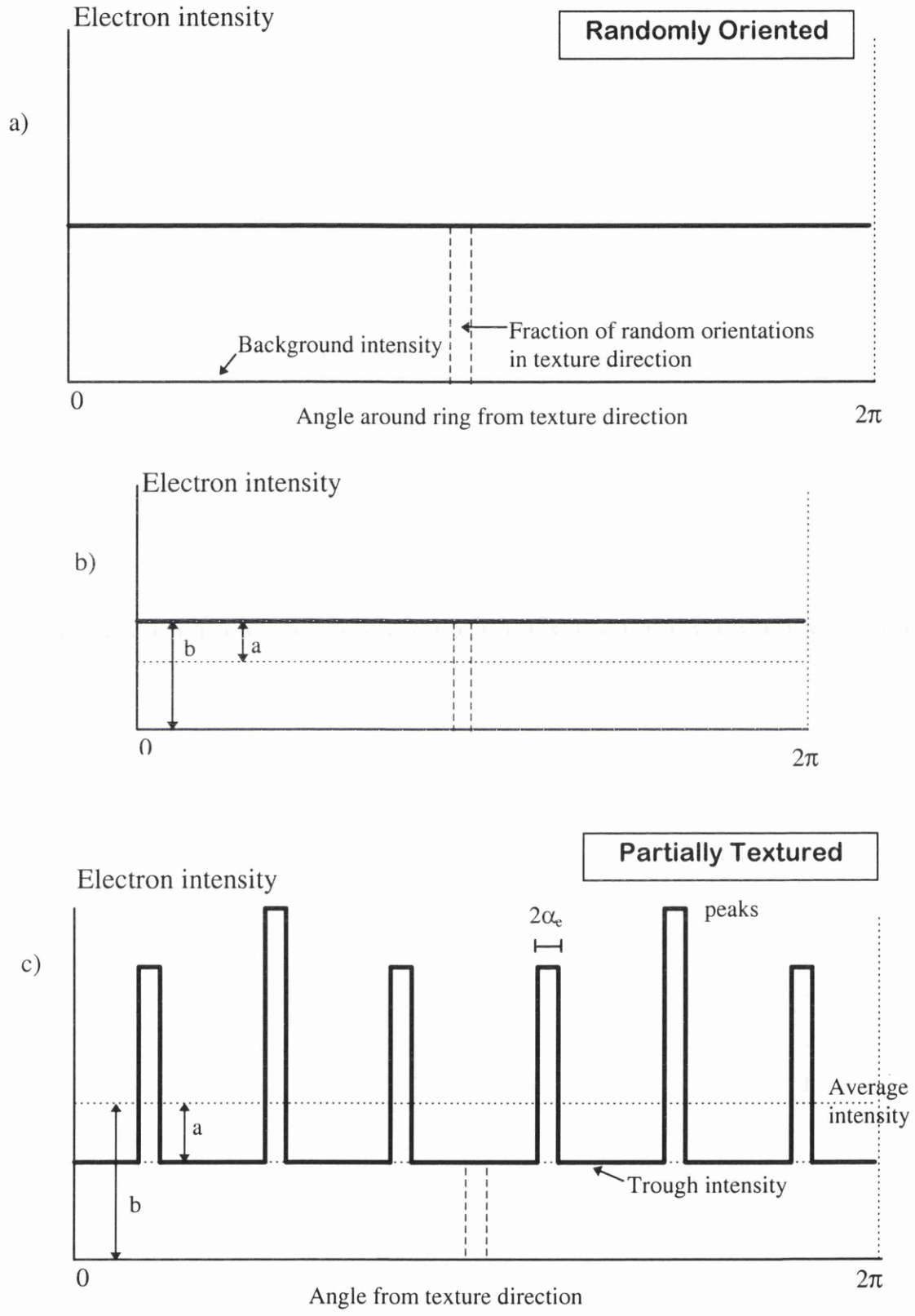

Figure 6.14: *Diagrams showing the model used to calculate the degree of texture from the intensity profile around the {111} ring*

avoids measuring peak heights which vary. An intensity profile of a randomly oriented volume is described in figure 6.14a. Now a fraction a/b of this volume (figure 6.14b) becomes oriented in the texture direction as shown in figure 6.14c. All the intensity above the trough line is considered as originating from grains in the texture direction and the intensity under the trough arises from randomly oriented grains. The peak intensities can vary according to reflection multiplicities and distance from the texture axis but the trough intensity should be constant around the ring. The fraction of the intensity in the peaks relative to the total intensity is defined as the texture fraction, T, and is given by a/b. However, it must be acknowledged that a small fraction of the randomly oriented grains are also oriented in the texture direction. This amounts to the fraction of the surface area of the reciprocal sphere which is contained within the solid angle described by the effective mosaic spread, $2\alpha_e$. Since there is no physical difference between say the [110] and [101] orientations this fraction is multiplied by the multiplicity, M, of the texture direction for the lattice structure. For [110] texturing in polySi, using the small angle approximation for the conversion from radians to steradians, this amounts to $\approx 12\pi\alpha_e^2/4\pi = 3\alpha_e^2$ of the fraction of the randomly oriented grains. For non-cubic structures, $M \neq 12$ for [110] texturing but instead depends on the number of identical <110> orientations. Therefore, from any single profile of any diffraction ring, the fraction of grains in the texture direction within the effective mosaic spread, G is given by equation 6.11.

$$G = \frac{a}{b} + \frac{M}{4}\alpha_e^2 \frac{(b-a)}{b} \qquad [6.11]$$

With $T = a / b$, we simplify equation 6.11 to:

$$G = T + \frac{M}{4}\alpha_e^2(1-T) \qquad [6.12]$$

In equation 6.12, $G \approx T$ for $\alpha_e < 10°$; except where $T \to 0$. Figure 6.15 shows how G relates to T as a function of the mosaic spread for M=12. It may seem that T may be more appropriate in describing the level of texturing since G increases with $2\alpha_e$ for a

given T, and a larger $2\alpha_e$ approaches the randomly oriented situation. However, it is very difficult to interpret T as a definition of the degree of texture as it has no physical meaning. If no tilt offset existed, a possible method of combining G and $2\alpha_e$ would be to describe the degree of texture as the relative height of the centre of the [220] peak in the texture direction. Here the peak height increases with the level of texturing and decreases with the mosaic spread. The main problems here lie with the difficulty in measuring an accurate peak height and defining what the maximum relative peak height can be to obtain quantitative information.

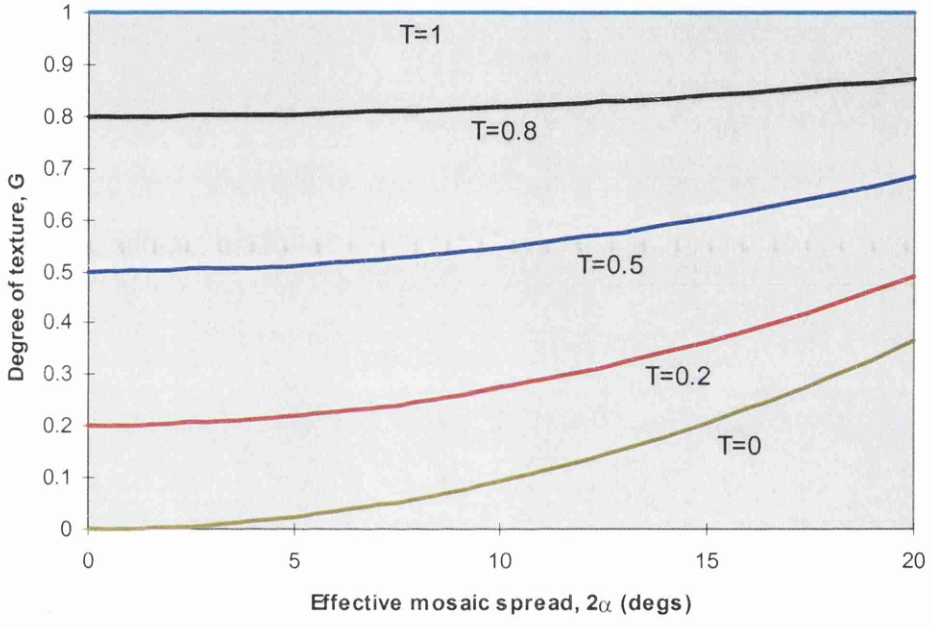

Figure 6.15: *The relationship between G and $2\alpha_e$ for a given T. G is similar to T for low $2\alpha_e$ and high T.*

6.4.6 Determination of the Azimuthal Distribution

It is helpful to get an idea of the uniformity of the azimuthal distribution of the grain orientations in a textured sample as this affects the level of confidence in the results. If the orientations were azimuthally uniform, the {111} peaks would have relative intensities determined simply from multiplicities and the distance from the texture axis.

A non-uniform azimuthal orientation distribution will vary the intensity of the {111} reflections which are perpendicular to the texture direction relative to the other {111} reflections, since they occur at different azimuthal positions in reciprocal space. Furthermore, if there is either a tilt offset or the specimen is not perpendicular to the beam in cross-section, then a non-uniform azimuthal distribution will cause horizontally opposite {111} reflections (where the texture direction is vertical) to have different intensities. Diagonally opposite reflections should always have the same intensity and thus offers a means of checking the sensitivity of the intensity measurements. From the example of the {111} intensity profile in figure 6.12, it is clear that diagonally opposite reflections are approximately equal but the upper and lower horizontally opposite reflections are clearly different. Also, for a random azimuthal distribution, the intensity of the {111} reflections perpendicular to the texture direction should be $\sqrt{2} \times$ the others. Figure 6.12 also shows that this is not the case for the film studied here, confirming that the distribution of grain orientations is not azimuthally random.

If the distribution is found to be non-uniform azimuthally, the analysis will only produce the degree of texture for the plane through the film perpendicular to the beam. For CVD grain growth on top of amorphous materials like the SiO_2 here, there is no reason to believe that the azimuthal distribution of orientations at the interface would be non-uniform. Only if the film deposition was on a crystalline material would non-uniform azimuthal orientations be possible during the initial grain growth. However, the situation can be more complicated as the film grows. As is shown later, the textured regions on the sample only exist between ≈300nm from the substrate surface to the top of the film. Beneath these textured grains lie small, randomly oriented grains which can influence their azimuthal orientations. One would imagine that the influence of the randomly oriented grains would be small in affecting the azimuthal orientations, but the intensity profiles in figure 6.12 show that the distribution is not uniform. If an insufficient number of grains were involved in the scan, the intensities could falsely imply a non-uniform azimuthal distribution. However, the fact that the trough intensity is approximately constant around the ring signifies that there are enough grains for accurate analysis.

6.4.7 Sub-texturing

Another point of interest is whether there exists any sub-texturing, or other preferred orientations. This would cause {111} peaks to appear between those associated with the prominent texture. For our polysilicon sample, the intensity between the peaks in the [110] textured regions is flat, indicating the absence of any sub-texturing. If sub-textures exist, equation 6.12 would be modified to determine the fraction textured in each direction. An estimate of the degree of texture in each direction could be obtained using a similar diagram to that shown in figure 6.14. The area underneath each {111} peak associated with a particular texture direction (excluding the contribution from random orientations) divided by the whole area allows the degree of texture for each direction to be found. This neglects the fraction of the randomly oriented grains which are in the texture directions but their effect is normally small. If peaks overlap, the multiplicities of each {111} reflection may be used to estimate the area under the peaks belonging to a given texture direction.

6.5 Results and Discussion

A number of linescans are positioned through a 715nm thick polySi film at regular distances from the substrate. At each position the diffraction pattern is photographed and then digitised. The patterns are shown sequentially in figure 6.16. By comparing theoretical textured diffraction patterns like those shown in figures 6.8 and 5.19, to the experimental patterns, the texture direction is found to be [110]. However it is clear from the images in figure 6.16 that significant texturing does not exist in the first few linescans closest to the substrate. For the textured patterns, the effective mosaic spread, $2\alpha_e$, is measured directly as the FWHM of a {111} peak, and is found to be 17±1°. The tilt offset, θ_0, and mosaic spread, 2α, are also measured as 7±1° and 3±0.5° respectively. These do agree as contributing linearly to the effective mosaic spread.

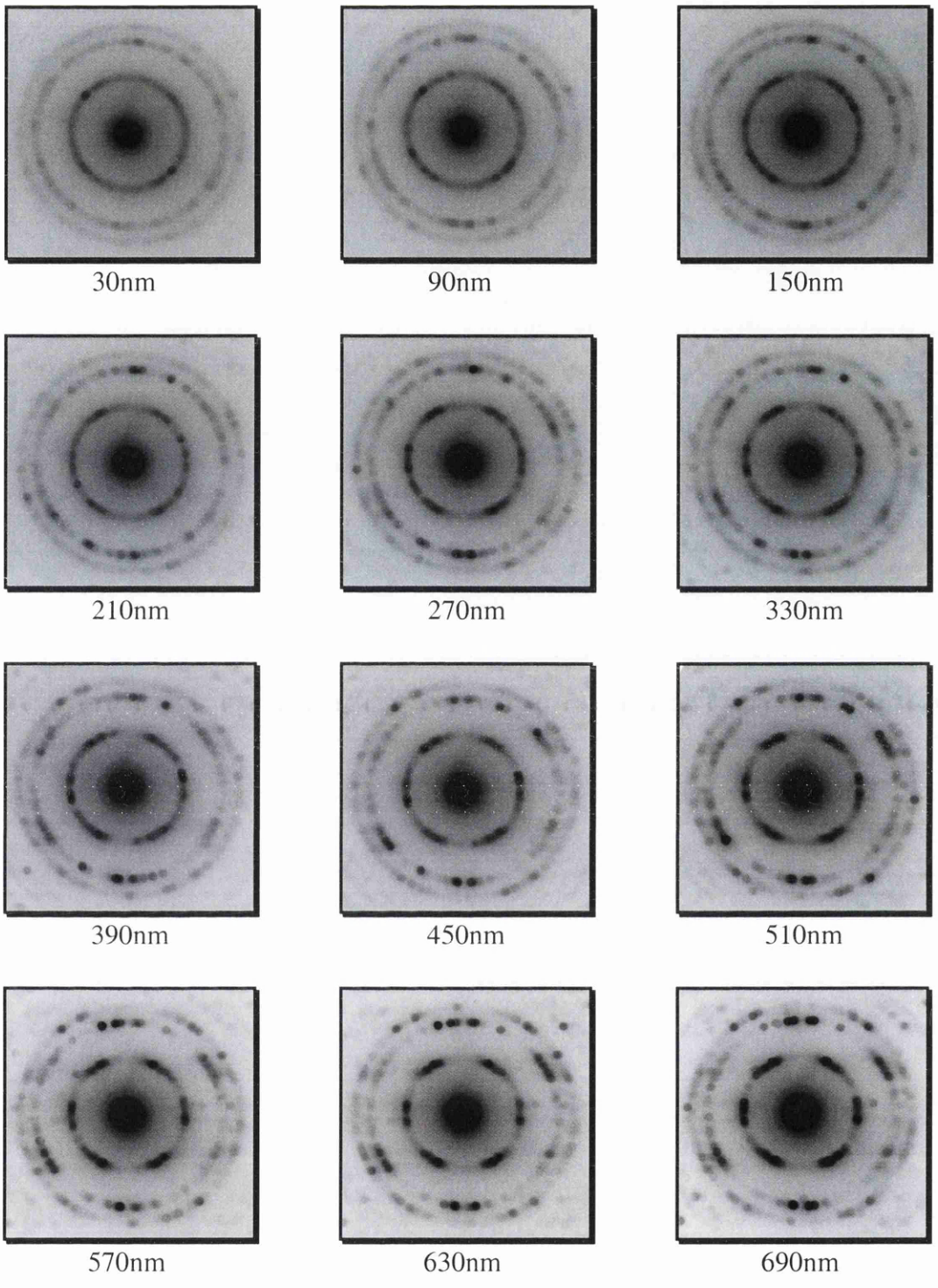

Figure 6.16: *The series of diffraction patterns from linescans through the film according to the distance from the substrate*

A C-program is written to extract the electron intensity, n_e around the innermost ring and the inelastic contribution to the intensity on each diffraction pattern at the ring.

Here, a spreadsheet in Excel is used to subtract the inelastic contribution and plot n_e as a function of angle around the ring. Figure 6.17 shows a graph of three of these plots from regions close to the substrate, half way through the film, and at the free surface. These correspond to the diffraction patterns in figure 6.16 at 30nm, 330nm and 690nm.

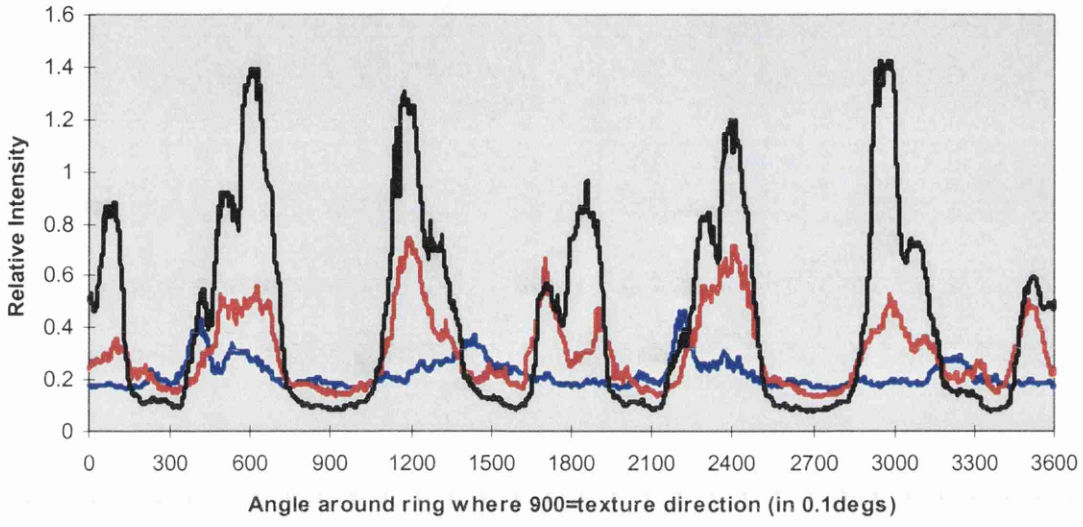

Figure 6.17: *Examples of the {111} intensity profiles for regions close to the substrate (blue), along the centre of the film (red), and close to the free surface (black)*

The spreadsheet then calculates the average intensity, b, and the average trough intensity, b-a, around the ring. Using this information, the degree of texture, G, is calculated using equation 6.12 for each diffraction pattern. The results are then plotted as a function of distance from the substrate to show the development of texture in the film. Figure 6.18 shows the gradual development of the texture through the film. The results imply that ≈1/6 of the volume of polySi close to the substrate interface is oriented in the texture direction whereas >90% of the surface is textured. Table 6.4 shows the values for the results graphed in figure 6.18.

The statistical accuracy in determining G depends primarily on the number of grains included in the scan. A large number of grains results in a more consistent trough intensity around the ring. The error in each measurement of G from the {111} ring

intensity is determined from the intensity profile itself. The standard deviation in the trough values, *da*, around the ring reflects the error in *G*, and is given by equation 6.13.

Table 6.4: *The spreadsheet used in the analysis for the texture development*

distance (nm)		*30*	*90*	*150*	*210*	*270*	*330*	*390*	*450*	*510*	*570*	*630*	*690*
average n_e	b	0.22	0.23	0.30	0.27	0.34	0.30	0.35	0.35	0.39	0.36	0.36	0.44
inelastic	n_i	0.10	0.09	0.12	0.11	0.12	0.10	0.11	0.10	0.10	0.09	0.09	0.07
trough	b-a	0.21	0.22	0.27	0.23	0.23	0.18	0.19	0.16	0.15	0.12	0.11	0.11
texture fraction	T	0.11	0.09	0.20	0.24	0.48	0.62	0.64	0.77	0.82	0.89	0.92	0.91
degree of texture	G	0.19	0.18	0.28	0.31	0.53	0.66	0.67	0.79	0.83	0.90	0.93	0.92
error	dG	0.07	0.10	0.11	0.11	0.09	0.08	0.12	0.03	0.06	0.07	0.04	0.05

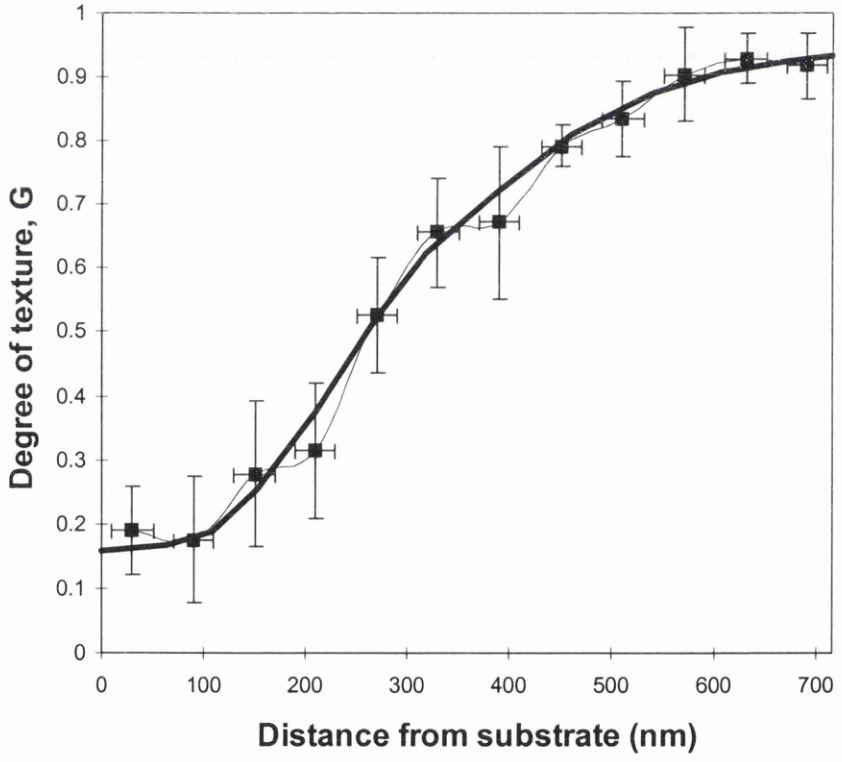

Figure 6.18: *The development of the degree of texture through the film*

$$dG = (1 - \frac{M}{4}\alpha_e^2)\frac{da}{b} \qquad [6.13]$$

In this equation there is no error in b as the average is known exactly if all the intensities around the ring are used to determine the average. Theoretically, it is very difficult to determine an accurate value of the dG in terms of the beam convergence angle and the number and size of grains. The main problem lies in defining the limits of the rocking curve from which a reflection contains significant intensity. Estimations have been made to determine the number of grains required for a given level of accuracy in G. To a rough approximation, several thousand grains are required to provide quantitative results. However, this number could range by over an order of magnitude depending on the angular quantities mentioned above. This specimen has ≈4000 grains and, experimentally, this gives an error in G of ±0.1. When the experiment is repeated on a different area of the polysilicon film, the values of G agree on average to within ±0.05 at a given distance from the substrate, demonstrating the consistency of the analysis. The results from both experiments are compared in figure 6.19.

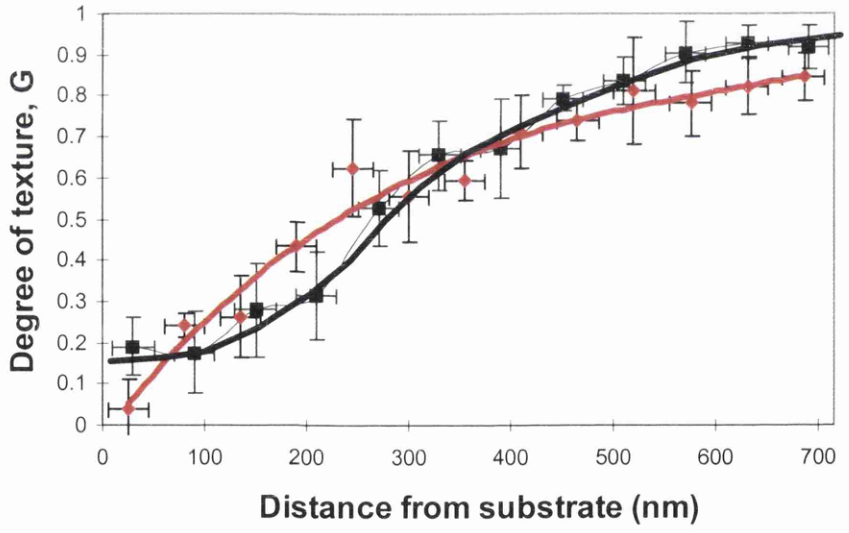

Figure 6.19: *The experiment is repeated and used to test the reproducibility of the analysis. Values of G differ by <0.1 at any point. Lines are drawn through the points for ease of interpretation.*

Using the values of G shown in table 6.4, an average value of 0.60±0.08 is obtained over the whole width of the film, and the corresponding value of T is 0.57±0.09. When the probe is scanned in a rectangular raster covering the whole area of the film from

substrate to surface, G is found to be 0.58±0.05. This result is in excellent agreement with the average of the individual values. The error in G is less for the rectangular scan having the same width as the film thickness due to the increased number of grains included. It is shown later that often the grains do not grow through the whole thickness of the film so more grains are sampled in the rectangular scan.

As mentioned earlier, the relative intensities of the {111} peaks do not agree with those predicted by theory for azimuthally random orientations. A more accurate description of the azimuthal orientation distribution can only be obtained by tilting the specimen about the surface normal direction. However, scanning a focused probe along a specimen of varying height in the microscope would reduce the resolution of the technique, limiting the tilt angle used in the investigation.

6.6 Summary

A definition of the degree of texture, G, is proposed as the fraction of the volume of a thin film which is oriented in the texture direction within the effective mosaic spread, $2\alpha_e$. If this value is to characterise a property of the film it should be accompanied by the texture direction and the effective mosaic spread itself. Many favourable properties of a film improve with a higher degree of texture and a lower mosaic spread. From a single diffraction pattern of a scanned area in cross-section various parameters describing the texture can be determined. These include, texture direction, mosaic spread, tilt offset, degree of texture and deviations from a random azimuthal orientation distribution. Using the relative electron intensity around the {111} diffraction ring, it is possible to use equation 6.12 to determine the degree of texture. Figure 6.18 shows the results of this analysis through a polySi film in the growth direction showing the gradual development of texture. The film is found to be textured in the [110] direction with an average degree of texture of 0.60±0.08 and a texture fraction of 0.58±0.09. A true mosaic spread of 3.5°±1° and a tilt offset of 7.0°±0.5° combine to give an effective mosaic spread of 17°±1°. There is evidence from the {111} peak intensities that the azimuthal distribution of grain orientations is non-uniform.

6.7 Dark Field Texture Analysis

6.7.1 Introduction

Another cross-sectional technique which can be used to map how the texture develops through a film is shown here. This method is similar to standard scanning BF imaging, only the intensity of a particular reflection is used to form the image instead of the unscattered beam. For a film textured in the [*uvw*] direction, the (*uvw*), or equivalent, reflection is directed onto the BF detector in scanning using the diffraction alignment coils. Thus the scanned image is similar to a [*uvw*] DF image where the grains which are oriented in the texture direction appear bright. The reason why the experiment is performed in scanning rather than CTEM DF imaging is due to the subsequent image processing analysis. Image processing is used to measure the degree of texture along a line parallel to the substrate surface by determining the fraction of the line which is bright.

The following analysis is modelled on a film which is only one grain thick in the beam direction. Later, it is shown to apply to this polySi film since it has a tilt offset. The principle behind the technique is not new. However, the remainder of this chapter describes an original approach to the technique, and shows how the results compare to those from the diffraction technique. Additional information on the grain growth of the polySi film is also produced and a discussion on the application and accuracy of the technique is given.

6.7.2 Experiment

Figure 6.20 shows an example of the type of cross-sectional DF image, where grains which have a [110] orientation appear bright. The image astigmatism is quite noticeable and is due to the off-axial reflected beam passing through the post-specimen lenses. This can be reduced by tilting the beam before the specimen to allow the reflection to be on-axis, but this alignment is not available in the scanning mode used.

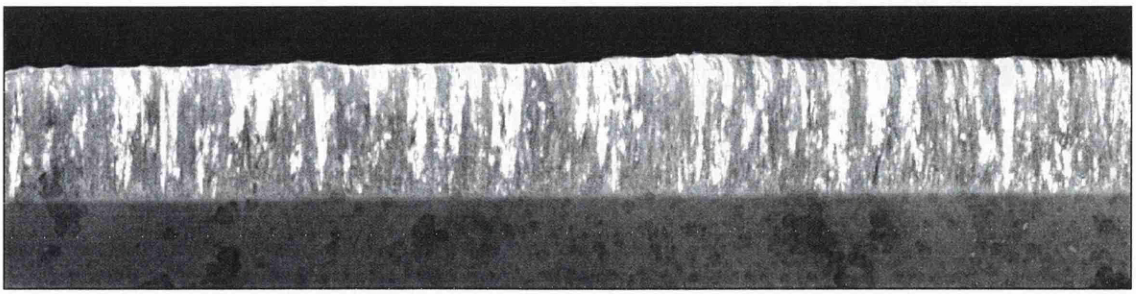

Figure 6.20: *[220] DF scanning image showing some of the textured grains. The curved image distortion is caused by the image acquisition software*

Image processing, as described later, can be used to determine the fraction of a line parallel to the substrate which is bright, i.e. textured. Thus, the development of the texture can be determined quantitatively. This method is accurate if the specimen is only one grain thick, otherwise quantitative analysis must involve the determination of the level of brightness at each point in the film in cross-section. If the specimen is several grains thick, then the technique can still be used to determine the texture development qualitatively if a tilt offset is present (see later).

Several other considerations must be made prior to the image processing. Firstly, the camera length must be set to fit into the detector aperture the [220] reflections which lie in the texture direction within the effective mosaic spread. It must also be adjusted to ensure no other reflections are detected. The BF aperture is known to be 7.5mm in diameter and the camera length is adjusted accordingly. Selecting all the textured [220] reflections is further complicated if a tilt offset exists. The presence of a tilt offset means that it is likely that not all the [220] reflections in the surface normal direction will be detected. This is a result of the 3-dimensional effect of the tilt offset in reciprocal space. The schematic diagram in figure 6.21 shows that the limits of the principal peak in the rocking curve gives the diffraction plane a certain 'thickness', or depth, in reciprocal space[19]. If the tilt offset, θ_0, is large enough, the out-of-plane [220] reflections will not be excited. This results in some of the textured grains not appearing bright in the scanned image. To excite those out-of-plane reflections the sample must be tilted through $2\theta_0+2\alpha$ around an axis parallel to the substrate surface and perpendicular to the beam. Thus a number of individual scanned images must be acquired at different

specimen tilts covering the whole tilt offset 'annulus' in reciprocal space. Possibly a more accurate method would be to expose the [220] DF image in CTEM on a photographic film while tilting the specimen. Here, the specimen would have to be tilted at a constant angular velocity for maximum accuracy. Blurring in the image will occur however if the angle tilted is significant. Also, the image processing is more complex using digitised negatives and image contrast and brightness is more difficult to control, so the scanning approach is used here.

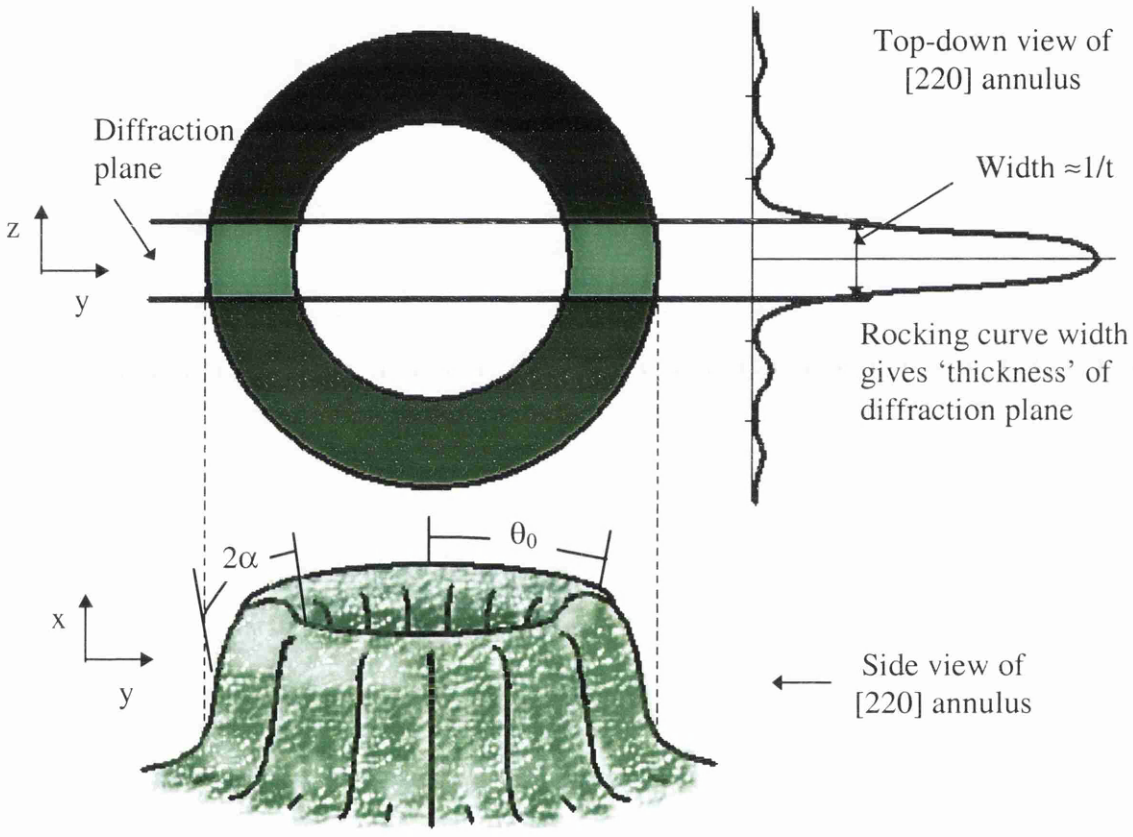

Figure 6.21: *Schematic showing how the fraction of the [220] reflections which are excited depends on the width of the rocking curve which, in turn, depends on the grain thickness*

To calculate the number of individual images required to detect every [220] reflection in the annulus, the width of the rocking curve has to be calculated for the polySi grain sizes. The angle subtended by the rocking curve at the [220] annulus is given by equation 6.14 for t=10nm grain sizes and the lattice parameter, a=0.543nm.

$$\beta_r = \frac{1/t}{g} = \frac{a}{t\sqrt{2^2+2^2+0^2}} \approx 1.1^\circ \qquad [6.14]$$

This means that the excited reflections are contained in a band ≈1.1° wide across a ring having inner and outer radii, 5.25° and 8.75° respectively. This would imply that ≈16 images, taken at regular tilt intervals of 1.1°, are required to detect every [220] reflection in the texture direction. Experimentally, only ≈3 images are required. This is determined from observation of the tilt required to bring a textured grain in and out of the diffraction plane. Care must be taken at this point to ensure only one particular grain is examined as the film is a few grains thick in the beam direction. The reason for this seeming large discrepancy between the numbers of images required is due to the limits of the rocking curve being poorly defined. It is clear from this, and everyday diffraction work, that a reflection can be appreciably excited beyond the first peak in the rocking curve. This analysis suggests that the effective width of the rocking curve could be as much as six times the principal peak width for appreciable reflection excitation.

Three images taken at tilt angles of 0°, +6° and -6° are used to extract quantitative texture information. For maximum accuracy, these images should not be analysed separately to determine the total degree of texture. This is partly due to the same textured grains being considered more than once, and also because the following calculations for the degree of texture would be more complicated (see later) if the images were analysed separately. Instead, these images are superimposed digitally and the greyscale threshold of 255, for white, ensures that if the same region in two images is bright it is only counted once. It should be noted that this method may underestimate G for highly textured regions where the specimen is >1 grain thick. However, without using complex statistical analysis, this method is still likely to be the most accurate. To superimpose the images they are aligned, if necessary, using a cropping mechanism and the surface topology is used to reference them. A set of three aligned images are shown in figure 6.22. A summing calculation is performed on the greyscale values at the same pixel in each image. Apart from the textured grains in each original, the image is very dark. So, by summing the pixel values, the dark regions having no textured grains are

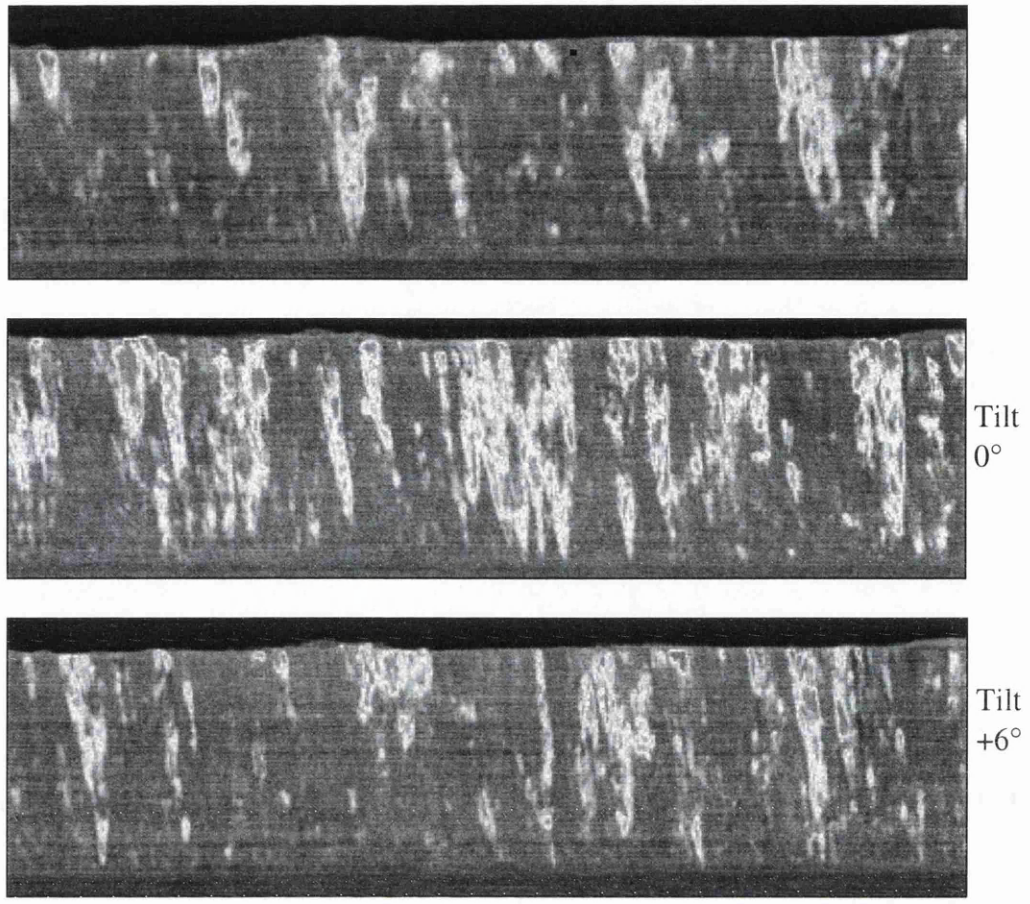

Figure 6.22: *Three DF images of the exact same region taken at different tilt angles through the annulus*

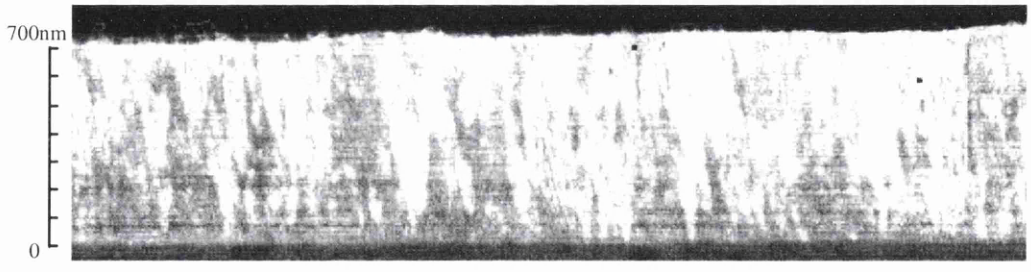

Figure 6.23: *Superimposed image of those in figure 6.22*

brightened only slightly. The resultant image contains all the bright regions from each original. This operation can be performed using the image processing package 'Paint Shop Pro' version 4.0 by JASC Inc, and the superimposed image is shown in figure 6.23. Using the C-program listed in appendix C, the image is then converted from greyscale to bitmap where greyscale values >100 (grey to white) are represented by bit 0

and ≤100 (dark grey to black) are 1. Thus, grains which are textured contain pixels of value 0. The program also outputs the image pixel values as a 2-dimensional array in a text file. The reason for this bitmap conversion is that, in order to calculate the fraction of a line which is bright, the highest possible line value has to be known, i.e. when all the line is dark. Figure 6.24 shows an example of such a binary image. The pixel

Figure 6.24: *The binary image of figure 6.23 used to allow simple calculations to determine the degree of texture through the film*

values, denoted by i_x, along a line parallel to the substrate is represented by a column in the spreadsheet. Therefore, in a line containing n pixels, the fraction of the pixel values which are set at 0 can be readily calculated as a function of distance from the substrate using equation 6.15. The results are graphed in figure 6.25 showing the texture development.

$$G = 1 - \frac{\sum i_x}{n} \qquad [6.15]$$

The error in each value is difficult to assign as it depends on the criteria in deciding whether the greyscale value is bright or dark. This is a systematic error and should affect the relative values of G. However, there is generally a clear difference in greyscale values for bright and dark regions so this error is not normally appreciable. With >100 data points in the graph, the random errors can be approximated, as it is likely that the true G at each distance does not fluctuate as much as the values suggest. The average random error is ±0.05. The average G from the values shown in figure 6.25 is 0.48±0.01.

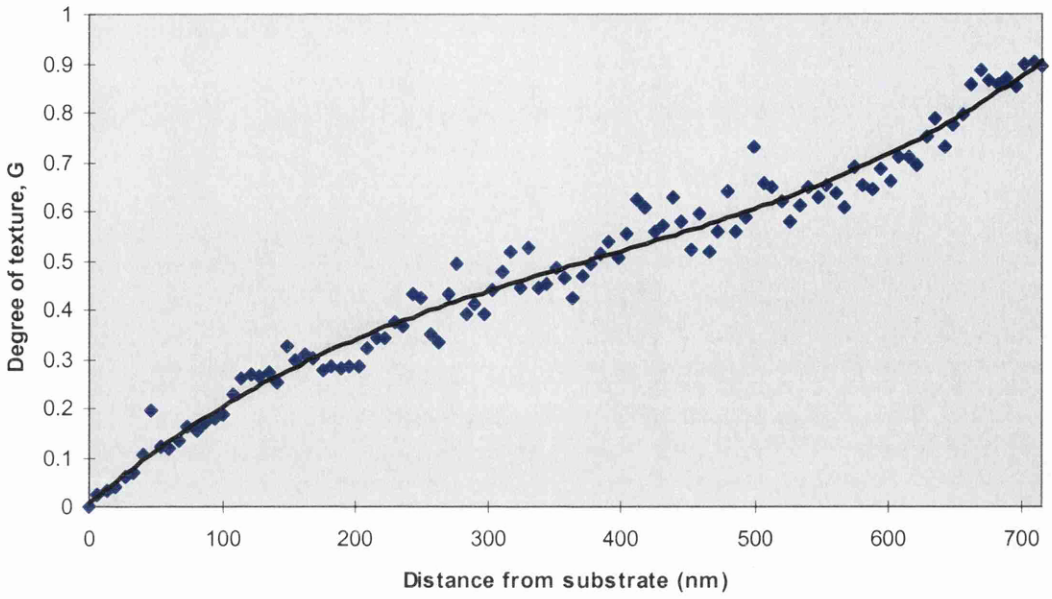

Figure 6.25: *The degree of texture calculated by the fraction of a line across a binary image of the film which is bright*

6.7.3 Discussion

There are several sources of error in this analysis for the determination of the degree of texture as a function of distance from the substrate. These are listed below along with their effects on the analysis.

Table 6.5: *Sources of error in DF imaging analysis*

Problem	***Effect***
Specimen >1 grain thick (no tilt offset, see later)	Reduced quantitative accuracy as a bright signal could arise from any or all of the grains at a given point in cross-section
Judging greyscale threshold	Particularly when combining images. Varying levels of brightness but not normally difficult to determine threshold
Judging tilt increment (only for tilt offset)	Difficult to ensure all possible textured reflections around the annulus are excited
Image astigmatism	Reduced image clarity and could marginally overestimate the degree of texture due to spreading of bright regions
Grain size distribution (only for tilt offset)	Results in a spread of rocking curve widths causing uneven weighting of grains on images taken through tilt angles

From table 6.5 it is clear that the most quantitative results can be obtained for a specimen whose thickness is one grain thick and the film does not have a tilt offset. Under these circumstances, quantitative information can be obtained accurately when the image is converted to a 2-dimensional array of binary values. Otherwise, it may be argued that it is more informative to attempt a qualitative approach by retaining the greyscale values and summing each row as before. This way the level of brightness at each point is accounted for, and hence the relative number of grains through the film which are textured. Problems with saturation (practical difficulty only) and relating the greyscale to the electron intensity are only some of the reasons for avoiding this approach. Instead, when the specimen is >1 grain thick, the results may only be used as a estimate of the degree of texture. However, since the same problems are present through the thickness of the film, the analysis can be used to provide a qualitative report of the texture development. Figure 6.26 shows how the results from the DF image analysis compare with two sets of results from the scanning diffraction technique

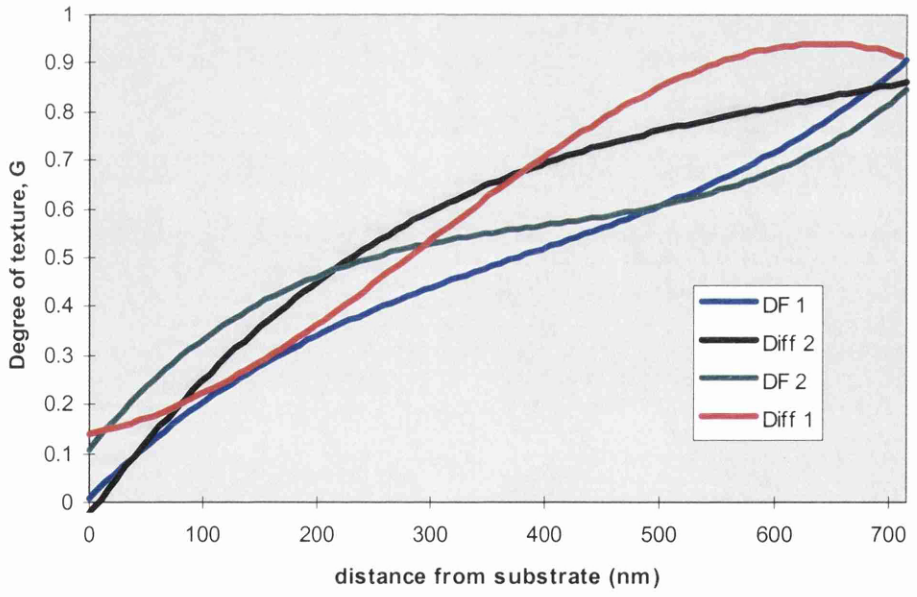

Figure 6.26: *Comparison of two results from the diffraction technique and two from the DF technique for the texture development in the polySi film*

described earlier. The comparison suggests that the DF analysis can be used to give a quantitative description of the degree of texture to an accuracy of $\approx\pm 0.15$. However this

level of accuracy can be affected by several factors as mentioned earlier. More complex image processing, starting at the initial DF image, could improve the accuracy of the results. The specimen could also be thinned to be one grain thick for further improvement in the accuracy. The average value, along with the average range, of all four sets of results is shown in figure 6.27. Clearly, both techniques are shown to produce quantitative and reproducible results.

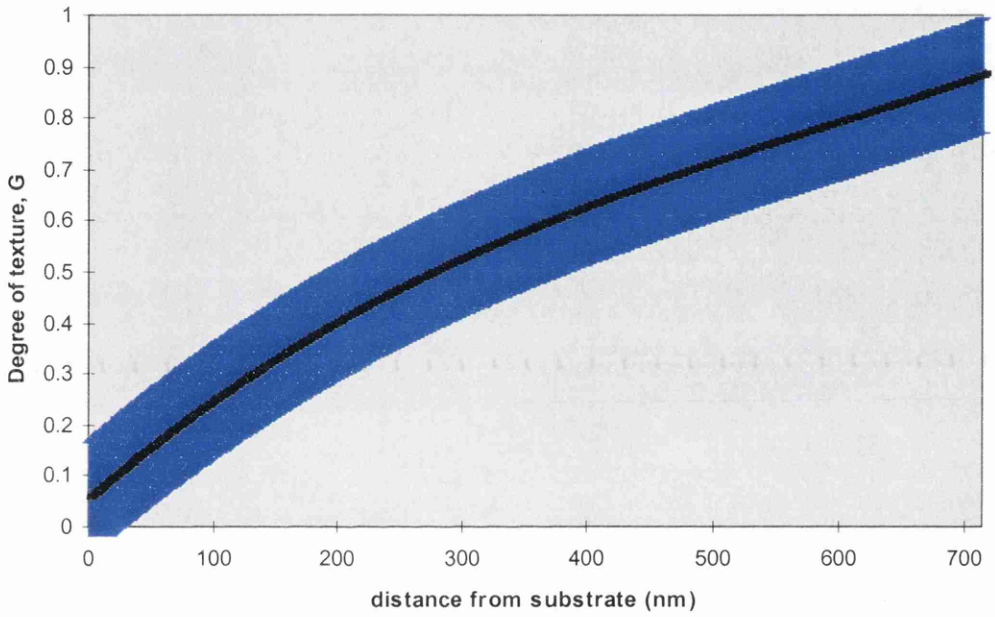

Figure 6.27: *The average G through the film showing the range of values obtained from the results in figure 6.26*

It should be noted that the degree of texture can be overestimated particularly at highly textured regions if the specimen is several grains thick. This is due to the projection of a plane through the film onto a line. For example, if 50% of the grains are textured along a line, it is still possible for the line to be completely bright if at least one grain is textured through the film at every point. The larger the number of grains through the specimen thickness, the less accurate any quantitative results. However, as figure 6.26 shows, the results agree within a 20% error margin at each point with the quantitative results from the diffraction technique described earlier.

Under the correct circumstances, the DF texture technique could provide more statistically accurate results than the diffraction technique. Unless there is a significant tilt offset, every grain which is oriented in the texture direction will be detected if the specimen is one grain thick. This is not the case when considering the {111} reflections in the diffraction technique. Thus the DF technique would be preferred when the specimen is thin, there is no tilt offset, and there are fewer grains present.

One major advantage of the DF technique is the ability to show how the textured grains evolve; whether they nucleate at positions through the film, or whether they nucleate at the substrate and grow laterally as the film grows. This information is not available from the analysis in the diffraction technique. In most cases, the qualitative results from the DF technique could complement the quantitative results from the diffraction one to produce a very descriptive interpretation of the growth processes in a textured film. For the polySi film studied here, the textured grains do grow laterally, but not to a significant extent. The average angle of the textured grain boundaries to the growth direction is ≈5° so the lateral growth rate is ≈1/80 of the surface normal growth rate. This is similar to the near-columnar grain structure described in chapters 4 and 5[20]. Most of the textured grains nucleate within ≈50nm of the substrate surface, however another large fraction nucleate at ≈250-270nm from the substrate as shown by the results from the diffraction technique and the DF images. Perhaps some aspect of the deposition conditions fluctuated here, e.g. the pressure dropped slightly. This observation is not very significant here, however it highlights the usefulness of the technique in identifying any fabrication process abnormalities.

6.8 Conclusions

Two techniques have been described which can be used to provide both a qualitative and quantitative description on the texture development in a polycrystalline film. To enable a quantitative description of the texture, a definition of the degree of texture is proposed as the volume fraction of grains which are oriented in the texture direction,

within the effective mosaic spread. On applying different analyses on the same, the quantitative results from both techniques are found to be similar (<20% error) but not identical. The reasons for the discrepancies between the results are well understood and can be improved upon if greater accuracy is required. The development of texture through the polySi film is shown to be gradual starting at ≈15% and rising to >90% through the ≈700nm thick film.

Both experiments are straightforward and can be performed in most STEMs without the need for peripheral attachments to the microscope. By repeating the experiments, the analyses are shown to be reproducible and accurate.

References for Chapter 6

[1] H. J. Bunge, *Experimental Techniques of Texture Analysis,* Deutsche Gesellschaft fur Metallkunde e.V, (1986), 1-12

[2] H. J. Bunge, Int. Mats. Revs., **32,** 6 (1987) 265

[3] B. K. Vainshtein, *Structure Analysis by Electron Diffraction,* Pergamon Press, (1964) 162

[4] D. B. Knorr, D. P. Tracy, K. P. Rodbell, Appl. Phys. Lett. **59,** 25 (1991) 3241

[5] H.J. Bunge, Zeitschrift fur Metallkunde, **76**, 7 (1985) 457

[6] K. H. Puch, H. Klein, H. J. Bunge, Zeitschrift fur Metallkunde, **75**, 2 (1984) 133

[7] R. A. Schwarzer, Ultramicroscopy, **67,** (1997) 19

[8] R. A. Schwarzer, Micron, **28**, 3, (1997) 249

[9] R. A. Schwarzer, Textures & Microstructures, **20,** (1993) 7

[10] H. Kakinuma, M. Mohri, M. Sakamoto, and T. Tsuruoka, J. Appl. Phys., **70**, 12 (1991) 7374

[11] R. F. Egerton, in *Electron Energy Loss Spectroscopy in the Electron Microscope,* Plenum New York (1985)

[12] A. J. Craven, W. A. P. Nicholson, R. Lindsay, Electron Microscopy and Analysis, IOP Conf. Ser. 153 (1997) 327- 330

[13] L. Reimer, *Physics of Image Formation and Microanalysis,* Springer-Verlag, (1984) 279-291

[14] M. M. Woolfson, *An Introduction to X-ray Crystallography,* Cambridge Uni. Press, (1970) 167-174

[15] D. B. Williams and C. B. Carter, *Transmission Electron Microscopy: Diffraction II,* Plenum, New York (1996) 204

[16] B. K. Vainshtein, *Structure Analysis by Electron Diffraction,* Pergamon Press, (1964) 197-202

[17] B. D. Cullity, *Elements of Electron Diffraction*, Addison-Wesley Publ. Comp. Inc. Reading (1956) 173

[18] M. M. Woolfson, *An Introduction to X-ray Crystallography,* Cambridge Uni. Press, (1970) 158

[19] G. Thomas, and M. J. Goringe, in *Transmission Electron Microscopy of Materials*, John Wiley & Sons, New York, (1979) 94

[20] C. V. Thompson, R. Carel, Mats Sci Eng, **32**, (1995) 211

CHAPTER SEVEN

Compositional Analysis of Materials used in ICs

7.1 Introduction

With layers of materials down to 10nm or less in thickness, it is becoming increasingly important to be able to perform compositional analysis on a nanometre scale in modern devices. Compositional analysis is required to measure the extent of the diffusion between neighbouring materials and identify contaminants. Problems arise if layers of materials either diffuse too much or too little into surrounding materials, and minute traces of contaminants can render a device inoperable.

As the beam in a TEM can be focussed down to ≈1nm, the TEM is an ideal instrument in which to use analytical techniques such as energy dispersive X-ray (EDX) analysis and parallel electron energy spectroscopy (PEELS). EDX is much more commonly found in failure analysis laboratories as it can be used in SEMs and the experimental set-up is significantly more user-friendly. However, some EDX systems cannot provide quantitative information on elements like nitrogen, boron or carbon, and sometimes oxygen, which can be found in today's devices. PEELS can detect almost every element and also provides information on the chemical environment of the element. For useful PEELS analysis, however, the specimen has to be ≤70nm thick, whereas EDX can produce meaningful results from a specimen ≈3 times that thickness.

With the emphasis on EDX, this chapter develops both compositional techniques in the TEM for use in device materials characterisation. First of all, the limits of EDX are explored in the TEM, in particular the spatial resolution and the sensitivity. EDX is then used to determine the effectiveness of a diffusion barrier in a modern device and identify the source of an unknown material found in a device structure. The value of PEELS is demonstrated in identifying an element according to its chemical environment and atomic structure. It is also used to complement the EDX data from the diffusion barrier experiment by highlighting the elements which are present in the barrier that are undetectable with the EDX system used.

In the following section the spatial resolution of EDX is determined experimentally for a dedicated STEM. Several authors[1],[2] have already produced theory and experimental results on the spatial resolution of similar microscopes. This section compares the experimental results measured here, but also describes the various stages of quantitative EDX analysis and addresses several interesting problems. Also described is the microscope configuration for EDX in the VG HB5 microscope.

7.2 Spatial Resolution of EDX

7.2.1 Introduction

It is of great interest to determine how small an area on a device can be probed in the TEM to identify the elements present at that point only. The spatial resolution of EDX analysis differs from the spatial resolution of scanned images[3]. The main reason is that, in the TEM, electrons which are scattered at large angles by the specimen do not contribute to the image as they are intercepted by the apertures. However, these electrons produce X-rays at significant distances from the centre of the beam, reducing the spatial resolution of the technique.

In the Philips CM20 microscope, the probe size can be reduced to ≈1nm by the condenser lens configuration (see chapter 2). The current in such a beam is too small to produce enough X-rays for useful EDX analysis. (Although, Philips claim a 1nA current in a $1nm^2$ probe for the CM20 at Glasgow. From the results in chapter 2 and from comparison to other microscopes where the current is known, this does not seem to be the case.) From experiments on the CM20, useful EDX information can only be obtained with a spot diameter ≈5nm or more to reach the current necessary for a reasonable signal to noise level. This means that the spatial resolution of EDX analysis in this microscope will be >5nm and dependent on beam spreading in the specimen. To obtain a more accurate account of the EDX resolution possible in TEM, a different microscope is used which produces a ≈1nm spot diameter with a current suitable for useful EDX microanalysis. The VG HB5 dedicated STEM has a cold field emission gun which can produce a probe diameter[4] down to ≈0.5nm having sufficient current for EDX microanalysis. For this reason, the HB5 is used for much of the microanalysis described in this chapter.

7.2.2 EDX on the VG HB5 STEM

A schematic diagram of the 100keV HB5 STEM is shown in figure 7.1. The relevant issues concerning EDX microanalysis on this microscope are described here. As with the Philips CM20 the X-ray detector is mounted at a 100.5° angle to the incident beam to optimise the signal to background X-ray detection. The dedicated specimen holder is a 60° double tilt cartridge which is controlled by motorised x and y tilts on the control panel. The detector is positioned at a 45° angle to both tilt axes and for maximum detection efficiency, the specimen should be tilted towards the detector by ≈20° in both directions.

As for the lens and aperture configuration, the smallest (50μm giving 5.5mrad convergence) virtual objective aperture (VOA) is used to minimise the probe size. The objective aperture is not inserted as this is very close to the specimen and electrons

scatter by it will produce unwanted X-rays. Stray electrons emerging at large angles from the VOA are removed by the insertion of a selected area aperture (SAA) which is positioned before the specimen. The C2 lens is switched off for normal microscope operation and C1 is the probe forming lens. This configuration optimises the beam current but produces a slightly larger (≈1nm) probe diameter.

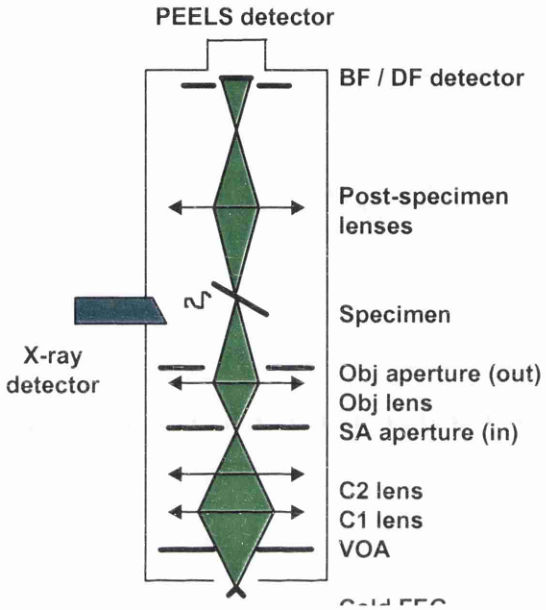

Figure 7.1: *Schematic of the HB5 with respect to EDX experimentation*

The EDX detector is controlled by a Link eXL system which is also used to acquire digital images. The software is set up to control acquisition parameters, e.g. duration, and display the spectrum for, typically, 0-20keV X-rays.

7.2.3 Specimen Alignment for EDX

One way of determining the spatial resolution of the EDX microanalysis is to trace the composition of a material across a very abrupt interface in a specimen. The sharpness of the step in the EDX analysis can readily be used to determine the spatial resolution. A cross-section of a GaAs quantum well structure is used to demonstrate the spatial

resolution as the quantum well interface is known to be <0.5nm wide[5]. The specimen used here is shown in figure 7.2 where a series of GaAs quantum wells (dark areas) of different thickness are embedded between much thicker layers of $Al_{0.3}Ga_{0.7}As$.

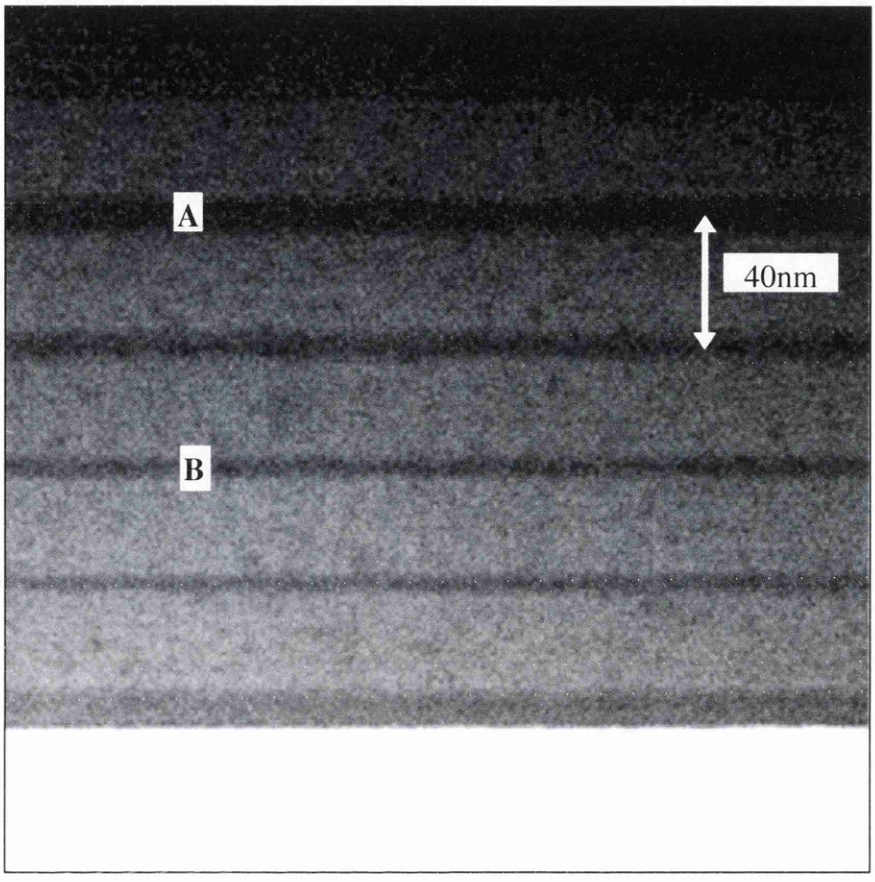

Figure 7.2: *STEM image of the quantum well specimen where the dark regions are the GaAs wells. The wells used for all of the EDX analysis are labelled 'A' and 'B'*

For maximum accuracy, the specimen has to be oriented to ensure the plane of the interface is parallel the beam. If not, the step in the compositional profile across the interface will be increased by θt, where t is the specimen thickness and θ is the angle between the beam and the interface plane. Since the specimen has to be tilted at a certain angle in two directions, thought has to be given to the orientation of the specimen in the tilt cartridge before it is inserted into the microscope. The plane of the interface should be aligned at approximately 45° to both tilt axes in the direction of the detector. This way, when the specimen is tilted for optimum detection efficiency, the

plane of the interface is approximately parallel to the incident beam direction. This set-up is shown in figure 7.3.

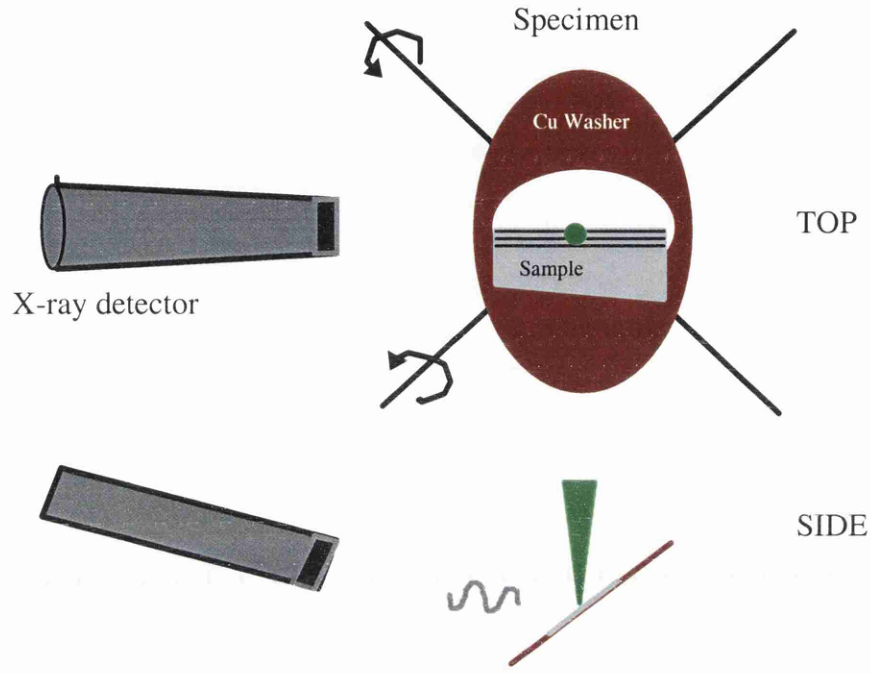

Figure 7.3: *The alignment of the specimen in the cartridge to ensure the electron beam is perpendicular to the interfaces when the specimen is tilted for maximum EDX detection efficiency*

Fine adjustments to the tilt of the specimen can be performed when it is inside the microscope. The best way to ensure that the interface is parallel to the beam is to use the Kikuchi diffraction pattern of the substrate if the substrate is crystalline and the growth direction is known. The substrate in the quantum well specimen is grown with the [110] direction normal to the bulk surface. In this case, when the specimen is perpendicular to the beam, i.e. untilted, the Kikuchi pattern resembles that of figure 5.1b corresponding to the $[\bar{1}10]$ zone axis. Indeed, this pattern could correspond to any region on the Si Kikuchi map which is perpendicular to [110], and is determined by the direction cleaved on the bulk sample during specimen preparation. As the specimen is tilted towards the X-ray detector in both directions, the centre of the pattern is made to remain between the two <110> Kikuchi lines by adjusting the tilt controls. This way the

[110] growth direction is kept perpendicular to the beam. As a result, the specimen is aligned as close as possible to the optimum detection angle while the interface is parallel to the beam.

The error, $d\vartheta$, in using the Kikuchi pattern to align the specimen in relation to the beam is determined using the angular resolution of the pattern. If the zone axis of the tilted specimen lies between the two (110) Kikuchi lines then the maximum $d\vartheta$ is given by the separation of the Kikuchi lines, 2θ, where θ is the (110) Bragg angle. This seems a pessimistic estimate of $d\vartheta$, but the level of contrast in the diffraction patterns obtainable on the screen on the HB5 is considerably low. Using equation 2.14, $d\vartheta$ is $\approx 0.5°$ for a 100keV electrons. For a 30nm thick specimen, this error corresponds to a loss of edge resolution of ≈0.3nm.

7.2.4 Experiment

Once the specimen is aligned using the Kikuchi pattern, the height of the specimen is brought into focus by using the z-shift. The mechanical z-shift is used as the objective lens strength is optimised for the post-specimen lenses and this corresponds to a fixed specimen height. Fine focus adjustments are made using the objective lens. The magnification of the microscope is increased so that the CRT screen contains the 10nm thick GaAs quantum well as well as a smaller region of the surrounding AlGaAs on either side. This image is shown in figure 7.4 and corresponds to area A in figure 7.2. This area is determined from PEELS to be ≈40nm thick (described in more detail in chapter 2). A transparent acetate film containing a ½cm grid is attached to the screen to provide a reference scale for the probe positions. The eXL program is configured to set the acquisition time to 30s to allow for good signal to noise levels while minimising the extent of specimen damage, drift and contamination.

The experiment consists of acquiring EDX spectra at regular distances through and beyond the GaAs quantum well using the reference grid. Here, eleven spectra are acquired and an example of one is given in figure 7.5 where the Ga and As K peaks are

shown in detail. Referring to the example, the peaks of interest are the Al Kα, Ga Kα and Kβ, and the As Kα and Kβ. The production of these X-rays is discussed in chapter 2 and reference [6].

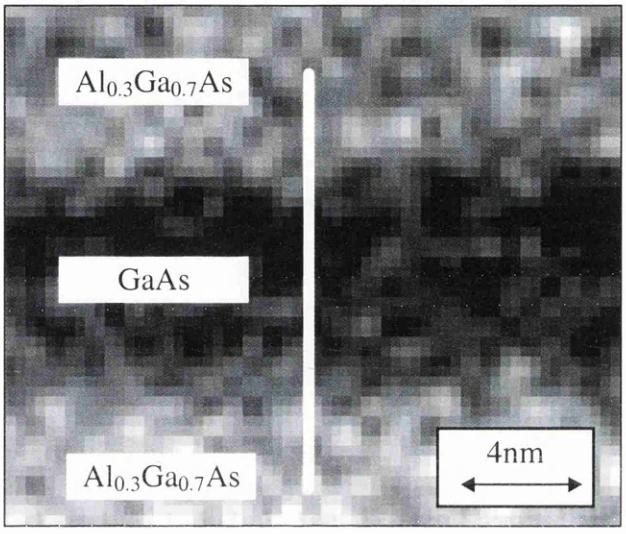

Figure 7.4: *Image showing the line of analysis through the GaAs quantum well*

It is decided that the best way to determine the material composition at a given point around the quantum well structure is to determine the ratio of Ga to As atoms. In the well, the atomic fraction of Ga/As is 1, whereas, in the AlGaAs regions, it is 0.7. Another possible approach of profiling the change in composition across the quantum well is to monitor the Al counts. However, these counts depend on both the specimen thickness and beam current. More importantly the signal to background Al count is low and the peak is very close to the As Lα so accurate results are difficult to obtain.

7.2.5 Analysis of the EDX Spectra

To calculate the atomic ratios, the relative number of Kα counts from each element is ascertained. The Kα counts are given by the integrated counts under the relevant peak

once the background counts have been removed. It can be seen from the example given in figure 7.5 that the background level at either side of the Ga and As peaks are

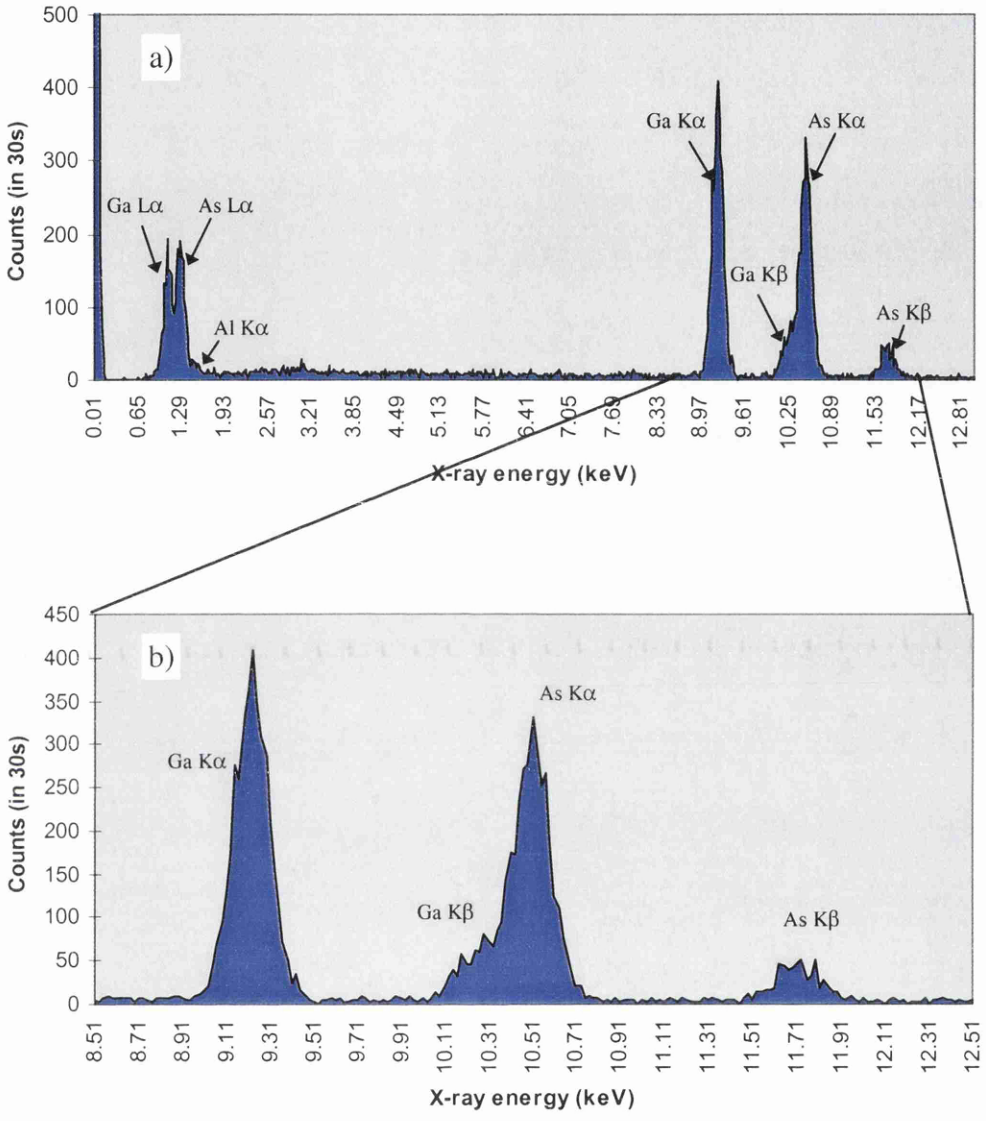

Figure 7.5: a) *An EDX spectrum from the GaAs region close to the AlGaAs interface showing the various peaks, and b) a close-up of the Ga and As K peaks used in the quantitative calculations*

insignificant. The background is calculated as being <3% of the peak counts so their removal is unnecessary for this experiment. The eXL program can be used to determine the integrated count from user-defined windows, but instead this procedure is implemented later. Here, the experimental spectra are read in to a spreadsheet where the

first column is the energy values and the subsequent columns correspond to the X-ray counts for the eleven acquisitions. In this way, the analysis and graphical representation can be fully customised. Equation 2.19a shows how the relative number of Kα counts can be used to determine the atomic ratio of two elements in an EDX spectrum. Table 7.1 lists the relevant parameters used in these equations for Ga and As.

Table 7.1: *Values used to calculate the atomic ratio of Ga to As*[7],[8]

Element	*Kα peak energy (keV)*	*Kα Cross-section, σ_c (barns)*	*Partition function, s*	*Kβ/ Kα*	*Detector efficiency, ε*
Ga	9.243	75.54	0.8726	0.146	1
As	10.532	67.99	0.8561	0.156	1

Since the Ga Kβ and the As Kα peak overlap in the spectra, an indirect method of determining the counts from each element is used for accurate results. The direct approach would consist of deconvoluting the peak shape into two Gaussian peaks, one from each element. However, it is decided to use the indirect approach as deconvoluting software is not readily available. To determine the Ga Kβ contribution to the overlapping peaks the partition function, *s*, is used. This function describes the fraction of all K X-rays (i.e. Kα + Kβ) which are Kα. This can simply be modified to determine the fraction Kβ/Kα as shown in table 7.1. Since the number of Ga Kα counts are known from the spectra, the Ga Kβ counts are readily determined, and hence subtracted from the total in the overlapping peak count.

7.2.6 Results

An excerpt from the spreadsheet showing the calculation of the atomic fraction of Ga and As across the well is given in table 7.2. The error, *dR*, in each value of the atomic ratio, *R*, is calculated from the random error in each peak count, *C*, and is given by equation 7.1.

$$\left(\frac{dR}{R}\right)^2 \approx \left(\frac{\sqrt{C_{Ga}}}{C_{Ga}}\right)^2 + \left(\frac{\sqrt{C_{As}}}{C_{As}}\right)^2 \qquad [7.1]$$

Table 7.2: *An extract from the spreadsheet used to map the Ga/As atomic ratio across the well*

distance (nm)	*0*	*2.3*	*4.6*	*6.9*	*9.2*	*11.5*	*13.8*	*16.1*	*18.4*	*20.7*	*23*
Ga (Ka) counts	3520	3459	3316	3478	3794	3952	3804	3580	3074	2630	2595
As(Ka)+Ga(Kb)	4230	3997	4093	4020	3892	3672	3630	3481	3364	3196	2936
As(Ka)	3716	3492	3609	3512	3338	3095	3075	2958	2915	2812	2557
kxI(Ga)/I((As)	0.85	0.89	0.83	0.89	1.02	1.15	1.11	1.09	0.95	0.84	0.91
error Ga (%)	1.69	1.70	1.74	1.70	1.62	1.59	1.62	1.67	1.80	1.95	1.96
error As (%)	1.64	1.69	1.66	1.69	1.73	1.80	1.80	1.84	1.85	1.89	1.98
total error (%)	2.35	2.40	2.41	2.39	2.37	2.40	2.43	2.48	2.59	2.71	2.79
abs error	0.02	0.02	0.02	0.02	0.02	0.03	0.03	0.03	0.02	0.02	0.03

The reason equation 7.1 is just an approximation is because the As counts are calculated indirectly and the exact equation is significantly more complicated. Since the Ga contribution to the overlapping peak is small, equation 7.1 stands as a good approximation. The results given in table 7.2 are graphed in figure 7.6a. The step widths are ≤3nm wide implying that the resolution of the analysis is ≤3nm. It is very difficult to reach a more conclusive value of the spatial resolution here since the distance between each EDX acquisition is 2.3nm. To perform higher resolution analysis, the 4nm thick GaAs quantum well (region B on figure 7.2) is used as an image containing the whole width of the layer can be obtained and used for scale referencing. The error in the quantum well thickness is <0.5nm according to the manufacturers[5]. The specimen thickness here is ≈20nm thick as determined from PEELS. The same experiment is performed across this well with 0.5nm between acquisitions. Great care has to be taken when acquiring the spectra to avoid the effects of specimen drift. The topography of the layer is drawn on the acetate sheet and the specimen is repositioned using the electrical shifts if necessary between acquisitions. The results of the analysis are shown in figure 7.6b. From figure 7.6b, the spatial resolution of the EDX analysis is shown to be ≈1nm. However, the errors in each value can accommodate a spatial

resolution down to ≈1.5nm. It is noticed in each case that there is a less abrupt interface at the top surface of the well (RHS of profile). It is likely that the introduction of the Al

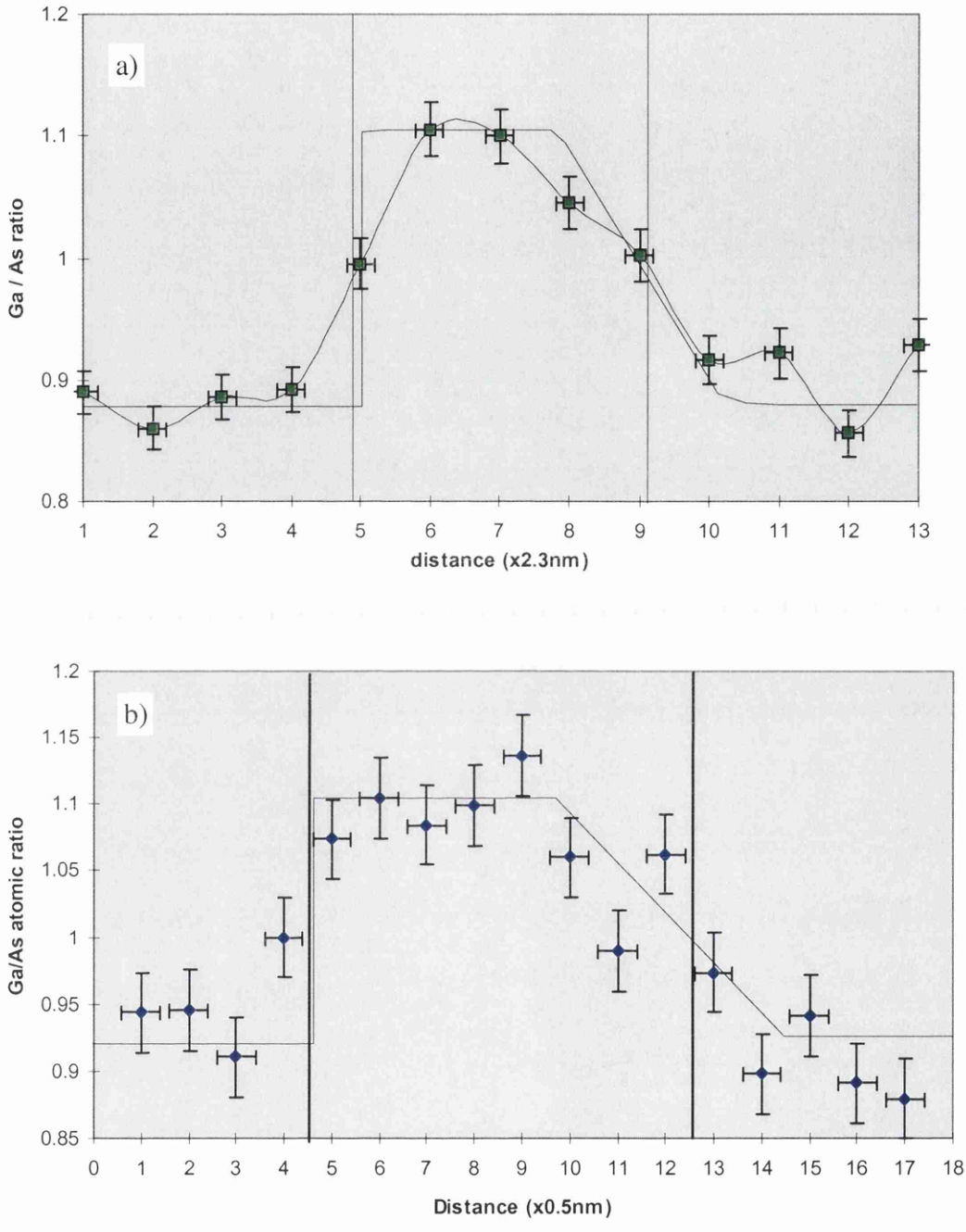

Figure 7.6: *Ga /As profiles across the a) 10nm and b) 4nm GaAs quantum well. The latter shows the spatial resolution possible with EDX. The superimposed curves are possible Ga/As profiles*

into the deposition chamber was more gradual than its removal. If it were a result of diffusion between the layers, one would imagine that the other interface would be similar. However, it is conceivable that AlGaAs could diffuse more rapidly into a GaAs surface than the reverse process depending on the bonding energies of the adatoms.

Table 7.3 lists the theoretical spatial resolution for a ≈1nm probe size using Monte-Carlo simulations on Ge for the same beam parameters used here in the HB5 microscope.

Table 7.3: *Results for Monte Carlo simulations to calculate EDX resolution*[1]

Specimen thickness	***Radius (X-ray generation)***		***EDX resolution***	
	50%	90%	50%	90%
20nm	0.05nm	0.2nm	1nm	1.1nm
40nm	0.2nm	2.0nm	1.1nm	4.1nm

The EDX resolution in table 7.3 is the diameter of the resulting area in which 50% and 90% of X-rays are generated. It is calculated by adding the incident beam diameter and the diameter of the region that X-ray are generated from in quadrature. Ga and As are very similar to Ge in atomic number and density so the results should be approximately the same for these elements. Since the beam diameter is known to be ≤1nm the spatial resolution of the EDX is ≤1nm for a 20nm thick specimen and between ≈1-4nm (depending on the choice of 50% or 90% of the X-rays) for a 40nm thick specimen using Monte-Carlo simulations. For simplicity, the spatial resolution is described hereon as the diameter of the area containing ≈70% (≈the standard deviation of the beam spread) of the generated X-rays. This conversion is approximated as a third of the way between the 50% and 90% values calculated using Monte-Carlo simulations. For the 40nm thick region, the spatial resolution is therefore ≈2nm and remains at ≤1nm for the 20nm thick region. The experimental results are in good agreement with the spatial resolution of ≤1nm determined here for the 20nm thick region and the spatial resolution of ≤3nm from the 40nm thick region. It is also shown[1] that the spatial resolution of

EDX worsens with $\tau^{3/2}$, so a spatial resolution of ≈1nm is only possible with specimens ≤30nm thick (for 70% of the X-rays).

It is noted that, in the quantum well, Ga/As>1. There are several reasons which could account for this discrepancy however they are all unlikely sources of error. The partition function or cross-sections could be inaccurate or the windows were not defined properly around the peaks. The latter reason is eliminated as various alterations on the window width were used but each still gave $R>1$. The fact that several repetitions of the experiment produce $R>1$ suggests the existence of a systematic error. This points to the source of error being the choice of the partition function or cross-section. However, both are compared with other values which are known to give Ga/As≤1 in GaAs and the values are very similar. Spectra are acquired from the GaAs substrate and the calculation of the Ga/As ratio is found to be 1.15±0.05 using the same cross-sections. This is similar to the values calculated in the quantum wells. It is possible to scale the values of R down by a factor of 1.15 to get the actual atomic ratio but the reason for this anomaly is still unclear.

The error in neglecting the removal of the background signal was shown earlier to be ≤3%. As this affects both peaks similarly, the resulting error in R, is insignificant. With the Ga and As Kα peaks so close in energy, it is very unlikely that the detector efficiency differs between them. There is also the possibility that R is actually greater than 1, but again this is very unlikely as the deposition of the quantum wells is stringently controlled. Even if there is still residual Al in the deposition chamber during the well fabrication, R should be always be less than 1. If the As Kα contribution in the overlapping peak is calculated from the As Kβ peak as shown in figure 7.5 using values in table 7.2, $R\leq 1$ in the wells. The corresponding results are graphed in figure 7.7. This approach should be less accurate as the larger As Kα counts are calculated from the smaller As Kβ ones. The error in the As Kα counts are given by equation 7.2.

$$\delta C_{AsK\alpha} = \frac{1}{0.156}\sqrt{C_{AsK\beta}} \qquad [7.2]$$

It seems, therefore, that a weighted value of R should be calculated according to the error, but it is clear that the results would be very similar to those from the first approach using Ga Kβ counts. Efforts could be made to calculate the Ga Kβ and the As Kα contributions to the overlapping peak using deconvoluting algorithms but the determination of the spatial resolution is not significantly affected by this anomaly. Only the step widths in the Ga/As profile are of major concern, not the step heights.

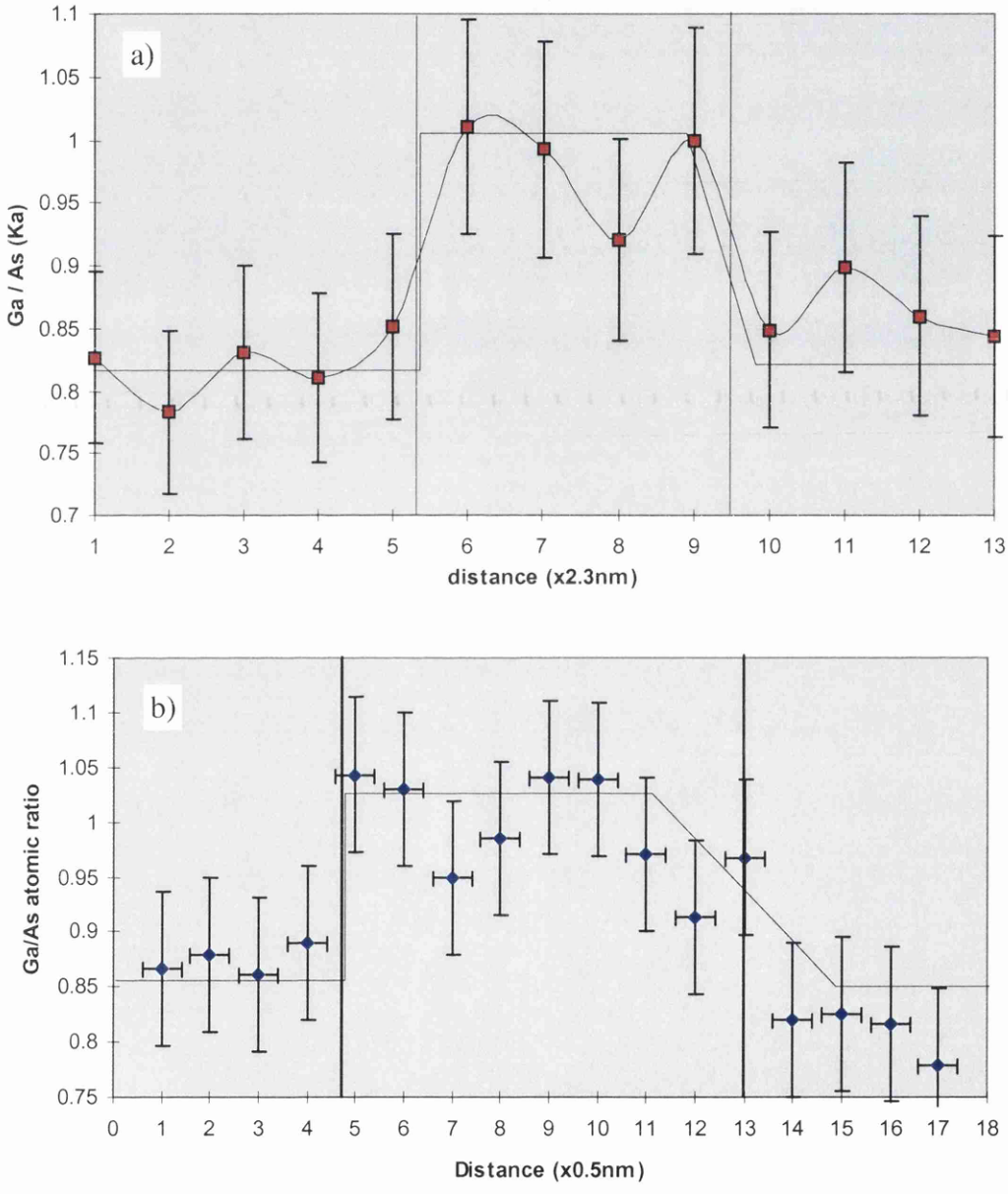

Figure 7.7: *The determination of Ga/As from the As Kβ counts for the respective results in figure 7.6. The errors are noticeably higher but Ga / As = 1 in the GaAs well*

7.2.7 Conclusion

The spatial resolution of EDX in the HB5 STEM is determined experimentally as ≈1nm for the 20nm thick GaAs specimen and ≈2±1nm for a 40nm thick specimen. Monte-Carlo simulations calculate these values as ≈1nm and ≈2nm respectively for a 1nm incident probe diameter. The resolution is described here as the diameter of the area in which 70% of the X-rays are generated from. Existing experiments[2] performed on a similar microscope show a ≈2nm resolution for a 40nm thick specimen. This resolution is possible since the beam diameter itself is known to be ≤1nm for the microscope configuration used. The spatial resolution in EDX does, however, increase markedly with specimen thicknesses and the density of the material.

From these results it is plausible to predict the spatial resolution for EDX in the Philips CM20 at Glasgow. To a good approximation, the resolution will be ≤1nm greater than the incident probe diameter if the specimen is <50nm thick. Again, this value increases rapidly for increasing specimen thickness and density.

7.3 Sensitivity of EDX

7.3.1 Introduction

With many regions in a silicon device containing small dopant concentrations in very shallow regions, compositional techniques are required to characterise the dopant concentration distribution on a nanometre scale. Depth profiling techniques which are dedicated to measuring the concentration of dopants in silicon substrates in devices are described in chapter 1. However, with these techniques subsequent re-analysis is seldom possible. EDX in the TEM is very versatile and can easily complement other investigations on a nanometre scale. So it is very informative to discuss the sensitivity of the technique in detecting low-concentrations of dopants in Si.

7.3.2 Experiment

To determine the sensitivity of EDX using the devices at hand, the As doped active regions on a transistor are used. Such a region is shown in figure 7.8 where the Al film contacts the doped substrate. Here As^+ ions are implanted into the Si substrate at an

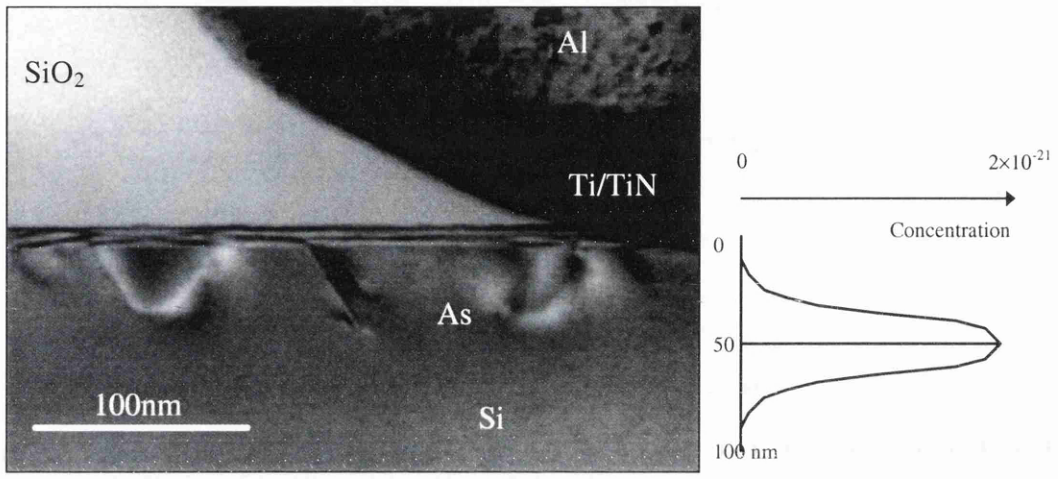

Figure 7.8: *Image and diagram illustrating the distribution of the As^+ ion concentration*

energy of 80keV and a dose of $7\times10^{15}cm^{-2}$. From this flux density the concentration distribution of the implant can be calculated. It is known[9], [10] that for 80keV As^+ ions the concentration distribution as a function of depth into the Si substrate is approximately Gaussian with a peak, d_p, at ≈50nm and a standard deviation, Δp, of ≈17nm. The concentration, N_p, at the peak is given by equation 7.3[11] where Q is the dopant dose mentioned above.

$$N_p = \frac{Q}{\sqrt{2\pi}\Delta p} \qquad [7.3]$$

The concentration reaches a maximum of $1.86\times10^{21}atoms/cm^3$ (atomic fraction of 3.6%) at ≈50nm from the surface and drops to $1.0\times10^{21}atoms/cm^3$ at a distance of 20nm from the peak. Now that the concentration distribution of the As is known, the sensitivity of EDX in detecting the As in Si can be investigated.

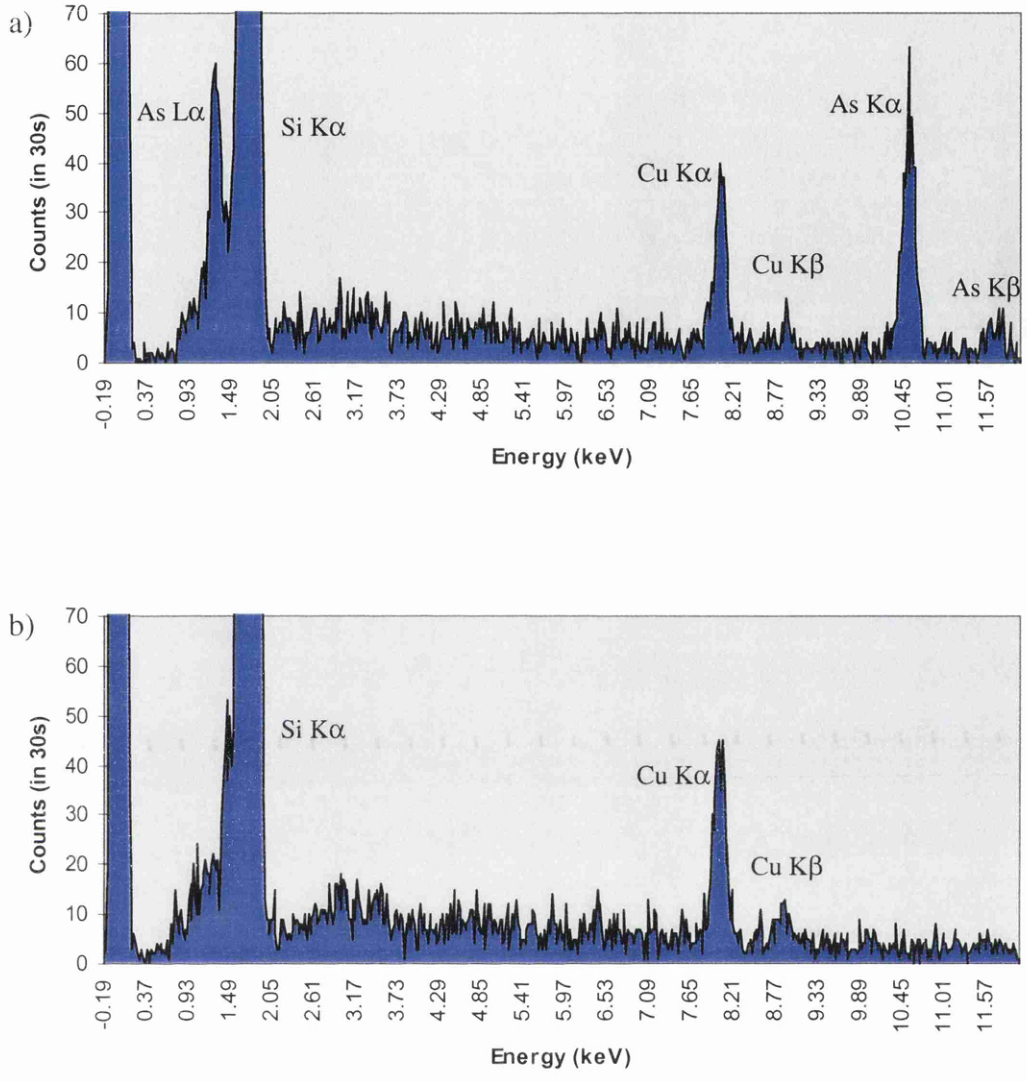

Figure 7.9: *a) EDX spectrum of the As doped Si substrate. Here EDX detects the existence of ≈600 As atoms b) EDX spectra from a neighbouring region of the substrate showing the absence of As for comparison*

In this experiment, the As^+ doped active region is probed and the resulting EDX spectrum is used to test for the detection of the As. The EDX spectrum from the centre of the implanted region is shown in figure 7.9a. The Cu peaks arise from the Cu washer which supports the specimen. Here, the microscope conditions are the same as in section 7.2 and the acquisition time is kept at 30s. Higher acquisition times would improve the signal to noise detection efficiency of dopants but significantly increases

the level of contamination. Contamination is a common problem in the HB5 microscope and is thought to be due to oil from vacuum pumps entering the column. Under the same conditions, and EDX spectrum is acquired from a neighbouring region of the substrate which is not ion implanted and is shown for comparison in figure 7.9b. The spectrum from the doped region clearly shows a significant As Kα and Lα peak. As explained in chapter 2, the Kα peaks can be used to obtain more accurate quantitative information than the Lα peaks.

7.3.3 Analysis and Results

It is interesting to determine what the count to atom ratio is for the given electron exposure to give a more quantitative description of the EDX sensitivity. In the doped region ≈480 As counts are acquired once the background is subtracted. This corresponds to the peak in the As concentration profile as described earlier. The area from which X-rays are generated is ≈2nm in diameter as calculated in section 7.2 for the ≈50nm specimen thickness, τ (measured using PEELS). The volume through which the beam passes in the specimen is approximated to a cylinder 2nm in diameter and 50nm long. The number of As atoms, N_{as}, contained in this cylinder is given by equation 7.4.

$$N_{As} \approx 50 \times \pi(1)^2 \times 10^{-27} \times 1.86 \times 10^{21} \times 10^{6} \approx 300 \qquad [7.4]$$

The number of 100keV electrons, n_e, passing through the specimen in 30s is given by equation 7.5 where the current is nominally ≈3nA for a 1nm incident beam diameter[4].

$$n_e = \frac{It}{e} = \frac{3 \times 10^{-9} \times 30}{1.6 \times 10^{-19}} \approx 5 \times 10^{11} \qquad [7.5]$$

Thus, to a good approximation, 5×10^{11} electrons at 100keV passing ≈300 As atoms produce ≈500 As Kα X-ray counts. The rate of Kα detection is therefore estimated at 1 count per 3×10^{11} electrons per atom. The number of counts, $C_{K\alpha}$, can be calculated

theoretically using equation 7.6[12] and 7.7 where the empirical constants, b_k, and c_k, are 0.62 and 0.9 respectively[13].

$$C_{K\alpha} = N\tau\sigma_{iK}\omega\varepsilon s\frac{\Omega}{4\pi}\frac{It}{e} = 1100 \qquad [7.6]$$

where,
$$\sigma_{iK} = \frac{4\pi e^4 b_K \ln\left(c_K T_0 / I_K\right)}{T_0 I_K} \qquad [7.7]$$

In equation 7.6, the detector solid angle, Ω=44mrads, and N is the As concentration, in atoms/cm^3, at the position probed. In equation 7.7, e is in c.g.s. units where 1 coulomb=3×10^{9}c.g.s units. T_0 is the incident electron energy and I_K is the K shell binding energy. T_0 and I_k are in eV. This formula does not take relativistic effects into account.

Experimentally, ≈500 As Kα counts were measured against the ≈1100 determined theoretically. Therefore, the theoretical rate of As Kα detection, T, is estimated at 1 count per ≈1.4×10^{11} electrons per atom. There are various sources of error in both approaches, but mainly the experimental approach. The main error arises in the determination of the concentration, N, of As atoms as, firstly, the concentration distribution calculated from the dosage, Q, is not exactly a Gaussian, and secondly, the accuracy in positioning the probe in the centre of the doped region is ±20nm. This alone produces an error in N, of ≈50%. Other sources of error include: $\Delta\sigma_{iK}$≈15%, $\Delta\Omega$≈10%, $\Delta\tau$≈20%, $\Delta C_{AsK\alpha}$≈5%, and to a lesser degree, the errors in ω and s are ≈2%. The error in the beam diameter could also be up to ≈30%. With all these factors considered it is possible to account for the difference in T from the experimental and theoretical approach.

Around 500 Kα counts are obtained from ≈300 As atoms in a 30s exposure to electrons, and the integrated background count is 75. It is known[3], [14] that for 95% confidence in the detection of a peak signal, S, on a background, B, equation 7.8 applies.

$$S / \sqrt{S + B} > 3 \qquad [7.8]$$

Using equation 7.8, the signal to background ratio is 21. Therefore the peak can still be detected if the number of atoms decrease by >7 times (as S will drop faster than B), i.e, the EDX system can detect ≈50 As atoms in the area probed. This corresponds to an atomic fraction of As in Si of ≈0.5%, and an As concentration of $\approx 2\times10^{20}$atoms/cm^3. To determine the theoretical signal to noise ratio for 3.6% As in Si the background count must be calculated. In a similar fashion to equation 7.6 the Bremsstrahlung counts from the Si can be calculated. Equation 7.9[12] shows the relation where σ_{bSi} is the cross-section for brehmsstrahlung production within an energy window dK into a small solid angle Ω.

$$C_{Si} = N_0 \rho \tau \varepsilon \sum \frac{N_{Si}\sigma_{bSi}}{A_{Si}} dK \frac{\Omega}{4\pi} \frac{It}{e} = 303 \qquad [7.9]$$

With this result, the theoretical signal to noise ratio is 29 as calculated by equation 7.10.

$$\frac{S}{N} = \frac{C_{AsK\alpha}}{\sqrt{C_{AsK\alpha} + C_{Si}}} = \frac{1100}{\sqrt{1100 + 303}} = 29 \qquad [7.10]$$

The theoretical results for the signal to noise compares very favourably with the experimental result of 21. This highlights the level of quantitative information obtainable through EDX analysis.

Tests have shown[4] that on the HB5 microscope, 5×10^{-20}g of ruthenium in carbon can be detected in a 2nm area. This amounts to the detection of ≈300 atoms of Ru in C so the results are comparable but should not necessarily be the same as C and Si have different Bremsstrahlung (background) intensities. Other studies have shown that the minimum mass fraction detectable is between 0.5wt% and 1wt%. This corresponds to 0.2at% and 0.4at% for As in Si which is similar to the values calculated here.

7.3.4 Conclusions

The results show that, under normal working conditions, the HB5 microscope can detect ≈50 atoms of As in Si, or a concentration of 0.5at%. Theoretical measurements imply that this should have been feasible, but experimentation has to be employed to check its practicability as this dopant is very commonly found in modern devices. Comparing the concentration sensitivity to that of the depth profiling techniques described in chapter 1, it is clear that the SIMS technique is far superior with a minimum concentration of $\approx 10^{14}$atoms/cm^3. The other techniques, RBS and AES, can detect $\approx 5\times 10^{19}$atoms/cm^3, so they are all more practical for device product analysis. However, the spatial resolution on the EDX in a TEM is far superior to the other techniques as quoted in table 1.1. It must also be noted that, as the TEM specimens are so thin and the area probed is very small, the actual sensitivity of the EDX system to a small number of dopants is better than all the others mentioned. For example, the other techniques would not compare so favourably in detecting a 2nm region of contamination.

7.4 EDX Analysis of a Diffusion Barrier

7.4.1 Introduction

In a silicon device, a diffusion barrier is used to prevent one layer of material from diffusing into a neighbouring layer. Diffusion of conducting materials severely degrades the electrical performance of a device. Having a high diffusion activation energy, the refractory metal barrier diffuses just enough into each layer for adhesion but further diffusion is not thermodynamically feasible[15]. So, if the barrier is thick enough, the materials to either side of the barrier are separated. However, the barrier materials have a significantly higher resistivity than the metal used in the device and also affects the Schottky barrier properties. This places a constraint on the barrier thickness between two conducting materials, e.g. Al and Si. The aim therefore, is to separate both materials while maintaining as thin a barrier as possible.

This section describes the investigation of the effectiveness of a Ti / TiN diffusion barrier in separating Al and polySi using EDX analysis. This type of diffusion barrier is very commonly found in modern devices[16]. The results can be used to determine the minimum thickness of the layer which will continue to separate the materials. Before the experimental procedure is described, the relevant background on Ti/TiN diffusion barriers is explained.

7.4.2 Background

When Al is deposited over polySi during device fabrication, there exists a thin native oxide above the polySi. This oxide must be reduced by the Al for intimate contact with the Si, so a short anneal above 300°C starts the reduction process[16]. However, the oxide on some patches of the Si surface will clear before the others allowing the Al to react with the Si. From phase diagrams[17], the solubility of Si into Al rises sharply at 300°C so Si rapidly goes into solution in the Al film where the oxide does not exist. The solubility of Al into Si is very low at these temperatures so the reverse process does not occur. As a result, voids appear in the Si which immediately fill with Al in the shape of spikes. This phenomenon is called junction spiking and can cause regions of high electric field at the tip, altering its electrical properties. The mechanisms for this reaction at the Al/polySi interface are shown in figure 7.10[16]. There is thus a need to obstruct this, and similar, reactions occurring during fabrication and operation of the device.

The use of simple diffusion barriers appears to be a convenient method of slowing down unwanted thin film reactions. Here the principle is that the introduction of an additional diffusion step in the overall chemical reaction will delay the onset of any deleterious changes in electrical or mechanical properties. However, even using a barrier which is not soluble in the materials to either side of it does not necessarily stop diffusion between the materials. Almost all vapour phase deposited conducting films are polycrystalline and the high density of grain boundaries will provide pathways for rapid

diffusion. Therefore, barrier materials are normally selected according to their grain boundary diffusivity. Refractory metals are the common choice for diffusion barriers on the principle that the higher the melting point the higher the activation energy for grain boundary diffusion. Examples of refractory metals are Ti, W, Mo, and Ta, and all have been used in diffusion barriers.

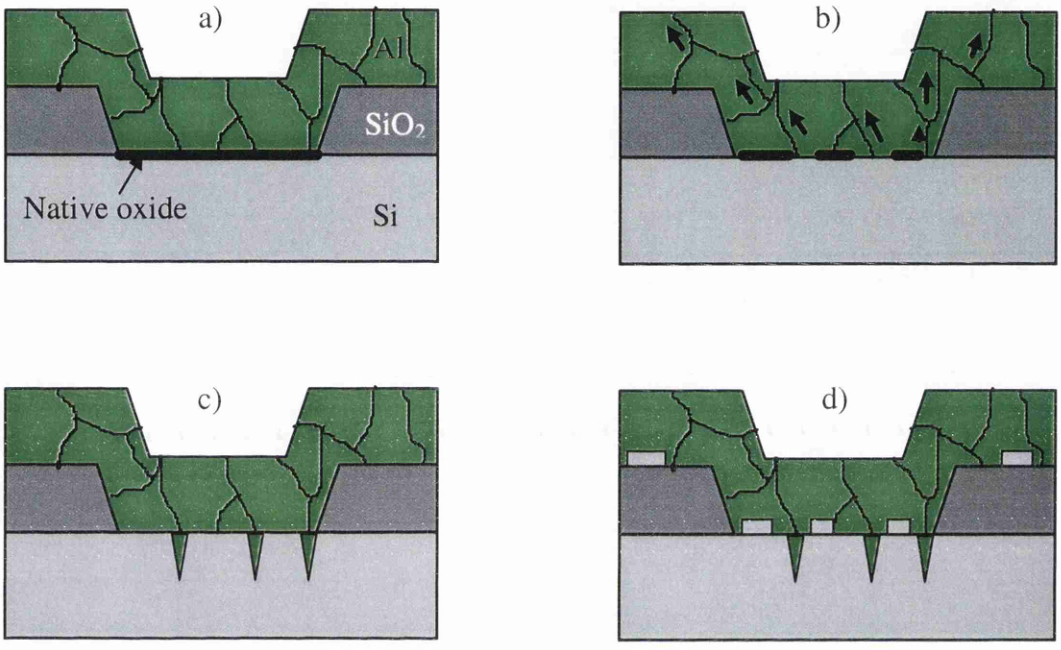

Figure 7.10: *The mechanisms of junction spiking. b) Some of the native oxide thins completely before others during annealing and the Si diffuses along the Al grain boundaries. c) the voids created in the Si are filled with Al, and d) the Si precipitates in the Al upon further annealing*

A common diffusion barrier consists of a sandwich layer of TiN and Ti. TiN is very stable in contact with Al or Si phases and grain boundary diffusion can be significantly reduced when it is contaminated with oxygen. It also does not react appreciably with Al or Si below 550°C[18] which is ≈100°C less than the melting point of Al. The Ti layer is generally used between the TiN and Si as the Ti provides a lower contact resistance and better adhesion to the Si than TiN alone[17]. It can also be shown that TiN thicknesses of <50nm can easily fail in some conditions.

7.4.3 Experiment

In this experiment, compositional analysis is performed through a polySi / Ti/TiN / Al diffusion barrier to determine the extent of the diffusion of the Si and Al through the barrier. Most of the basic experimental procedure for EDX analysis in the HB5 STEM is described in section 7.3, including detector and microscope configuration, specimen orientation and alignment, and acquisition parameters. Again, it is essential here that the specimen be aligned such that the interface planes are parallel to the beam. The Si Kikuchi pattern is used here again for accurate specimen alignment.

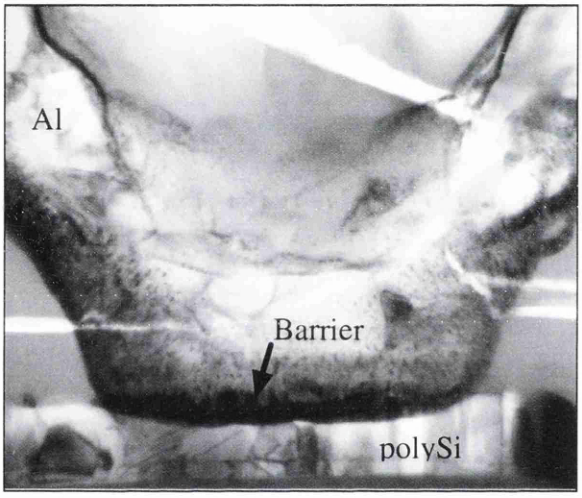

Figure 7.11: *Image of the Ti/TiN diffusion barrier where it separates Al and polySi*

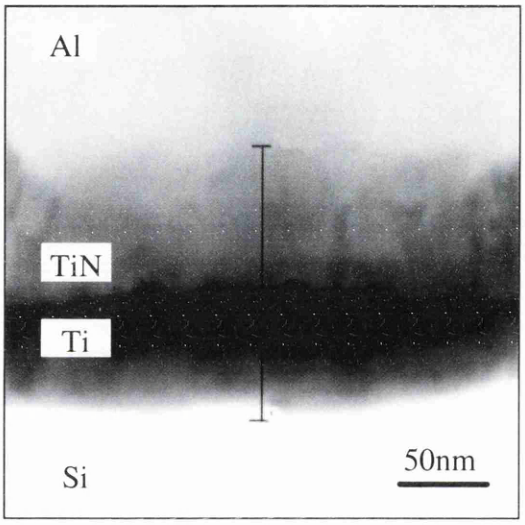

Figure 7.12: *Image of the diffusion barrier with the line of analysis as shown*

An image of the environment of the Ti/TiN barrier used in this experiment is given in figure 7.11. A series of EDX spectra are acquired along a line perpendicular the plane of the barrier layer as shown in figure 7.12. An example of a spectrum is shown in figure 7.13 where the acquisition time remained at 30s. Several repetitions of the experiment are made with ≈25 positions probed at ≈10nm intervals. Here the beam current is noted for each acquisition using the VOA current reading. The nature of the cold FEG dictates that the tip has to be flashed at regular time intervals as the tip emission drops when even tiny amounts of contamination deposit on it. The X-ray count depends on the beam current and so the relative current has to be noted for

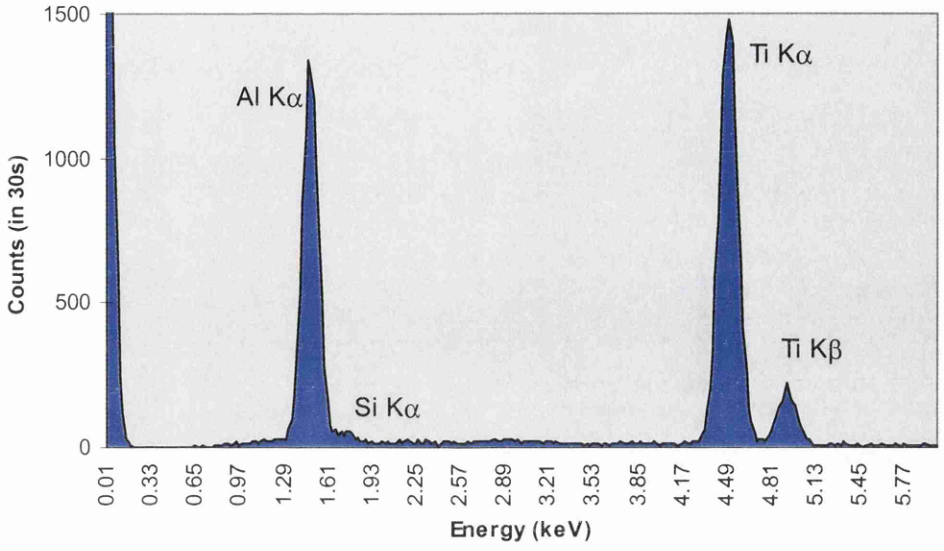

Figure 7.13: *An example of the spectra found in the barrier. The Si present most likely arises through specimen preparation*

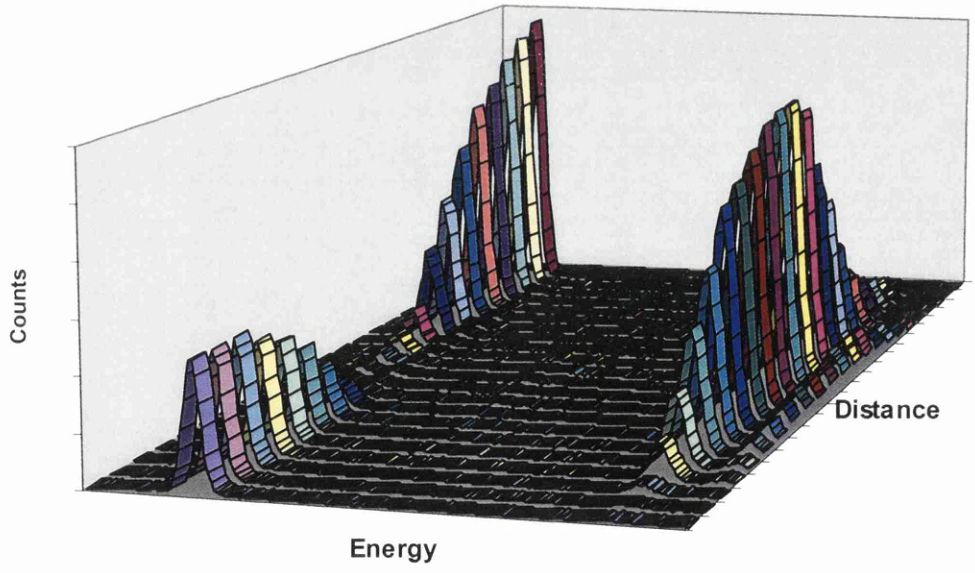

Figure 7.14: *A 3D representation of the relevant part of the spectra through the barrier*

quantitative analysis on multiple spectra. Again, the individual spectra are presented in separate columns in a spreadsheet in Excel and user-defined windows are created to select the integrated counts belonging to a specific peak. The elements recorded are Al, Ti and Si. Nitrogen is present but is not detected by the EDX detector on the HB5 as it

does not have an ultra-thin window like the CM20. It is detected by PEELS as shown later but it is not of significant importance here. Figure 7.14 shows the relevant sections of the spectra as a function of distance through the barrier, and figure 7.15 graphs the integrated X-ray counts for Al, Si and Ti across the barrier. The experiment is repeated across the same Ti/ TiN barrier but one which separates the Al from the Si substrate.

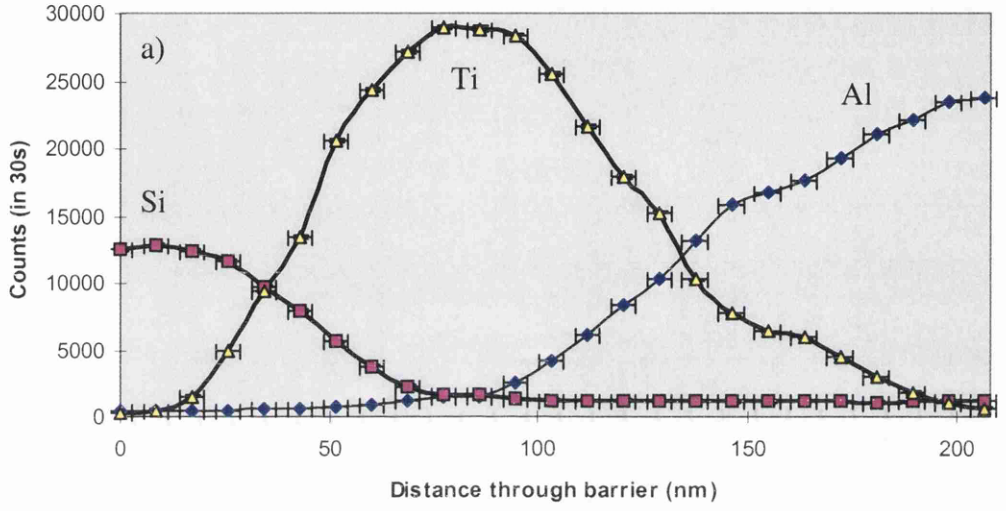

Figure 7.15: *Count profiles of Si, Al and Ti across the diffusion barrier between Al and polySi. The random error in each value is too small to be seen*

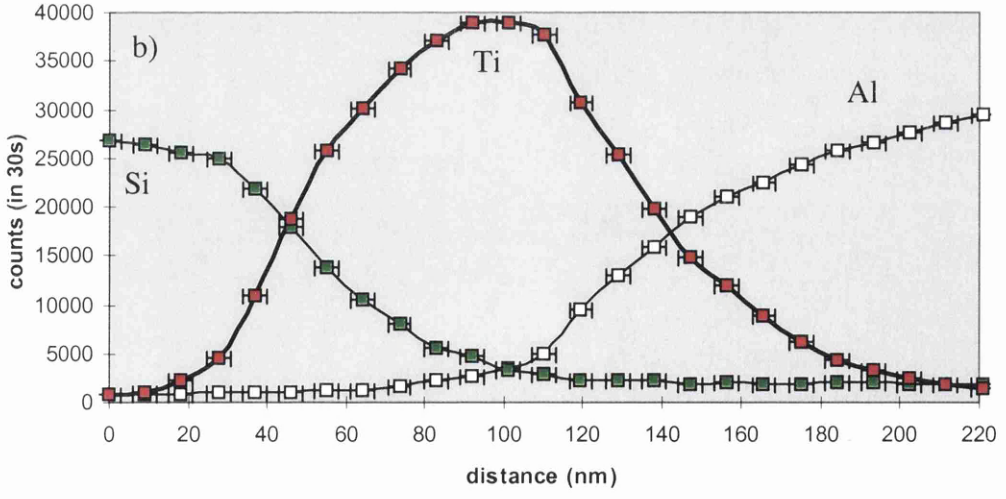

Figure 7.16: *Count profiles of Si, Al and Ti across the diffusion barrier between Al and the Si substrate. The increase in Si counts is due to the thicker substrate*

These results are shown in figure 7.16 and the only significant difference from the first results is the rise in Si counts at the substrate. From the image of the barrier shown in figure 7.11 it is noticed that the width of the barrier varies quite markedly. As a result, several compositional profiles are determined at various sites but each result produced a similar graph to figure 7.15a.

7.4.4 Results

The X-ray counts for the relevant elements shown in figure 7.15 do not yet reflect the atomic ratios of elements across the diffusion barrier. The atomic ratios of each element can be calculated, as before, using equation 2.19a, where k_{Si}=84.52barns, k_{Al}=81.94barns and k_{Ti}=90.40barns[7]. An interpretable approach to displaying the profile is to scale the Al and Ti counts by the fraction k_{Si} / k_{Al}, and k_{Si} / k_{Ti} respectively at each point leaving the Si counts as they are. Then all the values are scaled down so that the first Si data point is 1. This representation showing the relative number of atoms is shown in figure 7.17a and 7.17b for the barrier on the polySi and the substrate respectively. The relative error in each value is calculated as in equation 7.1.

A small amount of Si is detected even when probing the Al layer, but it is clear from its uniformity and considering the materials used in the specimen, that this signal is arising from stray electrons entering the surrounding Si regions. This is most likely from the substrate. Although less likely, traces of Si may actually be present on the Al surface as a result of specimen preparation. Bearing these points in mind, the results show that no Si is found in the Al and vice versa. In fact, there is scope for reducing the thickness of the layer by ≈25nm. Here, the Al would still not be present in the bulk Si film and likewise for the Si. It should be noted that the diffusion of the materials across the barrier will continue with operating time and its rate will depend on the operating temperature. Although the extent of the diffusion will normally be insignificant, reducing the barrier width by 25nm could be dangerous.

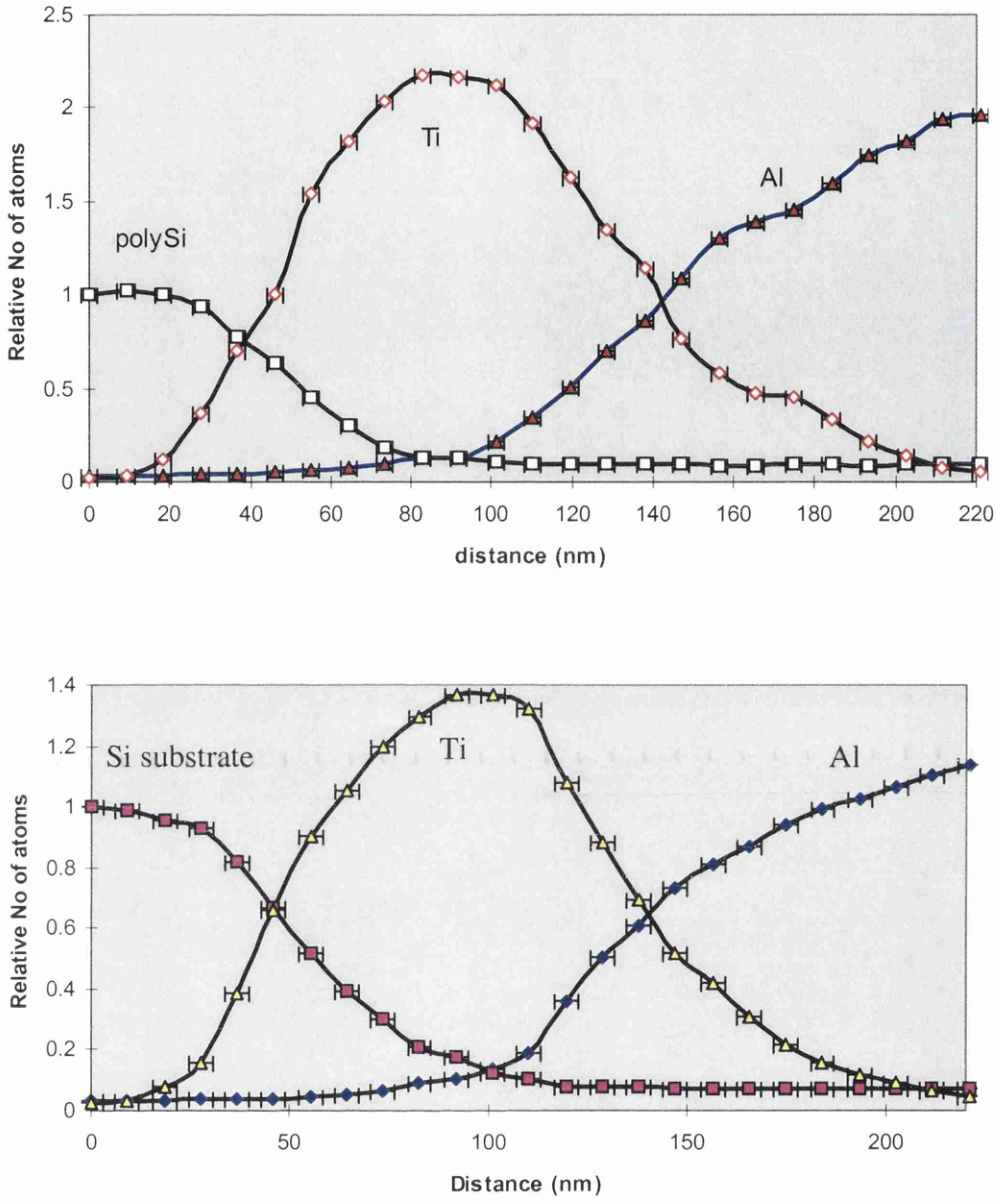

Figure 7.17: *Relative number of atoms present for each element across the barrier for the a) polySi and b) substrate cases*

There is little doubt that the thickness of the Ti / TiN film in the beam direction is a significant factor in the magnitude of the Ti profile. This is reinforced by images and is a known consequence of specimen preparation. It does not, however, affect the significance of the results. It is interesting to calculate the relative thickness of the materials to get an idea of their rate of thinning during specimen preparation. This is

done by scaling the relative number of atoms according to their density, ρ, and their atomic weight, A. Knowing Avogadro's number, N_A, equation 7.11 calculates the concentration of each element.

$$C = \frac{\rho N_A}{A} \text{atoms} / \text{cm}^3 \qquad [7.11]$$

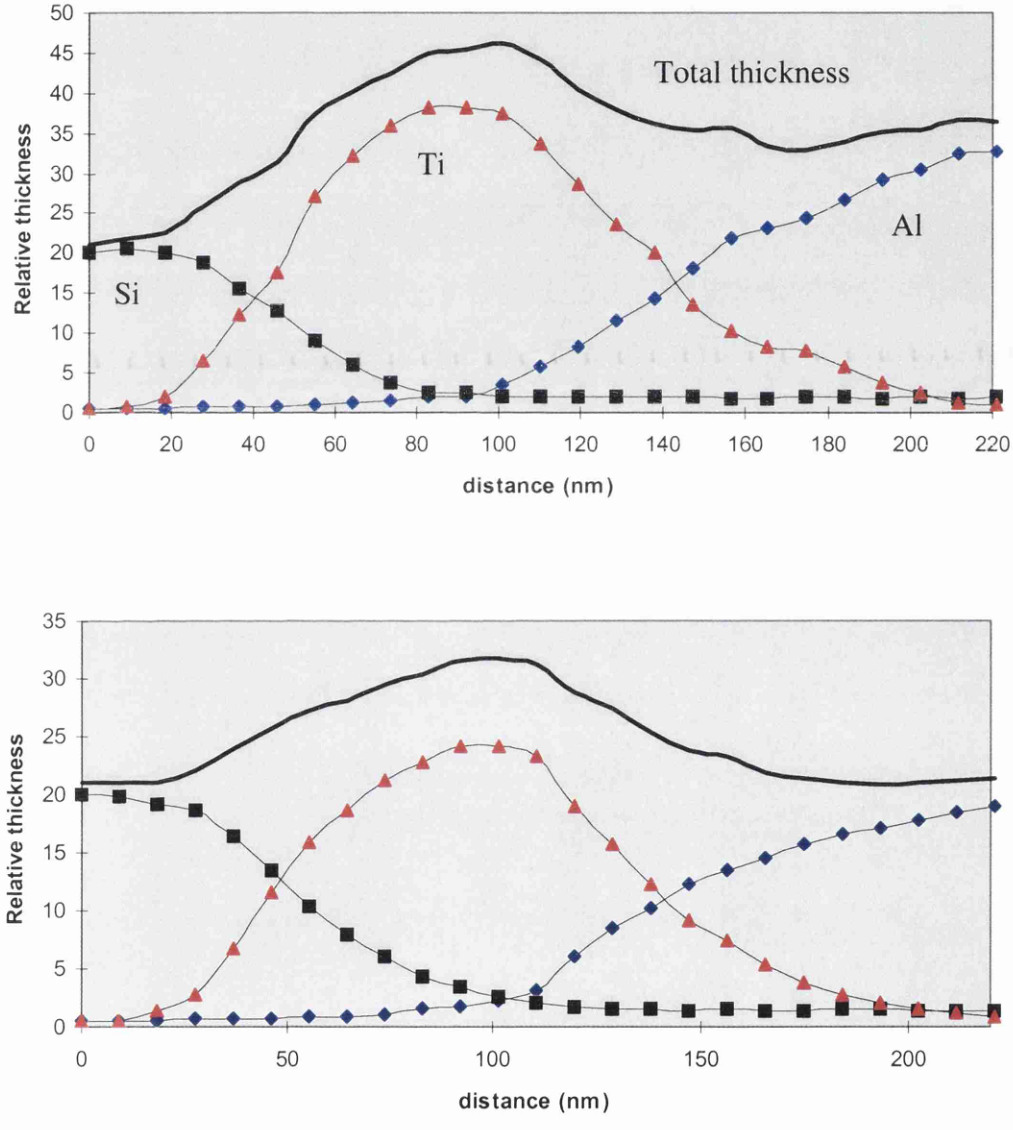

Figure 7.18: *Profiles of the relative thickness of the specimen as a function of distance through the barrier for the a) polySi and b) substrate cases*

Each value in figure 7.17a and 7.17b is therefore scaled by the factor k/C, where k is a constant of proportionality, to compute the relative thickness of the specimen at that point. The graphs shown in figure 7.18 shows the relative thickness of each element as a function of distance through each barrier. The values are also summed to give an approximate profile of the specimen thickness at each point. Nitrogen is also present in the barrier, and since it is not detected here, it will contribute to the specimen thickness where the TiN exists at the Al side in the barrier. The N content through the barrier is calculated later using PEELS. It should be remembered that, since there is a high level of atomic disorder at the interface region on either side of the Ti / TiN barrier, the actual densities of the materials at these regions are different from their elemental values. Thus the calculation of the relative thickness of the specimen at the interfaces is only an approximation.

These specimens were tripod polished then ion milled for ≈10mins. EDX analysis can be performed to compare the preferential thinning of the tripod polishing without the use of ion milling. The thinning rate of the Si substrate is relatively small compared to the polySi as there is less SiO_2 surrounding it which etches away very quickly. To a lesser extent, the presence of grain boundaries in the polySi reduces the mechanical strength of the film and thus its resistance to abrasion. In all the results, the Al thickness is always greater than that of polySi. The grains sizes in Al are ≈2-4× larger than Si, but the main reason for it thinning less readily is because the Al is protected by a harder TiN layer above and below it (a TiN anti-reflective coating resides above the Al).

7.4.5 Conclusions

The compositional profiles shown in figures 7.17a and 7.17b show that the diffusion barrier is effective in separating the Al and Si above and below it. Indeed, it may be argued that the barrier thickness could be reduced in thickness by up to 25nm. The relative thickness (see figure 7.18) of each material studied highlights the difference in etch rates during the final processes in specimen preparation. There is appreciable preferential thinning which is most likely due to the felt polishing and, to a greater

extent, the ion milling. Thus there is scope for this analysis to be used in comparing the extent of preferential thinning according to the preparation method.

7.5 Investigation of Unidentified Material using Various Approaches in EDX

7.5.1 Introduction

In a new 3-level metallisation device, an apparent anomaly in the fabrication was imaged in TEM. It seemed that the Al in metal 1 (the first Al layer) had penetrated through the diffusion barrier into the SiO_2 below. The situation is shown in the image in figure 7.19. If this were the case, the device would certainly have undesirable electrical

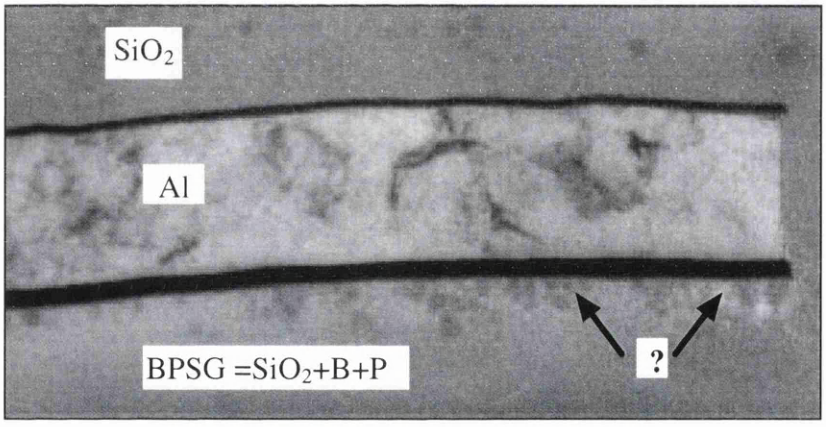

Figure 7.19: *Image of the unknown material used the lower Ti/TiN diffusion barrier*

properties and most likely cause electrical shorts in regions where the diffusion barrier is supposed to separate Al and Si at the contacts, as described in section 7.4. This section describes the various approaches used to identify the material and its source using different forms of EDX analysis and diffraction analysis. Here EDX mapping is used to provide compositional imaging of the cross-section around the material. EDX is also used to perform 1-dimensional compositional profiling for greater concentration sensitivity, and then to infer the thickness of the material in the beam direction.

Diffraction analysis is used to determine its atomic structure. The emphasis of this section, as with the most of the thesis, is to demonstrate the level of information available from the techniques as opposed to obtaining the specific results.

7.5.2 Experimental Procedure

For this experiment the Philips CM20 microscope is used as imaging and diffraction are more suitable for this analysis requirement. The spatial resolution of the HB5 is not needed here. The microscope configuration for EDX is described in chapter 2 and, as always, the specimen is oriented so that the interface planes are parallel to the beam. Here the C1 aperture is used as the beam defining aperture and the C2 aperture is used to intercept any stray electrons from it.

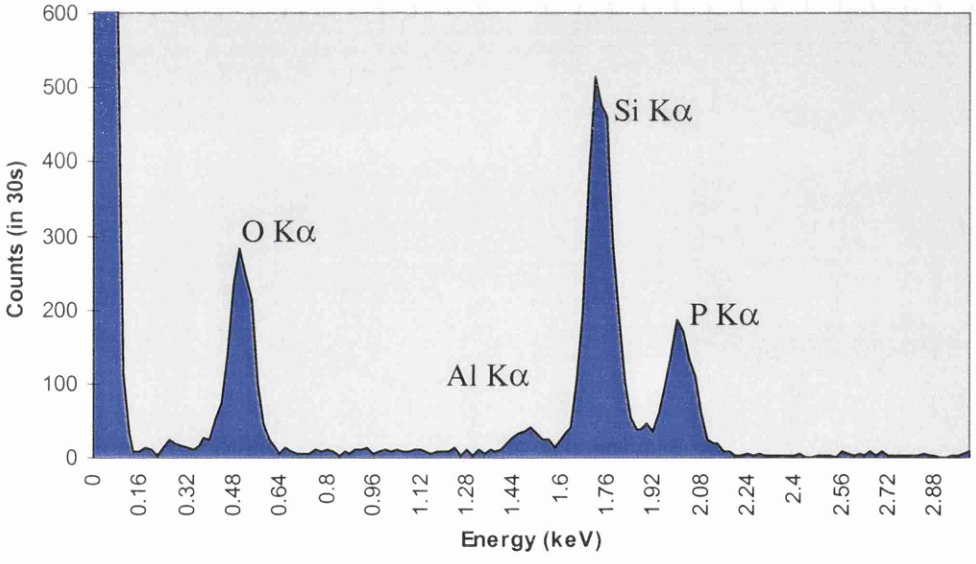

Figure 7.20: *The EDX spectra from a region on the unknown material. The Al count is very small, suggesting that the material is not Al alone but arises from*

Once the unknown material is imaged, the first step in its identification is to probe a region on it and examine the resultant EDX spectrum. The EDX spectrum is shown in figure 7.20. The only elements present here are Si, O, P, and traces of Ti and Al. The amount of Al is not substantial enough to indicate that the contrast is due to Al

protruding through the barrier. It is more likely that a very small amount arises through specimen preparation. At this point, it may just be that the unidentified material is of low concentration here as its contrast varies considerably along the length of the Al film. There is a need to provide a compositional image of this area rather than repeatedly probe small areas. EDX mapping is used to obtain a 2D compositional image of up to six different elements. In the technique, the microscope is set in scanning mode and the EDX counts are acquired while the beam increments slowly through the scan. At each step, the number of counts in each user defined energy window is converted to a level of grey and displayed according to its position in the scan. This way, a set of 2D images scans are built up simultaneously for each element and displayed on the screen. These images are saved separately for further image processing. A demonstration of the capabilities of this technique is given in figure 7.21.

Detailed EDX maps are acquired for the area surrounding the unidentified material and are shown in figure 7.22. The SiO_2 below the barrier (known as boron-phosphate-silicate-glass, or BPSG) is heavily doped with phosphorus and boron for more favourable insulation and dielectric properties. It is quite surprising to see that no appreciable contrast is produced by the X-ray maps which would substantiate the contrast present in the image under the barrier. There is possibly a slight increase in the Si counts immediately under the barrier but it could easily be due to random error. Repetition of this analysis using longer acquisition times at each position in the scan reveals no further information. There is the possibility of the image contrast arising from a change in structure of the BPSG from amorphous to crystalline. A diffraction pattern from the material immediately shows that no crystalline structure exists.

To increase the EDX resolution when analysing the material, a series of EDX acquisitions for 50s are performed across the material. Figure 7.23 shows the integrated X-ray count profile from the Al film to the substrate. Two pieces of interesting information are available from the profile. The thickness of the SiO_2 is seen to vary quite markedly from the substrate. This highlights the extent of the preferential thinning as discussed in section 7.4. More importantly, there is a definite increase in the Si

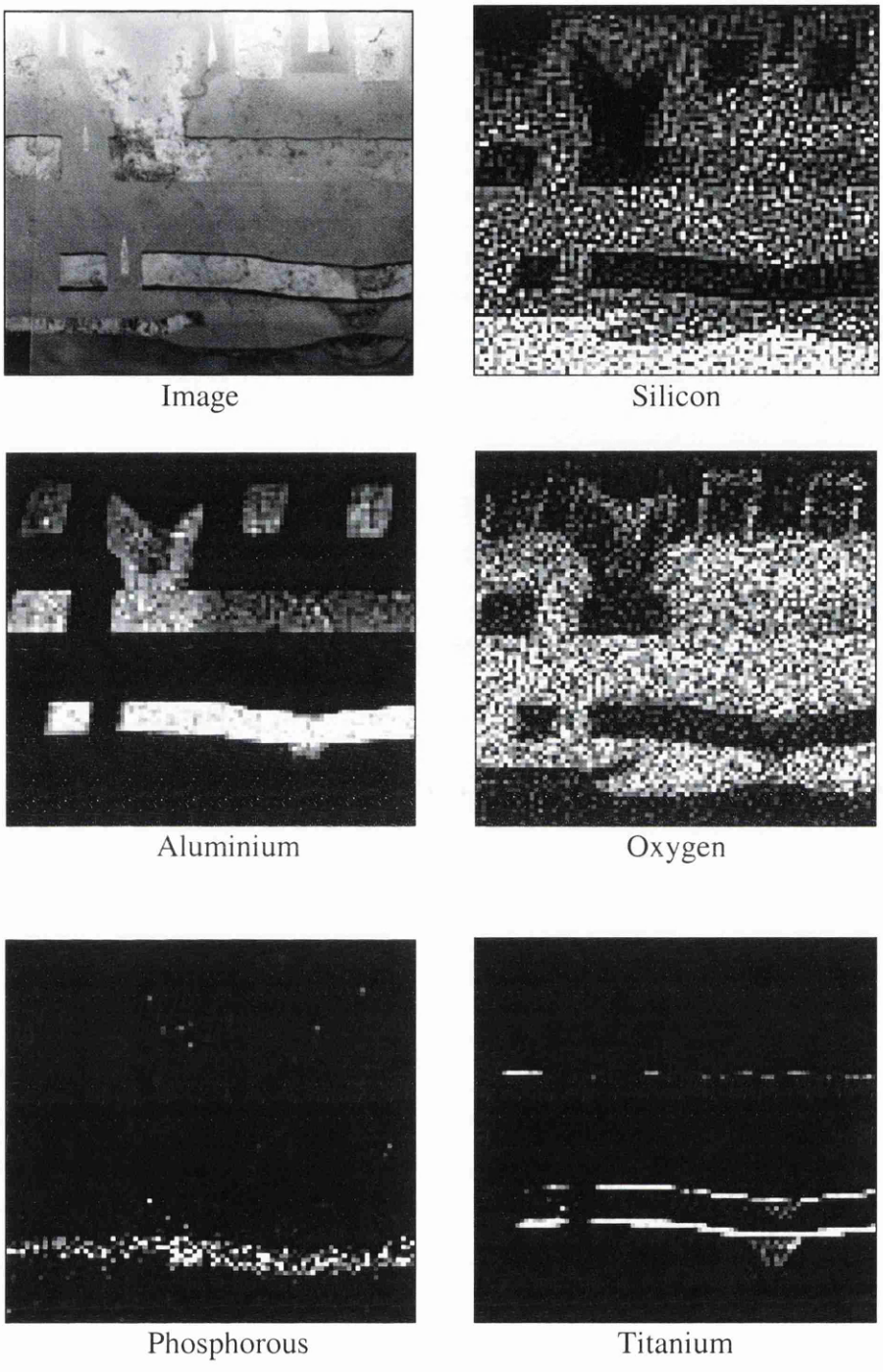

Figure 7.21: *An demonstration of the device materials detected by X-ray mapping*

counts immediately under the barrier. A repetition of the experiment reveals the same peak. This suggests that there is a build up of amorphous silicon at the barrier. This accumulation of Si could arise during device fabrication or specimen preparation. If the latter were the cause, the excess Si would not exist through the specimen at that

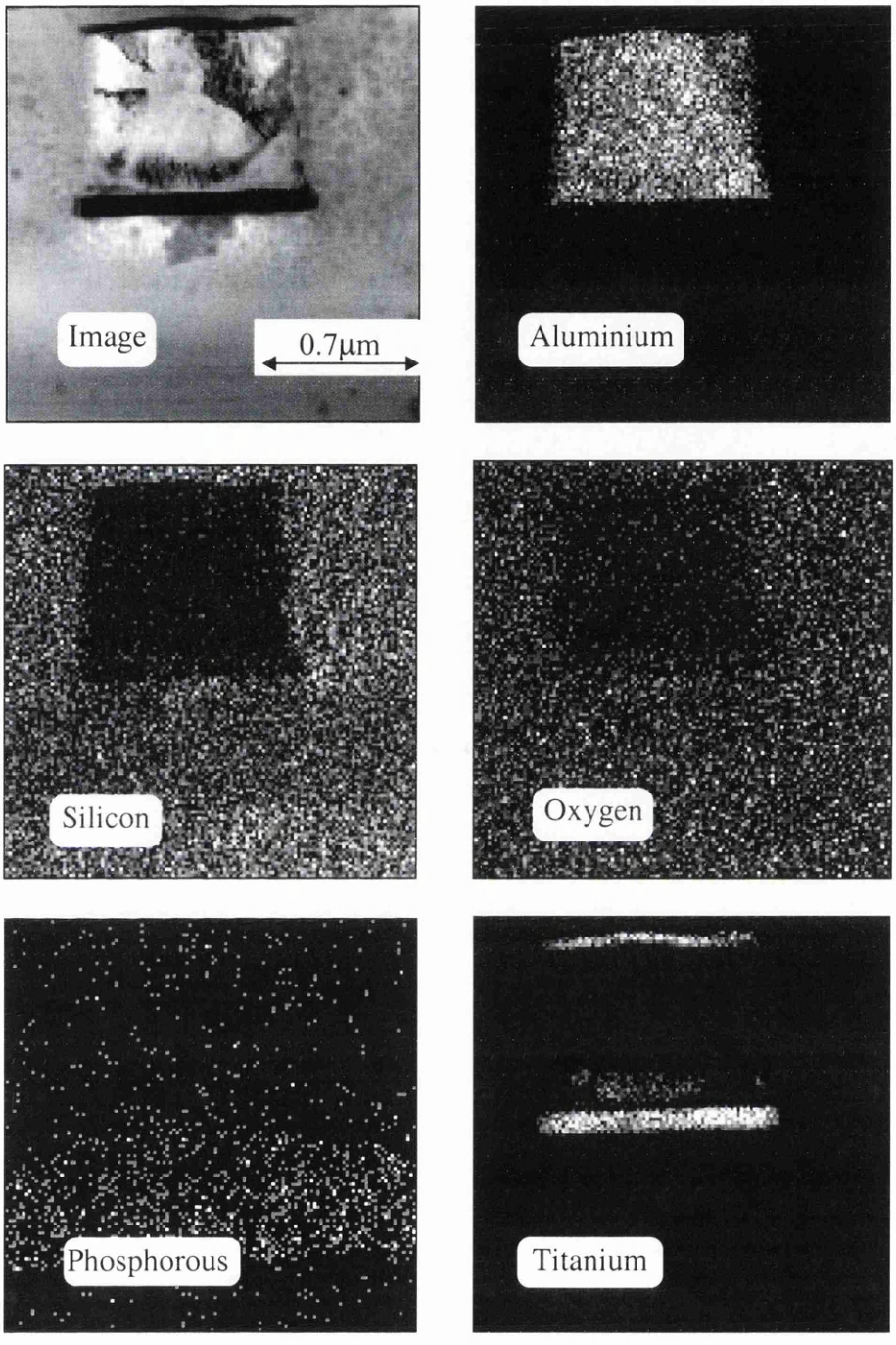

Figure 7.22: *EDX maps of the elements (all except B) in the area of interest. The only compositional difference under the barrier is a slight increase in Si counts*

point but only on its surface as it is likely to have been brushed here during the felt polishing. To test this theory the Si / P counts are calculated for the similar points along the material but at different specimen thicknesses. The principle behind this approach is that, if the excess Si resides on the specimen surface, the thickness of the brushed-up Si

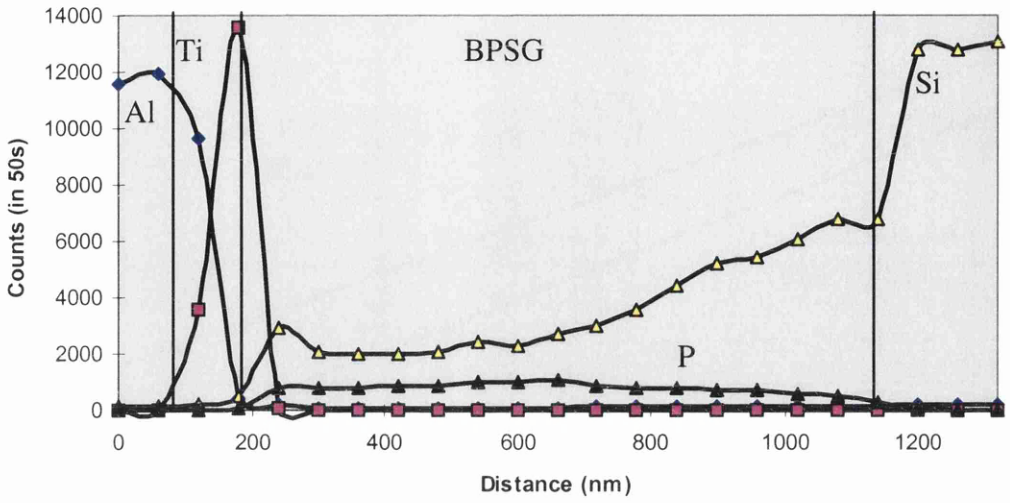

Figure 7.23: *The elemental profiles between the Al layer (left) down to the substrate (right). Just under the Ti/TiN barrier a significant increase in Si counts is observed*

on the surface would remain the same no matter the specimen thickness. Thus, if the bulk specimen has a fixed Si / P ratio, then the total Si / P ratio should increase the thinner the specimen is. The large electron transparent region is one advantage of preparing the specimen using the tripod polisher. Table 7.3 shows the results from the test.

Table 7.3: *Si / P ratio as a function of specimen thickness*

Thickness	***thin***	***quite thin***	***quite thick***	***thick***
Si counts	2544	3375	7294	9230
P counts	176	299	1422	1867
Si / P	14.5	11.3	5.1	4.9

Taking the relative P counts as being the relative thickness of the specimen (not including the surface Si) at each point, the Si counts are plotted against this thickness as shown in figure 7.24. Since P denotes the relative thickness, the relationship shown in figure 7.24 should be linear where the gradient is the Si/P counts from the bulk material

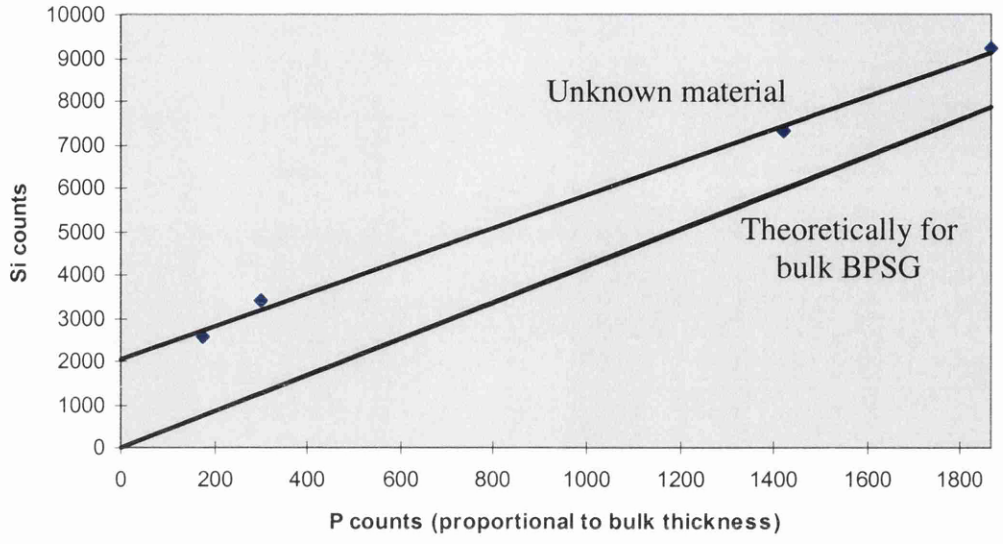

Figure 7.24: *The Si count rates as a function of specimen thickness (∝P counts) for the unknown material and from theoretical calculations. The similarity of the gradients demonstrates the level of quantitative information from EDX*

and the intercept is the counts from the surface Si. Knowing[19] that the P is 7.1 atomic % and the B is 3.1 atomic % in the BPSG, the Si / P atomic fraction is calculated as 4.29. Accounting for the difference in cross-sections, the Si / P X-ray count should be 4.20. Incorporating this relationship into figure 7.24, the trends can be compared. It is remarkable how close the gradients of each line are. It reflects upon the level of quantitative information available using EDX analysis. The mass of the Si can be calculated from the count rate, but, as the density of the amorphous Si is not known, the thickness of the Si on the surface cannot be determined accurately.

From these results, it is possible to conclude that the Si arises during specimen preparation. It is likely that the Si is brushed up from the substrate during the final felt polishing and accumulates below the 'wall' produced by the harder Ti / TiN barrier. This increase in specimen thickness at the diffusion barrier is shown in figures 7.17a and 7.17b. The specimen is further ion milled from both sides for 4mins with the beam parallel to the interface planes and, as predicted, TEM imaging shows that the anomaly has disappeared.

7.5.3 Conclusion

The unidentified material was found to be Si brushed up to the barrier during specimen preparation. Two things can be learned from this analysis. The first is that consideration must be given to the artefacts produced by the specimen preparation when performing materials characterisation. A significant amount of specimen damage can occur during tripod polishing. Most of the time this damage is localised and the large electron transparent area increases the chance of cross-sectioning a structurally sound part of the device. The material build up found under the barrier here had not been noticed in any other device and the fact that the effect was present across the whole device suggested a fabrication problem had caused it. It was noted however, that a particularly long time was spent felt polishing the final side of the specimen. With so much SiO_2 in the specimen it was not ion milled before TEM analysis was used in order to minimise preferential thinning. The second thing to be learned is that EDX analysis can be used in many forms besides identifying peaks in a spectrum. Here point analysis, X-ray mapping, compositional profiling, and thickness measurements were all performed using EDX and all played an integral part in diagnosing the source of a problem.

7.6 Compositional Analysis using PEELS

7.6.1 Introduction

In several ways, EDX analysis cannot be used to obtain the compositional information required. Some materials commonly found in modern devices, e.g. N and B (and sometimes O), are often not detectable using EDX. Silicon exists in several forms, e.g. SiO_2, Si_3N_4, and in elemental form, which cannot be differentiated using EDX. It is clear that, if compositional analysis has to be performed in the TEM, then PEELS must be used for these purposes. The remainder of this chapter demonstrates the strengths of PEELS in both identifying elements which cannot be detected using EDX, and

identifying the chemical environment of a particular element[20], [21], [22]. The theory and experimental procedure for PEELS data processing is described at the end of chapter 2.

7.6.2 Effect of Chemical Environment on Peak Shape

In this section, PEELS is used to identify the chemical state of an element. Attention is directed to the change of peak shapes according to the compound in which the element is found. As mentioned earlier, Si exists in several forms in devices. These are single crystal and polycrystalline Si, SiO_2, Si_3N_4 and silicides such as $TaSi_2$, WSi, NiSi, PtSi and MoSi. Several combinations of these materials contact each other in devices and the extent of the diffusion between them is often of critical importance. In the samples used in this work, no silicides were present, but this section serves as an illustration of how dramatically the peak shape changes with the chemical environment.

Figure 7.25a shows the original peaks for the various forms of Si found in the samples. The peaks are then stripped of the background signal, corrected for plural scattering and sharpened using the zero loss peak as described in chapter 2. The resultant peaks are shown in figure 7.25b where the variation of the peak shapes is very obvious. The specimen thickness significantly changes the peak to background ratio in the unprocessed peaks in figure 7.25a. The abundance of the Si atoms in the substrate is clear from the number of Si counts after the peak.

Unless the polySi grain sizes are very small, i.e. <<10nm, the effect on the peak shape due to the atomic disorder at the grain boundaries will be very small. Attempts were made to correlate any peak shape dependence on the texture of the polySi film examined in chapter 6 using a scanning beam while acquiring the PEELS spectra. The effect of the grain boundaries was found to be swamped by that of the grain core. Thus the PEELS spectrum is effectively the same for both single crystal and polycrystalline Si.

Nitrogen also exists in more than one form. In the samples used here, Si_3N_4 and TiN exist and the spectra shown in figure 7.26 highlight the differences in the peak shapes.

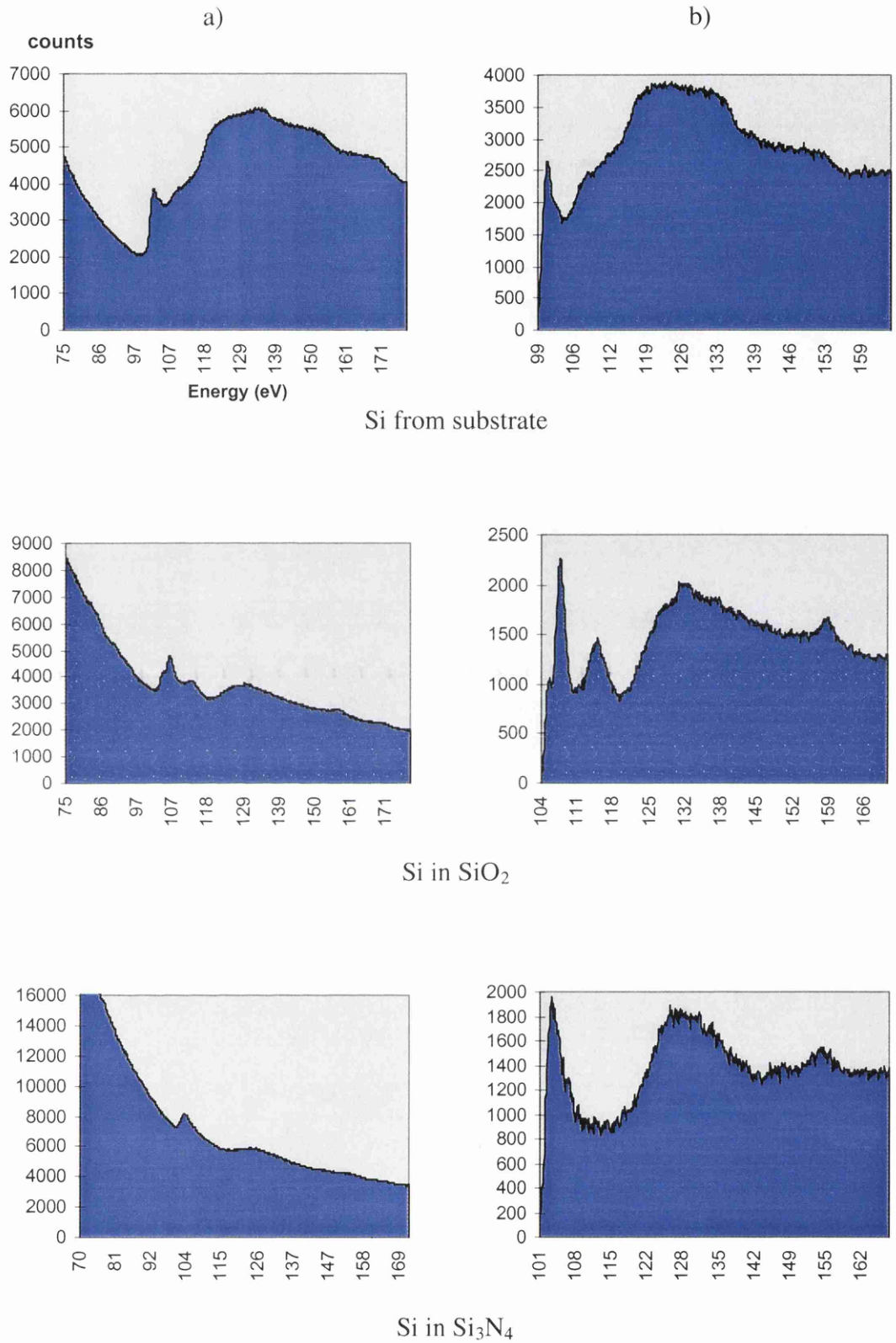

Figure 7.25: *a) The unprocessed Si peaks for the Si substrate, SiO_2 and Si_3N_4. b) the respective processed peaks*

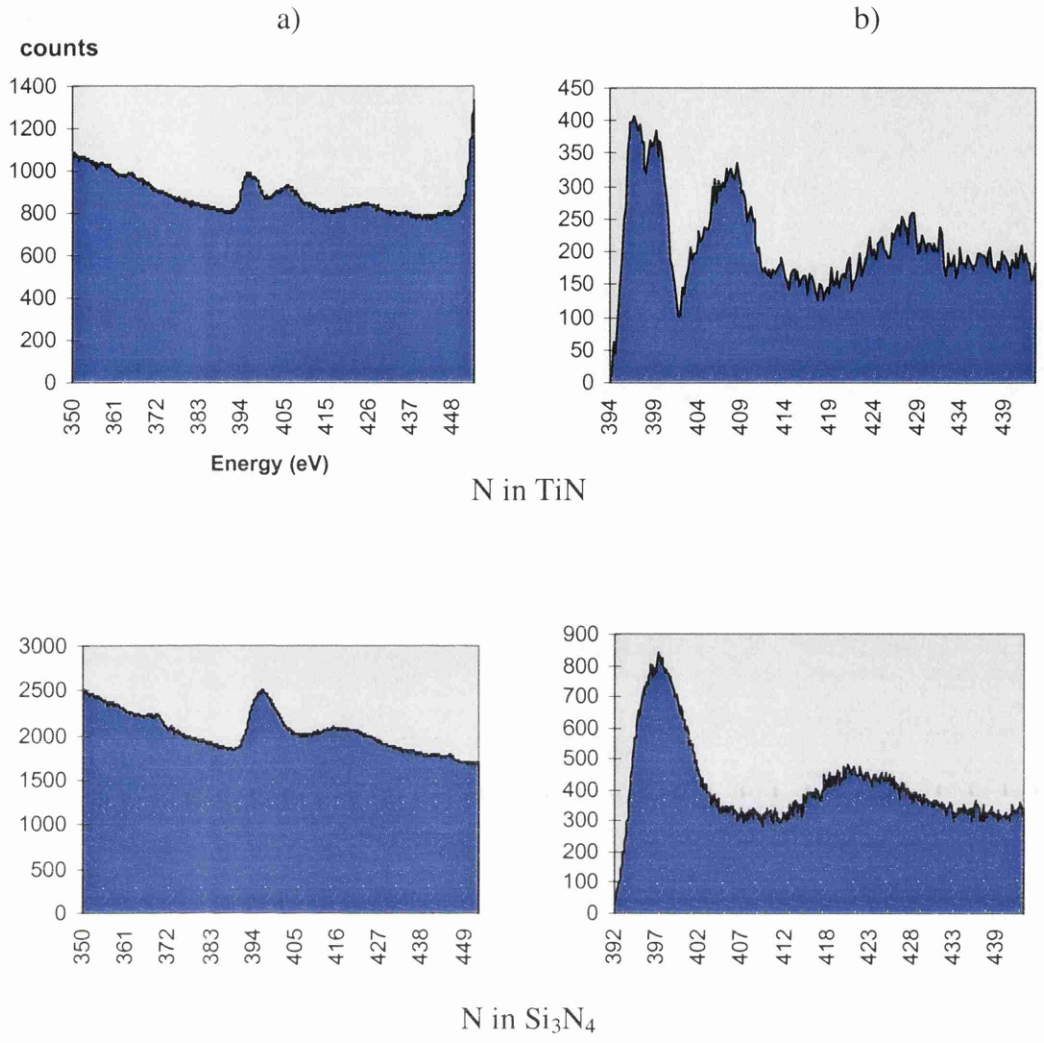

Figure 7.26: *a) the unprocessed N peaks for TiN and Si_3N_4 and , b) the respective peaks after processing*

With the energy resolution of ≈1eV found in PEELS, the shapes of the peaks can be used to determine more about the element's atomic environment e.g. the neighbouring elements. Studies have shown[23], [24], [25] that these peaks can provide information on the stress in a material. Some of the energy levels in stressed atoms are slightly different to relaxed ones and the energy discrepancy can be detected by PEELS. Stress is a very important aspect of device fabrication, and with the nanometre resolution available in the TEM, this technique will become more influential as film thicknesses continue to shrink through device miniaturisation.

7.6.3 Nitrogen profile through the Ti/TiN Diffusion Barrier

A weakness in EDX systems was encountered in profiling the elements present across the diffusion barrier as described earlier in this chapter. The barrier was found to effectively separate the Al and Si to either side of it, but the position and extent of diffusion of the Ti or TiN was unclear as the N was not detected by EDX.

In a similar experiment to the EDX analysis performed on the barrier, PEELS spectra are obtained as a function of distance through the diffusion barrier between the polySi and Al to profile the Ti and N composition. The PEELS analysis is performed on the Philips CM20 TEM. Before the spectra are acquired, the emission current on the microscope is reduced to avoid saturation in the photodiode array. Here the beam passes through a hole in the specimen. This is required if quantitative analysis is to be performed, otherwise the number of counts are not necessarily proportional to the composition. The beam is aligned in nanoprobe mode (see chapter 6) and the convergence angle of the beam is taken from table 2.1 for future reference. The selected area aperture is inserted to reduce the number of stray electrons. The camera length of the microscope is set to its smallest value which is 24mm and the astigmatism in the diffraction lens is corrected. The diffraction spot is directed onto the axis of the spectrometer using the diffraction shift controls while observing the height of the zero loss peak. The scanning DF image of the specimen can be acquired simultaneously as the beam passes through the middle of the annular detector. The focusing and calibration of the PEELS detector is described in chapter 2.

At each position through the barrier, the zero loss peak and the energy window containing the Ti and N peaks are acquired. The zero loss peak is used to both correct for multiple scattering beyond each peak and sharpen the peak profile (see chapter 2). It is also used to estimate the thickness of the specimen. The bare PEELS spectra for the Ti and N peaks as a function of distance through the barrier are shown in figure 7.27. For ease in comparing the results, the distance scale is matched to that of the scale in the EDX analysis of the same barrier performed earlier. For quantitative analysis the Ti

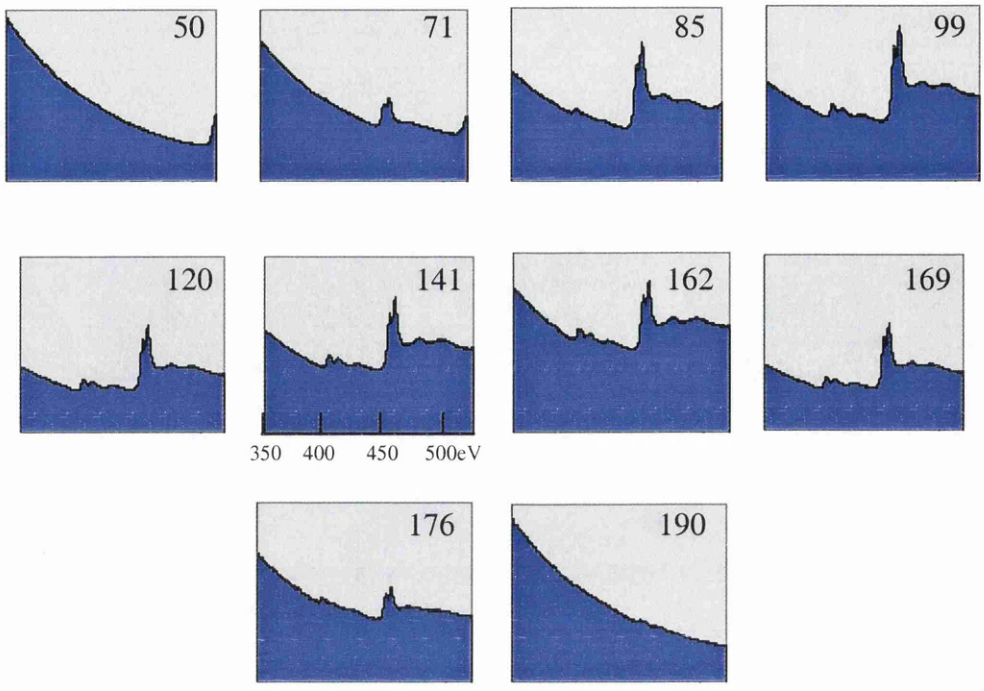

Figure 7.27: *The sequence of Ti and N peaks at the given distances (in nm) across the barrier. The distances (in nm) at the top right of each graph are relative to the origin used in the relevant EDX analysis*

and N peaks are stripped of the background, corrected for multiple scattering and sharpened by the EL/P software. Figure 7.28a shows the resultant N peak and figure 7.28b shows the Ti peak. The counts for each element are integrated over a 50eV energy window starting at the peak. Cross-sections, σ, are calculated using the Hartree-Slater[25] method which uses empirically obtained data from materials of known composition. This method is described in greater detail in reference [27]. The error in each cross-section is nominally 10%. Equation 7.12 (described in chapter 2) shows the calculation of the relative number of atoms, N, of each element from the number of counts, C, in each window. The cross-section itself depends on the energy window and should be calculated using the same value as the energy window used in the integrated counts.

$$\frac{N_N}{N_{Ti}} = \frac{\sigma_{Ti}}{\sigma_N}\frac{C_N}{C_{Ti}} \qquad [7.12]$$

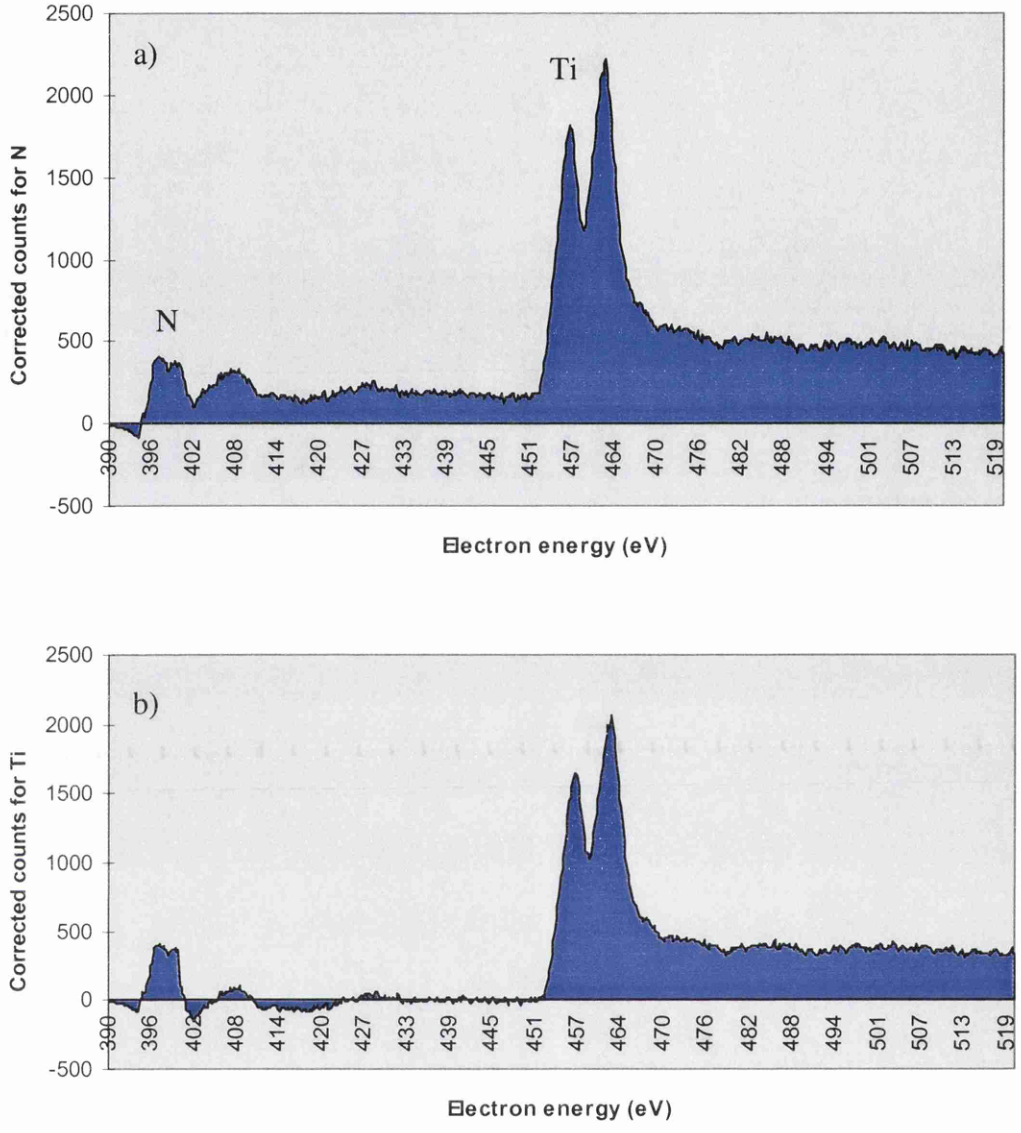

Figure 7.28: *The relevant N and Ti peaks processed for quantitative information on the Ti:N atomic ratios*

For an energy window of 50eV, σ_{Ti}=2031±200 barns and σ_N=780±80 barns using the Hartree-Slater method. Using these values, the atomic ratio of N to Ti atoms is plotted as a function of distance through the barrier as shown in figure 7.29 for the polySi / Ti/TiN / Al interface.

Using the compositional information on the Si, Ti and Al profiles across the barrier from the earlier EDX analysis, the N/ Ti ratio is incorporated into the profile to map all

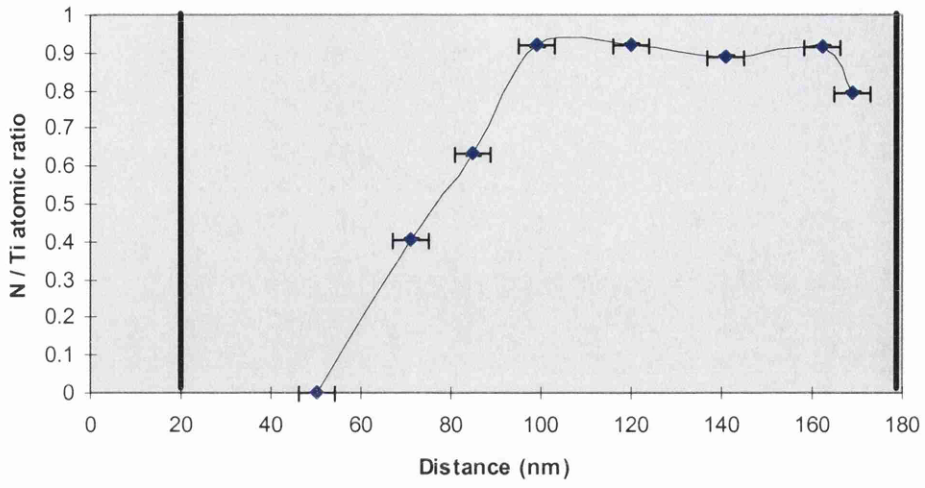

Figure 7.29: *The N / Ti profile through the TiN barrier. Approximate limits of the barrier are given by the vertical lines. Between 170-180nm, the Ti and N counts are both very low so the ratio is not calculated there*

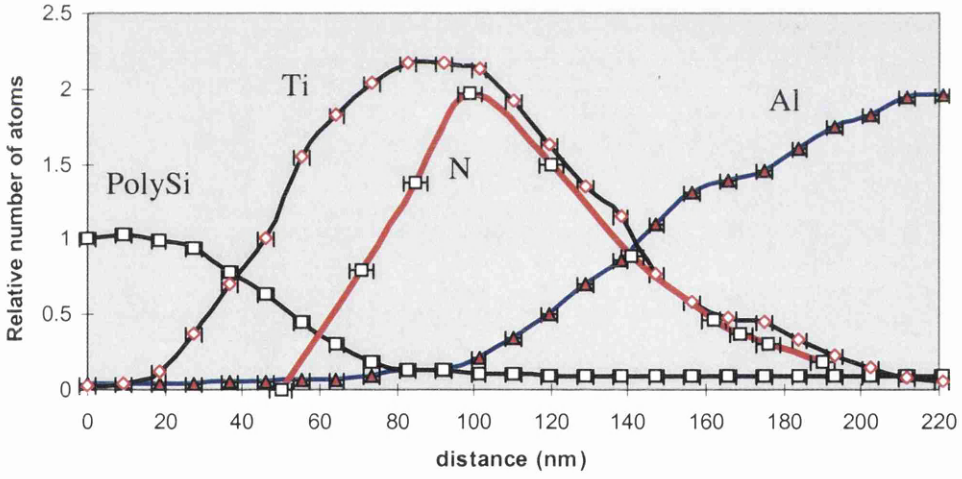

Figure 7.30: *Complete elemental profile of all four elements present in the polySi / Ti / TiN/ Al diffusion barrier using results from both EDX and PEELS*

the elemental profiles. This is shown in figure 7.30 for the polySi case. Assuming that the TiN has an atomic ratio of 1:1, then the profile of Ti and TiN can be separated to produce more interpretable information as shown in figure 7.31. The separation of the Ti and TiN not only provides a clearer description of the various elements through the

barrier but also allows more straightforward calculations in determining the specimen thickness through the barrier. However, it is possible that the profile is not quite this simple. The interface between the Ti and TiN may consist of sub-stoichiometric TiN_x with x gradually changing from 0 to 1[14]. Studies have shown[28] that it is possible to perform further PEELS analysis on such a TiN_x layer to determine the nature of the stoichiometry. For the thickness profile, equation 7.8 is used where $\rho_{TiN}=5.22gcm^{-3}$. The relative thickness of each element is shown in figure 7.32 along with the resultant specimen thickness. This gives a more accurate description of the specimen thickness than the EDX results alone as shown in figure 7.18.

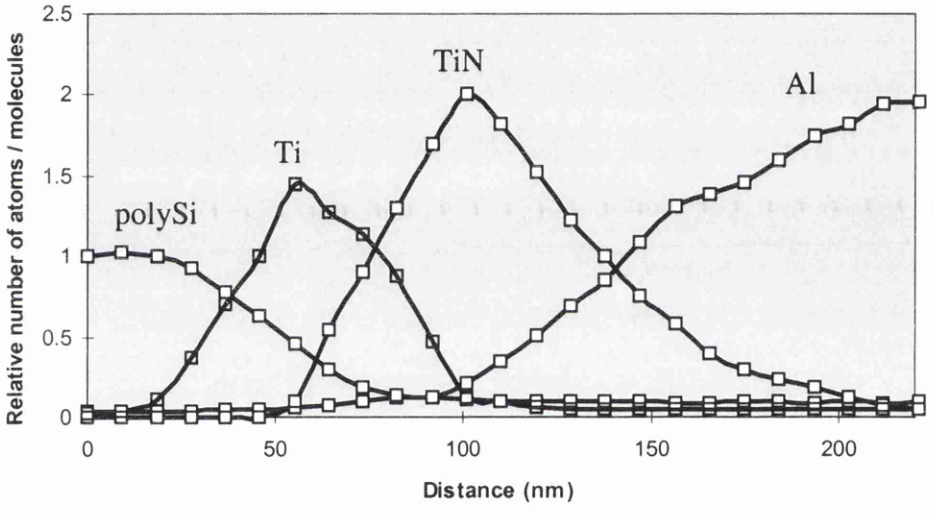

Figure 7.31: *The relative number of atoms/molecules across the barrier for the four films: polySi, Ti, TiN, and Al*

The thickness of the specimen can also be calculated directly from PEELS as described in chapter 2. However, the results from such calculations would be inaccurate. Firstly, the elements are not in their natural stand-alone phase and the low-loss peaks are sensitive to the atomic arrangement. This means that the error in using the mean free path for that element is relatively large when other elements are present. Secondly, the equation used to calculate the mean free path from the atomic number[29] is empirical and has a 20% error. Thirdly, the mean free path of TiN would have to be approximated

from that of Ti and N. For these reasons the calculation of the specimen thickness through the barrier is not performed.

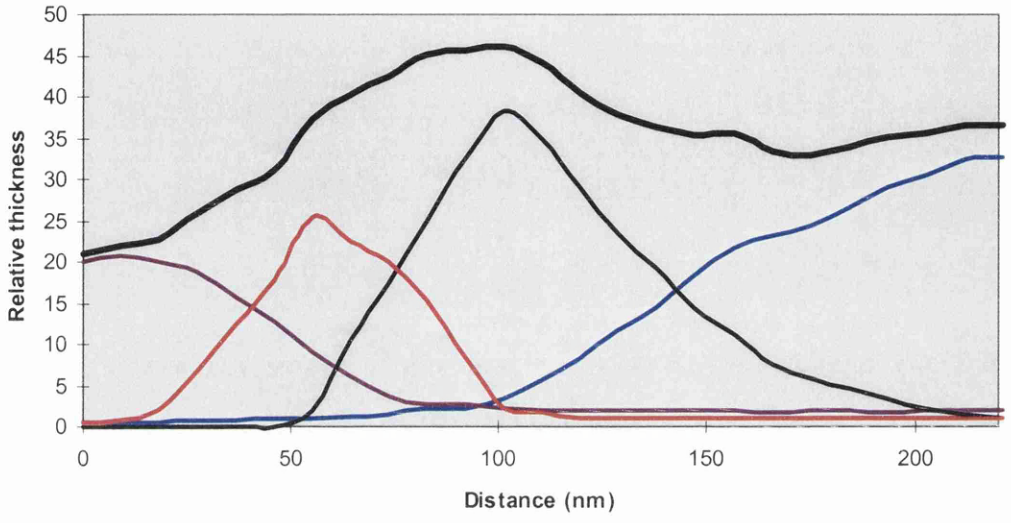

Figure 7.32: *The thickness of the materials at a given point around the barrier. The specimen thickness is the sum of each material thickness and the graph highlights the extent of preferential thinning*

7.6.4 Conclusion

A series of PEELS spectra are acquired as a function of distance through the Ti / TiN diffusion barrier between polySi and Al. The experiment is performed for two reasons. Firstly, to map the N content through the film, and secondly, to compare with the earlier EDX results in describing the compositional profile of Si, Ti, TiN, and Al along with a more accurate measurement of the specimen thickness through the barrier. The Ti:N ratio is found to be $\approx 0.9 \pm 0.1$ in the TiN. Here, this ratio should be 1 but it is likely that some Ti diffused into the TiN thereby reducing the fraction. Nevertheless, the 10% error in the cross-sections calculated using the Hartree-Slater method accounts for the discrepancy. The level of quantification from PEELS analysis is thus very high. The compositional profile of the elements at the diffusion barrier is given in figure 7.31 and the specimen thickness profile there is shown in figure 7.32.

PEELS has been successfully shown to both differentiate elements according to their atomic environment and quantitatively detect elements which cannot be detected using EDX.

7.7 Conclusions

The use of EDX and PEELS has been investigated for use in modern silicon devices as compositional analysis tools. The spatial resolution of EDX in TEM is shown to reach ≈3±1nm for a ≈1nm probe size using the VG HB5 STEM. At this probe size a concentration sensitivity of $\approx 3\times10^{20}$atoms/cm^3 or ≈60 As atoms in the volume of Si illuminated, is found. This is comparable to the manufacturers description of the detection of ≈300 Ru atoms in C with a 2nm probe size. The spatial resolution compares very favourably with compositional techniques as mentioned in chapter 1, but the concentration sensitivity is ≈2-6 orders of magnitude higher. However, the sensitivity to a small number of atoms in a small volume can be higher with EDX in the TEM. Thus the technique's strength lies in the detection of small regions of contamination or impurities.

EDX and PEELS combined allow for very quantitative measurements of the distributions of elements through a set of interfaces where the level of diffusion is of critical importance. This is the case for the diffusion barriers investigated here. The results clearly show that the diffusion barrier is effective in preventing the Si from diffusing into the Al and causing junction spiking. The combination of the two techniques also show that the final stages of polishing during specimen preparation introduce a significant degree of preferential thinning. It is for this reason that the unknown material accumulated under the thicker barrier. Using various modes of EDX analysis, this material was identified as Si brushed up from the substrate. The ability of PEELS in differentiating different phases of a material is also demonstrated and the technique could be very useful where different forms of Si are in contact in a device.

References for Chapter 7

[1] A. J. McGibbon, PhD Thesis, University of Glasgow, UK, (1989) 69

[2] A. J. Garrett-Reed and T. D. Mottishaw, Electron Microscopy and Analysis, *Inst Phys Conf. Ser 68* (1983) 221

[3] G. W. Lorimer, in *Quantitative Electron Microscopy,* Proceedings of the 25th Scottish Universities' Summer School, eds. J. N. Chapman and A. J. Craven, SSUSSP Publications, Edinburgh, (1983)

[4] VG microscopes technical manual

[5] Colin Stanley, University of Glasgow, *Private communication*

[6] C. C. Grey, PhD Thesis, University of Glasgow, UK (1981) 7

[7] H. A. Bethe, Ann. Der. Phys., **5**, (1930) 325

[8] M. O. Krause, J. Appl. Chem. Ref. Data, **8**, 2, (1979) 307

[9] D. H. Lee, and J. W. Meyer, *Proc. IEEE*, **62**, (1974) 1242

[10] Y. Xia, and C. Tan, Nucl. Inst. And Meth., **174**, (1986) 100

[11] L. J. Herbst, *Integrated Circuit Engineering,* Oxford University Press (1996) 36

[12] W. A. P. Nicholson, Mickrochim. Acta. **114/115**, (1994) 53

[13] J. H. Paterson, J. N. Chapman, W. A. P. Nicholson and J. M. Titchmarsh, J. Micros., **170**, 1 (1989) 1

[14] A. J. Craven, University of Glasgow UK, *Private Communication*

[15] M-A. Nicolet, Thin Solid Films, **52** (1978) 415

[16] C. R. M. Grovenor, *Microelectronic Materials,* IOP Publishing Ltd, (1989), 240

[17] E. Kobeda, J. D. Warnock, J. P. Gambino, S. B. Brodsky, B. Cunningham, and S. Basavaiah, J. Appl. Phys., **72**, 7, (1992) 2743

[18] A. Armigliato, and G. Valdre, J. Appl. Phys., **61**, (1986) 390

[19] Fabrication process build-up, Motorola Ltd, UK

[20] R. F. Egerton, in *Electron Energy Loss Spectroscopy in the Electron Microscope,* Plenum New York (1985) 298

[21] C. C. Ahn, and O.L. Krivanek, *EELS Atlas*, Gatan, (1983)

[22] P. E. Batson, J. Electr Micro., 45, 1, (1996) 51

[23] R.F. Egerton, J.M. Whelan, J. Electron. Spect. **3**, (1974) 232

[24] A. J. Bourdillon, S. M. El Mashri, and A. J. Forty, Phil. Mag. **49**, (1084) 341

[25] P. E. Batson, Ultramicroscopy, 59, 1-4, (1995) 63

[26] R. D. Leapman, P. Rez, and D. F. Mayer, J. Chem. Phys., **72**, 2 (1980) 1232

[27] M. MacKenzie, PhD Thesis, University of Glasgow, UK, (1997) 39

[28] A. Craven, Ultramicroscopy, 180, 3, (1995) 250

[29] R. F. Egerton, Ultamicr., **28**, (1989) 215

CHAPTER EIGHT

Conclusions and Further Work

8.1 Overall Aim

The overriding purpose of the project was to explore the capabilities of transmission electron microscopy in characterising materials used in modern and future silicon devices. There is a clear trend towards the implementation of thinner films in device fabrication and so most characterisation techniques require nanometre, or better, spatial resolution for useful information on these films. This thesis described various original TEM techniques which can be used to characterise these films thereby demonstrating the value of the TEM in failure analysis and device research. The studies showed that, upon continuing device miniaturisation, the TEM is very likely to become an integral part of materials characterisation in the device industry.

8.2 Characterising The Fine Structure Of Conducting Films

8.2.1 Introduction

One of the most important issues concerning device performance during miniaturisation is the conductivity of the 'wires', or interconnects, in the circuits. In a modern device there are now several miles of wiring so the performance of the device is increasingly

influenced by the interconnect properties and not so extensively by the transistor properties as before. With polycrystalline conductive films ranging in thickness between ≈50nm and ≈1μm, the resistance, and thus the *RC* time delay, is highly dependent on the fine grain structure in the film.

Studies show that many electrical and mechanical properties of the film are strongly influenced by the grain sizes and orientations. These properties include resistivity, electromigration, surface roughness and interdiffusion, and, generally, these properties worsen with small grains which are randomly oriented. There is thus a need to accurately describe a film by its distribution of grain sizes and orientations on a nanometre scale.

8.2.2 Determination of Grain Sizes

A new technique for determining the grain size distribution was described in chapter 4. There, the grain size distribution of a film was inferred from a distribution of distances between grain boundaries and applying Voronoi statistics and other statistical models. The positions of the grain boundaries were determined by scanning a focused probe along the length of the film and registering where the Kikuchi diffraction pattern changed. Many of the grain boundaries were not visible using bright or dark field imaging.

The STEM technique was shown to successfully identify the position of every grain boundary. Even if the specimen contained >1 grain through its thickness, the technique was shown to be valid. An advantage of this technique is its ability to determine the grain size distribution at a certain level in the growth direction of the film. This can be useful in describing the grain growth mechanisms for film deposition. The technique is ideally suited for the elongated rectangular shape of films in cross-section where one scan can readily determine the complete grain size distribution of the film.

Voronoi statistics are known to accurately describe grain size distributions for various grain types. The distribution of intercept lengths for two films were shown to be in

agreement with those predicted by the Voronoi statistics. Thus, the model was valid for application to the intercept data, allowing for an accurate description of the grain size distribution. Voronoi statistics could not evaluate the grain size distribution alone. Other theories were used along with original models which were evaluated in this work.

Two Al films, denoted metal 1 and metal 2, were used to demonstrate the technique as well as determine their grain size distribution. Metal 1 was 275nm thick and metal 2, 470nm. The distribution of grain sizes for both films was accurately described by either a gamma function or a log-normal distribution, i.e. similar to a Gaussian, but with a slight tail. The average grain size for metal 1 was 1.43±0.47 μm and 1.45±0.23 μm for metal 2. The errors there were statistical and dependent mainly on the number of intercept measurements taken. The standard deviation of the grain size distributions in the films were 0.38μm and 0.39μm respectively.

The technique itself can be implemented on most STEMs providing the scan time along the film allows for >1s per grain. The level of accuracy was influenced by the number of grains scanned and ≈100 were needed for 10% accuracy. This places restrictions on the area of the electron transparent region required. Specimen preparation using tripod polishing can produce a larger useful electron transparent area than any other cross-sectional TEM specimen. The strength of this technique lies in the ability to perform grain size determinations on films without removal of any subsequent layers of materials. The technique also allows for the determination of the development of grain sizes as the film grows. No other technique has been found in the literature which can perform this function with nanometre resolution.

8.2.3 Quantifying the Texture in a Film

Two original techniques were described in chapters 5 and 6 to obtain quantitative information on the texture of polySi films. The first was a variation on the determination of grain orientations by examining the Kikuchi diffraction patterns from individual grains. The second was a new technique whereby quantitative texture

information was derived from the distribution of intensities on the diffraction pattern from an area scanned on a film.

The Kikuchi technique was used on the two polySi films mentioned in the previous section to identify any texturing. The results showed that the grains were effectively randomly oriented in both films and the existence of preferred orientations was insignificant. The results from the scanning technique reinforced this assertion.

The diffraction patterns from the scanning technique were subject to various statistical and theoretical analysis to determine a reproducible method of obtaining quantitative information describing the texture of a film. To interpret the texture information from the analysis, a definition of the degree of texture had to be provided since no such definition existed. The degree of texture was defined as the volume fraction of grains which are oriented in the texture direction within the mosaic spread. In the analysis a C-program was written to calculate the electron intensity around a specified diffraction ring and the results were exported to a spreadsheet where the degree of texture was calculated. Along with the degree of texture, the texture direction and the mosaic spread and tilt offset were obtained which described the spread in orientations about a plane containing the texture direction. Information was also found indirectly on the distribution of orientations azimuthally around the texture direction. Indeed, the extent of any sub-texturing can be quantified with this analysis.

An experiment consisting of a series of linescans along a polySi film parallel to the substrate surface was performed. There, the diffraction pattern from each scan was recorded and analysis of each pattern showed that the texture developed gradually through the film. The free surface of the film was found to be textured in the [110] direction with a mosaic spread of 3.0±0.5° and a tilt offset of 7±0.5°. As described in chapter 6, this gave an effective mosaic spread (a more useful description of the orientation distribution around the texture direction) of 17±1°.

Both techniques allowed quantitative descriptions of the grain orientations in a film but each had its own strengths and weaknesses. The Kikuchi technique was suited for a small number of grains and the grain thickness >20nm for an appreciable Kikuchi

pattern or Kossel lines. Investigation of a large number of grains was very time consuming as the average experimentation and analysis time for each was ≥5mins. The scanning technique was ideally suited for a large number of small grains in a rectangular shaped film. In a typical device both large and small grains were found, providing the need for both approaches. The process time for the scanning technique was predominantly less and would always be used if ≈50 grains or more were present.

8.2.4 Discussion

Three new approaches used to characterise the grain structure of conducting films found in modern devices were described. The techniques can all be implemented on typical STEMs without the need for peripheral attachments. As all the techniques were performed on cross-sectional samples, analysis can be performed on fully-processed devices without the need for material removal. The results from these analyses on a conducting film can help in the prediction of the electrical and mechanical properties of the film. Already, electromigration, which is a common mode of failure of a device, can be quantified using X-ray peak intensities and grain size distributions. The exact relationship between the peak intensities and the degree of texture is not straightforward, but could be determined empirically with the correct resources. Currently the *RC* delay of an interconnect is of major importance. This depends on the resistivity of the film which, in turn, depends on the grain sizes and orientations. No simple equation relates these variables but empirical approximations can be used.

The use of electron probes of a few nanometres in diameter imply that these techniques can also be used as device miniaturisation continues. Indeed, many of the existing techniques which were commonly used to perform these functions will shortly become inadequate for fine structure characterisation. It is becoming apparent that much materials characterisation will be performed using TEMs in the future and there is thus a sense of urgency about developing TEM techniques to replace the functions of existing techniques. It is likely that something as big as the silicon device industry will increasingly encourage the development of electron microscopy as a dedicated analytical tool.

8.3 Compositional Analysis of Device Materials

8.3.1 Introduction

Chapter 1 described several tools commonly used for compositional analysis in modern devices. These tools do not allow any subsequent analysis and the spatial resolution available on them will not be sufficient for useful analysis in future devices. The nanometre spatial resolution provided by the TEM is ideal for the type of compositional information required as the layers of materials reduce in thickness down to tens of atoms thick. Two main aspects of compositional analysis were required to be considered in materials characterisation. These were the detection of minute traces of contaminants and dopants, and the measurement of the diffusion between neighbouring materials. Both have to be performed on a nanometre scale. In chapter 7, EDX and PEELS were explored for their strengths in materials characterisation with respect to the detection sensitivity and spatial resolution. EDX was also used to test the effectiveness of a diffusion barrier in separating metals in the devices.

8.3.2 Sensitivity and Spatial Resolution

For any compositional analysis on a nanometre scale the area of interest has to be imaged beforehand or during the analysis. For this, the TEM is clearly an ideal instrument. The imaging capabilities of the TEM with respect to identifying areas of interest on devices was demonstrated in chapter 3. For the modified Philips CM20, the image resolution was typically ≈0.5nm in practice in CTEM and ≈5nm in STEM with normal probe currents. The STEM resolution can reduce to ≈1-2nm under certain microscope conditions. In chapter 3 the specimen preparation was also described as it was very important for the work performed there that a large electron transparent region existed on the samples. This way, possible avenues of investigation were more easily identified. Section 7.5 describes a drawback in using the TEM for materials characterisation. There an anomaly appeared in the device structures and was originally thought to arise from a serious fault in the fabrication of the device. After various types of microanalysis, the anomaly was attributed to an artefact of specimen preparation.

It is also very important to grasp from how small an area useful microanalysis can be performed. Chapter 2 described many of the theoretical factors determining the beam parameters for microanalysis. The beam properties are determined experimentally for the most commonly used microscope. Typical probe diameters range from above 18nm down to ≈1nm for the CM20 at Glasgow with the probe current decreasing by a factor of ≈1000 between these values. Only relative probe currents were quoted as little faith was put on the constant used in the manufacturers calculation. The probe diameter defines the lower limits of the spatial resolution of any microanalysis on that microscope. For the HB5 STEM, the spatial resolution was ≈1nm for the normal microscope configuration since a field emission gun was used.

The concentration sensitivity of EDX was calculated as being $\approx 2\times10^{20}$ atoms/ cm^3 for As in Si. This amounts to 0.5at%. This figure was up to 10^5 times more than that possible using existing techniques but these use a much larger volume of material. With EDX ≈50 atoms of As can be detected in Si in a 1nm probe, the other techniques cannot achieve this. The spatial resolution of EDX was shown to be ≈1nm using the VG HB5 microscope on a 20nm thick specimen. This drops to ≈2nm for a 40nm thick specimen. For the Philips CM20 at Glasgow, the spatial resolution of EDX in Si will be approximately equal to the incident probe diameter for a specimen thickness ≤50nm. Above 50nm the beam spreading, t, in the specimen becomes appreciable and its effect varies as $t^{3/2}$.

8.3.3 Experiments

A series of EDX acquisitions across a Ti/TiN diffusion barrier showed that no Si penetrated through the barrier into the Al and vice versa. Indeed it was shown that the barrier may have been unnecessarily thick. EDX, along with additional information from PEELS, was also used to show the specimen thickness through the barrier thereby illustrating the extent of preferential thinning of the materials during the felt polishing stages of specimen preparation. The thicker Ti/TiN layer explained the nature of the unknown material immediately underneath it. This material was investigated using

many forms of EDX analysis, and its presence was established as being a result of Si from the substrate being brushed up to the thicker Ti/TiN wall where it had accumulated. PEELS analysis was used to demonstrate how the same element could be differentiated according to its chemical environment. With much of the device consisting of Si and (to a lesser extent) N in different forms, there is the need to differentiate between them for chemical analysis. PEELS was also shown to detect elements which cannot be detected using EDX.

8.3.4 Discussion

For the detection of contaminants and the profiling of interfaces, EDX rates highly among similar techniques. It was shown that EDX can even detect the commonly used As in the doped active regions of a transistor. However, quantitative analysis at such a level would not be very accurate. The sensitivity of the technique may not be close to the best of the existing ones when the dopants are distributed over a large volume, but the technique does not preclude further reanalysis and the spatial resolution is far superior. All the elements found in today's devices can be detected using PEELS. The spatial resolution was similar to the probe diameter and the sensitivity was similar to EDX for thin specimens. Owing to the high energy resolution of PEELS, material properties including stress and vacancies can be monitored. This will become a very important attribute as film thicknesses decrease, as stress there may cause the film to rip apart.

8.4 Further Work

In my opinion, the most productive avenue for further theoretical work in compositional analysis is in developing the understanding of PEELS spectra in identifying the atomic environment of the element. Already it is realised that PEELS can detect practically every element with high sensitivity and with this additional knowledge the atomic arrangement of a particular part of a device can be inferred. With advances in refined processing of spectra and TEM gun design for minimal electron energy spread, the

information available from the analysis can be substantial. Clearly much work on many controlled experiments will have to complement any theoretical understandings and this is already under serious consideration in some establishments.

Indeed, the information from PEELS may not only be confined to compositional information. The conductivity and electromigration resistance of a film depends highly on the orientation mismatch between two grains. Probing the grain boundaries using PEELS could perhaps identify this mismatch, or the extent of the electron trapping there, giving information on these properties of the material. Furthermore, the beam can be scanned in a similar experiment to the texture development investigation described in chapter 6. The more textured areas have less lattice mismatch at the grain boundaries than randomly oriented ones so the spectra from the linescan may be different for the two cases. (This experiment was attempted, but the differences were not resolved with the equipment used. However a higher energy resolution may differentiate the two for some films.)

Considering texture measurements, the most promising existing technique is that of the orientation image mapping performed in the SEM using backscattered Kikuchi patterns to determine the grain orientations. This fully-automatic planar technique was described in chapter 1. The severe limitation of this technique is its spatial resolution. This technique is not accurate when either the grains are small (<20nm) or the film is more than one grain thick. This size limitation could be overcome by its introduction into TEM. Using the tripod polisher it is possible to obtain a large electron transparent region in the plane of the device. The specimen would contain the top surface of the film of interest. A CCD camera would receive the transmission Kikuchi pattern and the existing Kikuchi recognition software should not require many alterations. In fact the definition in the Kikuchi pattern will be improved in the TEM, providing better angular resolution. If this can be implemented, the orientations of grain sizes down to 5nm or less can be identified quickly and accurately. This method could also be used to calculate grain sizes at the same time.

A very interesting project to undertake would be to relate the results from the analysis on texture and grain size distributions to the electrical and mechanical properties of the film. As mentioned earlier, the mean time to failure of a metal interconnect is described by the grain size distribution and the ratio of the {111} and {200} peaks for Al (see equation 4.1). This empirical relation clearly only works for fcc materials but this encompasses all interconnects used and likely to be used. It would seem possible to relate the degree of texture, as defined in chapter 6, to the ratio of the X-ray peak intensities. Thus the grain size distribution and the degree of texture of a film could lead to the prediction of its lifetime. This approach will be particularly useful as film thicknesses continue to decrease since meaningful X-ray diffraction analysis would be impossible. The resistance of various polySi films ranging from randomly oriented grains to single crystal can be determined. Complementing this experiment, the resistance of a film having differing grain sizes but at a fixed degree of texture can be measured. This way, the grain size and orientation distribution of a film could be used to predict the resistivity of a film. A similar approach can be used to predict the surface roughness.

These experiments are essentially the next steps to fulfilling the primary aim of the work described in this thesis. The end objective is to be able to identify every property of a material on a nanometre scale. This includes knowing exactly what is there at that point for failure analysis, and what the performance of a material will be for product analysis. The use of TEM in device technology has been proven in this work to be almost essential for many aspects and its value is increasing significantly as device miniaturisation continues.

Appendix A: *Spreadsheet used to calculate grain orientation from Kikuchi pattern*

To calculate new pole at an angle φ from a known pole

				Length
Approx pole, ap	-5	5	4	8.124038
Kikuchi normal, kn	-4	-4	0	5.656854

φ, cm	2.1	+/-	0.1
φ, deg	6.006	+/-	0.3

				Length
kn x ap	-16	16	-40	45.9565
ap x (kn x ap)	-264	-264	0	373.3524

new pole	-0.68	0.53	0.48
length	1.0000		

Ratioed, np = (	-1.4011	1.0989	1	)
Guess, np = (	-3	2	2	)
error	3.868 degs			

To calculate g from new pole

Film No	2	5	9
pole, P	-1.4	1.1	1
vector, V	-4	-4	0

θ =	35	degrees
+/-	2	degrees
φ +/-	0.25	cms
+/-	0.715	degrees
error	2.12	degrees

n 1	-0.723
2	-0.428
3	-0.5415

Cal φ	2.86
	degs / cm

P x V	4	-4	10
(P x V) x P	-15	-18	-1.2

len	(P)	2.04206
len	(P x V)	11.4891

len (n)	1

ratio	n = (	-1.687	-1	-1.262	)

P.n
0

guesses	(1)	n = (	-5	-3	-4	
	len, n = root	50	error		1.71	degrees

Verdict
fine

	(2)	n = (	-7	-4	-5	)
	len, n = root	90	error		1.23	degrees

Verdict
fine

Appendix B: *Determination of the greyscale values around the {111} ring*

```
#include <math.h>
#include <stdio.h>
#include <stdlib.h>

#define a          190
#define Pi        3.1415
#define DMS       36100

int   hcoord,th_deg,xi,yi,i,j;
float x,y,r,theta,hf;
unsigned char    white,circ[3600],H[DMS];

FILE *out_x,*out_xx;

main()
{
out_x=fopen("/home/bigvern/lindsayr/recent/rich_in.bin","rb");
fread(H,1,DMS,out_x);
fclose(out_x);

r=(a-8)/2;

for(th_deg=0;th_deg<=3599;th_deg++)

      {
      theta=(th_deg*Pi)/1800.0;
      x=(r*cos(theta))+(a/2.0);xi=x;
      y=(r*sin(theta))+(a/2.0);yi=y;
      hf=(a*yi)+xi;
      hcoord=hf;
      circ[th_deg]=H[hcoord];
      }

white=(H[27783]+H[33074]+H[2901]+H[4770])/4;
printf("background=%d",white);


out_xx=fopen("/home/bigvern/lindsayr/recent/rich_out.txt","w");
for(th_deg=0;th_deg<=3599;th_deg++)
        {
      fprintf(out_xx,"%d\n",circ[th_deg]);
      }
fclose(out_xx);

}
```

Program used to accept raw image and determine the greyscale values around the {111} ring

Reads in raw image greyscale values

Extracting the greyscale values around the {111} ring

Calculating the average inelastic intensity

Output information as a column in a text file

Appendix C: *Greyscale DF Image to Binary Text File*

Program used to convert a greyscale DF image to a binary text file ready for spreadsheet analysis

```
#include <math.h>
#include <stdio.h>
#include <stdlib.h>

#define a  512
#define b  128
#define DMS   65536

int   i,y;
unsigned char    map[b][a],H[DMS];

FILE *out_x,*out_xx;

main()
{
out_x=fopen("/home/bigvern/lindsayr/recent/rich_in.bin","rb");
fread(H,1,DMS,out_x);
fclose(out_x);

for(i=0;i<b;i++)
      {
      for(y=0;y<a;y++)
            {map[i][y]=H[a*i+y];
             if(map[i][y]>100){map[i][y]=0;}
             if(map[i][y]<101){map[i][y]=1;}
            }
      }

out_xx=fopen("/home/bigvern/lindsayr/recent/rich_out.txt","w");
for(i=0;i<a;i++)
        {for(y=0;y<b;y++)
           fprintf(out_xx,"%d\t",map[y][i]);
       fprintf(out_xx,"\n");
      }
fclose(out_xx);
}
```

Opens image file 'rich_in.bin'

Places x & y pixel values into a 2D array then converts the greyscale to binary

Outputs array to text file for further spreadsheet analysis

GLASGOW UNIVERSITY LIBRARY